

Seismo-acoustic investigations of shallow free gas in the sediments of the Baltic Sea

Dissertation
zur Erlangung des Doktorgrades der Naturwissenschaften
am Fachbereich Geowissenschaften
der Universität Bremen

vorgelegt von
Tóth Zsuzsanna

Bremen, August 2013



Gutachter:

Prof. Dr. Volkhard Spieß

Prof. Dr. Bo Barker Jørgensen

Contents

Thesis abstract	9
Zusammenfassung	11
1 Introduction	13
1.1 Shallow gas in marine sediments	13
1.2 Acoustic properties of gassy sediments	16
1.3 Expressions of shallow gas in seismo-acoustic records	18
1.4 Motivation and objectives	26
1.4.1 Shallow gas in Baltic Sea sediments	26
1.4.2 Baltic Gas	27
1.4.3 Research objectives	28
1.5 Outline of the research articles	29
1.5.1 Contributions to other research articles	30
1.6 Geological history of the Bornholm Basin	32
1.7 Data and methods	34
1.7.1 Data acquisition	34
1.7.2 Seismic data processing	37
2 Seismo-acoustic signatures of shallow free gas in the Bornholm Basin, Baltic Sea	42
2.1 Introduction	42
2.2 Geological setting	44
2.2.1 Quaternary sediments	44
2.2.2 Shallow gas in the Bornholm Basin	46
2.3 Seismo-acoustic dataset	46
2.3.1 Multichannel seismics	46

2.3.2	Parasound sediment echosounder	47
2.4	Results and discussion	47
2.4.1	Seismic stratigraphy	48
2.4.2	Seismo-acoustic gas signatures in the Bornholm Basin	48
2.4.3	Frequency dependence in the seismo-acoustic imaging of shallow gas	56
2.4.4	Shallow gas signatures in seismo-acoustic data	58
2.5	Conclusions	62
	Acknowledgments	63
3	Estimating the free gas content in Baltic Sea sediments using compressional wave velocity from marine seismic data	64
3.1	Introduction	64
3.2	Bornholm Basin	66
3.3	Data and methods	68
3.3.1	Seismo-acoustic data	68
3.3.2	Seismic processing and velocity determination	69
3.3.3	Geoacoustic model for estimation of the gas content	70
3.4	Results	71
3.4.1	Interpretation of the seismo-acoustic data	71
3.4.2	Interval velocities	73
3.4.3	Gas content	78
3.5	Discussion	79
3.5.1	Uncertainty of the interval velocities	79
3.5.2	Variability in the interval velocities	80
3.5.3	Velocity reduction - gas content	82
3.5.4	Gas distribution and amount in Bornholm Basin sediments	82
3.6	Conclusions	85
	Appendix - Geoacoustic model	86
	Acknowledgments	87
4	Frequency dependence in seismo-acoustic imaging of shallow free gas due to gas bubble resonance	88
4.1	Introduction	88
4.2	Theory of the acoustic behaviour of gas-bearing sediments	90
4.3	Geological setting in the Bornholm Basin	92

4.4	Surveys and data	92
4.4.1	Seismo-acoustic dataset	93
4.5	Amplitude analysis	97
4.6	Results	100
4.6.1	Multichannel seismic and echosounder data	100
4.6.2	Multiple filter analysis	102
4.6.3	Attenuation in the gassy sediment	103
4.6.4	Model-predicted bubble sizes and gas content	103
4.7	Discussion	106
4.8	Conclusions	109
	Appendix - Geoacoustic model	110
	Acknowledgments	112
5	Conclusions and outlook	113
	Appendix - Contributions	117
A	One year of continuous measurements constraining methane emissions from the Baltic Sea to the atmosphere using a ship of opportunity	117
B	A low frequency multibeam assessment: Spatial mapping of shallow gas by enhanced penetration and angular response anomaly	137
C	Sulphate and methane fluxes and organic matter mineralization across a Holocene mud layer of increasing thickness in Aarhus Bay (Baltic Sea)	144
	Bibliography	172
	Acknowledgement	181

List of Tables

1.1	Descriptions of seismo-acoustic shallow gas signatures and their terminology in the literature	23
1.2	Seismo-acoustic shallow gas signatures published in the scientific literature. Reference table with the equipment, frequency, location	24
2.1	Gas signatures and what they tell about shallow free gas in the Bornholm Basin	60
3.1	Values of parameters used to calculate gas content from interval velocities in the gassy sediments of the Bornholm Basin. Anderson & Hampton model, 'below resonance frequency'.	72
3.2	Average interval velocities in stratigraphic units, their average two-way travel time, depth, and gas content, calculated based on the compressible fluid model of Anderson & Hampton	77
4.1	Observed resonance peaks and the attenuation measured at Horizon 7 in the filtered Parasound and SES echosounder data, and predictions of the Anderson & Hampton model for bubble radius and gas contents	104
4.2	Values of parameters used to calculate bubble size and gas content in the gassy sediments of the Bornholm Basin. Anderson & Hampton model, including gas bubble resonance . . .	107

List of Figures

1.1	Decreasing sulfate and increasing methane concentration gradients indicating the sulfate-methane transition zone (SMTZ) in marine sediments	14
1.2	Physical models of gas-bearing marine sediments	16
1.3	Acoustic behaviour of fully water-saturated and gas-bearing marine sediments	17
1.4	Acoustic turbidity in a 3.5 kHz sub-bottom profile from the Eckernförde Bay, Baltic Sea .	20
1.5	Analogue sparker profile showing reversed polarity reflections and their strong multiples due to the presence of shallow gas, in front of the Belgian coast	21
1.6	Shallow gas contour map in the Kattegat, Skagerrak and western Baltic Sea, based on high frequency acoustic data (project METROL)	26
1.7	Paleogeographic maps showing the late and postglacial Baltic Sea stages during the last deglaciation	32
1.8	MSM16/1 (2010) cruise track, seismo-acoustic data and sediment cores in the Baltic Sea .	35
1.9	Profiles of the seismo-acoustic survey in the Bornholm Basin (MSM16/1, AL402)	36
1.10	Seismic data processing flows applied to shallow water data recorded during cruises MSM16/1 and AL402	38
1.11	The two-way travel times of a horizontal reflection in single channel and multichannel seismic data recording	39
2.1	Location of the study area in the the Bornholm Basin, Baltic Sea.	45
2.2	Lines of the Bornholm Basin seismo-acoustic survey. The location of the examples presented in the chapter are indicated with the respective number of the figures.	47
2.3	Seismic stratigraphy in the Bornholm Basin in high frequency Parasound echosounder and multichannel seismic data	49
2.4	Maps of the shallow gas front (top of acoustic blanking) on Parasound SLF echosounder data and seismic gas signatures found in lower frequency multichannel seismic data. . . .	50

2.5	Shallow gas imaged with the Parasound echosounder. Gas bubbles in the Holocene mud appear as a patch or layer of point scatterers with highly variable amplitudes, and they cause acoustic blanking as the scattering in the gassy layer disrupts the sediment layering.	52
2.6	The formation of seafloor - gas reflection interference and seafloor polarity reversal in multichannel seismic data at the edge of the area with shallow gas.	54
2.7	Polarity reversal due to the free gas in multichannel seismic data	55
2.8	Reverberation and strong multiples in multichannel seismic data due to the presence of shallow gas close to the seafloor.	57
2.9	Bubble resonance frequency as a function of gas bubble radius for Bornholm Basin sediments based on the theory of Anderson & Hampton	59
3.1	Map of the Bornholm Basin, Baltic Sea with the location of the seismic profile GeoB10-044	67
3.2	Stratigraphy of the Quaternary sediments in the Bornholm Basin represented in a high frequency Parasound profile	68
3.3	Marine seismic data processing flow applied to profile GeoB10-044.	70
3.4	Profile GeoB10-044. Multichannel seismic, Parasound echosounder data and their overlay	74
3.5	Stratigraphical interpretation of profile GeoB10-044	75
3.6	Interval velocities superimposed on the seismic traces of the profile GeoB10-044 and a close-up of the two gas patches with the layer boundaries, where average interval velocities were calculated	76
3.7	Average interval velocities in the stratigraphic units along profile GeoB10-044	78
3.8	The relationship between compressional wave velocity and gas content in the compressible fluid model of Anderson & Hampton	79
3.9	Schematic figure of the organic matter, dissolved methane and sulfate, and free methane gas concentration in the sediments of the Bornholm Basin.	84
4.1	Acoustic response of gassy sediments as a function of frequency based on the model of Anderson & Hampton	91
4.2	Location of the study area in the western part of Bornholm Basin at the edge of a small shallow gas patch	93
4.3	Multichannel seismic, Parasound and SES echosounder data along the same transect in the Bornholm Basin, Baltic Sea, imaging shallow free gas	95
4.4	Envelope stacks at the transition from non-gassy to gassy sediments, from which the maximum amplitude of the seafloor and denoted horizons beneath were analysed	98
4.5	Frequency spectra of the Parasound and SES echosounder data	99

4.6	Part of the transect in the PS 4.3 kHz echosounder data and after frequency filtering in the different 1 kHz wide frequency bands	101
4.7	Results of the amplitude analysis on the echosounder data. The amplitude loss measured at Horizon 7 in the gassy sediment as a function of the echosounder measurement frequency	102
4.8	Attenuation curves from the filtered multichannel seismic, Parasound 4.3 kHz and SES 4.1 kHz data, based on the amplitude losses measured at Horizon 7	105

Thesis abstract

Shallow methane gas is generated in Holocene muddy sediments in many areas of the Baltic Sea. Free gas poses a challenge for high frequency acoustics as it impedes imaging of the sedimentary structure. However, better understanding of methane-related processes in the Baltic Sea requires a more detailed study of the geological background of methane production, migration, depth distribution in the sediment and its potential release. Utilizing a variety of multichannel seismic and multi-frequency acoustic instruments, this thesis focuses on the investigation of the frequency dependence in seismo-acoustic imaging of shallow free gas and the development of methods to characterize free gas occurrences and estimate the content in Baltic Sea sediments. A seismo-acoustic data set collected over the gassy area of the Bornholm Basin, south-western part of the Baltic Sea, was processed and analysed. The data set included high frequency sediment echosounder data in nine frequency bands and low frequency multichannel seismic data, covering a frequency range between 0.2 and 43 kHz.

The identification and mapping of seismo-acoustic gas signatures in the Bornholm Basin revealed dependence on the measurement frequency as well as on the resonance of gas bubbles in the sediment. Free gas responds as an integrated field of point scatterers in high frequency acoustic data, and it causes several distinct phenomena: (a) extensive acoustic blanking zones, (b) reversed polarity reflection in the lower frequency seismic data, (c) depending on the proximity of the gas front to the seafloor, interference of the seafloor and gas reflection, (d) seafloor polarity reversal, and (e) reverberation. In the resonance frequency range of larger gas bubbles, between 3 and 5 kHz, high scattering causes complete acoustic blanking beneath the gassy sediment layer. In the wider resonance frequency range, between 3 and 15 kHz, the effect of smaller bubbles becomes dominant and lower attenuation allows reflections to be observed beneath the gassy sediment layer. Above resonance, beginning at ~ 19 kHz, attenuation causes decreased reflection amplitudes, while below resonance, below ~ 1 kHz, attenuation is generally very low and not dependent on frequency.

A 2D high resolution velocity field obtained from pre-stack time migrated seismic data revealed two low-velocity patches in mud-filled depressions, which extend from shallow reversed polarity reflections

down to the base of the Holocene mud layer. Compressional wave velocities in the sediment are highly sensitive to free gas, and very small amounts of gas cause a significant decrease in the medium velocity. Average interval velocity values within the gassy mud are lower by up to 500 m/s than the seafloor migration velocity. This interval velocity drop, using the geoacoustic model of Anderson & Hampton that relates compressional wave velocity to sediment physical properties and gas content, is caused by an average $\sim 0.045\%$ gas volume fraction in the sediment. Based on the high resolution interval velocity field and the seismo-acoustic profiles, shallow gas occurs throughout most of the Holocene mud. Although the depth distribution of free gas is patchy in the sediment, the gas concentration is likely to have a peak beneath the sulfate-methane transition zone and gradually decrease below.

At the edge of a gassy patch in the Bornholm Basin, compressional wave attenuation caused by the presence of gas bubbles was estimated from reflection amplitudes beneath the gassy sediment layer. Using the geoacoustic model of Anderson & Hampton, the observed frequency boundaries of the resonance effects suggest gas bubble sizes between 1 and 4-6 mm, and gas volume fraction in the sediment up to 0.0002% in a 2 m thick sediment layer where most of the gas bubbles seem to be concentrated. This small amount of gas already considerably attenuates the downward propagating acoustic waves, causing partial acoustic blanking.

This study demonstrated that interval velocities obtained from multichannel seismic data can be used for the assessment of free gas concentration at in situ pressure and temperature in shallow marine sediments. The measurement of the velocity reduction caused by free gas is possible even when only a small amount ($> 0.01\%$) of free gas is present in the sediment. Due to the frequency dependence of the seismic response from gas-bearing sediments, a low source frequency well below the resonance frequency of gas bubbles is needed to penetrate through the gassy sediment layer, but on the other hand sufficiently high as well to maintain high vertical resolution of the subsurface structures. With the multi-frequency acoustic approach, the measurement of the compressional wave attenuation allows quantification of free gas content in shallow marine environments as long as the measurement frequency reveals the resonance frequency peak. Certainly, the method presented in the Bornholm Basin case study, is limited to places with only moderate attenuation, where the amplitudes of a reflection can be analysed beneath the gassy sediment layer.

Zusammenfassung

Flaches Methangas wird in Holozänen Sedimenten in weiten Teilen der Ostsee produziert. Dieses freie Gas stellt eine Herausforderung für hochfrequente akustische Methoden dar, da es die Abbildung von sedimentären Strukturen erschwert. Ein besseres Verständnis von Prozessen in der Ostsee die mit Methangas zusammen hängen erfordert die detaillierte Untersuchung des geologischen Zusammenhanges der Methanentstehung und -wanderung sowie der Tiefenverteilung und möglichen Freisetzung des Gases. Diese Arbeit beschäftigt sich mit der Frequenzabhängigkeit der akustischen und seismischen Abbildung von flachen Gasvorkommen und der Entwicklung von Methoden zur Charakterisierung und Quantifizierung. Zu diesem Zweck werden eine Vielzahl von seismischen und akustischen Methoden angewandt, so etwa Mehrkanalseismik und akustische Systeme mit verschiedenen Frequenzen. Ein seismo-akustischer Datensatz im Bornholmer Becken in der südwestlichen Ostsee wurde hierzu aufgenommen, prozessiert und analysiert. Die Daten umfassen hochfrequente Sedimentecholotdaten in neun verschiedenen Frequenzbändern sowie niederfrequente mehrkanalseismische Daten. Die Methoden decken insgesamt einen Frequenzbereich von 0,2 bis 43 kHz ab.

Die Identifikation und Kartierung von seismo-akustischen Gassignaturen im Bornholmer Becken zeigte eine Abhängigkeit von der Messfrequenz sowie von der Resonanz der Gasblasen. Freies Gas zeigt eine Signatur von zusammenhängenden Punkstreuern in hochfrequenten akustischen Daten. Diese Signatur verursacht verschiedene Phänomene: (a) großflächige akustische Schattenzonen, (b) Reflektionen umgekehrter Polarität in niederfrequenten seismischen Daten, (c) Interferenz zwischen Meeresboden- und Gasfrontreflektion, abhängig von der Tiefe der Gasfront, (d) negative Polarität der Meeresbodenreflektion und (e) akustisches Nachschwingen. Im Bereich der Resonanzfrequenz von größeren Gasblasen, zwischen 3 und 5 kHz, zeigen sich starke Streueffekte die ein komplettes Auslöschen von akustischen Signalen unterhalb der gasführenden Schicht hervorrufen. Der breitere Resonanzfrequenzbereich von 3 bis 15 kHz zeigt einen vorherrschenden Einfluss der kleineren Gasblasen und geringere Dämpfung, die es ermöglicht auch Reflektionen unterhalb des Gases aufzunehmen. Über der Resonanzfrequenz, ab ca. 19 kHz, erzeugt die Dämpfung durch das Gas abgeschwächte Reflektionen. Frequenzen unterhalb der Resonanzfrequenz, also

unter ca. 1 kHz, zeigen sehr geringe Dämpfung die auch nicht frequenzabhängig ist.

Ein hochauflösendes 2D Geschwindigkeitsfeld erstellt mit Hilfe der pre-stack time migrated seismischen Daten zeigt zwei Stellen mit niedrigen Geschwindigkeiten in mit Schlick gefüllten Vertiefungen die sich von flachen Reflektionen mit umgedrehter Polarität bis hin zur Basis der Holozänen Schlickschicht erstrecken. Die Geschwindigkeit von P-Wellen im Sediment sind hochgradig abhängig von freiem Gas. Schon niedrige Gasgehalte können deutliche Verringerungen der durchschnittlichen seismischen Geschwindigkeit der Sedimente hervorrufen. Durchschnittliche Intervallgeschwindigkeiten innerhalb der gasführenden Schichten sind bis zu 500 m/s geringer als die Migrationsgeschwindigkeit des Meeresbodens. Dieser Abfall der Intervallgeschwindigkeit wird durch ein durchschnittliches Gasvolumen von $\sim 0,045$ Volumen-% des Sediments verursacht, wenn man das geoakustische Modell von Anderson & Hampton betrachtet, welches P-Wellengeschwindigkeit mit sedimentphysikalischen Eigenschaften und Gasgehalt in Zusammenhang bringt. Basierend auf hochauflösenden Intervallgeschwindigkeiten und seismo-akustischen Profilen wurde flaches Gas in den meisten Bereichen des Holozänen Schlicks gefunden. Obwohl die Gasverteilung im Sediment fleckenhaft ist, ist es wahrscheinlich, dass die höchste Gaskonzentration unterhalb der Sulfat-Methan Übergangszone liegt und allmählich nach unten hin abnimmt.

Am Rand einer gasreichen Gegend im Bornholmer Becken wurde die P-Wellendämpfung durch Gasblasen von Reflektionsamplituden darunterliegender Schichten abgeschätzt. Mit Hilfe des geoakustischen Modells von Anderson & Hampton wurde eine Abschätzung der Gasblasengrößen vorgenommen. Sie liegen zwischen 1 und 4-6 mm und das Gasvolumen im Sediment beträgt 0,0002% in einer 2 m mächtigen Schicht in der ein Großteil der Gasblasen auftritt, basierend auf den beobachteten Frequenzgrenzen des Resonanzeffektes. Dieser kleine Anteil von Gas im Sediment führt schon zu einer deutlichen Dämpfung der sich nach unten ausbreitenden akustischen Wellen, was zu teilweiser akustischer Schattenbildung führt.

Diese Arbeit zeigt, dass Intervallgeschwindigkeiten aus mehrkanalseismischen Daten zur Beurteilung des Gasgehalts bei in-situ Druck und Temperatur in flachen marinen Sedimenten benutzt werden können. Die Messung der Geschwindigkeitsverringerung durch freies Gas ist auch möglich falls nur ein geringer Anteil an Gas ($> 0,01\%$) im Sediment vorhanden ist. Eine niederfrequente seismische Quelle, unterhalb der Resonanzfrequenz, ist nötig um die unter dem Gas liegenden Schichten abbilden zu können, wegen der Frequenzabhängigkeit der akustischen Eigenschaften einer gasführenden Schicht. Gleichzeitig muss die Quelle aber genügend hochfrequente Signale aussenden um die Schichten möglichst hochauflösend abzubilden. Der akustische Ansatz mit mehreren Frequenzen erlaubt eine Messung der P-Wellendämpfung und damit eine Quantifikation des freien Gases in flachmarinen Gebieten solange die Resonanzfrequenz durch die benutzten Frequenzen abgedeckt ist. Beschränkt wird die Methode die im Bornholmer Becken angewandt wurde durch die Notwendigkeit der Amplitudenanalyse von Reflektionen unterhalb der gasführenden Schichten, wodurch nur Gegenden mit moderater Dämpfung untersucht werden können.

Chapter 1

Introduction

1.1 Shallow gas in marine sediments

The occurrence of shallow methane gas in marine sediments is widespread. Evidence for its presence has been reported from a wide variety of oceanographic and geological settings (Fleischer et al., 2001; Judd, 2003). Gas in marine sediments originates from either bacterial or thermogenic reduction of organic matter, however, in surficial, shallow-water sediments the methane is mostly of biogenic origin (Floodgate & Judd, 1992). Methanogenic microorganisms produce methane as a metabolic byproduct in anoxic conditions. Areas of rapidly accumulating, fine-grained muddy sediments rich in organic matter provide ideal environments for the production of this biogenic methane. Coastal areas, adjacent seas, river deltas and other high productivity areas of the continental shelf are therefore hotspots of methane formation, and only 5% of the worldwide marine methane production occurs at ocean depths greater than 1000 m.

Methane production

Methane (CH_4) is produced by archaea through the subsurface degradation of organic matter. Close to the seabed, microbial breakdown of buried organic matter is done by sulfate-reducing bacteria. Deeper in the sediment, where all sulfate has been exhausted in the sediment pore water, methane producing microorganisms and thus methanogenesis become dominant. As the CH_4 concentration builds up, CH_4 migrates upwards by diffusion or in the form of gas bubbles, and is oxidized to CO_2 in the sulfate-methane transition zone (SMTZ) (Fig. 1.1). Most of the CH_4 is effectively broken down at this depth by anaerobic methane oxidation (AOM) and this proves the SMTZ to be an effective barrier against methane escape (Reeburgh, 1969; Sansone et al., 1978; Boetius et al., 2000; Reeburgh, 2007). Supersaturation of CH_4 , however, often leads to the formation of free gas beneath the SMTZ (Fig. 1.1). Once the partial pressure

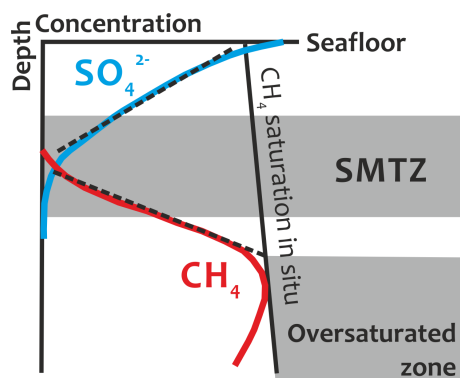


Figure 1.1: The decreasing sulfate (SO_4^{2-}) and increasing methane (CH_4) concentration gradients indicate the sulfate-methane transition zone (SMTZ) in marine sediments. In the SMTZ, methane is oxidized with sulfate as the terminal electron acceptor. The depth of the SMTZ can range from centimeters to meters under the seafloor surface depending on the local conditions. Below the SMTZ oversaturation of CH_4 can lead to free gas accumulation.

of CH_4 overcomes the ambient hydrostatic pressure, free methane bubbles will form. When gas-charged sediments lose their capacity to retain the gas bubbles or the escape of gas is triggered by external forces such as earthquakes or storms, methane is released through seepages or in an eruptive manner.

The formation of gas bubbles

Bubble formation in the sediment requires oversaturated conditions. For bubbles in water, there is an equilibrium bubble radius for any value of supersaturation; small bubbles theoretically will be driven into solution because the pressure from the surface tension at the bubble-water interface will increase as the bubble radius decreases (Anderson & Hampton, 1980). In sediments, bubbles form when there is sufficient pressure of dissolved gas to nucleate and maintain a bubble of equilibrium size. Analogously to bubbles in water, bubble pressure equilibrium in the sediment interstitial water will establish a minimum bubble size of 1-10 μm (Anderson & Hampton, 1980). There are no in situ observations regarding the nucleation of a bubble in sediments, but it is hypothesized that nucleation starts at a solid particle or there exist pre-formed bubbles to act as accretion sites (Boudreau, 2012). Depending on the gas, solubility/saturation and the molecular diffusion coefficient of the gas, the bubble grows in the porewater. Beyond the pore scale, in unlithified, surficial, cohesive, fine-grained sediments, bubbles may grow by an elastic fracture mechanism (Johnson et al., 2002; Boudreau, 2012). This theory assumes that the solid is not internally perfect, but contains flaws, which failure will lengthen as fractures. Nevertheless, bubbles may not always create their own fractures, as they can also encounter pre-existing cracks, fill and expand them (van

Kesteren & van Kessel, 2002).

Maximum bubble size will be determined by the ability of the sediment to resist the increasing buoyant force on bubbles of increasing size. As the bubble grows, it deforms the sediment framework, eventually it becomes large (mm size) and buoyant enough to migrate. Sometimes large bubbles (> mm size) are also observed to be held in place in the sediment. Average bubble sizes range from 0.5 to 5 mm, while bubble sizes in the order of cm are rarely observed (Anderson & Hampton, 1980; Abegg & Anderson, 1997; Wilkens & Richardson, 1998). As a result of the coupling between gas supply (methane production or supersaturation) and sediment mechanics, Algar & Boudreau (2010) show that it is possible for a bubble to stop growing even within a concentration gradient of dissolved methane, and reach an equilibrium between the gas flux into the bubble from below and the flux of gas out on the top.

Bubble growth by fracture should correspond to bubbles that are coin- or disk-shaped and fractures are favoured in the vertical (upward) direction (Johnson et al., 2002; Boudreau, 2012). In situ bubble sizes from 0.5 to 10 mm equivalent radius (diameter of a sphere with volume equal to the actual volume of the bubble) were observed in X-ray computed tomography (CT) scans of pressurized cores from the muddy sediments of Eckenförde Bay, Baltic Sea (Abegg & Anderson, 1997; Anderson et al., 1998). The lower detection limit of the method was ~ 0.42 mm, and most bubbles indeed were found to be 'coin shaped' oblate spheroids standing in a vertical orientation (larger bubbles) or near spherical (smaller bubbles).

Methane bubbles are also associated with methane hydrates, which form in low temperature environments, in polar regions or under sediments on the ocean floors. Free gas bubbles are both an underlying gas source for the formation of gas hydrates, which are only stable in the gas hydrate stability zone, and a product of their dissociation.

Physical models of gassy sediments

Anderson et al. (1998) proposed three basic types for the physical description of gassy sediments, depending on the relationship between gas bubbles, the interstitial water and sediment solid particles (Fig. 1.2). Type I, *interstitial bubbles* are very small bubbles wholly contained in the interstitial spaces of the sediment framework of solid particles (small bubble model); Type II, *reservoir bubbles* are occupying space bigger than the size of the pore space, but leave the sediment framework undistorted; and Type III, *sediment-displacing bubbles* or *gas voids* are large bubbles compared to the individual pore space and may slightly distort the sediment.

Small spherical Type I bubbles occur in sand-size sediments, although most gas bubbles observed in cores from fine-grained sediments are sediment-displacing or reservoir type bubbles (Anderson et al., 1998; Jackson & Richardson, 2007). A silty clay sediment would be unlikely to have interstitial pore sizes greater than 10 microns, so the interstitial small bubble model where gas is entirely surrounded by water

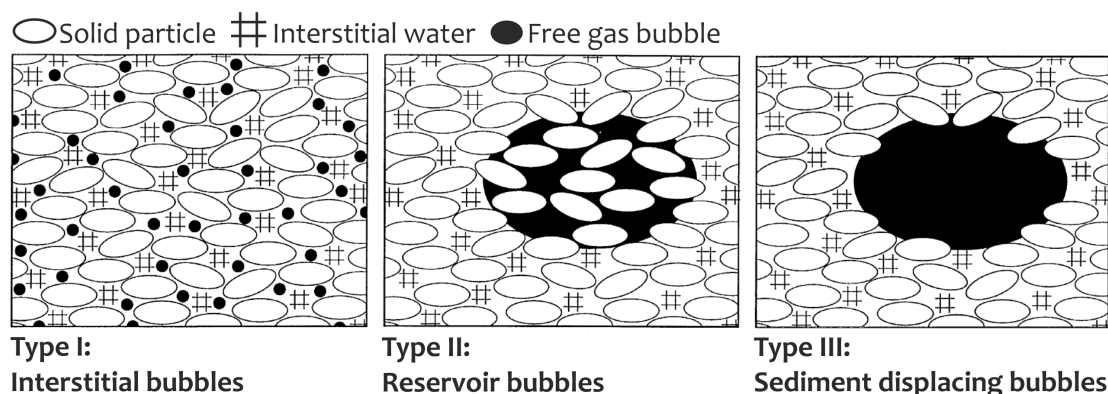


Figure 1.2: Physical models of gas-bearing marine sediments (after Anderson et al., 1998).

might not be an appropriate description for muddy gas-bearing sediments because of the restriction of minimum possible size of a gas bubble in water (Anderson & Hampton, 1980; Gardner, 2000).

Wheeler (1988) developed a conceptual model for the structure of sediments containing large bubbles, in which the matrix of saturated sediment surrounds isolated gas-filled pockets greater in diameter than sediment particles. This *large bubble model* assumes that bubbles are spherical gas cavities within sediments, which are forced open by the gas pressure working against the capillary pressure and the load of the overlying sediment and water column. The model was expanded in subsequent publications of Wheeler & Gardner (1989) describing the elastic moduli of sediments containing large bubbles, Wheeler (1988) discussing the movement of large gas bubbles, and Sills et al. (1991) about the behaviour of gassy sediments regarding strain and strength.

1.2 Acoustic properties of gassy sediments

Gas bubbles in the sediment under small strains (acoustic perturbations), oscillate radially or resonate at a fundamental frequency related to their size. The theory of Anderson & Hampton (1980) predicts that bubble resonance dominates the sound speed and attenuation of unconsolidated gas-bearing sediments (Fig. 1.3). Sound speed and attenuation are therefore controlled by gas bubble size, the acoustic frequency, and their mutual relation.

For acoustic frequencies well *below bubble resonance* (when the wavelength is considerably greater than the bubble size), the acoustic response is that of the bulk medium, that is only the bulk properties of the gas-water-sediment mixture matter. In this case the compressional wave velocity may be significantly reduced even by small amounts of free gas. *At or near resonance frequency* (when bubble sizes are in

Compressional wave	Fully saturated sediments (without any gas content)	Gas-bearing sediments		
		below f_0	at or near f_0	above f_0
velocity	function of porosity, generally increasing with depth; slightly frequency dependent	reduced	rapidly exceeds the gas-free velocity	equals the gas-free velocity
attenuation	function of grain size, porosity, generally increasing with depth; linearly dependent on frequency	higher than in gas-free sediment	strongest	higher than in gas-free sediment

Figure 1.3: Acoustic behaviour of fully water-saturated and gas-bearing marine sediments. Different compressional wave velocity and attenuation are predicted in gas-bearing sediments due to the resonance of gas bubbles (after Anderson & Hampton, 1980; Jackson & Richardson, 2007).

the same order of magnitude as the wavelength), the gassy sediment is highly dispersive and the velocity can greatly exceed the gas-free velocity. Compressional wave attenuation is highest at a frequency near the bubble resonance frequency. At frequencies *above bubble resonance* (when bubble sizes are approx. same order of magnitude as or larger than the wavelength), the bubbles scatter the sound. The acoustic response is essentially that of the surrounding medium, so the sound speed remains constant at a value commensurate with the gas-free sediment. Attenuation decreases rapidly below and above bubble resonance, though it still will be higher than in the gas-free sediment. Above bubble resonance, attenuation will be increasingly affected by increasing quantities of gas.

The theory of Anderson & Hampton was studied and evaluated against laboratory sediment samples containing large gas bubbles by Gardner (2000). Based on velocity and attenuation measurements, they concluded that the acoustic response of gassy sediments is broadly as predicted below and above the resonance frequency range of bubbles, but probably inappropriate within the resonance frequency range. At frequencies below resonance, sound speed based on bulk material properties of gassy sediment samples containing large bubbles was shown to match the measurements better than sound speed based on the compressible fluid model of Anderson & Hampton (Gardner & Sills, 2001). The abrupt change in velocity, caused by the substantial compressibility of gas, happens to a lesser extent when considering large bubbles, because the gas is contained in structural pockets in the saturated matrix, and it has a lower compressibility than a gas bubble formed in fluid. The attenuation measurements of Gardner (2003) demonstrated that the Anderson & Hampton model is valid for the lower frequencies of bubble resonance, but very sensitive to inaccurate sediment elastic and damping properties, into which the model superimposes the acoustical effects of bubble resonance.

1.3 Expressions of shallow gas in seismo-acoustic records

Attenuation of the acoustic signal in the mud-filled basins changes from very low to very high where free gas bubbles are present, thus the detection of shallow gas by acoustic methods has been also called 'the basin effect' (from the German 'Beckeneffekt'). Certain anomalies, acoustically turbid or blank zones on sub-bottom profiles were inferred to be indicative of free gas already during early applications of echosounders for seafloor exploration. The phenomena were first described by Schüller (1952) on echograms from the south-western Baltic Sea, indicating cloudlike features found in mud layers and characterized as acoustically impenetrable sediment zones.

The presence of gas in shallow marine environments is easily detected by geophysical surveys, as free gas content in seafloor sediments severely affects the propagation of acoustic energy. This leads to the creation of a variety of seismic signatures on seismo-acoustic profiles. Acoustic turbidity and blanking are the most frequently cited seismo-acoustic evidences (Fleischer et al., 2001), but other signatures such as reflectors with enhanced amplitude or reversed polarity, reverberation, and velocity pull-down are also well-known indicators of free gas. Often only one kind of feature refers to the presence of gas, but mostly their combination appears. Although only indirectly, topographic features, e.g. pockmarks and seabed domes seen on acoustic data can also point to free gas accumulations in the subsurface.

In this section, we review the seismo-acoustic expressions of shallow gas in the scientific literature. A summary of the descriptions of the gas signatures and their terminology is listed in Table 1.1, while equipment, frequency of the acoustic/seismic sources, locations, and references are listed in Table 1.2.

Acoustic turbidity and blanking

The most commonly cited evidence of the presence of gas in shallow marine sediments are *acoustic turbidity* and *acoustic blanking* (Fleischer et al., 2001; Judd & Hovland, 2007), which are mostly recognized on high frequency acoustic data (Table 1.2).

Acoustic turbidity is described as part of the acoustic section where reflections are chaotic (turbid) or revealing a variable degree of disturbance. These reflections often resemble a dark smear (higher amplitudes) and obliterate other reflections originating from internal stratification of the sediment. The high amplitude smear can either be large in its vertical extent and entirely mask the underlying sediment layering (Anderson & Bryant, 1990; Taylor, 1992), or relatively thin and associated with the total loss of acoustic returns from below (Anderson & Bryant, 1990; Garcia-Gil et al., 2002; Baltzer et al., 2005; Bertin & Chaumillon, 2005). Sometimes, in these acoustically turbid zones, faint but coherent reflectors can be followed despite their reduced amplitude (Taylor, 1992; Garcia-Gil et al., 2002). The blank patches beneath the high amplitude smear or sometimes a stronger reflector, where reflections are completely absent, is referred to as *acoustic blanking*, *acoustic masking* or *wipeout zones*. The upper boundary of

acoustic turbidity and/or blanking is the *gas front* (Judd & Hovland, 2007), which denotes the top of the gas-charged sediment layer. In some cases the gas front can be identified as a strong, coherent reflector, sometimes even with a clear reversed polarity (Garcia-Gil et al., 2002; Baltzer et al., 2005; Mathys et al., 2005). The top reflection of the gas-charged sediment can have various shapes: from the sharp, consistent, seafloor simulating reflection to moderately or highly irregular top reflection (for example, see the classification of Kim et al. (2008)).

Both acoustic turbidity and blanking are common and easily recognized, although their description is often mixed and the terms being used for both phenomena (e.g. see Fig. 1.4 and 1.5). Different descriptive terms based on the extent of the turbidity and/or blanking zone and a few other characteristics exist, e.g. blanket, curtain, column, plume (Taylor, 1992; Garcia-Gil et al., 2002; Baltzer et al., 2005), mainly referring to the horizontal extent (Table 1.1). The edges of the blanking zones also seem to be variable in shape and are therefore distinguished: they can be distinct and sharp, abruptly terminated, or they can have a characteristic convex shape and downward dipping reflectors on the sides (Taylor, 1992; Garcia-Gil et al., 2002; Baltzer et al., 2005). However, these different terms are not used consistently between authors. Judd & Hovland (2007) in their summary of geophysical indicators of shallow gas preferred to accept that shallow gas, in the form of acoustic turbidity, which is or is not associated with blanking, may occur in areas of any shape and size. In their opinion the term acoustic blanking itself is not an indicator of the presence of free gas, rather a zone devoid of reflections.

The high amplitude smear and the chaotic seismic texture of acoustic turbidity is attributed to scattering of acoustic energy by the gas bubbles (Judd & Hovland, 1992). This kind of reflection pattern can also be caused by other point scatterers, such as coarser grains in poorly sorted sediments. However, stratigraphic interpretation, other recognizable gas signatures or the possibility of establishing the connection to the source of gas can make the identification unambiguous. Acoustic blanking is the result of strong attenuation of the acoustic signal due to absorption and scattering by gas bubbles to the extent that there is no penetration deeper. Blanking can also be caused by the reflection of a high proportion of the acoustic energy at a hard sediment interface, e.g. in sand. The seismic facies appear homogeneous and characterized by the absence of sediment layering, which resembles acoustic blanking. The difference between acoustic turbidity and acoustic blanking, by some of the authors, is suspected to be the amount of free gas accumulated in the sediment (e.g. Baltzer et al., 2005).

Enhanced reflections

Coherent reflectors which have an anomalously increased amplitude over some distance are called *enhanced reflections* in shallow acoustic profiles (Judd & Hovland, 2007). When high-amplitude reflectors, often with a clear reversed polarity, show the presence of gas along specific horizons, they are termed *gas*

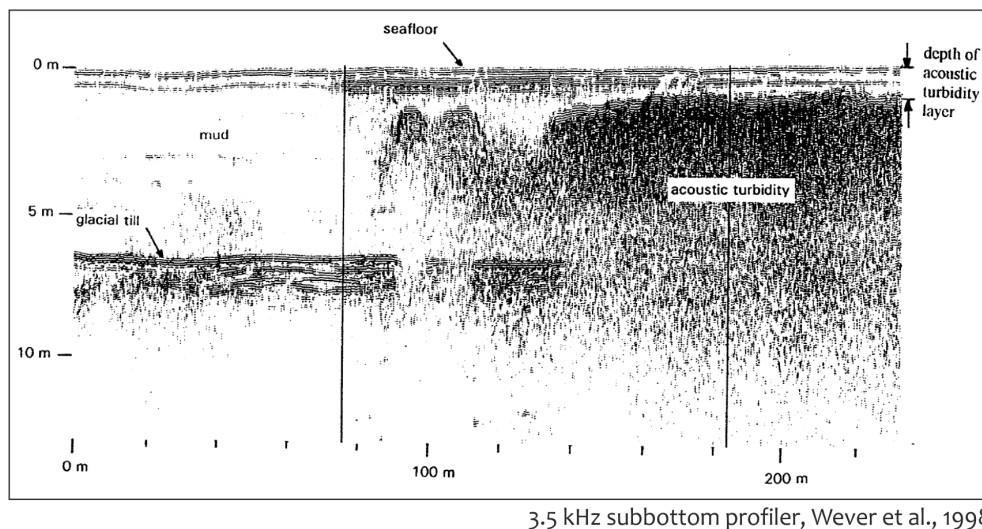


Figure 1.4: Acoustic turbidity indicating free gas in a 3.5 kHz sub-bottom profile from the Eckernförde Bay, Baltic Sea.

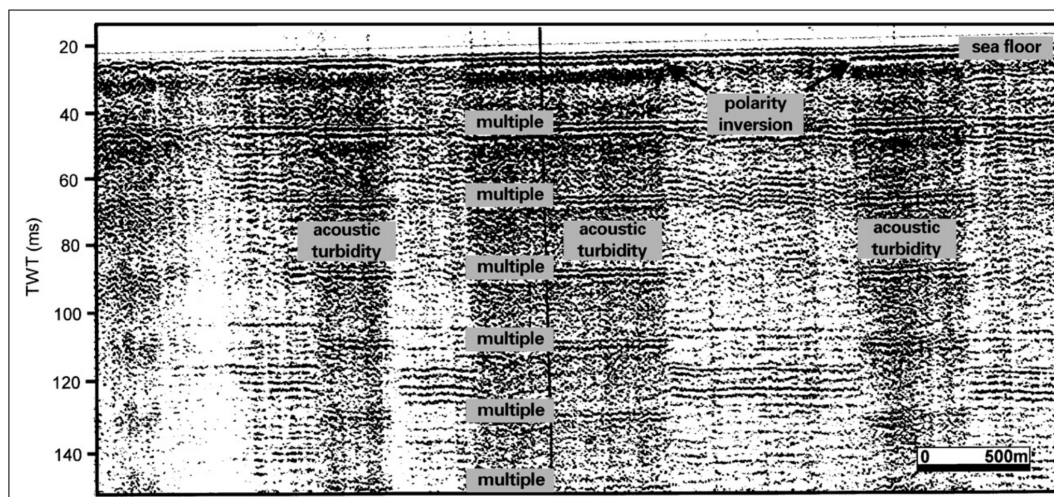
brightening. The high amplitude results from a large acoustic impedance contrast between the water saturated and gas-charged sediment layers, the latter having significantly lower velocity and bulk density.

Enhanced reflections in high frequency data are sometimes observed in association with zones of acoustic turbidity, the brightened horizons being above or laterally adjacent to the turbid areas (Judd & Hovland, 1992; Hart & Hamilton, 1993; Popescu et al., 2007). It is suspected that enhanced reflections occur where the fine-grained, gassy sediment includes layers of coarser and/or more permeable sediment, and gas bubbles along this horizon are able to occupy space larger than the interstitial pore space (Judd & Hovland, 2007). Enhanced reflections are also thought to be the shallow equivalents of *bright spots* observed in deep seismic data (Judd & Hovland, 2007). Bright spots are defined as amplitude anomalies caused by a strong acoustic impedance contrast due to hydrocarbons in porous rock.

Polarity reversal

Polarity of the seismic wavelet describes whether the acoustic impedance, the product of seismic velocity and bulk density of the medium, increases or decreases at an interface. The seafloor is usually marked by an increase in acoustic impedance due to the higher density in the seabed, thus a positive polarity (according to the normal polarity SEG standard for a zero-phase wavelet)¹. Free gas in the sediment will decrease the acoustic impedance as a consequence of lower density and reduced compressional velocity,

¹The SEG polarity convention specifies that the normal polarity display corresponds to an increase in acoustic impedance with depth, that is registered (on the field tapes) as a negative number and displayed on the seismic section by a white loop, being a trough to the left of the wiggle line.



Analogue sparker profile, Missiaen et al., 2002

Figure 1.5: Analogue sparker profile showing reversed polarity reflections and their strong multiples due to the presence of shallow gas, in front of the Belgian coast.

therefore the reflection from a gas-charged layer can have a negative polarity (following the SEG standard) or a *polarity reversal*.

Polarity reversal caused by shallow free gas is only reported in a few cases, after having carefully checked the polarity of reflectors (e.g. the polarity analysis of Baltzer et al., 2005). Shallow gas is more frequently surveyed with high frequency sources, and during acquisition, the amplitude and polarity information is not always preserved. Reflectors with reversed polarity indicating the presence of shallow gas are described together with other shallow gas indicators, as top reflections of acoustic blanking zones in high frequency data (Garcia-Gil et al., 2002) or associated with acoustic turbidity and reverberation as shown in Fig. 1.5) (Missiaen et al., 2002). Evans et al. (2007) observed reversed polarity of the seafloor reflection in seismic data on top of mud volcanoes in the Caspian Sea, and synthetic seismograms demonstrated in their study that these seabed anomalies are gas-related phase reversals due to the lower density and velocity in the gassy surficial sediment.

Reverberation

At the water-sediment interface, the acoustic impedance increases because of higher density of the seabed. In some cases, when the seafloor sediment, for example, has high sand content, the reflection coefficient is so high that several strong multiples of the seafloor reflection will appear on the acoustic or seismic section. The same can happen with gassy horizons at shallow depths or at the seafloor: most of the energy of a downward propagating acoustic wave will be reflected by the gassy layer and then propagate

upward to be re-reflected at the sea surface. Many repetitions of these low loss reflections can occur at the water - air and water saturated - gassy sediment interfaces. A resulting characteristic indication is many multiples of the initial strong reflection from the gassy horizon (Fig. 1.5). This is referred to as *reverberation* or *ringing*. Phase of the seismic wavelet shifts upon reflection both at the water - gassy sediment and water - air interfaces, both times 180° , so reverberation multiples resulting from a gassy horizon will have constant negative polarity (Davy, 1992).

Reverberation is observed on both acoustic and seismic data (e.g. Baltzer et al., 2005; Popescu et al., 2007; Evans et al., 2007). The analyses of Baltzer et al. (2005) found that the gassy seafloor reflection with a succession of multiples observed in areas of very high organic matter input can be characterized with extremely high amplitudes.

Velocity pull-down

The apparent downward deflection of horizontal reflectors is called *velocity pull-down*. They result from the reduced velocity in an overlying gassy sediment layer: the reflections from below will have later arrival times and appear deeper than their true depth. The pull-down effect is apparent if the gas-charged sediment is thick enough to significantly increase the travel times. It is often observed at the edges of gassy or acoustic blanking zones (e.g. Anderson & Bryant, 1990; Mathys et al., 2005).

Table 1.1: Descriptions of seismo-acoustic shallow gas signatures and their terminology in the literature

Shallow gas signature	Description in the literature	Additional terms
Acoustic turbidity	sub-bottom detail is lost; chaotic reflections or reflection pattern; high amplitude/dark smear obliterating all other reflections; variable degree of disturbance, sometimes allows coherent reflections to be followed; amorphous sub-bottom returns that cut across and mask internal stratification; zones of amorphous returns presenting a turbid appearance	acoustic/gas masking acoustic void acoustic shadow general terms acoustic transparency acoustic smearing wipe out (zone/region) reflector termination
	patches where reflections are faint or absent; amorphous echoes that cut across and mask internal stratification of the sediment body; a transparent or signal-starved domain in the seismic section, topped either by an enhanced reflection, broken or coherent, or by acoustic turbidity; anomalously void areas, returns from subsurface reflecting horizons are abruptly terminated; complete masking of the underlying seismic record	acoustic/gas curtain blanket plume pocket indicating gas migration columnar disturbance gas chimney
Enhanced reflection	coherent, high amplitude reflector; increased amplitude for part of their extent (equivalent to bright spots); coherent reflections that are markedly higher in amplitude (darker) over some of their length	gas brightening, bright spot
Polarity reversal	phase inversion of the acoustic signal due to the presence of free gas which causes a negative reflection coefficient	
Reverberation	succession of strong multiples; many repetitions of low loss reflections	(acoustic) ringing
Velocity pull-down	reflections are deflected downwards by the decrease in the acoustic velocity in the gas-bearing zone; apparent down-warping of actually horizontal reflecting layers	

Table 1.2: Seismo-acoustic shallow gas signatures published in the scientific literature. The selection and summary for this table was carried out based on the published figures of acoustic and seismic data.

Shallow gas signature	Frequency (kHz)	Equipment	Location	Reference
AT		minisparker	Gulf of Mexico	Anderson & Bryant (1990)
AB		minisparker		
AT		airgun		
AT		boomer	no specific location	Judd & Hovland (1992)
AT		pinger		
AB		boomer		
-		EG&G Uniboom sub-bottom profiler	UK coastal areas	Taylor (1992)
AT	3.5	sub-bottom profiler	eastern Skagerrak	Hovland (1992)
AT	0.3-1	sparker	western Irish Sea	Yuan et al. (1992)
AB	0.4-2	EG&G Uniboom sub-bottom profiler		
AT	3.5	sub-bottom profiler	Stockholm Archipelago	Laier et al. (1992)
AT	3.5	3.5 kHz sub-bottom profiler	Georgia, British Columbia	Hart & Hamilton (1993)
AT	0.8-10	boomer (Huntec deep tow seismic system)		
AT	3.5	3.5 kHz sub-bottom profiler	Aegean and Ionian Seas, Greece	Papatheodorou et al. (1993)
AT		airgun		
AT			Eckernförde Bay, Baltic Sea	Wever & Fiedler (1995)
AT	2-15	chirp profiler (EdgeTech-Subscan)	Chesapeake Bay	Hagen & Vogt (1999)
AT/AB		EG&G Uniboom Catamaran Model 230	Ria de Vigo, NW Spain	Garcia-Gil et al. (2002)
AB	3.5	ORE 3.5 kHz sub-bottom profiler		
AT	1	Uniboom/boomer	Belgian coastal zone	Missiaen et al. (2002)
AT	4	Seistec		
AT	1	sparker		
AB	1-10	Seistec boomer	lakes in Scotland	Baltzer et al. (2005)
AB	1-10	Seistec boomer	French Atlantic coast	Bertin & Chaumillon (2005)
AB	3.5	3.5 kHz sub-bottom profiler	S North Sea	Schroot et al. (2005)
AT/AB	0.600-2.6	boomer	Arkona Basin	Mathys et al. (2005)
AB	38	Simrad EK-60 echosounder		
AT	0.5-6	boomer (Nautik UWAK 04)	Arkona Basin	Thießen et al. (2006)
AT/AB	1.5-10	chirp (Datasonic CAP-6000W)	Ria de Aviero, Portugal	Duarte et al. (2007)
AB	0.25-1.4	EG&G Uniboom boomer		
AT/AB	3.5	3.5 kHz sub-bottom profiler	Black Sea	Popescu et al. (2007)

Continued on the next page...

Table 1.2 – Continued

Shallow gas signature	Frequency (kHz)	Equipment	Location	Reference
Enhanced reflection	AB	GI gun, miniGI gun		Popescu et al. (2007)
	AT/AB	chirp	Skagerrak, western Baltic Sea	Laier & Jensen (2007)
	AT/AB	sparker		
	AT/AB	chirp	Jinhae Bay, southern Korea	Kim et al. (2008)
	AT/AB	chirp	Aarhus Bay, Baltic Sea	Jensen & Bennike (2009)
	AT/AB	sparker		
		boomer	no specific location	Judd & Hovland (1992)
		sparker		
	3.5	3.5 kHz sub-bottom profiler	Georgia, British Columbia	Hart & Hamilton (1993)
	0.08-0.5	airgun		
Polarity reversal	3.5	3.5 kHz sub-bottom profiler	Aegean and Ionian Seas, Greece	Papatheodorou et al. (1993)
		EG&G Uniboom	Ria de Vigo, NW Spain	Garcia-Gil et al. (2002)
		ran Model 230		
	4	Seistec	Belgian coastal zone	Missiaen et al. (2002)
		industrial seismic	S North Sea	Schroot et al. (2005)
	0.6-2.6	boomer	Arkona Basin	Mathys et al. (2005)
	1.5-10	chirp (Datasonic)	Ria de Aviero, Portugal	Duarte et al. (2007)
		6000W		
	3.5	3.5 kHz sub-bottom profiler	Black Sea	Popescu et al. (2007)
	0.07-0.15	GI gun, miniGI gun	Black Sea	
Reverberation		high resolution 2D and 3D seismic	Caspian Sea	Evans et al. (2007)
	1	sparker	Belgian coastal zone	Missiaen et al. (2002)
		airgun	Gulf of Mexico	Anderson & Bryant (1990)
		EG&G Uniboom boomer	Lake Rotoura, New Zealand	Davy (1992)
	1	sparker	Belgian coastal zone	Missiaen et al. (2002)
	1-10	Seistec	lakes in Scotland	Baltzer et al. (2005)
	3.5	3.5 kHz sub-bottom profiler	Black Sea	Popescu et al. (2007)
		high resolution 2D and 3D seismic	Caspian Sea	Evans et al. (2007)
Velocity pull-down	0.08-0.5	airgun	Gulf of Mexico	Anderson & Bryant (1990)
	0.6-2.6	boomer	Arkona Basin	Mathys et al. (2005)
	0.25-1.4	EG&G Uniboom boomer	Ria de Aviero, Portugal	Duarte et al. (2007)

1.4 Motivation and objectives

1.4.1 Shallow gas in Baltic Sea sediments

Shallow free gas has been detected in many areas throughout the Baltic Sea. Acoustic turbidity and blanking in high frequency acoustic data were observed in the Skagerrak, Kattegat (Hovland, 1992; Laier et al., 1992; Hempel et al., 1994; Laier & Jensen, 2007), in Aarhus Bay (Jensen & Bennike, 2009), in Eckernförde Bay (Wever & Fiedler, 1995; Abegg & Anderson, 1997), in the Arkona Basin (Mathys et al., 2005; Thießen et al., 2006) and in the Bornholm Basin (Laier & Jensen, 2007). A free gas contour map was created in the METROL project based on acoustic data of a variety of high frequency (0.6-18 kHz) instruments (Borowski et al., 2005; Laier & Jensen, 2007) (Fig. 1.6). In spite of large differences in water depths, free gas depth was found to vary little within the region, in most areas it is 2-4 m below seafloor, but it also depends on the sediment type and the sedimentation rate (Laier & Jensen, 2007; Jensen & Bennike, 2009). The depth of the gas front in acoustic data also shows seasonal variations as studies found in Eckernförde Bay sediments, and there is an annual period which correlates to the temperature cycle of the atmosphere (Wever & Fiedler, 1995; Wever et al., 1998). Warming of the sediment (with a phase lag up to 3-4 months) decreases the solubility of methane in the pore water and gas bubbles become shallower, while cooling of the sediment will increase solubility and the gas horizon is at its deepest level.

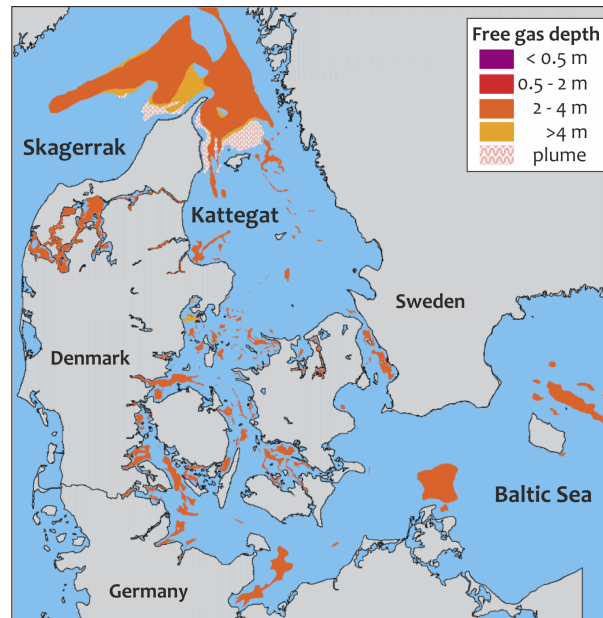


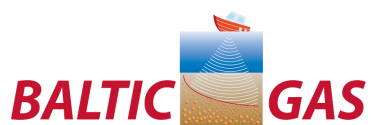
Figure 1.6: Shallow gas contour map in the Kattegat, Skagerrak and western Baltic Sea, based on high frequency acoustic data from the Final report of project METROL (Borowski et al., 2005).

Stable carbon isotope analyses of methane from diffusive gas accumulation systems indicate biogenic origin (Borowski et al., 2005; Thießen et al., 2006). Free gas is observed in locations where the organic-rich Holocene mud layer exceeds a certain thickness, 4-10 m in the western Baltic, up to 25-30 m in the eastern Kattegat (Borowski et al., 2005; Thießen et al., 2006; Laier & Jensen, 2007).

Methane in the seabed is an important but poorly understood component of the Baltic ecosystem response to natural and human induced impacts. Since the last glacial maximum, extremely low-organic late glacial clay was replaced by organic-rich Holocene mud, which provides an ideal setting for methane production and accumulation. A strong salinity gradient established from the Belt Sea to the bottom waters of the Bothnian Sea caused a gradient in the magnitude and depth of the sulfate barrier against methane emission. There is also a long-term natural and anthropogenic eutrophication occurring in the Baltic Sea. Predicted climate change may affect not only temperature but also the inflow of salt water from the North Sea, algal productivity, and distribution of anoxia, all of which are important parameters as they will affect future methane production and methane fluxes.

1.4.2 Baltic Gas

Several research projects have been dedicated to the study of shallow gas in the Baltic, e.g. The Coastal Benthic Boundary Layer (CBBL) research program of the Naval Research Laboratory in Eckernförde Bay (1993-1995); project METROL, an EU funded project uniting several marine science institutes, addressing 'Methane fluxes in ocean margin sediments: microbiological and geochemical control' (2002-2005).



The present study is part of an international research project called *Baltic Gas*, funded by BONUS+ (The Baltic Organisations Network for funding Science). Baltic Gas was active between 2009-2011 and involved 12 partner institutions from 5 Baltic Sea countries: Denmark, Germany,

Sweden, Russia and Poland and the Netherlands. The main motivation of the project was the study of methane production, accumulation and emission in Baltic Sea sediments and the water column.

The long-term eutrophication and environmental changes in the Baltic Sea ecosystem tend to enhance gas accumulation in the sediment. The emission of methane to the water column and across the water-air interface would release a powerful greenhouse gas into the atmosphere that can potentially cause a positive feed-back in the whole process by warming and increasing primary production. Moreover, the emission of toxic hydrogen sulphide by methane ebullition from the seabed into the lower, oxic water column can have significant biological effects. Shallow gas also poses potential hazard for seabed structures, e.g. pipelines, cables, offshore drilling platforms and windfarms. Baltic Gas therefore planned to (1) quantify and map the distribution and flux of methane in the Baltic Sea, (2) analyse the controls on the relevant key biogeochemical processes, (3) integrate seismo-acoustic mapping with geochemical profiling, (4) model

the dynamics of methane in the past (Holocene period), present (transport-reaction models) and future with predictive scenarios in relation to climate change and continued eutrophication, and (5) identify hot-spots of gas and potential future methane emission in an integrated database.

The project investigated shallow gas in Baltic Sea sediments using seismo-acoustic techniques, geochemical measurements and modeling. Main results of the project are summarized in the Baltic Gas final report (2012), while the seismo-acoustic investigations are presented in this thesis.

1.4.3 Research objectives

High frequency sediment echosounders provide the most suitable technique for the detection and mapping of shallow gas, because acoustic signals are distinctly scattered by gas bubbles. However, shallow free gas also imposes an 'acoustic problem' as it impedes imaging of the sedimentary structure. Often only the upper boundary of the gas-charged sediment layer, the gas front is visible. This prevents analysis of the depth distribution of free gas and the acoustic characterization of the sediment below, as sub-bottom penetration is restricted. Better understanding of the methane cycle and free gas formation in marine sediments, e.g. through geochemical modeling, however, requires information on the source of methane, possible migration pathways in the sediment, the thickness of the methanogenic sediment layer and sedimentation rates. So far, for smaller shallow gas occurrences, sediment thickness was interpolated from adjacent areas, but this is not possible where gassy sediments cover a large area, like in the northern Kattegat or in the Bornholm Basin. To overcome this acoustic problem, lower frequency seismic waves (< 0.5 kHz) were used in this study, for imaging gassy sediments in the Baltic Sea. Seismic waves are able to penetrate beneath the gas-charged sediment layer and thus offer the opportunity to investigate the geological background of methane production and free gas in the sediment.

The use of lower frequency seismic sources results in lower vertical resolution and thus different gas signatures in seismic data. The frequency of the profiling systems varies in geophysical surveys worldwide and free gas is known to appear in different ways in seismo-acoustic data. This entails natural frequency dependence from the instrumental side in imaging shallow free gas. On the other hand, physical modeling of gas-bearing sediments predicts the resonance of gas bubbles in marine sediments, which means a frequency dependent acoustic behaviour determined by the measurement frequency, sediment physical properties and concentration and size of gas bubbles. The seismo-acoustic image of gassy sediments will therefore be influenced by gas bubble resonance. This has consequences for the detection of free gas, spatial assessment of gassy areas and the expressions of gas in seismo-acoustic data.

The first main research objective therefore is to

- (1) investigate the frequency dependence in seismo-acoustic imaging of shallow free gas. First, to
 - (a) identify the various expressions of shallow free gas in seismo-acoustic data and to investigate the

physical background of their formation, with special focus on the lower frequency seismic data for its potential in studying gassy sediments. Second,

(b) using a wide range of measurement frequencies in imaging gassy sediments, to identify the frequency range where gas bubble resonance dominates. This multi-frequency approach in turn can characterize gas bubbles through a geoacoustic model.

Since methane is a powerful greenhouse gas, efforts have been made worldwide to explore the global distribution of free methane gas and gas hydrates in marine sediments, to estimate gas flux rates at seabed seeps and the direct contribution of these natural gas seeps to the atmosphere. These crude estimates are based mainly sporadic data and on extrapolations. Also, little is known about the amount of methane produced and stored in marine sediments and their potential release. On the small scale, the quantity of free gas in the sediment is difficult to measure, because methane degases during core recovery, when the sediment is brought to ambient pressure. Pressurized core samplers, which could better maintain the in situ gas content, are expensive and only rarely used. A simple technique for measuring in situ gas concentration would thus have great advantages, especially if it is via remote sensing. As free gas has significant effects on the acoustic properties of the sediment, such as the compressional wave velocity and attenuation, potentially they could be used as a measure for estimating free gas content.

The second objective of this study is therefore to

(2) develop ways to estimate free gas content in marine sediments using sediment acoustic properties and seismo-acoustic methods.

1.5 Outline of the research articles

In Chapter 2, the first manuscript addresses the frequency dependence of seismo-acoustic gas signatures. Shallow gas signatures are identified, described and mapped in high frequency Parasound sediment echosounder and lower frequency multichannel seismic data.

The manuscript in Chapter 3 presents results from a detailed velocity analysis of a seismic profile from the Bornholm Basin. The high resolution interval velocity field is used to estimate free gas content in the muddy sediments along a seismic line, and to assess the depth distribution of free gas.

The manuscript in Chapter 4 presents seismo-acoustic data collected over shallow free gas in 10 frequency bands, covering a frequency range between 0.2 and 43 kHz. At the edge of a gassy patch in the Bornholm Basin, by measuring the attenuation caused by gas bubbles from reflection amplitudes, the resonance frequency range of gas bubbles is identified and the free gas content is estimated.

1.5.1 Contributions to other research articles

In addition to the three manuscripts presented in this thesis, I contributed to three other research studies during my PhD. The research articles are included in full length in the Appendix, while here my contributions are summarized.

Gülzow et al., 2013: One year of continuous measurements constraining methane emissions from the Baltic Sea to the atmosphere using a ship of opportunity (Appendix A)

In February 2010, extraordinarily high methane concentrations were measured in the surface waters of the Arkona Basin, Baltic Sea. These elevated methane concentrations in the surface water were accompanied by a longer period of strong winds, which resulted in an oscillation of the sea level of almost 1.5 m within a day in the Arkona Basin. Based on a seabed feature found in seismo-acoustic data in the region, a pressure-induced seepage event was suggested to have caused the high methane values in the entire water column. The pockmark is shown in a seismic section, where a subtle 1 m deep depression in the seafloor with a maximum diameter of 120 m is associated with a reversed polarity seafloor return and structural disturbance beneath, indicating the actual presence of free gas at the seabed.

Contributions: seismic data processing, seismic and stratigraphical interpretation, writing

Schneider von Deimling et al., 2013: A low frequency multibeam assessment: Spatial mapping of shallow gas by enhanced penetration and angular response anomaly (Appendix B)

This study highlights the potential of using a low frequency multibeam echosounder for detection and visualization of shallow gas occurring several meters beneath the seafloor. The edge of a gassy area in the Bornholm Basin, Baltic Sea, was surveyed with a 95 kHz and a 12 kHz multibeam echosounder (MBES). The bathymetric measurements with 12 kHz provided depth values systematically deeper by several meters compared to 95 kHz data. This observation was attributed to enhanced penetration of the low frequency signal energy into soft sediments. Consequently, the sub-bottom geoacoustic properties contributed highly to the measured backscattered signals. Those appeared higher inside the shallow gas area compared to reference measurements outside and could be linked to the gas front depth below seafloor. No elevated backscatter was visible in 95 kHz MBES data, which in turn highlights the potential of low frequency MBES to image shallow sub-seafloor features. The presence of shallow gas was verified, with standard geochemical core analysis and sub-bottom profiling.

Contributions: handling of Parasound sediment echosounder data, interpretation

Flury et al., in prep.: Sulphate and methane fluxes and organic matter mineralization across a Holocene mud layer of increasing thickness in Aarhus Bay (Baltic Sea) (Appendix C)

In this study, gravity cores were taken in the transition from gas-free into gas-bearing sediment in Aarhus Bay (Denmark) with the objective to understand how methane flux is affected when the in situ solubility threshold for methane is exceeded. The pore water was analysed for dissolved methane, sulfate, total dissolved carbon dioxide, ammonium, while sulfate reduction rates were measured experimentally by radiotracer method. To determine the base of the Holocene mud beneath the gas-bearing sediment, multichannel seismic data were collected along the coring transect in April 2012. Migration Velocity Analysis was carried out on pre-stack time migrated data in order to correct properly for the velocity decrease in and beneath the gas-bearing sediment layer. The depth of the Holocene mud was found to increase along the transect and shallow gas appears when the mud thickness exceeds 8-9 m. The deepening of the methanogenic mud layer has apparently little effect on the methane flux, but shallowing of the SMTZ has a large effect, because the highest rates of methanogenesis take place in the youngest sediment. As the deep and the shallow enhanced methanogenesis are coupled, there is a positive feedback which explains the abrupt appearance of gas when a threshold thickness of mud is exceeded.

Contributions: seismic data processing, migration velocity analysis, seismic and stratigraphical interpretation, writing

1.6 Geological history of the Bornholm Basin

The Bornholm Basin is situated in the south-western part of the Baltic Sea, northwest of the island of Bornholm. The Baltic Sea is a brackish enclosed sea in Northern Europe, only connected to the oceans by the narrow and shallow waters of the Sound and the Belt Sea, which limit the exchange of water with the North Sea. Salt water inflows from the North Sea, transporting oxygen into the Baltic deeps, happen only infrequently (5-10 years), while the water level is more dependent on the regional wind situation than on tidal effects. The Baltic Sea fills a complex depression with a series of sub-basins, which are mostly separated by shallow sills formed during the Pleistocene. The weight of the last ice cover during glaciation produced a long-term isostatic rebound.

The basement of the southern Baltic basin is dominated by Cambro-Silurian and Cretaceous bedrock. The Mesozoic sedimentary rocks within the Fennoscandian Border Zone, across Scania, Bornholm and further southeast into Poland, are block-faulted along mainly NW-SE fault lines (Flodén & Winterhalter, 1981). The bathymetric Bornholm Basin is located in a major structural depression which subsided during the deposition of Upper Cretaceous sediments, thus pre-Quaternary sediments in the area consist mainly of Upper Cretaceous limestone topped with an unconformity surface. The development of the Bornholm Basin was controlled by the tectonic structure and later modified by glacial erosion, although the pre-Quaternary terrestrial relief survived the glaciations fairly well (Kögler and Larsen, 1979; Björk, 1995).

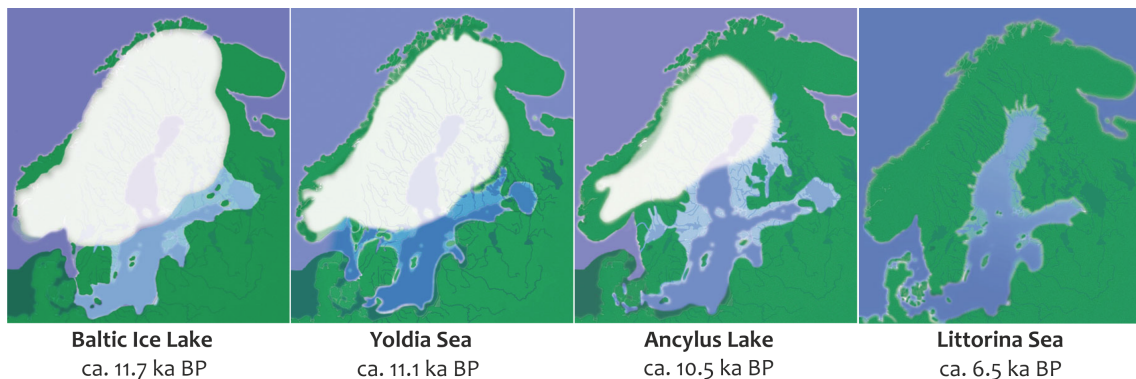


Figure 1.7: Paleogeographic maps showing the late and postglacial Baltic Sea stages during the last deglaciation (after Andrén et al., 2011).

After the last deglaciation of the Baltic Sea basin, the isostatic uplift together with eustatic sea-level changes resulted in a series of lacustrine and marine phases in the Baltic Sea sedimentation (Björk, 1995; Andrén et al., 2011). Retreat of the ice started ca. 16 ka BP in the south, when the embryo of the Baltic Ice Lake (BIL) was conceived (Björk, 1995; Andrén et al., 2011). In this first stage, (16.0-11.7 ka BP),

sedimentation was dominantly glaciolacustrine resulting in conformable glacial varved clay (closer to the ice sheet) or more homogeneous glacial clay (in more distal areas) (Kögler and Larsen, 1979; Andrén et al., 2011).

At the start of the Holocene period, in the partly brackish Yoldia Sea stage (11.7-10.7 ka BP), saline water entered the narrow straits of the southern Swedish lowland, but the area rapidly became shallower. During this stage, most of today's Baltic Sea basin deglaciated and was characterized with postglacial sedimentation, with the exception of the Bothnian Bay. In the next, fresh-water Ancylus Lake stage (10.7-9.8 ka BP), transgression took over in the south, regression in the north as the outlet areas were rising isostatically faster than the sea level. These stages are characterized with the deposition of homogeneous clays and they form an almost continuous cover over the deeper part of the eastern Bornholm Basin (Kögler and Larsen, 1979).

Beginning of the next, brackish Littorina stage (9.8 ka BP) is a sharp lithostratigraphic boundary, as saline water entered the Baltic basin again and deposition of soft marine mud rich in organic matter started. This Holocene mud is laminated at the bottom, but this laminated structure is not well developed in the upper, post-Littorina sequence. The organic carbon content measured in core samples shows a gradual increase from the beginning of the initial Littorina stage, and has a maximum in the end of post-Littorina Sea (Andrén et al., 2000). The transition to the recent Baltic Sea stage (c. 800 ka BP to present) is recorded as a biostratigraphical change in the muddy sediment (Andrén et al., 2000). In the Bornholm Basin, the Holocene mud has filled the depressions, but its deposition is non-uniform as a consequence of near-bottom inflow currents, which have been active during the entire marine Holocene period (Sivkov et al., 2002; Christoffersen et al., 2007).

1.7 Data and methods

The investigation of shallow gas in Baltic Sea sediments is mainly based on a data set collected during the R/V Maria S. Merian cruise MSM16/1. The largest field expedition of the Baltic Gas project, covering nearly all major basins of the Baltic (Arkona Basin, Bornholm Basin, Gotland Basin, Bothnian Bay and Bothnian Sea) took place from 30 July to 22 August in 2010 (Fig. 1.8). During the cruise, seismic and acoustic measurements were carried out, including high frequency multichannel seismics, using an airgun as a source, Parasound sediment echosounder profiling, as well as multibeam swath bathymetry and backscatter measurements. Extensive seismic data acquisition was focused on the known gassy part of the western Bornholm Basin. This thesis presents results from the multichannel seismic and Parasound sediment echosounder data collected in the Bornholm Basin survey (Fig. 1.9), although the understanding of free gas occurrences and their effect on seismic and acoustic waves greatly benefited from the processing and interpretation of seismo-acoustic data from the Bay of Mecklenburg, Arkona Basin, and the south-eastern Gotland Basin.

Additional data were collected in the Bornholm Basin in October 2012, in a Baltic IODP pre-site survey during R/V Alkor cruise AL402, with the same multichannel seismic system and a SES parametric sediment echosounder. Part of this data set was processed for the thesis (Fig. 1.9). The existing Bornholm Basin data set was complemented with additional long transects running across the basin and sediment echosounder data using different measurement frequencies. These were specifically collected along profiles that became the subject of detailed analyses.

1.7.1 Data acquisition

For seismic data acquisition during MSM16/1b, two streamers in three different configurations were used, in order to collect data with high resolution and large offsets, necessary for precise imaging of shallow gas. The shallow water streamer is a special 50 m long streamer with 48 single-hydrophone channels and a channel spacing of 1 m. This was towed in a depth of ~ 1.5 m with the help of 10 buoys, attached every 5 m with rubber bands. In addition to the shallow water streamer, a long, deep water multichannel seismic streamer was also used for recording, although separately only in the Bothnian Sea. The streamer's active sections contain eight 6.25 m long hydrophone groups, from which altogether 64 channels were connected to the recording unit. This streamer was kept at 3 m depth below the surface with the help of 5 attached birds, which force the streamer to the chosen depth by adjusting their wing angles accordingly. In the Bornholm Basin survey, a combination of the two streamers were applied, as two sections of the deep water streamer were attached to the shallow water streamer. A set of 21 buoys took over the task of birds, keeping the streamer at a depth of ~ 1.5 m. In the present study, the seismic data recorded with

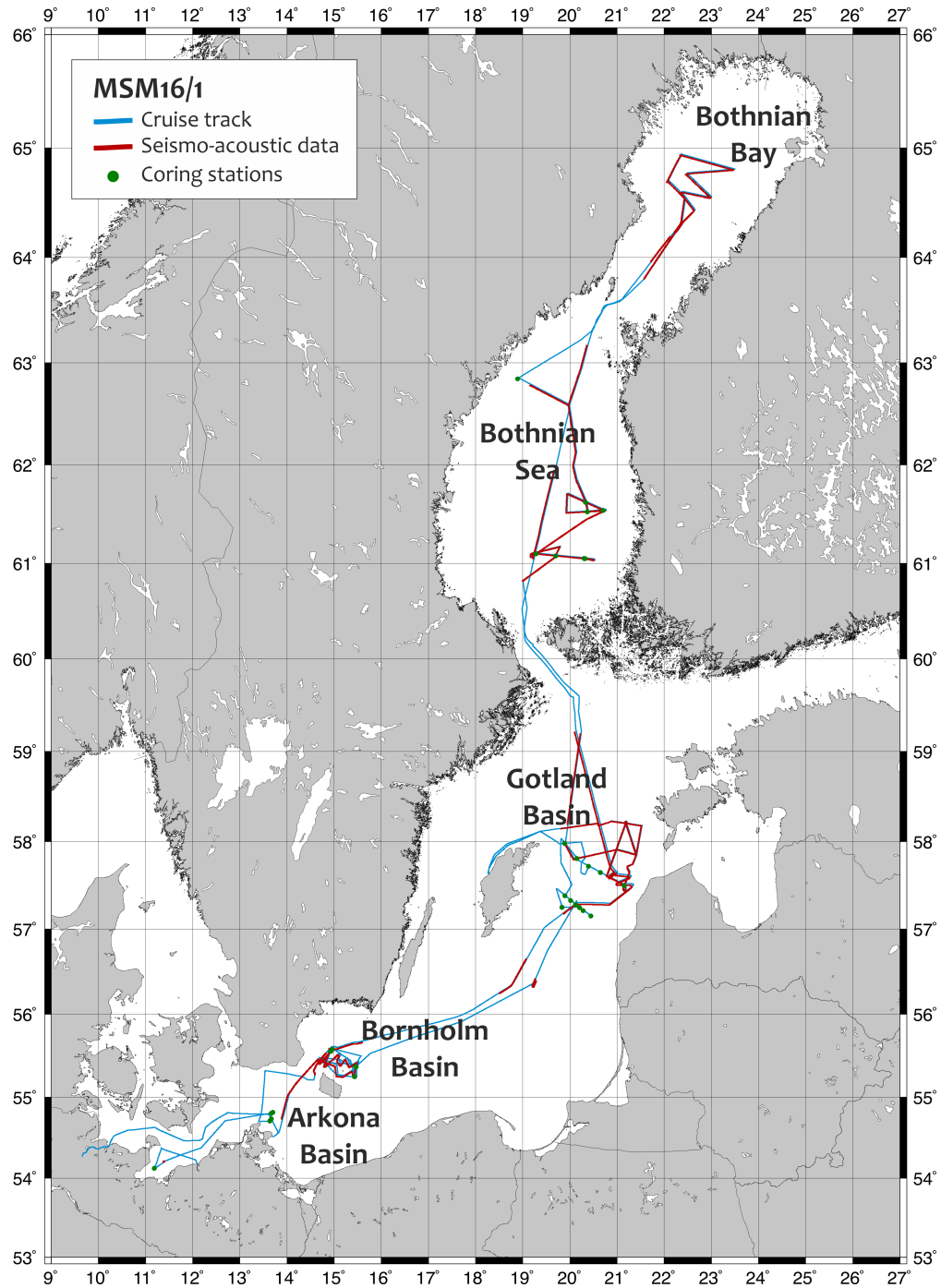


Figure 1.8: The seismo-acoustic data and sediment cores collected during the cruise MSM16/1 (2010) in the Baltic Sea.

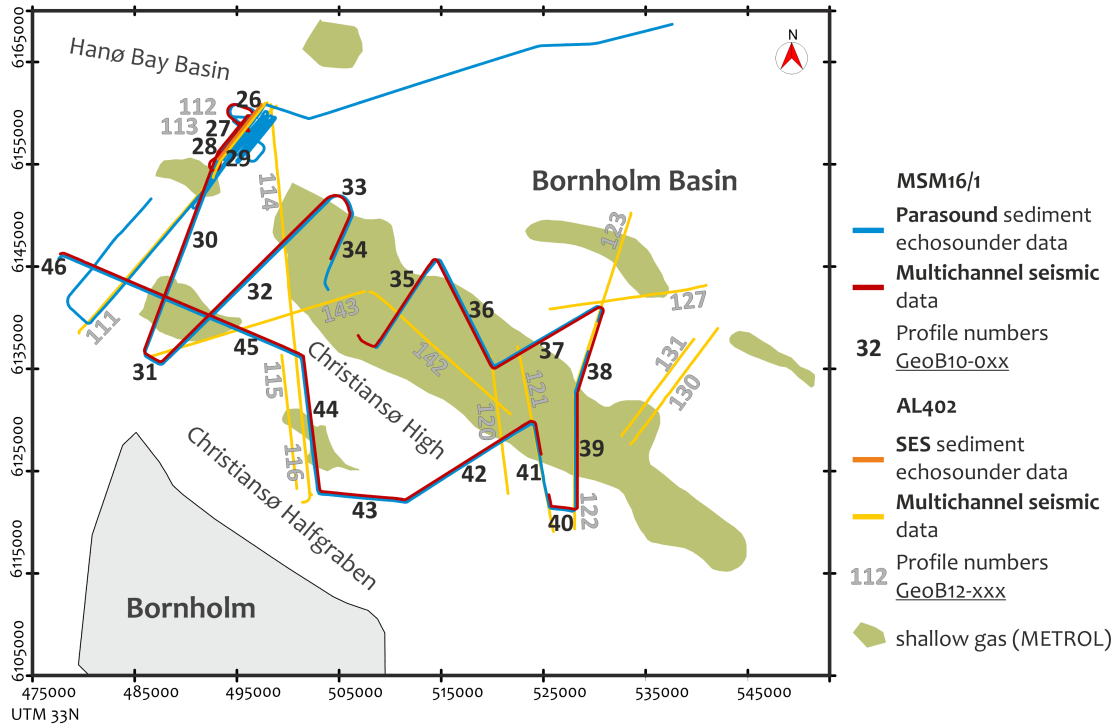


Figure 1.9: Profiles of the seismo-acoustic survey in the Bornholm Basin, Baltic Sea, from the R/V Maria S. Merian cruise MSM16/1, and complementary seismo-acoustic data from the R/V Alkor cruise AL402.

the shallow water streamer were analysed in detail.

As seismic source, a Soderia micro Generator-Injector (GI) airgun with reduced chamber volumes (0.1 l both, frequencies between 100-1000 Hz signal frequency) was towed 0.7 m below the water surface at the end of the ship. In the Bornholm Basin survey, shot rate was set to 1.5 s, achieving an approximate shot distance of 3 to 4 m at profiling speeds of 4.5 to 5.5 knots. The source was shot at an air pressure of approximately 150 bar provided by the compressor container on the ship. For data recording, a custom-designed digital seismograph, the MARine MUltiChannel Seismics (MaMuCS, ©Hanno Keil) was used. Data were recorded at a sampling frequency of 10 kHz (100 μ s) over time intervals of 1.3 s. The raw seismic data were stored in the standard seismic SEG-Y format.

The same GeoB high-resolution multichannel seismic equipment with the shallow water streamer was used during the cruise AL402 in the Bornholm Basin.

The parametric sub-bottom profiler Parasound was running simultaneously during the entire MSM16/1b survey. The continuous sediment acoustic records were used to select stations for water column and sediment sampling. The hull mounted Parasound DS3 (Atlas Hydrographic) works as a narrow beam sediment

echosounder, providing primary frequencies at ~ 18 (PHF) and adjustable 18.5-28 kHz, thus generating parametric secondary frequencies in the range of 0.5-10 kHz (SLF) and 36.5-48 kHz (SHF). The secondary frequencies develop through nonlinear acoustic interaction of the primary waves at high signal amplitudes. This takes place only in the emission cone of the high frequency primary signals which is limited to an aperture angle of only 4° . This is achieved by using a transducer array of 128 transducers on a rectangular plate of approximately 1 m^2 in size. Therefore the footprint size is only 7% of the water depth and vertical and lateral resolution is significantly improved, compared to conventional 3.5 kHz echosounder systems. During MSM16/1, the first primary frequency of Parasound was set to 19.231 kHz, which resulted in the generation of secondary frequencies at 4.273 kHz (SLF) and 42.735 kHz (SHF). The pulse length was set to 0.25 ms. Sample rate was 12.2, 6.1 and 6.1 kHz for the SLF, PHF and SHF, respectively. For the SLF and SHF frequencies, no gain was applied while recording, for the PHF gain was set to -35 dB (not time variable). All raw data were stored in the ASD (Atlas Hydrographic) data format, which contains the full water column of each signal as well as the full set of system parameters. Additionally, all the data were stored in compressed PS3 data format and standard SEG-Y.

The SES-2000 (medium type) parametric sub-bottom profiler (Innomar Technologie) is also mounted on the ship's hull (R/V Alkor) and works based on the same principle as the Parasound. The system operates with primary frequencies of 94 and 110 kHz and generates low secondary frequencies between 4 and 15 kHz, three at a time. In one setting the low secondary frequencies are 4.095, 7.876 and 14.628 kHz, and in another setting 6.023, 10.239 and 12.799 kHz. Sample rate was 50 kHz ($10 \mu\text{s}$) and constant gain (19 dB) was applied during recording. These data were stored in the RAW data format and later converted to SEG-Y.

1.7.2 Seismic data processing

Multichannel seismic data requires data processing, with the goal of improving the quality of the seismic image through the reduction of noise. By using several channels to record the reflected seismic waves, multiple coverage of the subsurface is obtained. With the technique of common midpoint (CMP) stacking, the channels which have a common reflection point are stacked, after appropriate corrections for travel time to a reference level have been applied (Mayne, 1962). In this process, reflections which follow the assumed travel paths are greatly enhanced, and other events, the noise and multiples are reduced.

Geometry setup, CMP binning, trace editing

Before CMP stacking of the seismic traces, a number of processing steps have to be carried out (Fig. 1.10). Pre-processing includes the geometry setup, where based on the GPS data, source and receiver positions (measurement geometry), the coordinate of every trace is calculated. The geometry setup was

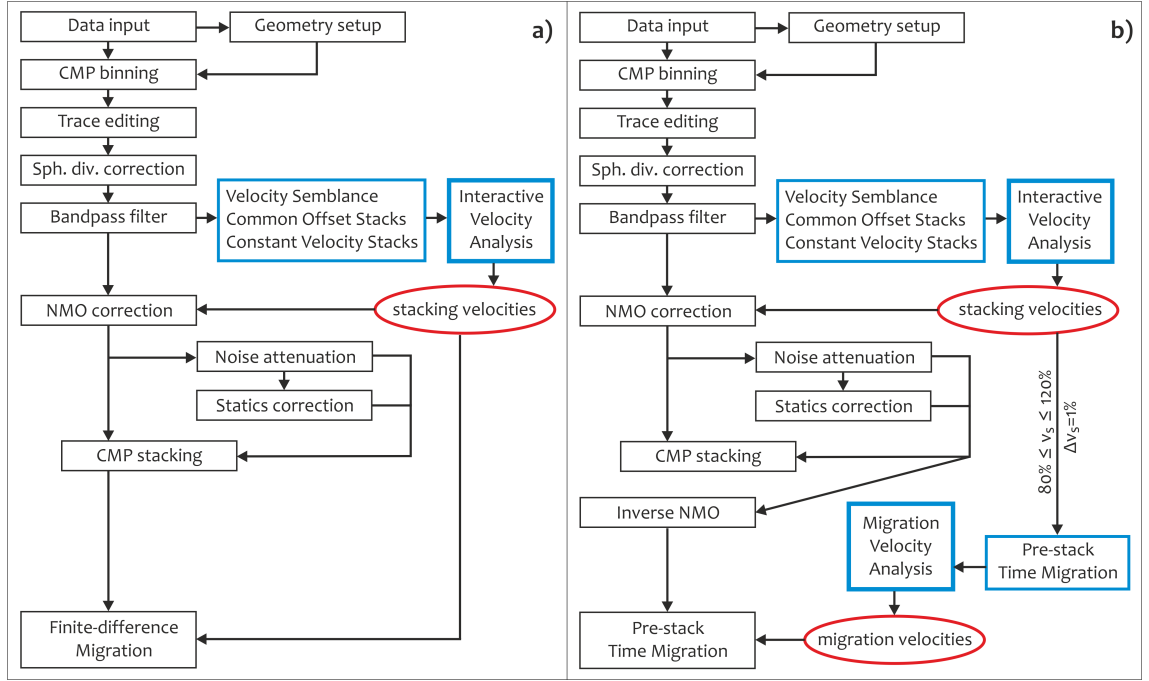


Figure 1.10: Seismic data processing flows applied to the multichannel seismic data recorded during cruises MSM16/1 and AL402. a) Standard seismic processing flow. b) For high resolution velocity analysis.

done using 'WinGeoApp', a custom-developed software (©Hanno Keil). From the source and receiver coordinates then, the midpoints are calculated and binned along the profile, creating CMP gathers. The CMP bin size is set depending on a compromise between the fold (number of traces per gather) and the horizontal resolution one wants to achieve. In the Bornholm Basin seismic data, in spite of a number of dead channels in the streamer, the high fold resulting from the high shot rate, allowed the use of a 1 m binsize. Thus the horizontal resolution of the profiles is ~ 1 m. For binning and the rest of the data processing, the commercial software VISTA 2D/3D Seismic Data Processing (GEDCO) was used.

After CMP binning, the traces of dead and noisy channels need to be deleted. Additionally, a bulk shift in time needs to be applied, which corrects for the gun delay. This is the time between the trigger signal and the actual release of the air bubble into the water, which is usually either roughly estimated from the data or imposed empirically. The gun delay together with the geometry setup influences the two-way travel time of reflections, and their correct setting can be checked by using the direct wave. The direct wave is the wave traveling from the source to the receivers in the water, therefore its velocity must be close or equal to the speed of sound in water. Sound velocity can be estimated from the direct waves in the shot gather display in Vista.

For the spherical divergence, the apparent energy loss from a seismic wave as it spreads during travel, an amplitude correction (gain) was applied using a velocity of 1500 m/s. Additionally, a broad Ormsby bandpass filter (filter flanks: 55-110 and 600-900 Hz) was used to suppress high-amplitude low (electric) and high frequency noise.

Velocity analysis

In order to correct for the normal moveout (NMO) of reflections, a velocity analysis was carried out. NMO is the effect that the source and receiver distance (the offset) has on the arrival time of reflections in the form of an increase of time with offset (Fig. 1.11). For this effect to be pronounced and measurable, the size of the offset (streamer length) has to be commensurate with the water depth.

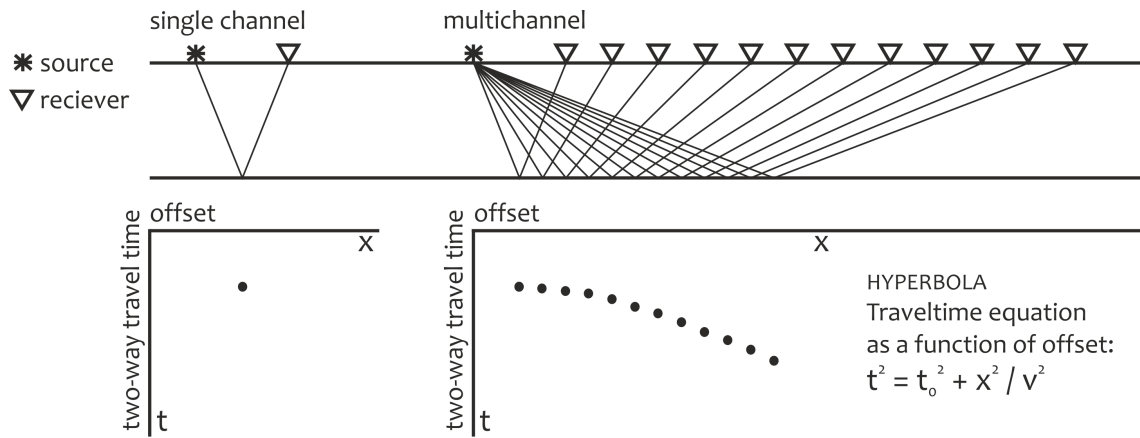


Figure 1.11: The two-way travel times of a horizontal reflection in single channel and multichannel seismic data recording. Multichannel seismic data requires the determination of the seismic wave velocity (v) in order to correct for the hyperbolic travel time difference (normal moveout) with increasing offset.

The velocity analysis was carried out with the Interactive Velocity Analysis tool of Vista, which offers the simultaneous analysis of previously generated velocity semblance, common offset stacks (COS) and constant velocity stacks (CVS) (Fig. 1.10.a). The velocity of reflections can be picked at selected CMPs along the profiles. The root-mean-square (rms) velocities are best determined for the seafloor and the first few prominent reflectors, where it is possible to fit the hyperbola to the travel time trajectories with certainty, aided by the velocity semblance and the CVSs. These rms velocities allow the optimal stacking of traces in the CMPs (stacking velocities), thus provide the best quality stack.

NMO and residual statics correction, CMP stacking, Migration

The NMO correction was then applied with the velocity functions created along the profile. Afterwards, within CMP gathers, the reflections in all traces should appear at the same two-way travel time. However, due to oceanographic and weather conditions during surveying, the streamer usually cannot swim perfectly at the same level below the water surface, so minor variations in reflection times still appear. Therefore residual statics corrections in the form of small vertical travel time shifts need to be applied before stacking. These were calculated and applied using an automatic residual statics correction module in Vista.

After additional noise attenuation (e.g. 2D Despiking tool for random high amplitude spikes) when it was needed, the traces in the CMP gathers were stacked together. As a last step of processing, the stacked profile was migrated using the stacking velocity field. Migration is an imaging process, which moves dipping reflections to their true subsurface positions and collapses diffractions, thus increasing spatial resolution and yielding a seismic image of the subsurface (Yilmaz, 2001). For all of the seismic profiles, 2D Finite Migration was applied.

Pre-stack time migration, Migration velocity analysis

For improving the stacking velocity field, a different processing sequence was worked out, which is shown in Fig. 1.10.b. This processing flow was applied to profile GeoB10-044 presented in Chapter 3. Although considerably more time-consuming and computationally intensive, this flow allows the creation of a very high resolution velocity field using migration velocity analysis (MVA) on pre-stack migrated seismic data. Pre-stack time migration moves up the migration step to precede CMP stacking. This way, by migrating each of the NMO-corrected common-offset sections, one has the opportunity to update the velocity field, because a second velocity picking can be done at reflections which are at (or at least closer to) their true subsurface positions, and this also improves the migrated stack in the end (Yilmaz, 2001). In principle, rms velocities are most appropriately estimated from pre-stack time-migrated data and the acquired migration velocity is, in theory, the medium velocity independent of the dip of the reflecting interface (Yilmaz, 2001).

As opposed to the stacking velocity estimation, where the moveout correction is done in individual CMPs, the MVA requires the complete pre-stack data, because the process of migration moves energy spatially from one CMP location to the other. So for the MVA, the entire pre-stack seismic profile was time-migrated varying the stacking velocities by 1% each time between 80 and 120%. The rms velocity functions were picked again in the Migration Image Velocity Analysis tool of Vista, where the best 'image velocity' was selected for every reflector. Picking velocities is partly subjective, because it is simply a matter of deciding which velocity gives the best image at each time. But when the velocity in the

migration equals the medium velocity, the seismic event is well-compressed (the diffraction hyperbola is collapsed in its apex), therefore the correct migration velocity can be estimated by evaluating the quality of focusing (at zero offset) and by choosing the best value between undermigrated (too low velocity) or overmigrated (too high velocity) events. The velocity function at the CMPs are easily picked, however, a priori knowledge about the type of sediments and possible gas content inferred from gas signatures help as well to narrow down the correct velocity functions.

Chapter 2

Seismo-acoustic signatures of shallow free gas in the Bornholm Basin, Baltic Sea

Zsuzsanna Tóth¹, Volkhard Spieß¹, Jørn Bo Jensen²

¹ Department of Geosciences, University of Bremen, 28359 Klagenfurter Str., Bremen, Germany

² Geological Survey of Denmark and Greenland, Ø. Voldgade 10, 1350 Copenhagen, Denmark

2.1 Introduction

Methane (CH_4) in marine sediments is formed by archaea through the anaerobic degradation of buried organic matter. Coastal areas and adjacent seas are hotspots of methane formation, since in these environments great amount of fine-grained organic-rich sediments have been deposited during the present interglacial period. Most of the methane is effectively broken down sub-surface when reaching the sulfate-methane transition zone (SMTZ), either aerobically in the presence of oxygen, or consumed by microorganisms during anaerobic oxidation (Reeburgh, 1969; Sansone et al., 1978; Boetius et al., 2000). However, as methane is poorly soluble in seawater, free gas bubbles may develop below the SMTZ when the CH_4 concentration exceeds saturation and the partial pressure of CH_4 overcomes the ambient hydrostatic pressure. Occurrence of free methane gas in marine sediments is quite widespread and evidence for its

presence has been reported from a wide variety of oceanographic and geological settings (Fleischer et al., 2001; Judd, 2003).

Shallow free gas imposes an 'acoustic problem' as it impedes imaging of the sedimentary structure. Observations made using high frequency (> 0.5 kHz) acoustic profilers report *acoustic turbidity* (chaotic reflections) and *acoustic blanking* (absence of reflections) in muddy sediments (e.g. Garcia-Gil et al., 2002; Mathys et al., 2005; Laier & Jensen, 2007). Gas bubbles act as scatterers of acoustic energy, so high frequency acoustic waves are strongly attenuated in the gas-charged sediment. This prevents analysis of the depth distribution of free gas and the acoustic characterization of the sediment below, as sub-bottom penetration is severely restricted. Often only the top of the shallow gas accumulation, the *gas front* is visible (Judd & Hovland, 2007).

Free gas causes other characteristic features in seismo-acoustic data as well. *Enhanced reflections* due to increased reflectivity show the presence of gas along specific horizons, usually observed together with zones of acoustic turbidity (Judd & Hovland, 1992; Hart & Hamilton, 1993; Popescu et al., 2007). Reflections with *reversed polarity* indicate reduced seismic velocity and a lower density in gas-charged sediments (Garcia-Gil et al., 2002; Evans et al., 2007). *Reverberation* or *ringing* is the succession of strong multiples and it can result from the high reflectivity in gas-charged seabed sediments or at gassy horizons (Davy, 1992; Baltzer et al., 2005). *Velocity pull-down* is the apparent downward deflection of otherwise horizontal reflectors due to the reduced velocity in the overlying gas-charged sediment (e.g. Anderson & Bryant, 1990; Mathys et al., 2005).

The frequency of the profiling systems used in geophysical surveys varies, consequently the appearance of gas-bearing sediments can be different on seismo-acoustic data (see e.g. Hart & Hamilton, 1993; Hempel et al., 1994; Mathys et al., 2005). In addition to this basic frequency dependence from the instrumental side, the acoustic response of gassy marine sediments also depends on frequency. Gas bubbles, when excited, are capable of vibratory motion with a sharply peaked resonance at a fundamental frequency, therefore the acoustic response of gas-bearing marine sediments will be different below, close to, or above the resonance frequency of gas bubbles (Anderson & Hampton, 1980).

Shallow free gas has been detected in many areas throughout the Baltic Sea. Acoustic turbidity and blanking on high frequency acoustic data were observed in the Skagerrak, Kattegat, and western Baltic Sea (Laier & Jensen, 2007), in Eckernförde Bay (Wever & Fiedler, 1995; Abegg & Anderson, 1997), in Aarhus Bay (Jensen & Bennike, 2009), in the Arkona Basin (Mathys et al., 2005; Thießen et al., 2006). In the Bornholm Basin, shallow gas occurrences were detected in the Holocene mud in a large area (Laier & Jensen, 2007). Mapping and quantification of shallow gas in the Baltic is becoming increasingly important, because nutrient flux and primary production and thus organic matter deposition to the seafloor have increased in the last decades due to enhanced eutrophication (HELCOM, 2009). Abnormally high levels

of methane in seafloor sediments could pose a major hazard to coastal populations within the next 100 years through their impact on climate change and sea level rise (Best et al., 2006), as methane is an effective greenhouse gas and if released, it heats the atmosphere with an efficiency 25 times that of CO₂ (IPCC, 2007).

In this study, we analyse high frequency acoustic and lower frequency seismic data collected in the Bornholm Basin, southern Baltic Sea, where free gas occurs in extensive areas very close to the seafloor. The lower frequency seismic waves (< 0.5 kHz) are able to penetrate below the gas-charged sediment and this offers the opportunity to investigate the depth distribution and amount of free gas, as well as the geological background of methane formation and accumulation in the area. However, due to the above mentioned frequency dependence, free gas causes different signatures in acoustic and seismic data. Our objective is therefore to identify the various seismo-acoustic expressions of shallow free gas, and to investigate the geophysical background of their formation, with special focus on the lower frequency seismic data. This in turn can help with the assessment and characterization of free methane gas in the sediments of the Baltic Sea.

2.2 Geological setting

The Bornholm Basin is situated northeast of the island of Bornholm in the southern Baltic Sea (Fig. 2.1). The seafloor topography is relatively smooth, except the NW-SE trending Christiansø High and adjacent highs, where the pre-Quaternary bedrock crops out (Kögler and Larsen, 1979). The maximum water depth is approx. 100 m in the central part of the bathymetric basin (Fig. 2.1).

The Bornholm Basin is located in a major structural depression that subsided during the deposition of Upper Cretaceous sediments, thus pre-Quaternary sediments in the area consist mainly of Upper Cretaceous limestones topped with an unconformity surface, and in some parts north of the Christiansø High, deposits of Paleogene age occur in small basins above the unconformity (Sviridov et al., 1995). The development of the basin was controlled by the tectonic structure and later modified by glacial erosion (Kögler and Larsen, 1979). The Quaternary basin fill is composed of a unit of glacial deposits and on top a succession of late and postglacial lacustrine and marine sediments (Sviridov et al., 1995).

2.2.1 Quaternary sediments

After the last deglaciation of the Baltic Sea basin, the isostatic uplift together with eustatic sea-level changes resulted in a series of lacustrine and marine phases in the Baltic Sea sedimentation (Björk, 1995; Andrén et al., 2011). In the first stage, the Baltic Ice Lake (BIL) (16.0-11.7 ka BP), conformable stratification of glacial (varved) clays and silt happened, their thickness reaches up to 8 m in the central

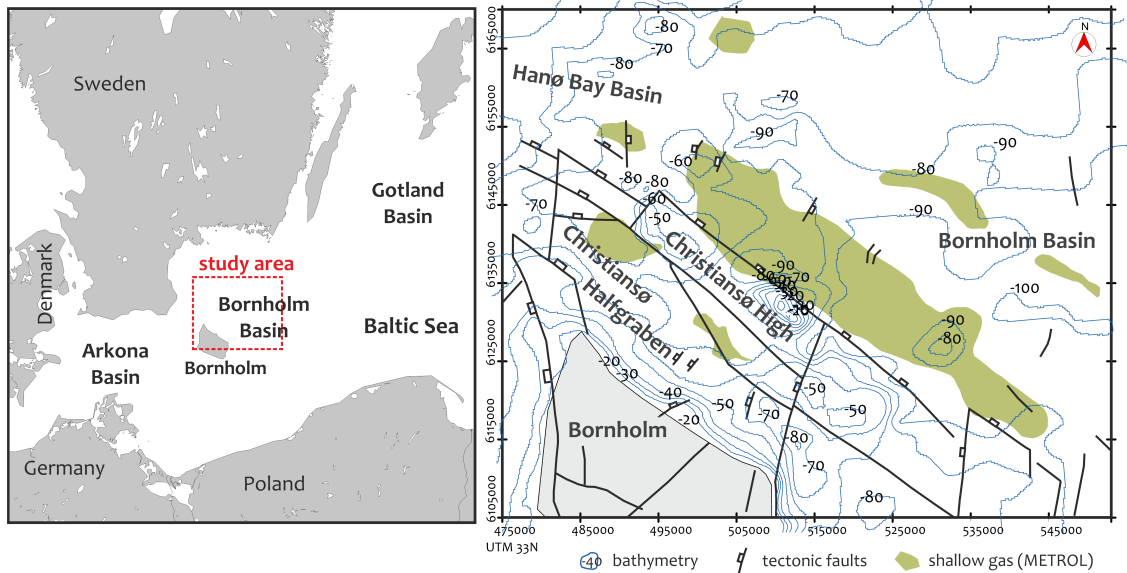


Figure 2.1: Location of the study area in the the Bornholm Basin, Baltic Sea. Green denotes areas in the basin where the shallow gas front in high frequency acoustic data was found at a depth of 2-4 m below seafloor (after Laier & Jensen, 2007). (The map was compiled after Vejbæk, 1985; Laier & Jensen, 2007; Graversen, 2009).

part of the basin (Kögler and Larsen, 1979). This was followed by the partly brackish Yoldia Sea stage (11.7-10.7 ka BP) and the fresh-water Ancylus Lake stage (10.7-9.8 ka BP), characterized with the deposition of homogeneous clays. The Ancylus-Yoldia (AY) clays form an almost continuous cover over the deeper part of the eastern Bornholm Basin, and are represented as a clearly recognizable banded layer on acoustic profiles (Kögler and Larsen, 1979). Beginning of the next, brackish Littorina stage (9.8 ka BP) is a sharp lithostratigraphic boundary, as deposition of soft marine mud rich in organic matter started. This Holocene mud is laminated at the bottom, but this laminated structure is not well developed in the upper, post-Littorina sequence. The organic carbon content measured in core samples shows an increase from the beginning of the initial Littorina stage, and has a maximum in the end of post-Littorina Sea (Andrén et al., 2000). The transition to the recent Baltic Sea stage (c. 800 ka BP to present) is recorded as a biostratigraphical change in the muddy sediment (Andrén et al., 2000). This entire mud unit seems homogeneous and is acoustically transparent on acoustic profiles. The Holocene mud has filled the depressions, but the deposition is non-uniform throughout the basin as a consequence of near-bottom inflow currents, which have been active during the entire marine Holocene period (Sivkov et al., 2002; Christoffersen et al., 2007). This variation in the accumulation rates is also reflected in the thickness of the mud.

2.2.2 Shallow gas in the Bornholm Basin

Degradation of organic matter has produced methane in the organic-rich Holocene mud in the Bornholm Basin, and in places where the thickness of this unit exceeds a certain limit (4-10 m) (Kögler and Larsen, 1979; Borowski et al., 2005), free gas is observed. Shallow gas occurrences were mapped in the area during the METROL project, based mostly on the observation of acoustic blanking and turbidity in high frequency acoustic data (Borowski et al., 2005). Shallow gas occurs in an extensive area and some smaller patches in the eastern Bornholm Basin (see map on Fig. 2.1.) The depth of the shallow gas front was found to be 2-4 m below the seafloor (Laier & Jensen, 2007).

2.3 Seismo-acoustic dataset

The acoustic and seismic data analysed for gas signatures in this study were acquired in August 2010 on the German R/V Maria S. Merian. The cruise MSM 16/1 took place throughout the Baltic Sea as a major field campaign of the project *Baltic Gas*. As part of the multidisciplinary research addressing shallow gas on the expedition, an extensive seismo-acoustic survey was carried out in the Bornholm Basin using high resolution multichannel seismics (MCS) and the ship's Parasound (PS) sediment echosounder, running simultaneously. The lines of the entire dataset are shown on Fig. 2.2.

2.3.1 Multichannel seismics

The seismic data were recorded with the GeoB high resolution shallow water MCS system, which includes a micro GI gun (Sodera) with reduced chamber volumes of 0.1 l, and a 50 m long analogue streamer with 48 single hydrophones and 1 m channel spacing. The central frequency of the source is around 200 Hz, while the recorded frequency content ranges from approx. 100 to 600 Hz. Shot rate was 1.5 s, average speed of the ship was ~ 4 knots during the survey. The MCS data were recorded with the acquisition software MaMuCS, with a sampling rate of 100 μ s, and recording length of 1.3 s. The MCS dataset was processed using the software package VISTA 2D/3D Seismic Data Processing (GEDCO). Seismic data processing followed a standard marine flow including common midpoint binning, bandpass filtering, normal move-out correction, stacking, noise attenuation, correction of residual statics and FD time migration. The CMP binsize was chosen to be 1 m to yield high horizontal resolution. Due to the effects of gas on seismic velocity, special emphasis was given to the velocity analysis in order to produce the correct and best possible seismic image. For display and interpretation of the seismo-acoustic data the commercial software package KINGDOM (IHS Global Inc.) was used.

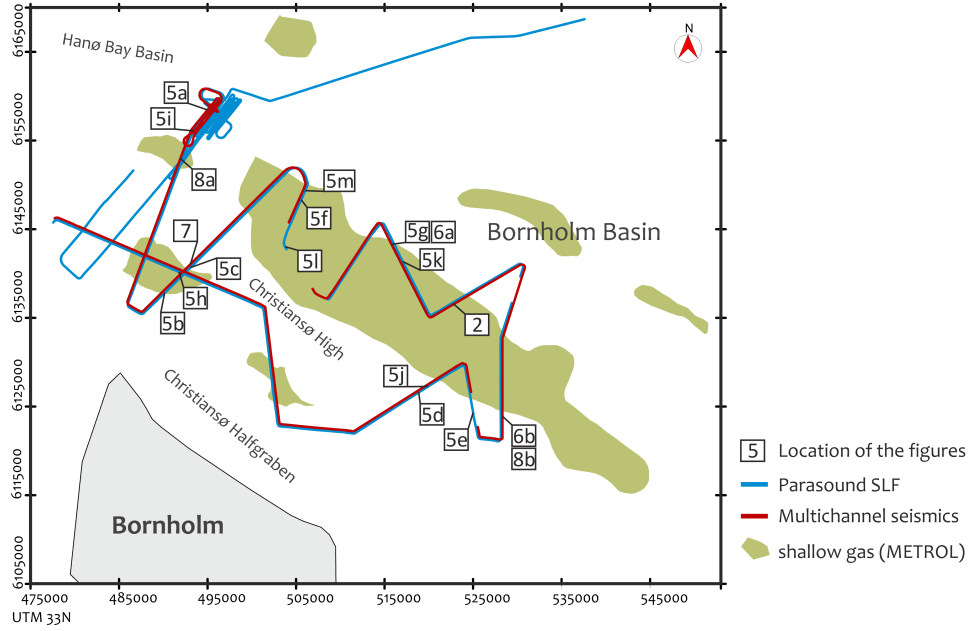


Figure 2.2: Lines of the seismo-acoustic survey in the Bornholm Basin, southern Baltic Sea (August 2010) over the area with shallow gas. The location of the examples presented from this seismo-acoustic dataset are indicated with the respective number of the figures.

2.3.2 Parasound sediment echosounder

High-resolution sediment echosounder data were acquired with the parametric narrow beam sub-bottom profiler Parasound DS3 onboard R/V Maria S. Merian. The transducers are mounted to the ship's hull and simultaneously emit pulses at two primary high frequencies, 19.3 kHz (PHF) and 23.5 kHz, generating parametric secondary frequencies in the water through the acoustic interaction of the primary waves at 4.3 kHz (SLF) and 42.8 kHz (SHF). The emitting cone of Parasound has an angle of only 4° , which reduces the area of the reflecting surface considerably, thus ensuring very high resolution.

2.4 Results and discussion

We identified signatures of shallow gas on the MCS data and the low frequency PS SLF (4.3 kHz) echosounder data. Given the different frequencies and thus different vertical resolution, we first address in general the seismic stratigraphy in the basin and identify the units, then we describe the seismo-acoustic expressions of shallow gas, which were found in the dataset.

2.4.1 Seismic stratigraphy

The PS SLF (4.3 kHz) profiles have a penetration down to 50 m below seafloor and are able to image the sedimentary units in the basin generally down to the base of the BIL deposits (Fig. 2.3.a), although in some places towards the rim of the basin or at the Christiansø High, the high frequency signal is more quickly attenuated at the surface of the outcropping Mesozoic bedrock. The signal penetration into the bedrock is rather low, so the internal structure can hardly be recognized on the PS SLF data, however the bedrock's erosional surface, when imaged, appears as an uneven high amplitude boundary. The glacial till where present has a hummocky surface with little and chaotic internal structure. The BIL clays can be characterized with the absence of internal reflections and low amplitude returns, only the upper part of the unit turns into a hummocky but still low amplitude appearance. As a consequence of deposition in a calm lake setting, the thickness of this unit always follows the underlying rugged topography. The following AY clays are shown as a band of several strong parallel horizons conformably lying on top of the substratum. The marine mud is either acoustically almost transparent with only low amplitude internal reflectors or is shown with weak but well-defined horizontal layering. The surface of the mud is almost always horizontal and smooth, although in some places contourite-type deposition can also be observed.

The MCS data due to its lower frequency penetrates deeper down to ~ 200 m and reveals the complex geological structures of the Pre-Quaternary bedrock (Fig. 2.3.b). The surface of the Pre-Quaternary is a high amplitude, rugged erosional unconformity with truncation of reflections, significant dips and channels. Northeast of the Christiansø High on the flanks of the bedrock, a thick unit generally transparent with low amplitude continuous reflectors appears, which can be interpreted as the BIL deposits. The post-glacial AY clays are shown as a continuous coherent double reflector draping onto the flanks of the outcropping bedrock or the hummocky and chaotic glacial till, which in some places can be observed overlying the Mesozoic bedrock. On top the Holocene mud is an acoustically transparent unit with a relatively weak seafloor reflection.

2.4.2 Seismo-acoustic gas signatures in the Bornholm Basin

Shallow gas is detected on almost every profile in the dataset (Fig. 2.4). Most reliable detection happens with the low frequency signal of the PS, as gas bubbles in the sediment severely attenuate the acoustic signal and cause extensive (1) *acoustic blanking* zones. The top of these blank zones, defined as the gas front is located at different depths below seafloor (Fig. 2.4.a). On the lower frequency MCS profiles, depending on the depth of the gas front, the free gas modifies the reflection of the seafloor by (2) *interference*, (3) *change its polarity*, or it appear as separate a *reflection with reversed polarity*. In some places free gas causes (4) *reverberation* and stronger multiples (Fig. 2.4.b).

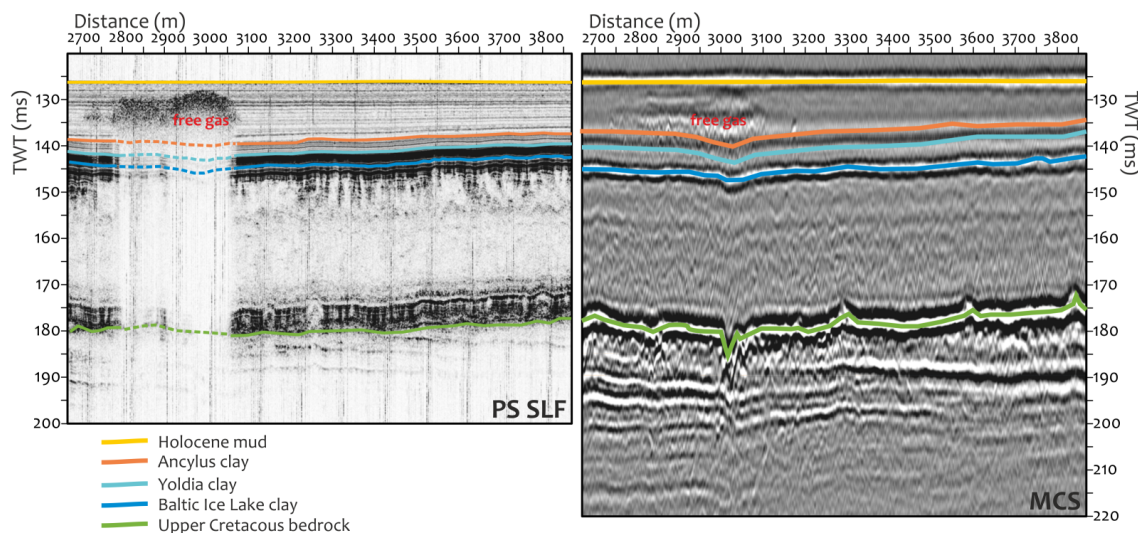


Figure 2.3: Seismic stratigraphy in the Bornholm Basin in a high frequency Parasound profile (on the left) and multichannel seismic data (on the right), at the same location. Exact location is indicated on the map in Fig. 2.2.

Point scatterers and acoustic blanking

Shallow gas on the PS SLF (4.3 kHz) data appears as a patch or layer of *point scatterers* which have variable amplitudes, and reflections of the sediment layering below are considerably weaker than in the gas-free areas or completely absent. The collection of examples in Fig. 2.5. are from throughout the basin (exact locations are indicated on the map in Fig. 2.2).

At this high frequency the sediment layering is disrupted by the presence of free gas and the subsurface below the free gas layer cannot be imaged: the gas bubbles scatter the sound wave to the extent that it does not penetrate deeper. The degree of attenuation in the gas layer varies in different places (Fig. 2.5a-c), especially at the edge of the gassy areas. In these transitions, horizons denoting larger acoustic impedance contrasts (boundaries of the AY and BIL clays) can be traced even below the gas-charged layer, but inside the gassy areas complete *acoustic blanking* is typical.

The gas layer is not a coherent reflection, rather a stack of point scatterers which do not always follow any particular horizon in the mud (Fig. 2.5.b, c, j). The small point scatterers with highly variable amplitudes are visible in an incredibly high resolution and in some patches even the individual scatterers can be separated from each other within the cloud (Fig. 2.5.a). The concentration of the gas bubbles might be reflected in the amplitude and/or the thickness of the cloud of point scatterers (see Fig. 2.5.c, g, or compare h-m), and both change laterally, within a few hundred meters (Fig. 2.5.d, g, j). However,

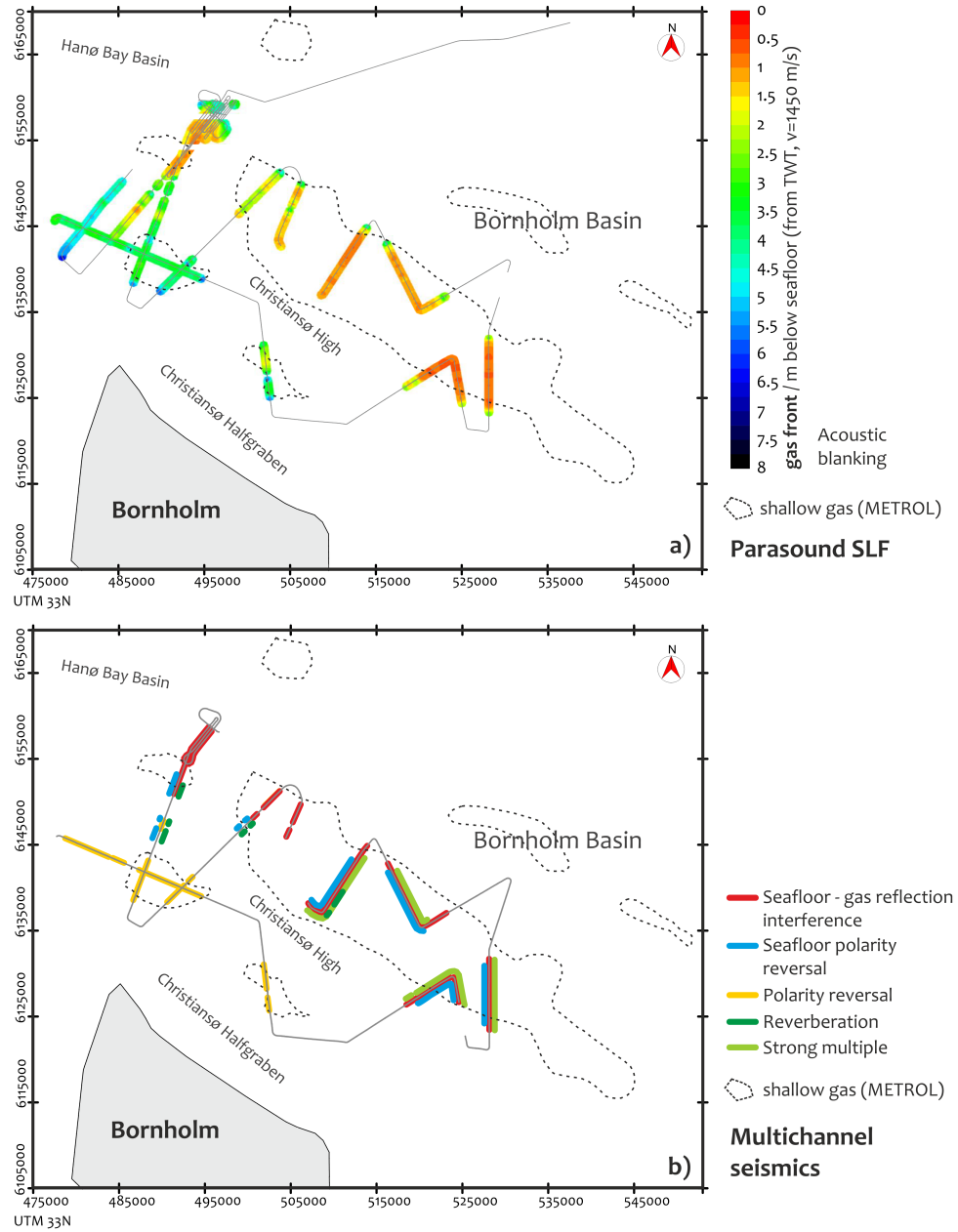


Figure 2.4: a) The shallow gas front (top of acoustic blanking) mapped in Parasound SLF (4.3 kHz) sediment echosounder data. b) Seismic shallow gas signatures in lower frequency multichannel seismic data.

part of this cloudy appearance might be attributed to the 'prolonged echo' of the PS. Although the beam

of the PS is very narrow and the reflecting surface area is only $\sim 7\%$ of the water column, still there is a small travel time difference between the center and the side of the beam - the waves reflected on the side arrive somewhat later than the one reflected in the center of the beam, therefore the reflections on the side appear deeper on the acoustic record. This vertical stretching can be striking if there is a hard interface which is made of strong scattering objects such as the accumulation of gas bubbles in the sediment. It is likely that if the gas bubbles are accumulated in a layer, the top ones in the accumulation scatter the sound waves to the degree that they cannot penetrate into the sediment layer hosting the gas bubbles, so the cloud appearance in the end might be a visual artifact.

The edges of the acoustic blanking zones are either sharp (Fig. 2.5.d, e), or more typically, gradually decreasing in depth below the seafloor as going towards the center of the gassy area (Fig. 2.5.c, f, g).

The shallow gas layer in the PS profiles is always seen in the marine Holocene mud close to the seafloor (Fig. 2.4.a). Average depth of the gas front below seafloor is 1 m in the eastern part of the basin, northeast of the Christiansø High, whereas the gas front is observed at a depth of 3-4 m in the western part of the basin, north of the tip of Bornholm (Fig. 2.4.a).

Seafloor–gas reflection interference

The seafloor reflection is a 'known' acoustic impedance contrast (AI, the product of seismic velocity and bulk density of the medium), normally a positive event, and the corresponding wavelet is a good estimate of the general wavelet shape and its polarity in the seismic data (Simm & White, 2002). The seafloor reflection in the MCS data, although slightly variable, has a characteristic wavelet shape: small trough (loop left to the wiggle line), somewhat bigger peak (loop to the right), and a smaller trough again. A close-up of the seafloor wavelet is displayed on Fig. 2.6. A and D. The seafloor seems to have a different appearance in the gassy areas with a more complicated wavelet shape and/or reversed polarity (Fig. 2.6.a-b/C-F). Its amplitude is significantly higher compared to the seafloor reflection amplitude in gas-free areas.

The change of the normal wavelet shape becomes evident when one follows the seafloor reflection from non-gassy to gassy parts (Fig. 2.6.a/B-C). At this transition, the amplitude of the second trough of the wavelet increases, then another peak appears also with gradually increasing amplitude (Fig. 2.6.B-C). This reflective behaviour denotes *interference* between two close interfaces: the seafloor, which in case of the mud is a rather small increase in AI, and the top of the gas-charged sediment layer, which is a large decrease in AI. Interference happens when the distance of these two interfaces is equal to or less than a quarter of the wavelength (Widess, 1973; Kallweit & Wood, 1982), which is confirmed by the higher resolution PS data. The wavelength in the MCS data is ~ 7.5 m, $\lambda/4 = 1.875$ m, and the gas front is at a depth of ~ 1 m below seafloor on the example on Fig. 2.6.a. Here the top of the gas-charged layer, clearly

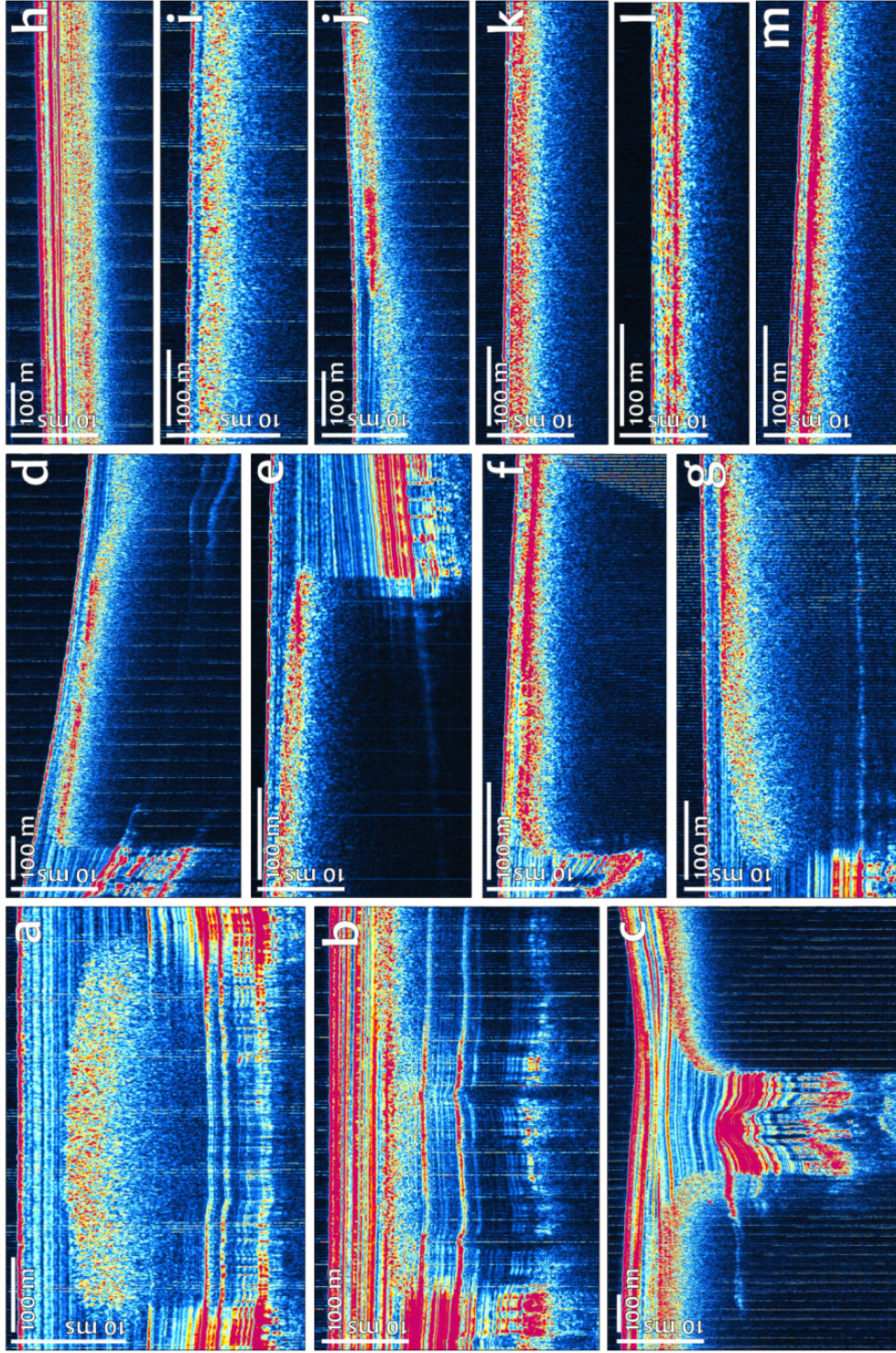


Figure 2.5: Shallow gas imaged with the Parasound sediment echosounder (SLF 4.3 kHz, envelope display). Gas bubbles in the Holocene mud appear as a patch or layer of point scatterers with highly variable amplitudes, and they cause acoustic blanking as the scattering in the gassy layer disrupts the sediment layering.

seen in the high frequency data, cannot be resolved as a separate reflector, only the seafloor's changed wavelet shape and higher amplitude points to its presence.

The amplitude of this *composite seafloor-gas reflection* being considerably higher than that of the normal muddy seafloor is the result of *constructive interference* due to the thin layer that the two interfaces create (event tuning). Probably the large AI contrast that the free gas represents (large decrease in the velocity and density) also contributes to the amplitude becoming larger than the real reflectivity. In case the sediment layer hosting gas bubbles is thick enough, the AI increase at the base of this gas-charged layer may also play a role in shaping the interference pattern.

Below the seafloor-gas reflection interference, the otherwise acoustically transparent mud layer becomes *turbid* and disturbed, as well as the otherwise continuous reflectors of the underlying clays. This points to scattering of the seismic wave.

The interference of the seafloor and gas reflection is observed in most of the MCS profiles in the north-eastern part of gassy area (Fig. 2.4.b), where the gas front comes up to 0.5-1.5 m close to the seafloor (Fig. 2.4.a).

Polarity reversal

Polarity of the seismic wavelet describes whether the AI increases or decreases at an interface. The normal seafloor reflection in marine seismic data should be a strong positive reflector representing the AI increase between water and sediment (following the American/SEG standard in the polarity display for a zero-phase wavelet). However, free gas in the sediment will decrease the AI as a consequence of reduced velocity and/or density, therefore the reflection from a gas-charged layer will have a negative polarity or a *polarity reversal*. Negative polarity at the seafloor is detected in the MCS data in places where the gas front is very close (> 0.5 m) to the sediment surface (Fig. 2.4.b). The *polarity reversal of the seafloor reflection*, where the gas front becomes increasingly shallow, can be observed at transitions from non-gassy to gassy areas (Fig. 2.6.b). Here, the wavelet of the normal seafloor reflection (trough-peak-trough) changes to a more complicated shape with a negative peak at the start. The changed shape of the wavelet having additional peaks and troughs, again points to interference between the seafloor and gas reflection. This time, however, the wavelet shows a reversed polarity due to the proximity of the gas front to the seafloor. In most cases the seafloor polarity reversal in the Bornholm Basin is observed as part of an interference pattern (Fig. 2.4.b).

Shallow gas in the mud, due to the decrease the free gas causes in AI, is also indicated as deeper negative polarity reflections in the MCS data. An example is shown on Fig. 2.7. The gas front observed on the PS SLF profile appears in the mud at a depth of ~ 6 m, and reflections are almost completely absent below. On the MCS profile this is indicated as a reflector with reversed polarity below the seafloor

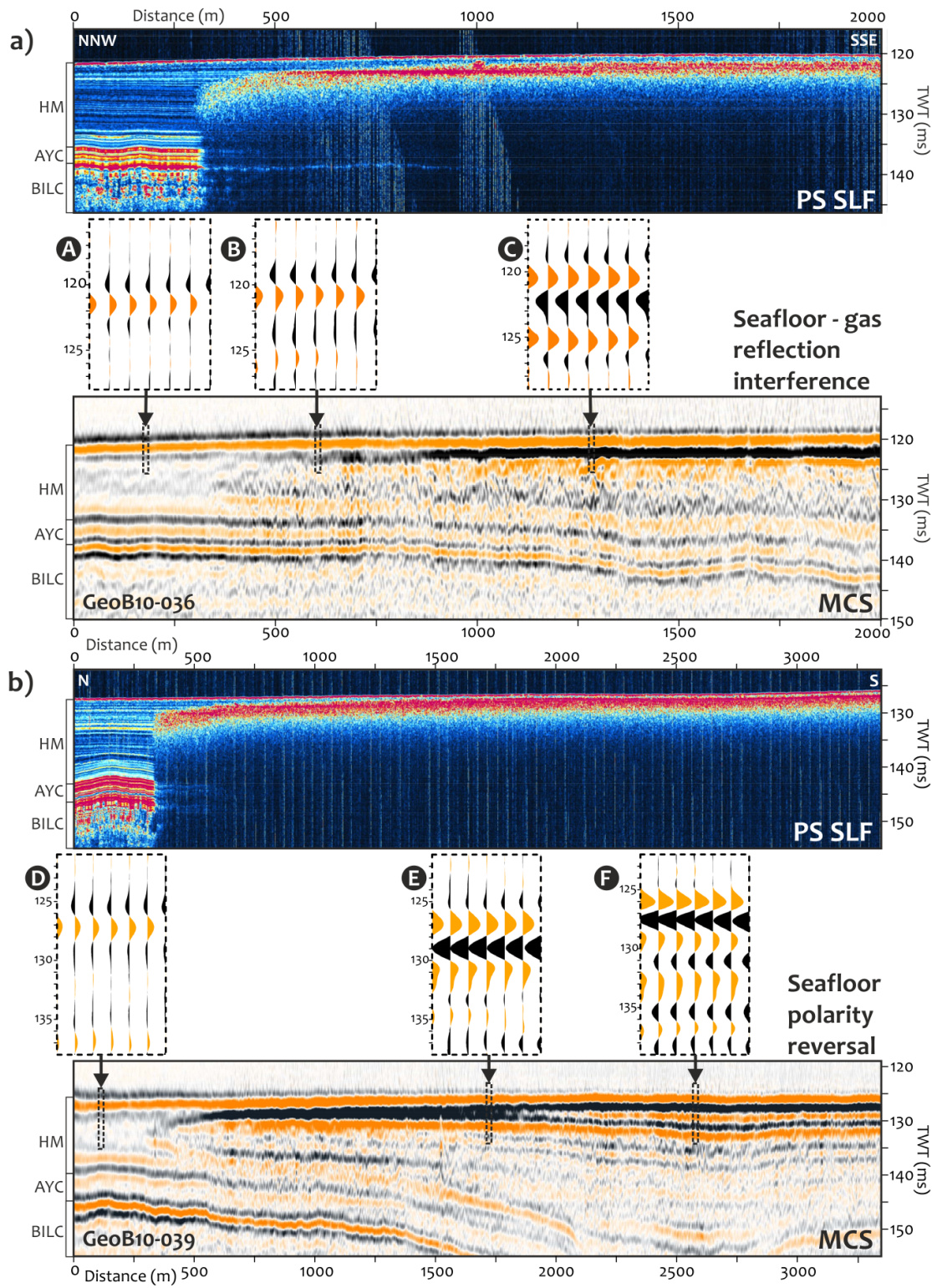


Figure 2.6: The formation of a) sea floor - gas reflection interference (GeoB10-036) and b) sea floor polarity reversal (GeoB10-039) in multichannel seismic data at the edge of the area with shallow gas. HM=Holocene mud, AYC=Ancylus and Yoldia clays, BILC=Baltic Ice Lake clay. For locations of the profiles see the map on Fig. 2.4.

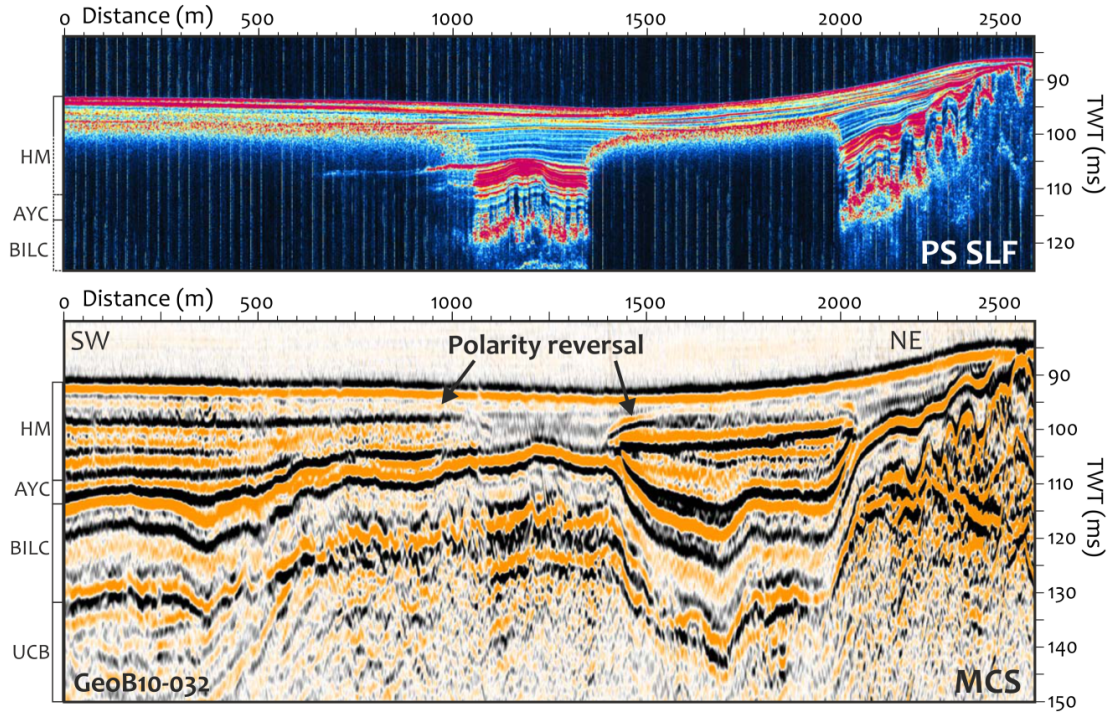


Figure 2.7: Polarity reversal due to the free gas in multichannel seismic data (GeoB10-032). HM=Holocene mud, AYC=Ancylus and Yoldia clays, BILC=Baltic Ice Lake clay, UCB=Upper Cretaceous bedrock. Location of the profile is on Fig. 2.4.

but without interference. Shallow gas appearing as reversed polarity reflectors can be found in the western part of the Bornholm Basin (Fig. 2.4.b), where the gas front is 3.5-7.5 m deep below the seafloor (Fig. 2.4.a).

Reverberation and stronger multiples

Multiple reflections arise from an interface with a strong AI contrast such as the water bottom. When the reflection coefficient (R) is very high at the water-sediment interface, for instance due to high sand content or gassy horizons at shallow depths, *reverberation*, the succession of several strong multiples can occur on the seismo-acoustic record. Most of the energy of the downward propagating seismic wave is reflected at the interface with high R , and propagates upward to be re-reflected at the sea surface. Many repetitions of these low loss reflections can take place then at the water-air and water saturated-sandy/gassy sediment interfaces. A resulting characteristic indication is many multiples of the initial strong reflection. In case of a gassy horizon, phase of the seismic wavelet shifts upon reflection both at the water-gassy sediment

and water–air interfaces, both times 180° , consequently reverberation multiples from a gassy horizon will have constant negative polarity (Davy, 1992).

Reverberation caused by a gas reflection can be seen on a few profiles in the MCS data, in places where the seafloor reflection has negative polarity and interference is also observed (Fig. 2.4.b). The most extensive one in the Bornholm Basin is shown on Fig. 2.8.a. Here, in a 2.5 km long part of the profile, the multiples have very high amplitudes and constant phase, i.e. always negative polarity. Reflections beneath the seafloor reflection are weak and the deeper structures are already completely masked by the first strong multiple. (This makes the phenomenon quite similar to acoustic blanking observed in the high frequency PS data.) The reverberation lasts quite long in time, at least for half a second. These characteristics all show that a very high proportion of the seismic energy is reflected back from the gas-charged sediment layer and remains long in the water column bouncing up and down until it is slowly attenuated. We can estimate the reflection coefficient from the amplitude of the seafloor reflection and its first multiple ($R \approx A_{multiple}/A_{seafloor}$). In the example in Fig. 2.8.a, R at the reverberating seafloor reflection (between 750-1800 m) is ~ 0.18 . Reverberation from non-gassy seafloor reflection with almost the same characteristics also occurs in the MCS data, these can be seen in parts of the Bornholm Basin, where the bedrock crops out at the seabed. Confirmation of the outcrop is given by the normal polarity of the reflection and the alternating phase of the multiples.

Due to the very high R , the gassy seafloor can trap the seismic energy almost entirely in the water column, although this happens only in a few places (Fig. 2.4.b). Generally transmission is sufficiently high, but the resulting strong multiples of the gassy seafloor reflection can obscure imaging of the deeper sedimentary structures. The example on Fig. 2.8.b. shows a stronger multiple of the gassy seafloor reflection, R at the seafloor (between 2750-4500 m) determined from the amplitude of the seafloor and its multiple here is ~ 0.09 (Fig. 2.8.b).

2.4.3 Frequency dependence in the seismo-acoustic imaging of shallow gas

Gas bubbles in the sediment under small acoustic perturbations oscillate radially and can resonate at a fundamental frequency (f_0) related to their size (r), and the acoustic behaviour of unconsolidated gas-bearing sediments is therefore dominated by the resonance of gas bubbles (Anderson & Hampton, 1980). Compressional wave velocity and attenuation will be different at acoustic frequencies below, at and above bubble resonance. The resonance frequency for 0.5 through 5 mm average size gas bubbles in shallow muddy sediments is predicted to be in the range of 1.5 to 20 kHz (Fig. 2.9) (Anderson & Hampton, 1980; Wilkens & Richardson, 1998).

For acoustic frequencies *below* f_0 , when the wavelength (λ) is considerably greater than the bubble size ($\lambda \gg r$), the acoustic response is that of the bulk medium. In this case the compressional wave

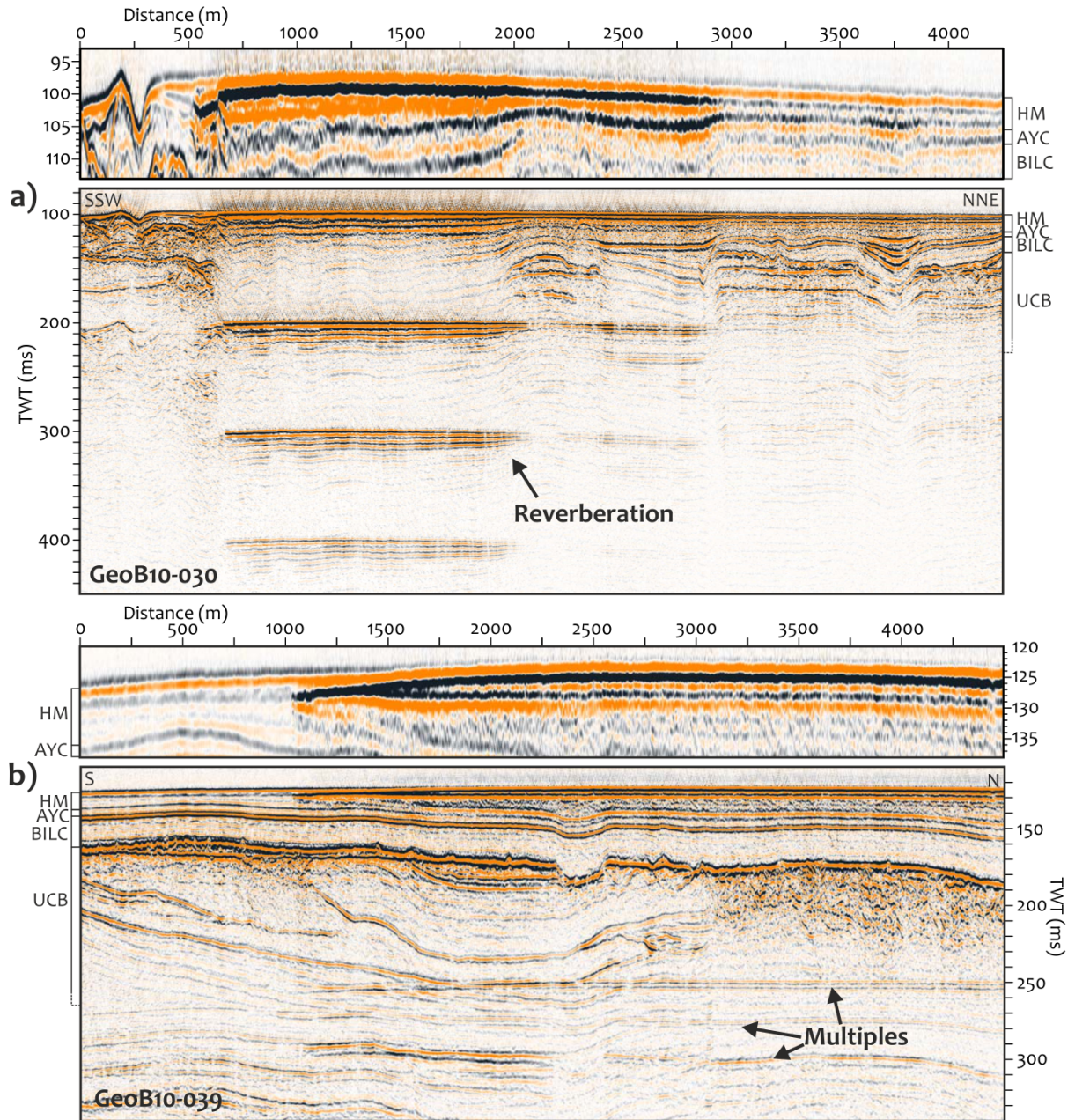


Figure 2.8: a) Reverberation (GeoB10-030) and b) strong multiples (GeoB10-039) in multichannel seismic data due to the presence of shallow gas close to the seafloor. Free gas is indicated by the negative polarity of the seafloor reflection (upper part of the figures). HM=Holocene mud, AYC=Ancylus and Yoldia clays, BILC=Baltic Ice Lake clay, UCB=Upper Cretaceous bedrock. For the locations see the map on Fig. 2.4.

velocity may be significantly reduced even by a small amount of free gas. *At or near f_0 ($\lambda \gtrsim r$)*, the gassy sediment becomes highly dispersive and the velocity can greatly exceed the gas-free sediment velocity. At frequencies *above f_0 ($\lambda \approx r$ or $\lambda \lesssim r$)*, the bubbles simply scatter the sound, but the acoustic response is essentially that of the surrounding medium, so the velocity remains constant at a value commensurate with the gas-free sediment. Attenuation is highest at a frequency near the bubble resonance frequency and decreases rapidly below and above f_0 , though it still will be higher than in gas-free sediments.

While gas bubbles in the sediment scatter the high frequency acoustic waves, low frequency seismic waves undergo reflection from a gas-charged sediment layer. Scattering and reflection are two physical processes, which are distinguished by the relation between the size of the scattering object (r), i.e. the gas bubbles, and the wavelength of the seismic wave (λ) (Fig. 2.9). There is overlap between these phenomena, but this is the reason why the difference between the frequency of acoustic and seismic instruments results in different gas signatures in seismo-acoustic data.

In practice, the wavelength of the PS 4.3 kHz signal is 35 cm ($\lambda = v/f$; $v = 1500$ m/s), commensurate with average gas bubble sizes (one order of magnitude larger, so $\lambda \gtrsim r$). The PS SLF frequency is therefore in the range where bubble resonance effects dominate, and so are other conventional high frequency sediment echosounders, 3.5 kHz profilers. The gas bubbles will strongly scatter the acoustic energy of these sources, and the significantly higher attenuation due to bubble resonance will further prevent transmission through the gas-charged sediment layer. The resulting appearance of shallow gas on the PS data is a cloud of *point scatterers* and *acoustic blanking*.

The wavelength of low-frequency seismic sources is considerably larger than the size of gas bubbles in the sediment ($\lambda \sim 7.5$ m for the 200 Hz signal of the airgun, $v = 1500$ m/s, so $\lambda \gg r$). At this low frequency the free gas content changes the medium's overall properties: it reduces the compressional wave velocity and slightly increases attenuation. Since these waves with long wavelengths do not backscatter from the small bubbles, penetration to greater depths is achieved because of the lesser attenuation owing to both scatter and absorption. At this frequency, the gassy layer is represented as a single *reflector with reversed polarity*, since the gas-charged layer is simply a part of the medium with lower velocity and/or density.

2.4.4 Shallow gas signatures in seismo-acoustic data

Gas signatures are affected by several parameters: differences in the amount of gas, concentration of gas bubbles, distribution of bubble sizes, depth of the gas front beneath the sediment surface, the geological structure. Table 2.1 summarizes what the formation and characteristics of the acoustic and seismic gas signatures could indicate about these parameters.

For the high frequency PS echosounder data, a particular depth of the shallow gas front will not

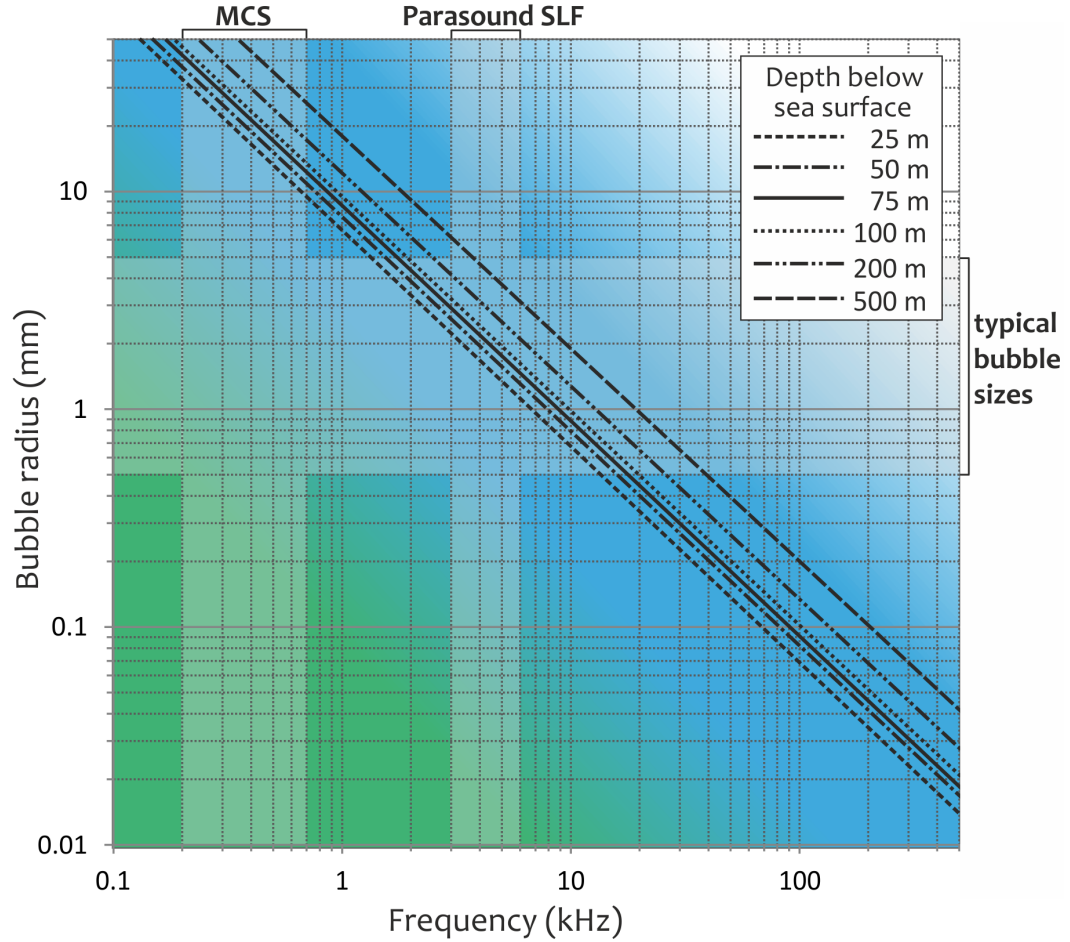


Figure 2.9: Bubble resonance frequency as a function of gas bubble radius for Bornholm Basin sediments based on the theory of Anderson & Hampton (1980) ($n_g = 0.01\%$). Typical water depth of 75 m for the Bornholm Basin is indicated with the continuous line. Since hydrostatical pressure influences the gas bubble size, resonance frequency for the same bubble radius will be different in various water depths (dashed and dotted lines). Green denotes where reflection is dominant, while blue the regime of scattering.

Table 2.1: Gas signatures and what they tell about shallow free gas in the Bornholm Basin, Baltic Sea.

Wavelength vs bubble size regime	Reflection ($\lambda \gg r$)	Scattering ($\lambda \gtrsim r$)
Gas signature	reversed polarity reflection	point scatterers (and acoustic blanking)
Depth of the gas front	close	gas front appears where it is, acoustic blanking beneath
	very close	gas front appears where it is, acoustic blanking beneath; reverberation is more likely
Number of gas bubbles per unit volume	small	partial acoustic blanking (or acoustic turbidity)
	large	complete acoustic blanking
Gas bubble size	small	higher resonance frequency, thus complete acoustic blanking at higher frequency
	large	lower resonance frequency, thus complete acoustic blanking at lower frequency
Amount of gas	small	less scattering, acoustic turbidity, partial acoustic blanking
	large	more scattering, higher probability of reverberation, complete acoustic blanking

affect the appearance in the seismic image because of the high resolution, but in the MCS data it can alter the character of the seafloor reflection. In the Bornholm Basin MCS dataset, a reversed polarity reflector marks the top of the gas-charged sediment layer when the gas front is located relatively deep in the sediment (3.5-7.5 m). Interference between the gas reflection and the seafloor reflection can modify the seafloor wavelet shape and increases its amplitude, which points to the gas front being closer to the sediment surface (0.5-1.5 m). In general, this transition will shift with the main frequency of the seismic source, and interference becomes more likely with lower seismic frequencies. When the polarity of the gas-seafloor reflection composite turns from positive to negative, then the gas front is very close (> 0.5 m) to the sediment surface. In the latter case, in addition to the seafloor polarity reversal, reverberation of the seafloor-gas reflection composite can occur, because free gas represents such a high acoustic impedance contrast that it causes the seismic energy to be trapped in the water column. Reverberation of the seafloor reflection due to the presence of free gas close to the seafloor has been observed in high frequency data as well (e.g. Missiaen et al., 2002; Baltzer et al., 2005; Popescu et al., 2007). This is especially striking when the water is shallow, and maybe this is the reason why no reverberation of the gas front is observed in the PS data when the free gas is extremely close to the sediment surface—the water in the Bornholm Basin is deeper and the penetration of the high frequency signal is less than the travel time of the first multiple.

The concentration of gas bubbles (number of gas bubbles per unit volume) might be directly related to the reflection coefficient at the top of the gassy sediment layer, which is in turn linked to the amplitude of the reflection and its multiples. Higher concentration of gas bubbles is associated with a higher R at the top of the gassy sediment layer, and in MCS data this might enhance reverberations of the gas reflection. A smaller number of gas bubbles in the sediment leads to a lower R with weaker multiples of the gas reflection. In the high frequency PS data, the degree of attenuation depends on the concentration of gas bubbles. Lower number of bubbles in a sediment layer may cause moderate attenuation and partial blanking with a few recognizable reflections beneath, while higher concentration of gas bubbles could lead to complete acoustic blanking and enhanced reflections on top of the blanking zone.

The size of gas bubbles has a very different effect on the propagation of seismic waves for different frequencies. While at lower seismic frequencies, only bulk sediment properties and the reflection coefficients change, resonance effects significantly influence attenuation at higher frequencies (Fig. 2.9). Theoretically, for any size of gas bubbles, maximum attenuation and thus complete acoustic blanking occurs around the resonance frequency, which would be shifted to lower frequencies for increasing bubble size. Since gassy sediments likely contain a variety of bubble sizes, highest attenuation and acoustic blanking occur over a wider acoustic frequency range. In the Bornholm Basin, complete acoustic blanking over the gassy areas suggests that the 4.3 kHz PS signal is close to the resonance frequency of gas bubbles in the sediment,

more precisely close to the resonance frequency of those gas bubble sizes that are at the peak of the bubble size distribution.

The amount of gas in the sediment can be only indirectly inferred from seismo-acoustic gas signatures, because already small amounts of free gas cause significant changes in the physical and geoacoustic properties. Although exact gas transport mechanisms in the sediment are unknown, in a steady state situation the depth of the gas front can indicate the upward methane flux, as a shoaling of the gas front results from increasing methane flux (Dale et al., 2009). In reality this is influenced by several parameters, the rate of methane production and consumption, methane solubility, diffusion rate, sulfate supply etc. Nevertheless, essentially this means that the higher the amount of gas in the sediment is, the closer to the sediment surface the gas front is likely to be and the higher the probability of observing interference and polarity reversal of the seafloor and gas reflection composite. At high acoustic frequencies, a high amount of gas leads to stronger scattering, a shallower gas front, and a higher probability of reverberation.

Velocity pull-down, the downward deflection of reflections below the low-velocity gassy layer, was not unambiguously observed in the Bornholm Basin dataset. The reason for this is that the gas-charged sediment layer in the Holocene mud is relatively thin, so the travel path in the low-velocity layer is only a small fraction of the total travel path. Even if the interval velocity in this gassy layer is very low (e.g. 300 m/s over an interval of 2 meters), it only results in a small decrease in the rms velocity of deeper sediments beneath the gassy layer, thus the travel time effect is hardly detectable (e.g. 0.7 ms travel time anomaly leading to a drop of 27 m/s in rms velocity for 90 m depth).

2.5 Conclusions

Seismo-acoustic signatures of shallow gas were identified and mapped in Parasound sediment echosounder and multichannel seismic data from the Bornholm Basin, Baltic Sea. The 4.3 kHz PS SLF signal is scattered by gas bubbles and thus strongly attenuated in gas-charged sediment layers. The resulting appearance of shallow gas in the high frequency PS data is a cloud of point scatterers and acoustic blanking. Depending on the proximity of the top of the free gas layer to the seafloor, which can be determined from the PS data, the wavelet shape of the seafloor reflection in the lower frequency MCS data is modified by the free gas. When the shallow gas layer is close enough to the seafloor (0.5-1.5 m), interference between the seafloor and the gas reflection results in a more complicated wavelet shape and considerably increases the amplitude of the composite reflector; when the gas bubbles are very close to the seafloor (> 0.5 m), the seafloor reflection shows a reversed polarity. High reflectivity at this interface can cause stronger multiples and reverberation of the water bottom reflector, as most of the seismic energy becomes trapped in the water column and attenuates slowly with time. When the gas-charged layer is

deeper in the sediment, it appears as a single reflection with reversed polarity in the seismic data.

The seismo-acoustic gas signatures show that free gas in the Bornholm Basin is restricted to the Holocene mud, where the free gas depth varies between 0.5-7.5 m below the sediment surface.

Our study highlights the use of several frequencies in the detection and assessment of shallow gas in marine sediments. While the strong attenuation of high frequency acoustic waves in the resonance range of gas bubbles can be used for the reliable detection of free gas, low frequency high resolution multichannel seismics below this resonance range is able to provide information on the depth distribution and geological background. The expressions of shallow gas in seismo-acoustic data are dependent on the measurement frequency. Better understanding of their formation reveals details about free gas in the sediment.

Acknowledgments

We thank Luisa Palamenghi for useful comments on the early version of the manuscript. This research has received funding from the European Community's Seventh Framework Programme (FP/2007 - 2013) under grant agreement nr. 217246 made with the joint Baltic Sea research and development program BONUS. The educational user-license grant of Seismic Micro-Technology and the support of GEDCO allowed us to use the softwares The Kingdom Suite and VISTA Seismic Data Processing.

Chapter 3

Estimating the free gas content in Baltic Sea sediments using compressional wave velocity from marine seismic data

Zsuzsanna Tóth¹, Volkhard Spieß¹, Jørn Bo Jensen²

¹ Department of Geosciences, University of Bremen, 28359 Klagfurter Str., Bremen, Germany

² Geological Survey of Denmark and Greenland, Ø. Voldgade 10, 1350 Copenhagen, Denmark

3.1 Introduction

Methane (CH_4) is commonly produced by microbes in fine-grained sediments through the degradation of organic matter and large amounts of this greenhouse gas can be found in unconsolidated marine sediments. Most of the methane is effectively broken down in the subsurface, either aerobically in the presence of oxygen (Reeburgh, 1969), or consumed by microorganisms in a process called anaerobic methane oxidation (AOM), which occurs in the sulfate-methane transition zone (SMTZ) (Sansone et al., 1978; Reeburgh, 2007; Boetius et al., 2000; Milucka et al., 2012). Below the SMTZ, however, dissolved

CH_4 in the pore water can accumulate to levels which exceed supersaturation. Under low pressures and high temperatures typical of non-polar continental shelves, once the partial pressure of CH_4 overcomes the ambient hydrostatic pressure, free methane gas forms as discrete bubbles.

Observations in Baltic Sea sediments suggests that free gas formation occurs in the organic-rich, fine-grained mud that has been deposited in the Baltic Sea since its opening to the North Sea roughly 9.8 ka (Andr  n et al., 2011). Free gas has been observed in locations where this mud layer exceeds 5 to 10 m in thickness (Borowski et al., 2005; Thie  en et al., 2006; Jensen & Bennike, 2009). The accumulation of CH_4 gas in the sediment therefore seems to be largely controlled by sedimentation rate and the flux of organic matter to the seafloor (Mogoll  n et al., 2012). Moreover, the depth of the SMTZ is a controlling factor as well, as the thickening of the organic-rich mud and the associated increase of the upward CH_4 flux causes the shallowing of the SMTZ. This exposes more sediment with fresh organic carbon to methanogenesis and leads to more CH_4 production, thus free gas formation (Flury et al., in prep).

Little is known about the amount, vertical distribution and migration of gas bubbles in gas-bearing marine sediments. Observational evidence provided by acoustic measurements is often restricted to imaging a snapshot in time. High frequency sediment echosounders provide the most suitable technique for the detection and mapping of shallow gas, because acoustic signals are distinctly attenuated by the scattering of gas bubbles (e.g. Judd & Hovland, 1992). Regions of shallow, gas-bearing sediments appear impenetrable in acoustic profiles, thus often blank or turbid in acoustic facies. Extensive areas of acoustic blanking and turbidity were reported and mapped in many areas of the Baltic Sea using high frequency sources (Mathys et al., 2005; Thie  en et al., 2006; Laier & Jensen, 2007). As a consequence of the strong attenuation, however, acoustic profilers often only image the upper boundary of the gassy sediment (gas front on top of the acoustic blanking zones) and fail to provide information about the vertical gas distribution in the sediment. Computed tomography (CT) scans of ~ 5 m long pressurized cores from Eckernf  rde Bay (Western Baltic Sea) showed that the bubble distribution in the sediment is not uniform and that gas bubbles exist within 2 to 20 cm thick intervals which are separated by gas-free intervals (Abegg & Anderson, 1997; Anderson et al., 1998).

Transport of methane in the sediment can occur by diffusion (in the fluid phase), advection of the pore water (Albert et al., 1998), or advection driven by the buoyancy of gas bubbles. Gas bubbles formed at depth may either become trapped or migrate toward the sediment-water interface (Tr  hu et al., 2004; Liu & Flemings, 2006). Indirect evidence of bubble migration include the observation of seeps–gas bubbles rising up through the water column (e.g. Judd, 2004), and migration pathways observed on seismo-acoustic data, e.g. columnar disturbances and gas chimneys (e.g. Judd & Hovland, 1992). Mechanisms for gas bubble formation and migration within ‘impermeable’ mud are currently subject to debate. Gas injections into gelatin and mud showed that bubbles grow as highly eccentric oblate spheroids (disks)

by fracturing the cohesive host medium or by reopening preexisting fractures (Boudreau et al., 2005). Likewise, computer simulations suggest that sediment fracturing may also trigger bubble rise (Algar et al., 2011); however, the estimated rising speeds of bubbles may be unrealistically high (Boudreau, 2012).

The quantity of free gas in the sediment is difficult to measure, because methane degases when the sediment is brought to ambient pressure during core recovery. Pressurized core samplers, which could better maintain the in situ gas content, are expensive and only rarely used. A simple technique for measuring in situ gas concentration would thus have great advantages. In deep sea sediments, hydrate and free gas contents have been previously estimated using seismic velocities (Lee et al., 1993, 1996; Wood et al., 1994; Ecker et al., 2000). At low (seismic) frequencies, a small amount of free gas in the sediment reduces compressional wave velocity significantly (Anderson & Hampton, 1980). The acoustic impedance contrast between the fully water saturated and the gas-bearing sediment layers results in a reversed polarity reflector in marine seismic profiles. Based on a reduction of compressional wave velocity in gassy sediments, in situ amounts of free gas may be estimated using the velocity field obtained from seismic data.

Our goals in this study, using a 2D shallow seismic profile from the Bornholm Basin, Baltic Sea, are (1) to investigate shallow gas-bearing sediments and the geological background of free gas formation; (2) to obtain compressional wave (seismic) velocity and estimate the free gas content in the sediment; (3) and to characterize the vertical distribution of gas bubbles in the sediment.

3.2 Bornholm Basin

The Bornholm Basin is located in the southern Baltic Sea, northeast of Bornholm island (Denmark) and southwest of mainland Sweden (Fig. 3.1). This present sub-basin of the Baltic Sea is situated in a major structural depression that subsided during the deposition of Upper Cretaceous sediments (Sviridov et al., 1995). The pre-Quaternary bedrock in the basin consist mainly of these late Mesozoic limestones topped with an unconformity surface, and the Quaternary basin fill is composed of a unit of glacial deposits, and a succession of late- and postglacial lacustrine and marine sediments (Kögler and Larsen, 1979).

After the last deglaciation of the Baltic Sea basin, isostatic uplift together with eustatic sea-level changes resulted in 4 to 5 distinct phases in sedimentation (Björk, 1995; Andrén et al., 2011) (Fig. 3.2). In the Baltic Ice Lake stage (BIL, 16.0-11.7 ka BP), glacial (varved) clays and silt deposited conformably on the rugged pre-Quaternary surface shaped by glacial deformation and the deposits of glacial till in some places. The partly brackish Yoldia Sea stage (11.7-10.7 ka BP) and the fresh-water Ancylus Lake stage (10.7-9.8 ka BP) were characterized with the deposition of homogeneous clays (AY clays), which together with the BIL clays form an almost continuous cover over the deeper part of the eastern Bornholm

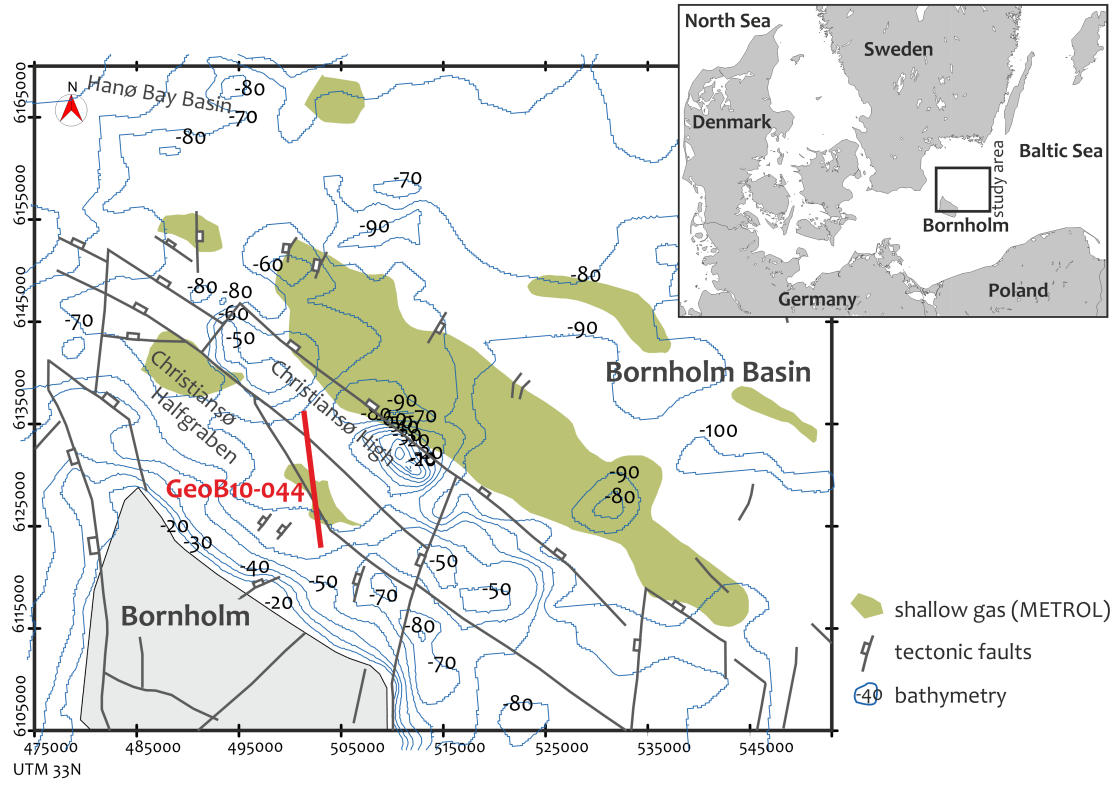


Figure 3.1: Location of the seismic profile GeoB10-044 in the Bornholm Basin, Baltic Sea. Green color denotes areas with free shallow gas in the Holocene mud. (The map was compiled after Vejrbæk, 1985; Laier & Jensen, 2007; Graversen, 2009).

Basin (Kögler and Larsen, 1979). Beginning of the subsequent brackish Littorina stage (9.8 ka BP) is a sharp lithostratigraphic boundary with a change to deposition of fine-grained mud, rich in organic matter. The organic carbon content (TOC) measured in core samples shows an increase from the start of the initial Littorina stage, and has a maximum in the end of post-Littorina Sea (6-7%) (Andrén et al., 2000). The transition to the recent Baltic Sea stage (c. 800 ka BP to present) is recorded as a biostratigraphical change in the mud (Andrén et al., 2000).

Degradation of organic matter has produced CH_4 predominantly in the Littorina mud (Fig. 3.2). Free methane gas is observed in the basin where the thickness of the mud exceeds 5 to 10 m (Kögler and Larsen, 1979; Borowski et al., 2005). These areas were mapped during the METROL project (Borowski et al., 2005) based on the observation of acoustic blanking and acoustic turbidity in high frequency echosounder data (Laier & Jensen, 2007). Shallow gas occurs in an extensive area in the eastern part of the basin and in smaller patches in the vicinity (Fig. 3.1).

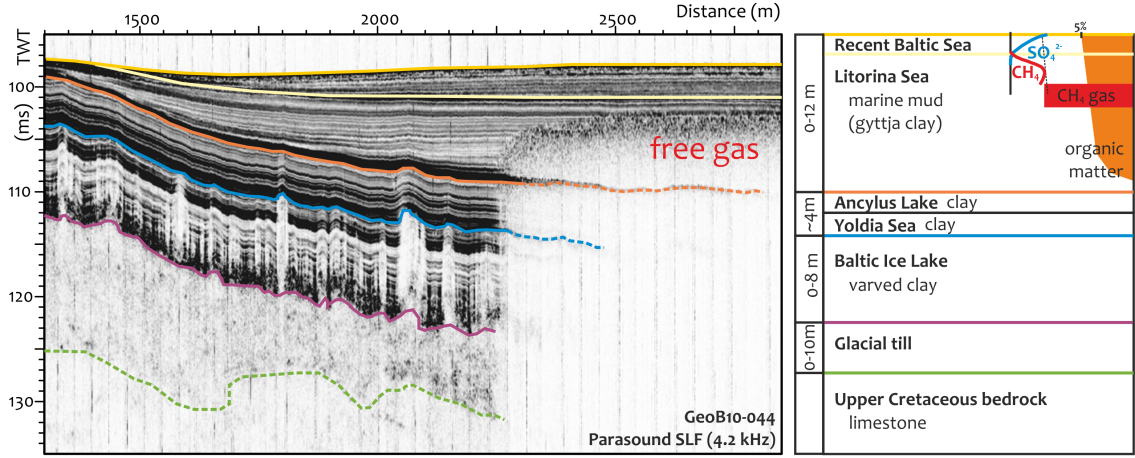


Figure 3.2: Stratigraphy of the Quaternary sediments in the Bornholm Basin after Kögler and Larsen (1979); Andrén et al. (2000) represented in a high frequency Parasound profile (part of the line GeoB10-044).

3.3 Data and methods

3.3.1 Seismo-acoustic data

The seismic data used in this study were acquired in August 2010 on the R/V Maria S. Merian cruise MSM 16/1. We selected profile GeoB10-044 from the western part of the Bornholm Basin for detailed analyses (Fig. 3.1). The seismic data were recorded with the GeoB high resolution shallow water multi-channel seismic (MCS) system, which includes a micro GI air gun (Sodera) with reduced chamber volumes of 0.1 l, and a 50 m long analogue streamer with 48 channels and 1 m channel spacing comprising single hydrophones. The central frequency of the source is around 200 Hz, while the useful frequency content recorded with the streamer ranges from approx. 100 to 600 Hz. Shot rate was set to 1.5 s, average speed of the ship during the survey was ~ 4 knots. The MCS data were recorded with the acquisition software MaMuCS (H. Keil), with a sampling rate of $100 \mu\text{s}$ and recording length of 1.3 s. For receiving high-precision coordinates, a differential GPS (Trimble) was used, whose two antennas were installed on the navigation deck of the ship.

High-resolution sediment echosounder data were acquired in parallel with the ship's parametric narrow beam echosounder Parasound DS3 (PS). Parasound emits both primary and secondary signals within a cone of only 4° opening angle, which ensures very high lateral resolution by considerably reducing the area of the reflecting surface. The transducers of Parasound are mounted to the ship's hull and simultaneously emit pulses at 19.2 kHz and 23.5 kHz, generating parametric secondary frequencies in the water at 4.3 kHz

and 42.7 kHz. We complemented the seismic data with the 4.3 kHz echosounder data in this study.

For display and interpretation of the seismo-acoustic data, we used the commercial software package KINGDOM (IHS Global Inc.).

3.3.2 Seismic processing and velocity determination

The MCS dataset was processed using the software package VISTA 2D/3D Seismic Data Processing (GEDCO). Seismic data processing partly followed a conventional marine processing flow including common midpoint (CMP) binning, spherical divergence correction, bandpass filtering, normal move-out (NMO) correction, noise attenuation and correction of residual statics (Fig. 3.3). The geometry (source and receiver positions) was calculated from the GPS data using the custom software WinGeoApp. The CMP binsize was chosen to be 1 m to yield high horizontal resolution, the fold was average 8.

The preliminary velocity analysis was carried out with the Interactive Velocity Analysis tool of VISTA, where the velocities of reflectors are picked at selected CMPs along the profile based on previously generated velocity semblance, common-offset stacks (COS), and constant velocity stacks (CVS), which all cover the possible range of true velocities. The root-mean-square (rms) velocities are best picked here for reflectors, where it is possible to fit the hyperbola to the travel time trajectories with certainty, aided by the velocity semblance and the CVSs. Having the aim of NMO correction, the rms velocities picked here allow the optimal stacking of traces in the CMPs, thus providing the best quality stack (stacking velocities). The resulting velocity field is, however, limited in resolution and vertical extent, because the velocity can only be picked at the first few prominent reflectors.

In order to refine this initial velocity field, we carried out a second, migration velocity analysis (MVA) (Fig. 3.3). In principle, rms velocities are most appropriately estimated from prestack time-migrated data and the acquired migration velocity is, in theory, the medium velocity independent of the dip of the reflecting interface (Yilmaz, 2001). As opposed to the stacking velocity estimation, where the moveout correction is done in individual CMPs, the MVA requires the complete pre-stack data, because the process of migration moves energy spatially from one CMP location to the other. So for the MVA, the entire pre-stack seismic profile was time-migrated varying the stacking velocities by 1% each time between 80 and 120%. The rms velocity functions were picked again in the Migration Image Velocity Analysis tool of VISTA, where the best 'image velocity' was selected for every reflector. Picking is partly subjective, because it is simply a matter of deciding which velocity gives the best image at each time. But when the velocity in the migration equals the medium velocity, the event is well-compressed (the diffraction hyperbola is collapsed in its apex), therefore the correct migration velocity can be estimated by evaluating the quality of focusing and by choosing the best value between undermigrated (too low velocity) or overmigrated (too high velocity) events. A priori knowledge about the type of sediments

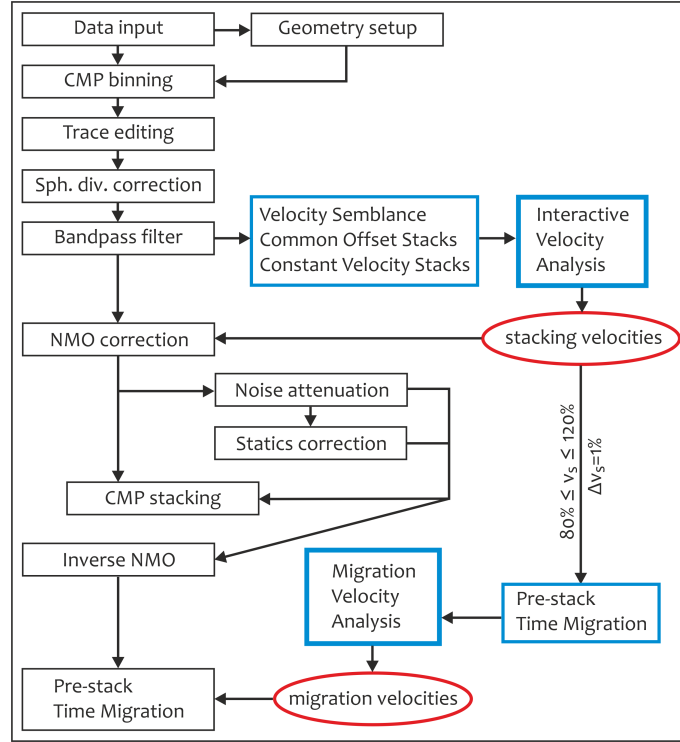


Figure 3.3: Flowchart of the marine seismic data processing applied to profile GeoB10-044. Apart from the conventional Interactive Velocity Analysis, a second velocity analysis was carried out using pre-stack time migration, which resulted in a detailed migration velocity field.

and possible gas content inferred from gas signatures help as well to narrow down the correct velocity functions.

The seismic profile significantly improved with the migration velocities in the final pre-stack migration (Fig. 3.4). Finally, the obtained rms migration velocities were converted into a physical interval velocity model (output of VISTA) using the Dix conversion (Dix, 1955).

3.3.3 Geoacoustic model for estimation of the gas content

The comprehensive theory of Anderson & Hampton (1980) along with analogue laboratory experiments show that the sound speed, attenuation and reflectivity of gassy marine sediments is dominated by the resonance of gas bubbles. Gas bubbles in marine sediments resonate at a fundamental frequency, and as a consequence the acoustic response of gassy sediments is dependent on frequency. The relatively low frequency of the seismic source, 200 Hz, used in our survey is well below the resonance frequency of gas bubbles. Assuming typical bubble sizes of 0.5 – 5 mm, bubble resonance frequencies for Bornholm

Basin sediments (~ 90 m water depth) are at $f_0 \cong 1.8 - 18$ kHz (based on Anderson & Hampton, 1980; Wilkens & Richardson, 1998). Seismic wavelengths are considerably greater than the range of bubble sizes, therefore only the bulk properties of the medium contribute to the acoustic response of the sediment. The sediment acoustic behaviour below the resonance frequency of gas bubbles is described by the Anderson & Hampton model, which relates the compressional wave velocity (v) to the bulk elastic properties (K and G) and density (ρ_s) of the sediment. It includes the modifying effect of free gas on fully saturated sediments by introducing a 'compressible fluid' (for the model equations see the Appendix). We use this model to estimate the gas content from the interval velocities obtained from the seismic data.

In the model, the sediment is described as a comparatively stiff saturated material. The overall gas content is small, i.e. no expansion happens due to the free gas. It is assumed then that if the greater compressibility of the gas increases the compressibility of the pore water without changing the mineral and frame compressibility and shear rigidity, sound speed can be derived from the stiff saturated sediment, where the bulk modulus of the pore water is modified by the bulk modulus of gas. Using this 'compressible fluid model', compressional wave velocity in gassy marine sediments is predicted to decrease rapidly with increasing gas content at frequencies well below resonance. Gas content as small as 1-2% reduces the velocity to only a few hundred m/s.

The physical property values used in the calculation of the gas content are listed in Table 3.1. The sediment bulk density and porosity are average values from measurements on samples of gravity cores along the profile, which were taken on an earlier cruise (R/V Gunnar Thorson cruise in 2004, project METROL) (Fossing, 2005). The mineral bulk modulus and sediment shear modulus values were taken from the study of Wilkens & Richardson (1998), the latter was measured in the Eckernförde Bay, Baltic Sea. The value of the sediment frame bulk modulus is from the table of Anderson & Hampton (1980) regarding sound speed and frame elastic properties (Part II, Table III).

3.4 Results

3.4.1 Interpretation of the seismo-acoustic data

The 13 km long profile GeoB10-044 crosses a small mud-filled depression with free gas in the western part of the Bornholm Basin (Fig. 3.1) and reveals along the profile two, 2-3 km long gas patches (Fig. 3.4). In the high frequency PS data (Fig. 3.4.a), the gas patches are clearly recognizable as zones of acoustic blanking. The acoustic blanking is caused by the strong attenuation of the high frequency acoustic signal due to absorption and scattering of gas bubbles in the sediment. As a consequence, only the top of the free gas layer, the gas front, is imaged and reflections are almost completely absent beneath. The reflection from the surface of the AY clays, probably due to the large acoustic impedance contrast remains traceable

Table 3.1: Values of parameters used to calculate gas content from interval velocities in the gassy sediments of the Bornholm Basin. References are in the text.

Shear modulus of the sediment (G)	$2.81 \cdot 10^5 \text{ Pa}$
Sediment bulk density (ρ_s)	$1.35 \cdot 10^3 \text{ kg/m}^3$
Mineral particle bulk modulus (K_m)	$3.6 \cdot 10^{10} \text{ Pa}$
Sediment frame bulk modulus (K_f)	$1.4 \cdot 10^7 \text{ Pa}$
Fractional porosity (n)	0.8
Pore water bulk modulus (K_w)	$2.14 \cdot 10^9 \text{ Pa}$
Ratio of specific heats of gas (γ)	1.31
Hydrostatic pressure at 1 atm (P)	$1.01325 \cdot 10^5 \text{ Pa}$
Seawater density (ρ_w)	$1.013 \cdot 10^3 \text{ kg/m}^3$

near the edges of the blanking zones, but no reflections are visible further towards the center. The gas front in the PS data appears in the mud at depths ranging from ~ 7 to 2 and 4.5 to 3.8 m in the southern and northern patch respectively.

This gas front is not clearly visible on the multichannel seismic data (Fig. 3.4.b-c). Only when looking closely, it can be seen that the gas front is a separate, negative polarity reflector having a peak-trough wavelet shape as opposed to the positive trough-peak wavelet of the seafloor reflection. The reversed polarity is the result of decrease in acoustic impedance (reduced compressional velocity and lower density) due to the presence of free gas. Towards the edges of the gas patches, where the sub-bottom depth of the gas front gradually increases, the separation is somewhat clearer, otherwise the reflections of the seafloor and the gas front blend in.

Beneath the negative polarity gas reflections, two depressions are revealed by the lower frequency MCS data. The shape of the southern depression is easier to infer from the AY-BIL clay layers at its base which conformably cover the eroded surface of the bedrock, but beneath the northern gas patch a deep glacial valley is exposed. While the AY clays form only a thin layer in both depressions, the seismic unit identified as BIL clays appears thicker towards the north.

Beneath the reversed polarity reflector representing the gassy layer, the seismic data show one or two more, roughly horizontal reflectors in the otherwise acoustically transparent mud layer. They show a low-amplitude, rather disturbed and fuzzy seismic appearance and it is hard to decide whether they have a normal or reversed polarity due to possible interference, although the first positive peak seems more pronounced suggesting a decrease in acoustic impedance. This is coupled with a very high amplitude

reflection at the base of the Holocene mud in the southern depression. Here, the significant amplitude increase can be the result of constructive interference between a reflection in the mud and underlying reflector of the AY clays.

3.4.2 Interval velocities

The interval velocity field obtained from the MCS data is displayed in Fig. 3.6.a with the velocity picks at the selected CMP locations. For a sediment layer or unit, the interval velocity is calculated between the reflectors at which the rms velocities were picked, and determination of a layer interval velocity requires a reflector/pick at the base. Interval velocities are displayed without any interpolation or smoothing. Therefore on Fig. 3.6.a, cells defined by the velocity picks are colored based on the interval velocity values in them. The horizontal boundaries of these cells are the picks/reflectors (indicated in the middle of the cell) and the vertical boundaries are the CMPs where the velocities were picked. Evident are the two low velocity patches between CMP 2500-4500 and 5500-8500 in the vertical range of 105-130 ms TWT. The top of these low velocity zones coincide with reversed polarity reflections verifying the decrease in acoustic impedance as indicated by the polarity change (Fig. 3.4). The interval velocity inside the patches varies between 1400 and a minimum of 200 m/s. These low velocities confirm the presence of free gas in the sediment.

The interval velocity is laterally highly variable within layers and stratigraphic units. These lateral changes can result from variations in thickness and sub-bottom depth. To get a better idea about the interval velocities in each stratigraphic unit and the distribution and content of free gas, average values were calculated around the gas patches for layers 1, 2a-c, 3, 4 and 5 as shown in Fig. 3.6.b (Table 3.2). Based on the reflections where the velocities were picked in the Holocene mud unit, layer 2 (gassy mud), was divided to two and three sublayers in the northern and southern patch respectively. These reflections in the mud occur probably due to changes in grain size. The interval velocities averaged horizontally within the layers, split between the northern and southern patch, are summarized in Fig. 3.7.

The first picks at the seafloor determine the sound speed in the water column (w), which is around 1540 m/s. This is higher than the expected 1450-1500 m/s for seawater velocity. The average interval velocity in layer 1, which is the top of the mud layer and its base is the gas front, thus gas-free, is 1902 m/s. This is anomalously high as expected velocities for a high-porosity surficial muddy sediment are close to sound speed in seawater or even lower due to the low rigidity and high compressibility of water, so ≤ 1450 to 1500 m/s.

The low-velocity patches in the mud (layers 2a-c) have average interval velocities here ranging from 1040 to 1223 m/s, consistent with velocity decrease caused by free gas. Beneath these zones, the interval velocity of layer 3 is 1700 m/s, which corresponds to the dense clays beneath the mud. Layer 4 below

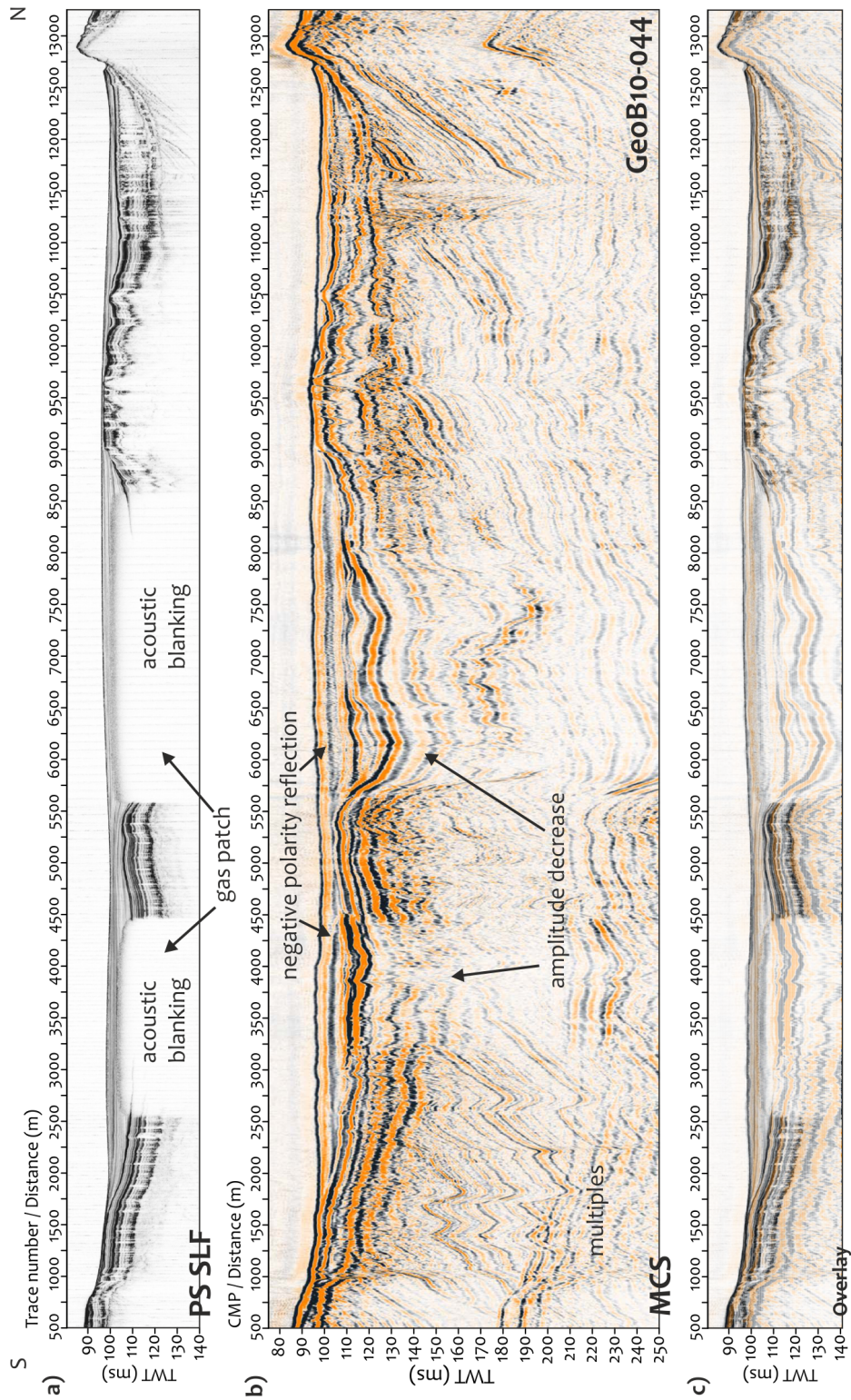


Figure 3.4: Profile GeoB10-044, on top the a) Parasound SLF (4.3 kHz, envelope display), in the middle the b) multichannel seismic data, and on the bottom c) their overlay. The vertical exaggeration is $\sim 58x$. For the location of the profile see the map on Fig. 3.1.

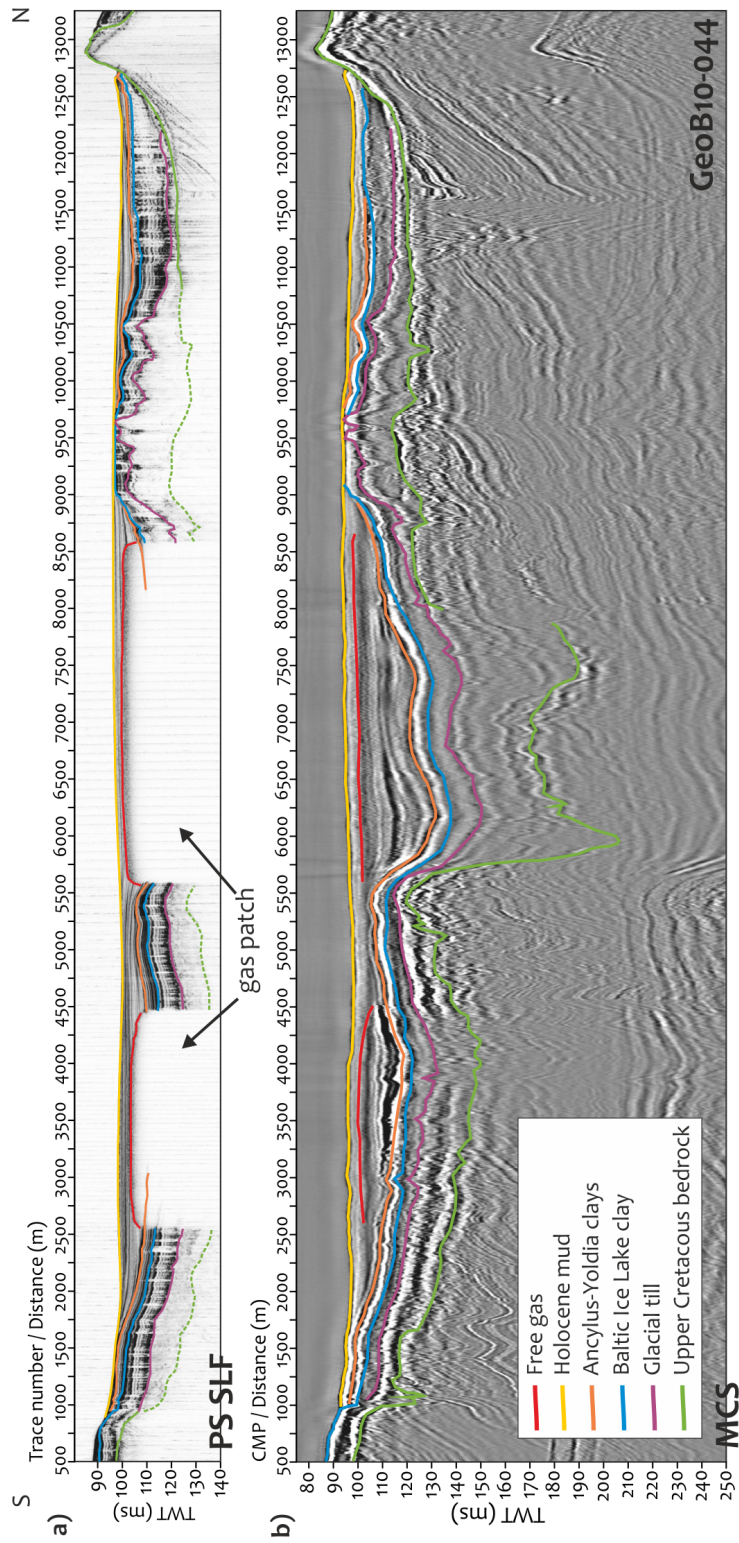


Figure 3.5: Stratigraphical interpretation of profile GeoB10-044, a) on top the Parasound SLF (4.3 kHz, envelope display), b) on the bottom the multichannel seismic data. The vertical exaggeration is $\sim 58x$. Location of the profile is on Fig. 3.1.

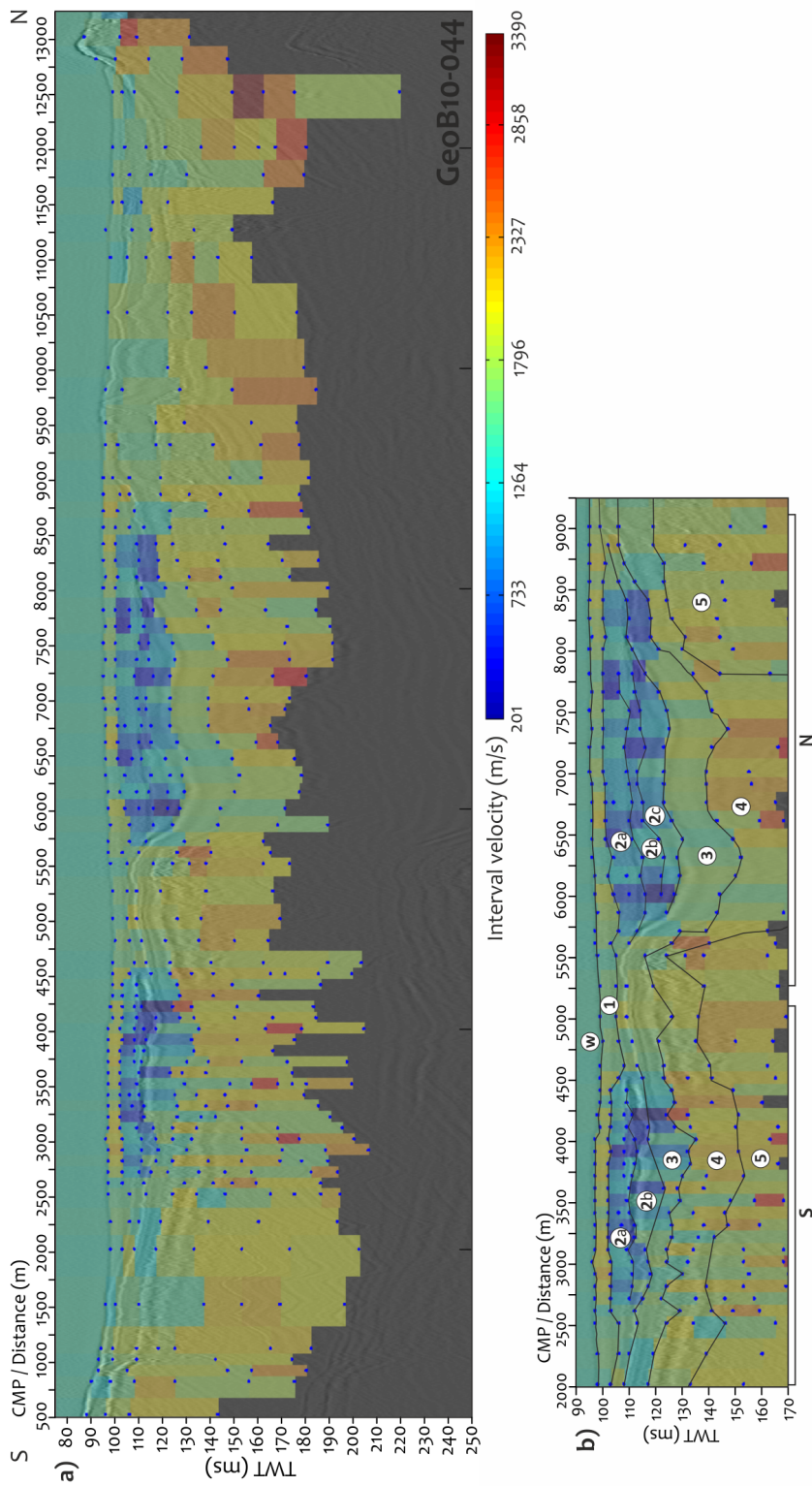


Figure 3.6: a) Interval velocities superimposed on the seismic traces of the profile GeoB10-044. The velocity picks from the Migration Velocity Analysis are indicated with blue dots in each CMP where the velocity of reflectors were picked. The picks and CMPs define cells, which are colored respectively to the interval velocity values in them. b) A close-up of the two gas patches with the layer boundaries, where average interval velocities were calculated.

Table 3.2: Average interval velocities in the layers on Fig. 3.6.b, their average two-way travel time, depth, and gas content calculated based on the compressible fluid model. S denotes the layers within and below the southern gas patch, N the ones in the northern gas patch.

Layer	TWT (ms)	Depth (m*)	Interval velocity (m/s)		Δv (m/s)	Gas content (%)					
water column	96	73.92	1540		0	0					
layer 1	(gas-free mud)	100	1902		361	0					
	S	N	S	N	S	N	S				
layer 2a	(gassy mud)	105	105	80.85	1184	1223	-356	-317	0.04	0.03	
layer 2b	(gassy mud)	115	115	88.55	1164	1040	-376	-500	0.04	0.07	
layer 2c	(gassy mud)	120	92.4		1129	-411		0.05			
layer 3	(clays)	122	122	93.94	1700	1678	159	138	0	0	
layer 4	(till, valley fill)	125	135	96.25	103.95	2055	2177	515	637	0	0
layer 5	(bedrock)	150	155	115.5	119.35	2198	2162	657	622	0	0

$\ast v = 1540$ m/s

* $v = 1540$ m/s

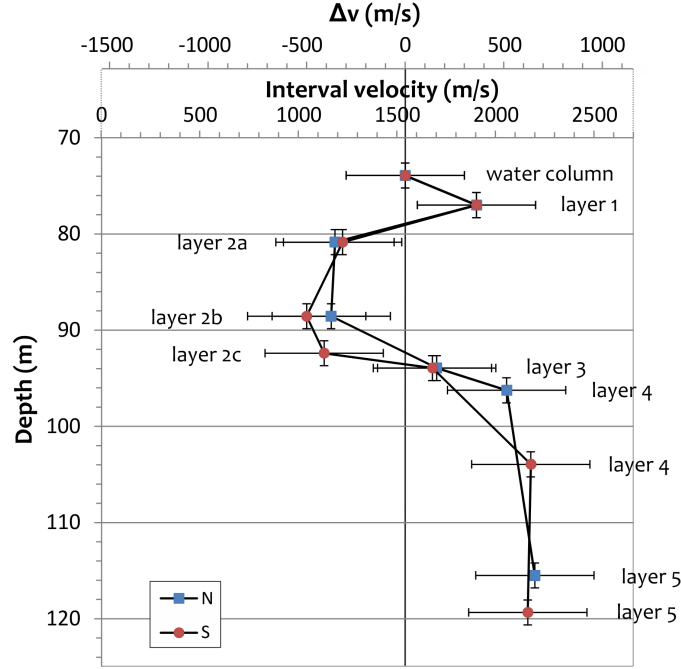


Figure 3.7: Average interval velocities in the layers denoted on Fig. 3.6.b. The water velocity is indicated with the vertical line. The interval velocities of layers 2a-c on the left of this line indicate the presence of free gas. These layers correspond to the Holocene mud below the gas front. The bars indicate the error ranges.

(glacial till) and layer 5 (bedrock) reach interval velocities of 2055-2198 m/s.

3.4.3 Gas content

Finally, we calculated the free gas content (n_g , gas porosity = gas volume / total sediment volume) based on the average interval velocities of the layers using the compressible fluid model. Since the relative gas content is dependent on the ambient hydrostatic pressure, for each layer an average depth was used in the calculation (Table 3.2). The relationship between compressional wave velocity and gas content is shown in Fig. 3.8. This curve was plotted for typical muddy sediments of the Bornholm Basin, 3 m below the sediment surface in a water depth of 73 m. Even very small amounts of gas cause a significant decrease in the compressional wave velocity: 0.1% gas volume is associated with a 50% drop, 1% decreases the velocity to 300 m/s and 3% to only 200 m/s (Fig. 3.8).

Based on the compressible fluid model, compressional wave velocity would be 1400 m/s in a muddy seabed sediment with zero gas content and physical properties listed in Table 3.1 (Fig. 3.8). Since this

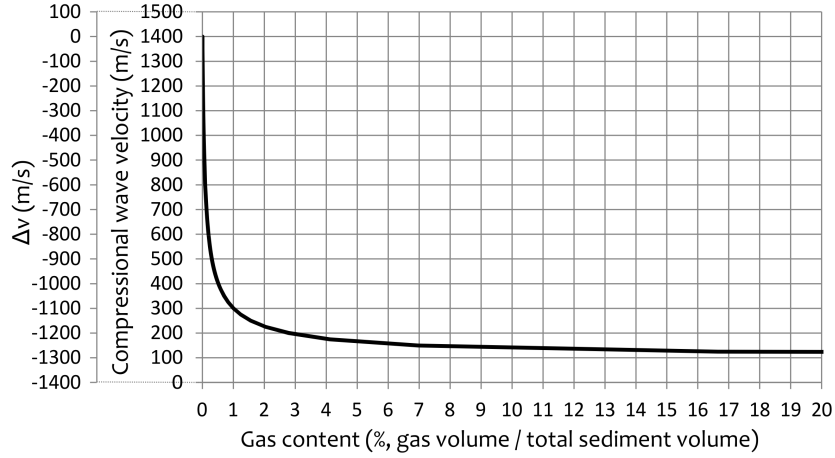


Figure 3.8: The relationship between compressional wave velocity and gas content in the compressible fluid model of Anderson & Hampton (1980). Same values were used for this plot as listed in Table 3.1. The curve shows the gas content in muddy sediments, 3 m below sediment surface in a water depth of 73 m.

is lower than the velocity measured for seabed sediments, we modify the calculation of the gas content using the velocity drop (Δv) referred to a gas-free seabed sediment velocity of 1540 m/s. Any decrease of the average migration rms velocity is then attributed to the presence of gas (Table 3.2). Accordingly, the velocity drop in layers 2a-c is caused by 0.03-0.07% gas volume in the sediment. The average gas content in these layers is 0.045% overall.

3.5 Discussion

3.5.1 Uncertainty of the interval velocities

The accuracy and resolution of velocity estimations from seismic data depends on several factors. Since velocity is determined directly from the data, essentially, both the setting and the equipment determine accuracy and resolution. The source frequency and data bandwidth define the basic resolution. The water depth together with the offset (streamer length) and the ship's speed influence the fold and the measurability of hyperbolic move-out. The signal-to-noise ratio in the data influences the overall accuracy.

Parameters that influence the measurement of travel time are the primary error sources in the velocity determination. These parameters are related to the positional geometry of the source and the receivers. While a centimeter accuracy is realizable in measuring the momentary distances of the source and receiver positions (both horizontally and vertically), these are measured once and assumed to be constant during

the entire survey. Nevertheless, variable weather and oceanographic conditions, as well as waves and their effects on the equipment movement may lead to relatively small scale displacements. Their effect on the velocity is difficult to estimate, because the deviation from the assumed positions is unknown. Additionally, the 'gun delay', the time between the trigger signal and the actual release of the air bubble into the water is usually either roughly estimated from the data or imposed empirically. Ultimately, the geometry, gun delay, and thus the velocities can be calibrated with the velocity of the direct wave, which must be close or equal to the speed of sound in water.

Furthermore, errors in the determination of interval velocities may result from uncertainties in the rms velocity measurements. The travel time errors are secondary in the derivation of interval velocities, although the effect of the timing error becomes more important at reflection times less than 1 s (Hajnal & Sereda, 1981). We can estimate the error in the velocity estimates by evaluating the accuracy of the MVA method. Errors in the MVA result from the inaccuracy of velocity picking. Since the stacking velocities beforehand are varied by 1%, the error in the migration rms velocity is at least ± 15 m/s. However, the best 'image velocity' can be picked from a larger range, about $\pm 2\%$. Also, picking is partly subjective, therefore the confidence range of the migration rms velocity can be estimated to be about ± 30 m/s. Picking in time in the MVA has an error of about ± 1 ms. These together can cause errors of as high as 300 m/s in the interval velocities (based on the uncertainty formula of Hajnal & Sereda, 1981). The confidence range of the best 'image velocity' in the MVA gets wider at deeper reflections. This is expected as the lack of the significant moveout at deeper reflections inhibits velocity discrimination. The uncertainty in the computed interval velocity of a layer consequently will increase with reflection time.

It should be also noted that the resolution of the velocity field is affected by the reflector locations where the velocity of an event can be picked. It is thus greatly influenced by the variability of the geological structure and the vertical resolution. The uncertainty in the interval velocity of a layer is inversely proportional to the interval travel time of that layer (Hajnal & Sereda, 1981), which in case of our high resolution picking (layer thickness of 3-4 ms TWT) may lead to larger error ranges.

3.5.2 Variability in the interval velocities

Based on our MVA, the migration rms velocity of the seafloor reflection (and thus the interval velocity/sound speed in the water column) is both 50-100 m/s higher than expected and 30-60 m/s higher than the best stacking (NMO) velocity of the seafloor reflection (1460 m/s). These latter values compare well with in situ CTD measurements in the Bornholm Basin, which determined the sound velocity near the seabed to be 1459 m/s (Schneider von Deimling et al., 2013). Although the reasons are unclear, our higher migration velocities at the seafloor may indicate that the values for entire velocity field are higher than the real medium velocity values.

The anomalously high average interval velocity of layer 1, corresponding to gas-free mud at the seabed, likely shows the effect of thin layers on the interval velocity. Compressional wave velocity in gas-free muddy seabed of the Eckernförde Bay, Baltic Sea (similar environment and sediment) was measured in situ using an acoustic lance and it was found to be 1430-1480 m/s (Fu et al., 1996; Wilkens & Richardson, 1998). The ~ 400 m/s deviation here can probably be attributed to rms velocity picks at too close time intervals, which can yield anomalous interval velocities from the Dix conversion, even though the increase in rms velocity with depth is small (Yilmaz, 2001). For example, in case of rms velocities 1500 and 1550 m/s at the top and base of a 3 m thick layer (4 ms TWT), the interval velocity is 2452 m/s. Therefore, the 1902 m/s interval velocity of layer 1 is a consequence of the vertically high resolution velocity picking and the derivation of the interval velocity, and it does not characterize the sediment layer between the bounding rms velocity picks.

The interval velocities within layers/stratigraphic units (Fig. 3.6.a) appear highly variable. This variability can result from the method of velocity determination and/or reflects small changes in the sediment lithology, gas content, etc. While such big changes in lithology within stratigraphic units are not likely in Bornholm Basin sediments, variations in layer thickness and depth can result in slightly different interval velocities. In the Dix conversion, the underlying assumption is that the earth model comprises horizontal isovelocity layers. Therefore, decreasing layer thicknesses lead to increasing interval velocities and larger uncertainties in the computed interval velocities of the deeper layers. As a consequence, the interval velocity determined between closely spaced reflectors in a complex geological structure will likely reveal highly variable values.

Apart from this, variabilities in the distribution, amount, and concentration of gas bubbles may also cause subtle changes in the compressional wave velocity. Abegg & Anderson (1997) found in the Eckernförde Bay sediments that gas bubble distributions are variable vertically on a centimeter scale (thin gassy and non-gassy layers a few cm thick in 5 m long cores) and horizontally on a meter scale (from cores collected 2-20 m apart). Actual gas volume concentrations measured in cores kept under in situ pressure and temperature using the CT scanning technique revealed highly variable free gas concentrations, from 0.1% to 9%, changing both vertically and laterally (Abegg & Anderson, 1997; Anderson et al., 1998). This means that alternating layers of low and high velocities in the sediment are likely (Wilkens & Richardson, 1998). While high concentrations of gas bubbles represent small heterogeneities in the medium when compared to the wavelength of the seismic wave (the wavelength $\lambda \sim 7.5$ m for the 200 Hz signal of the airgun), given the high sensitivity of compressional wave velocities to changing gas content (Fig. 3.8), thin gassy sediment layers can cause considerable variability in the interval velocities. Measured velocities thus represent an average of lower velocities in gassy sediments and higher velocities in gas-free sediments.

3.5.3 Velocity reduction - gas content

Gardner (2000) performed controlled experiments on silty clay samples prepared in laboratory containing 1-2% gas volume with a uniform distribution of 0.2-1.8 mm sized gas bubbles. The acoustic response of the gassy sediments was broadly as predicted by the compressible fluid model, with measurements of compressional wave velocities as low as 220 m/s below the resonance frequency of the bubbles. However, a subsequent study by Gardner & Sills (2001) revealed that velocities based on bulk properties of sediments containing 'large bubbles' match the actual velocity measurements better than velocities based on the predictions of the compressible fluid model. In the 'large bubble model', gas is contained in structural pockets in the saturated sediment (Wheeler, 1988; Wheeler & Gardner, 1989). This is probably a more appropriate physical description of gas-bearing sediments, as typical gas bubbles are bigger than clay or silt particles and cannot be wholly contained within the pore water in typical fine-grained sediments. The large bubbles have a lower compressibility than the small bubbles formed within the fluid. Consequently, the velocity reduction due to free gas happens to a lesser degree, because the abrupt increase in the bulk compressibility is smaller (Eq.(3.1) in the Appendix). This means that the reduction in the interval velocities might be caused by an even larger amount of gas in the sediment than the compressible fluid model suggests (for more detail see Gardner & Sills, 2001). Our calculated free gas contents may thus represent a lower estimate of gas contents.

3.5.4 Gas distribution and amount in Bornholm Basin sediments

The depth distribution of gas bubbles in the sediment is difficult to investigate, because information about the free gas zone derived from seismo-acoustic data is limited. In the PS profiles, the top of the free gas zone is marked by the strongly scattering gas front, but because of the strong attenuation of the high frequency signal, nothing deeper can be inferred from inside the acoustic blanking zones (Fig. 3.4.a). In the lower frequency seismic data, a horizon in the same depth as the gas front in PS data appears as a reversed polarity reflection (Fig. 3.4.b), and although penetration through the gassy layer is achieved, the base of the gas-charged sediment layer is difficult to identify. If the gas bubbles are concentrated in a thin layer, it might not be possible to resolve the layer boundaries as separate reflections. If the gas bubbles are distributed in a thicker layer, but with a gradual decrease of gas bubble concentration with depth, then again only one reflection may be observed, which would then mark the top of the gas-charged sediment layer. The gradual increase of velocity and/or density (gradient zone) in the medium will not cause a sharp acoustic impedance contrast, thus reflection amplitude may be (much) smaller than expected from the total impedance contrast.

The interval velocity field determined from the MCS data (Fig. 3.6.a) reveals presence of free gas through the reduction of compressional wave velocity ($v < 1540$ m/s, blue colors). Low interval velocities

characterize the Holocene mud layer beneath the gas front. The velocity drop is confined to the mud (layer 2a-c), whereas the clays below (layer 3) show higher interval velocities well above 1540 m/s (Fig. 3.6.b and Table 3.2). This suggests that gas bubbles are present throughout the Holocene mud beneath the gas front. The velocities for all layers represent average values for these units, and thus do not take into account any intralayer vertical variations and inhomogeneities. Also, the long seismic wavelength and the vertical uncertainty of the reflector picks limit the velocity resolution for thin layers. Accordingly, the velocity drop with respect to the velocity in gas-free sediment (the reference value) indicates average free gas content.

The average interval velocities in layers 2a-c suggest that in the northern gas patch the highest free gas concentrations occur in the middle of the mud unit. This is not well resolved in the southern patch, where the two layers in the mud unit appear to have similar gas contents. The distribution of gas bubbles in the sediment is locally controlled by the concentration of methane, the hydrostatic pressure, and the methane solubility (which is determined by the temperature, the hydrostatic pressure and the salinity). The concentration of methane is influenced by the methane flux, which is controlled by the rates as methane diffuses from the level of methane formation both downward and upward, and also the rate of methane production and consumption. Where free gas bubbles are formed, the buoyancy of the gas bubbles drives them further up towards the sediment surface. Based on the seismo-acoustic data, the gas distribution with depth, as drawn on in the sketch in Fig. 3.9, is likely to reveal a peak below the SMTZ, as the equilibrium situation causes a linear methane concentration gradient downwards. Where the methane concentration is above solubility, a reversed polarity reflection will appear as a consequence of the bulk property change of the medium due to gas bubbles. Further downward, free gas concentration will likely increase, gradually towards a peak value. As methane content is minimal in glacial clays, both free gas concentration, and further downward, concentration of dissolved methane, will decrease from this point following a diffusion gradient (Fig. 3.9). From available organic matter and associated potential of its degradation and the formation of methane, the zone where gas bubbles exist can extend almost down to the base of the Holocene mud. Since a minimum thickness of the methanogenic mud is required for free gas to form, the lower most section may not contain free gas (Mogollón et al., 2012).

Certainly, the vertical distribution of free gas probably depends highly on the sediment physical properties and on the local geochemistry. High variability of the interval velocities and measured gas volume concentrations point to a patchy distribution. Nevertheless, even if not evenly, free gas is vertically distributed throughout most of the Holocene mud beneath the gas front, and not only concentrated in a 1 or 2 m thick layer. If this situation is true, then there is no 'accumulation' of free gas occurring, which would concentrate gas bubbles. The present vertical distribution is rather a snapshot of a system in equilibrium, where methane production, migration, gas formation, and methane consumption is ongoing

and shape both the dissolved methane and free gas concentration curves.

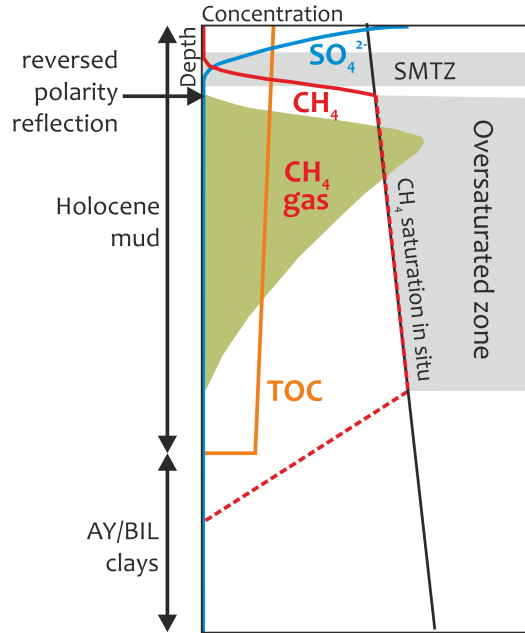


Figure 3.9: Schematic figure of the organic matter (TOC), dissolved methane (CH_4) and sulfate (SO_4^{2-}), and free methane gas concentration in the sediments of the Bornholm Basin.

The average gas content of 0.045% from our calculation is comparable with the results of other studies from the Baltic Sea. Methane gas concentrations at in situ pressure and temperature were only measured in the muddy sediments of Eckernförde Bay. Over the depth zone of 50 to 120 cm, at a water depth of 26 m, the average gas concentration was found to be approx. 0.02% (Abegg & Anderson, 1997; Anderson et al., 1998; Martens et al., 1998). Modeling studies by Martens et al. (1998) and Albert et al. (1998), which quantitatively couple the biogeochemical processes to the input flux of reactive organic carbon in the sediment, predicted gas concentrations of $\sim 0.3\%$, for essentially the same depth zone where the gas bubbles were observed in the pressurized cores. Mogollón et al. (2011) used a reactive transport model to investigate the seasonal dynamics of the methane cycle. Their model predicted (depth-averaged) gas volume fractions of 0.25% for the early fall months in the Eckernförde Bay sediments, and early spring values were as low as 0.021%. This model study also indicated that there can be considerable variations in the position and thickness of the free gas layer due to the seasonal fluctuations of heat propagation. This needs to be taken into account when comparing measured values of free gas concentration.

In our study, the interval velocities in individual cells of the velocity field are reduced to 201 and 262 m/s in the southern and northern gas patch, respectively. This predicts up to 3.4% and 1.6% gas content in the volumes of the sediment bounded by the rms velocity picks. These values seem high compared to

the average gas content, but not unlikely, as pressurized cores from the pockmark site in the Eckernförde Bay reached as high values as 9%. Based on model predictions, Mogollón et al. (2011) argues that high free gas concentrations are unlikely near the gas front due to seasonal production and migration of free methane gas. Deeper gas layers may thus be a product of gas burial and accumulation over a long period of time.

3.6 Conclusions

We performed detailed velocity analyses on a 2D shallow marine seismic profile from the Bornholm Basin, Baltic Sea. Although it is time consuming and computationally intensive, migration velocity analysis offers quite an accurate method to obtain high resolution velocity fields from pre-stack time migrated data. Beyond ensuring accurate geometry and travel times in the seismic data, precise velocity determination is important, as small errors in the migration rms velocities can result in large errors in the interval velocities.

The seismic profile GeoB10-044 crosses two depressions filled with organic-rich Holocene mud, where shallow free gas is observed. Free gas in the sediment is indicated by acoustic blanking zones on the high frequency acoustic data, and the same horizon as the gas front appears as reversed polarity reflection on the lower frequency seismic data. The interval velocities obtained from the seismic data reveal two low-velocity patches along the profile, which extend from the reversed polarity reflections down to the base of the Holocene mud layer. Average interval velocity values within the gassy mud are lower than the seafloor migration velocity by up to 500 m/s. This decrease in interval velocity, using the geoacoustic model of Anderson & Hampton (1980) that relates compressional wave velocity to sediment physical properties and gas content, is caused by an average $\sim 0.045\%$ gas fraction in the sediment. Compressional wave velocities in the sediment are highly sensitive to free gas, and very small amounts of gas cause a significant decrease in the medium velocity. Based on the seismo-acoustic data and the derived interval velocities, shallow gas occurs throughout most of the Holocene mud. Although the distribution of free gas is patchy in the sediment, the gas concentration is likely to have a peak below the sulfate-methane transition zone and gradually decrease below.

Interval velocities obtained from multichannel seismic data can be used for the assessment of free gas concentration at in situ pressure and temperature in shallow marine sediments. The measurement of the velocity reduction caused by free gas is possible even when only a small amount ($> 0.01\%$) of free gas is present in the sediment. The high resolution velocity field offers the opportunity to investigate the free gas distribution with depth as well. Although limited in resolution because of the requirement of reflectors, together with the stratigraphical interpretation of the seismic data, geological units containing free gas

can be identified. Due to the frequency dependence of gas-bearing sediments and the seismic method, relatively low source frequency is needed, which is well below the resonance frequency of gas bubbles and provides penetration through the gassy sediment layer, but sufficiently high as well to provide high vertical resolution in the imaging of the subsurface.

Appendix - Geoacoustic model

The relationship between compressional wave velocity and the physical and elastic properties of gas-bearing sediments at acoustic frequencies much less than the bubble resonance frequency is given by the following equations after Anderson & Hampton (1980) and Wilkens & Richardson (1998).

Compressional wave velocity in gas-bearing sediments is given by the wave equation:

$$v = \sqrt{\frac{K + \frac{4}{3}G}{\rho_s}}, \quad (3.1)$$

where K is the bulk modulus of the gas-bearing sediment, G is the sediment shear modulus, and ρ_s is the sediment bulk density. The sediment composite bulk modulus is calculated based on Gassmann's expressions (Gassmann, 1951):

$$K = K_m \left(\frac{K_f + Q'}{K_m + Q'} \right), \quad (3.2)$$

where

$$Q' = K'_w \left(\frac{K_m - K_f}{n(K_m - K'_w)} \right). \quad (3.3)$$

Here K_m and K_f are the mineral and frame bulk moduli, n is the fractional porosity, and the bulk modulus of the pore water (K_w) is modified by the addition of gas (K'_w), introducing a compressible pore fluid:

$$K'_w = \frac{K_w K_g}{n'_g K_g + (1 - n'_g) K_g}. \quad (3.4)$$

In case of adiabatic compression, the bulk modulus of the gas is $K_g = \gamma P_0$, where γ is the ratio of specific heats of gas and P_0 is the ambient hydrostatic pressure. The fraction of sediment pore space occupied by gas (n'_g) is the gas volume (n_g) divided by the fractional porosity (n):

$$n'_g = \frac{n_g}{n}. \quad (3.5)$$

Acknowledgments

We wish to thank Niklas Allroggen and Marius Becker for their help with Matlab, Sabine Flury for useful comments on an early draft of the manuscript. We also thank José Mogollón for helpful discussions and comments on the manuscript. This research received the funding from the European Community's Seventh Framework Programme (FP/2007 - 2013) under grant agreement nr. 217246 made with the joint Baltic Sea research and development program BONUS. The educational user-licence grant of Seismic Micro-Technology and the support of GEDCO allowed us to use the softwares The Kingdom Suite and VISTA 2D/3D Seismic Data Processing.

Chapter 4

Frequency dependence in seismo-acoustic imaging of shallow free gas due to gas bubble resonance

Zsuzsanna Tóth¹, Volkhard Spieß¹, Hanno Keil¹

¹ Department of Geosciences, University of Bremen, 28359 Klagfurter Str., Bremen, Germany

4.1 Introduction

Poor signal penetration on acoustic profiles often indicates free gas in marine sediments (Fleischer et al., 2001; Judd & Hovland, 2007). This shallow gas is primarily biogenic methane, which forms through the sub-surface degradation of buried organic matter. Microbes known as methanogens produce methane as a metabolic byproduct in anoxic conditions. The methane accumulates in the muddy seabed and since it is poorly soluble in seawater, gas bubbles develop when the dissolved methane concentration in the pore water exceeds saturation. Gas bubbles create various features in seismo-acoustic profiles, because their presence causes significant changes in the physical and acoustic properties of the sediment (Anderson & Bryant, 1990; Judd & Hovland, 1992). The expressions of free gas and the penetration through the gassy layer is strongly dependent on the measurement frequency (Hart & Hamilton, 1993; Mathys et al., 2005; Schneider von Deimling et al., 2013). High frequency acoustic waves are strongly scattered by gas

bubbles, this results in chaotic reflections and blank zones in acoustic profiles (Judd & Hovland, 1992). Low frequency seismic waves undergo reflection from a gas-charged sediment layer and free gas appears as an enhanced reversed polarity reflection in seismic data (Chapter 2).

The model of Anderson & Hampton (1980), based on gas bubble resonance in water, predicts acoustic resonance behaviour in gassy marine sediments under small acoustic perturbations. Compressional wave velocity and attenuation is therefore expected to depend on frequency. There have been observations and measurements, both in laboratory and in situ that support the idea of gas bubble resonance in sediments. Wilkens & Richardson (1998) studied the frequency dependence of acoustic waves in gassy sediments of Eckernförde Bay (Baltic Sea) using different measurement techniques and frequencies between 5-400 kHz. Their study provided indirect evidence for resonance effects which were consistent with the size distribution of gas bubbles observed on the computed tomography scans of pressurized cores. Gardner (2003) measured the attenuation in laboratory silty clay samples which contained different amounts of gas bubbles with variable sizes. The measured and predicted values of attenuation showed that the Anderson & Hampton model is valid for the frequencies of bubble resonance, but very sensitive to inaccurate sediment elastic and damping properties. Best et al. (2004) carried out an in situ acoustic experiment on shallow gassy sediments using a continuous frequency range between 600-3000 Hz, over two tidal cycles, to demonstrate shifts in resonance frequency as a consequence of pressure and thus bubble size changes. Their measured attenuation-frequency curves provided evidence for gas bubble resonance in situ, although they drew attention to limitations of the model. The estimated change in bubble size (assuming spherical bubbles) as a result of changes in hydrostatical pressure alone could not account for the magnitude of the observed shifts in bubble resonance. Thus, other controlling parameters such as gas diffusion or different bubble shapes need to be taken into account when bubble populations are determined through resonance frequencies.

In this study we will investigate the frequency dependence, which gas bubbles cause in acoustic imaging of gassy sediments, by using several different frequencies at the same location. The transect, along which the seismo-acoustic data were collected, is located at the edge of an extensive gassy area in the Bornholm Basin, Baltic Sea. The seismo-acoustic data consists of high-resolution multichannel seismic data and parametric sediment echosounder data, covering frequencies between 0.2 and 43 kHz. By analyzing the reflection amplitudes in the gassy and non-gassy sediment along the transect, we will estimate the attenuation caused by the gas bubbles as a function of frequency. The highest attenuation points to the resonance frequency of gas bubbles, which according to the model is mainly a function of bubble size, moreover, the degree of attenuation may be used to estimate the gas content in the sediment.

Frequency dependent acoustic imaging of gassy sediments has consequences for the spatial assessment of gassy areas, as detection of gas and the expressions of gas in seismo-acoustic data are influenced by

the resonance of gas bubbles.

4.2 Theory of the acoustic behaviour of gas-bearing sediments

The presence of gas bubbles in shallow marine sediments results in a fundamentally different acoustic response than that of fully water saturated sediments. The Anderson & Hampton (1980) model describes the effect of free gas on the compressional wave velocity and attenuation of acoustic waves in marine sediments. Gas bubbles in the sediment oscillate radially under small acoustic perturbations, and can resonate at a fundamental frequency related to their size. Bubble resonance therefore dominates the geoacoustic properties of gassy sediments.

The attenuation of water-saturated muddy sediments is small and shows relatively small variation over a wide range of measurement frequencies (Hamilton, 1972; Richardson & Briggs, 1996; Best et al., 2001; Breitzke, 2006). But in gassy marine sediments, in addition to the sediment intrinsic attenuation, absorption due to loss mechanisms associated with bubble motion and scattering also contribute to the attenuation of acoustic waves. At resonance, gas bubbles absorb energy through oscillation, thus resulting in higher attenuation of the acoustic wave.

The following expression can be used to derive frequency dependent attenuation (α) due to losses associated with bubble motion:

$$\alpha = \frac{\pi f}{c_0} \frac{c}{c_0} \frac{KY_1}{\gamma P_0 + \frac{4}{3}G}, \quad (4.1)$$

where f is the acoustic frequency, c_0 and c are the saturated and gassy sediment sound speed values (c is also frequency dependent), γ is the ratio of specific heats of methane, P_0 is the ambient hydrostatic pressure, K and G are bulk and shear modulus of the sediment, and Y_1 is a frequency dependent coefficient of the gassy medium, which includes terms for resonance frequency, gas fraction, and acoustic damping for a single bubble size (see the Appendix for full expressions).

The resonance frequency (f_0) of a gas bubble depends on the bubble radius (r), thermal properties of the gas and the physical properties of the sediment, and the ambient hydrostatic pressure:

$$f_0 = \frac{1}{2\pi r} \sqrt{\frac{3\gamma P_0}{A\rho_s} + \frac{4G}{\rho_s}}. \quad (4.2)$$

Here A is the gas polytropic coefficient and ρ_s is the sediment bulk density.

The response curves in Fig. 4.1 show the acoustic behaviour of gassy sediments for the Bornholm Basin. The values of the input parameters were taken from core samples from the Bornholm Basin or from the literature (see section 4.6.4 and Table 4.2). For acoustic frequencies below resonance, the velocity

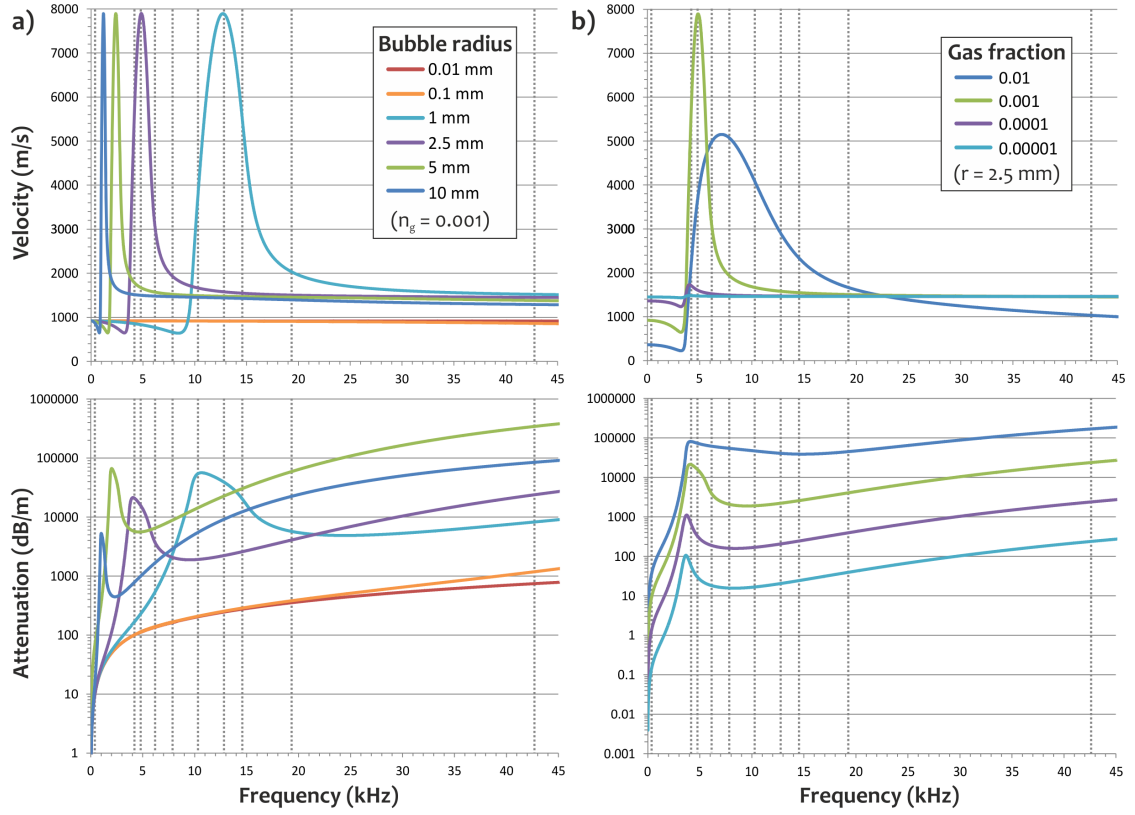


Figure 4.1: Acoustic response of gassy sediments as a function of frequency based on the model of Anderson & Hampton (1980). See Table 4.2 for input parameters. Changes in compressional wave velocity and the attenuation coefficient with a) different bubble sizes and constant gas content of $n_g = 0.001$ and b) for different gas contents and one bubble size $r = 2.5$ mm. Vertical lines indicate the 10 measurement frequencies used in this study.

is significantly reduced, the attenuation is higher than in gas-free sediments. Above resonance frequency, the bubbles scatter the sound and the acoustic response is essentially that of the surrounding medium, so the velocity remains constant at a value commensurate with the gas-free sediment, while the attenuation is higher than in gas-free sediment and increases with frequency.

At resonance, the gassy sediment is highly dispersive and the velocity can greatly exceed the gas-free velocity, but the model predicts velocities that are unrealistically high. Attenuation is highest at a frequency near the bubble resonance frequency. The resonance frequency of a gas bubble mainly changes with the radius of the bubble (Fig. 4.1.a). Since real gassy sediments most probably have a variety of bubble sizes, resonance effects will spread over a wider range of acoustic frequencies (see the measurements

of Best et al., 2004).

It should be noted that the attenuation coefficient calculated with this model is only related to bubble motion (in the model, damping due to bubble motion in sediments consists of radiation, thermal and internal friction terms) and does not include contribution from the gas-free sediment. However, attenuation due to scattering is generally considered to be insignificant in saturated marine sediments when the wavelength is much larger than the sediment grain size.

4.3 Geological setting in the Bornholm Basin

The study area is located in the Bornholm Basin, a 90 m deep sedimentary basin in the southwestern part of the Baltic Sea (Fig. 4.2). The basin is a major structural depression that subsided during the deposition of Upper Cretaceous sediments. Overlying the Mesozoic bedrock, the Quaternary basin fill is composed of a unit of glacial till and on top a succession of late and postglacial lacustrine and marine sediments (Björk, 1995; Sviridov et al., 1995). Since the last deglaciation of the Baltic Sea basin, isostatic uplift and eustatic sea-level changes resulted in several distinct phases in the sedimentation. Deposition of the uppermost organic-rich marine mud has started after the Littorina transgression, 9.8 kyr BP (Andrén et al., 2011). Sedimentation rate and morphology of this Holocene mud layer have been influenced by the postglacial development of the Bornholm Basin and bottom inflow currents. In the Holocene mud layer, where the thickness of the mud exceeds 5-10 m, generation and migration of shallow methane gas can be observed (Kögler and Larsen, 1979; Borowski et al., 2005). The free gas front was mapped based on acoustic data collected with a variety of high frequency (0.6-18 kHz) instruments (Borowski et al., 2005; Laier & Jensen, 2007), and was found to be 2-4 m below seafloor (Fig. 4.2)

4.4 Surveys and data

One part of the seismo-acoustic data were acquired on the R/V Maria S. Merian cruise MSM 16/1 in August 2010 using high resolution multichannel seismics (MCS) and the ship's Parasound (PS) sediment echosounder. The MCS system covered a relatively low frequency range from 100-800 Hz and the PS provided data at three higher frequencies (4.3, 19.2 and 42.8 kHz). Both systems were used simultaneously¹ along the line GeoB10-027 in order to ensure accurate positioning. Since the low frequency GI gun shots caused noticeable noise on the 4.3 kHz Parasound data (noisy traces on Fig. 4.3.c), a section of the profile with the transition from non-gassy to gassy sediment was rerun using only the PS echosounder.

¹At the same time a 95 kHz and a 12 kHz multibeam echosounder (MBES) were running as well, the results of those measurements have been published by Schneider von Deimling et al. (2013). Given the enhanced penetration of the 12 kHz signal into the soft muddy sediment, the stronger backscatter inside the shallow gas area could be clearly attributed to the shallow gas front depth down to 5 m below seafloor, while no elevated backscatter was visible in 95 kHz MBES data.

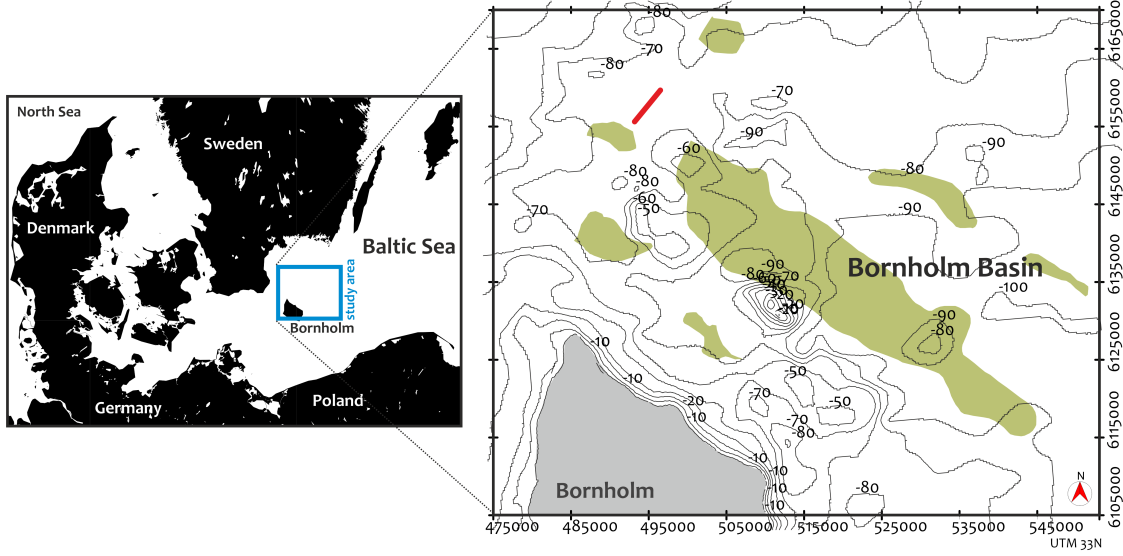


Figure 4.2: Location of the study area north of Bornholm in the Baltic Sea. The seismo-acoustic profile used in this study is located in the western part of Bornholm Basin at the edge of a small shallow gas patch. Green color denotes the areas with shallow gas after Laier & Jensen (2007).

Later in October 2012, the survey area was revisited during R/V Alkor cruise AL402. This time, data were collected along the exact same transect using the same MCS system (same frequency range), but in combination with a SES-2000 parametric sub-bottom profiler. The SES provided acoustic data at six additional frequencies, roughly at 4.1, 6, 7.9, 10, 12.8, and 14.6 kHz (along the lines GeoB12-112 and 113).

4.4.1 Seismo-acoustic dataset

Parasound sediment echosounder

One part of the high-resolution sediment echosounder data was collected using the parametric narrow beam sub-bottom profiler Parasound DS3 (Atlas Hydrographic). The transducers of PS are mounted to the ship's hull (R/V Maria S. Merian) and simultaneously emit pulses at two primary high frequencies, around 18 kHz (PHF) and adjustable 18.5–28 kHz, thus generating parametric secondary frequencies in the range of 0.5–10 kHz (SLF) and 36.5–48 kHz (SHF) respectively. The secondary frequencies develop through nonlinear acoustic interaction of the primary waves at finite signal amplitudes. This takes place in the emission cone of the primary signals, which is limited to an aperture angle of only 4° for the PS DS3. The transducer array of 128 transducers is located on a rectangular plate of approximately 1 m^2

in size, thus the footprint size is only $\sim 7\%$ of the water depth. The area of the reflecting surface is therefore considerably reduced with respect to conventional echosounders (e.g. 3.5 kHz), and the vertical and lateral resolution of PS is significantly improved.

During the cruise MSM16/1, the first primary frequency of Parasound was set to 19.231 kHz, which resulted in the generation of secondary frequencies at 4.273 kHz (SLF) and 42.735 kHz (SHF). The pulse length was set to 0.25 ms, the sample rate to 12.2, 6.1 and 6.1 kHz for the SLF, PHF and SHF, respectively. For the SLF and SHF frequencies no gain was applied while recording, for the PHF gain was set to -35 dB (not time variable). The echosounder profiles were recorded at ship speeds of 2 to 5.5 knots when surveying. All raw data were stored in the ASD (Atlas Hydrographic) data format, which contains the full water column of each signal as well as the full set of system parameters. Additionally, all the data were stored in compressed PS3 data format and standard SEG-Y.

SES-2000 parametric sub-bottom profiler

The other part of the high frequency data was recorded with a SES-2000 (medium type) parametric sub-bottom profiler (Innomar Technologie), which is also mounted to the ship's hull (R/V Alkor) and works based on the same principle as the PS described in the previous section. The system operates with primary frequencies of 94 and 110 kHz and generates low secondary frequencies between 4 and 15 kHz, three at a time: in one setting 4.095, 7.876 and 14.628 kHz, and in another setting 6.023, 10.239 and 12.799 kHz. Sample rate was 50 kHz (10 μ s) and constant gain (19 dB) was applied during recording. These data were stored in the instrument raw data format and later converted to SEG-Y.

Multichannel seismics

The seismic data were recorded with the GeoB high resolution shallow water MCS system, which includes a micro GI gun (Sodera) with reduced chamber volumes of 0.1 l, and a 50 m long analogue streamer with 48 single hydrophones and 1 m channel spacing. Shot rate was 1.5 s. The central frequency of the source is around 200 Hz, but the overall frequency range covers approx. 100 to 600 Hz. The MCS data were recorded with the acquisition software MaMuCS, with a sampling rate of 100 μ s, and recording length of 1.3 s. The MCS dataset was processed using the software package VISTA 2D/3D Seismic Data Processing (GEDCO). Seismic data processing followed a standard flow including common midpoint binning, bandpass filtering (using a wide range), normal move-out correction, stacking, noise attenuation (despike), correction of residual statics and FD time migration. The CMP binsize was set to 1 m to yield high horizontal resolution.

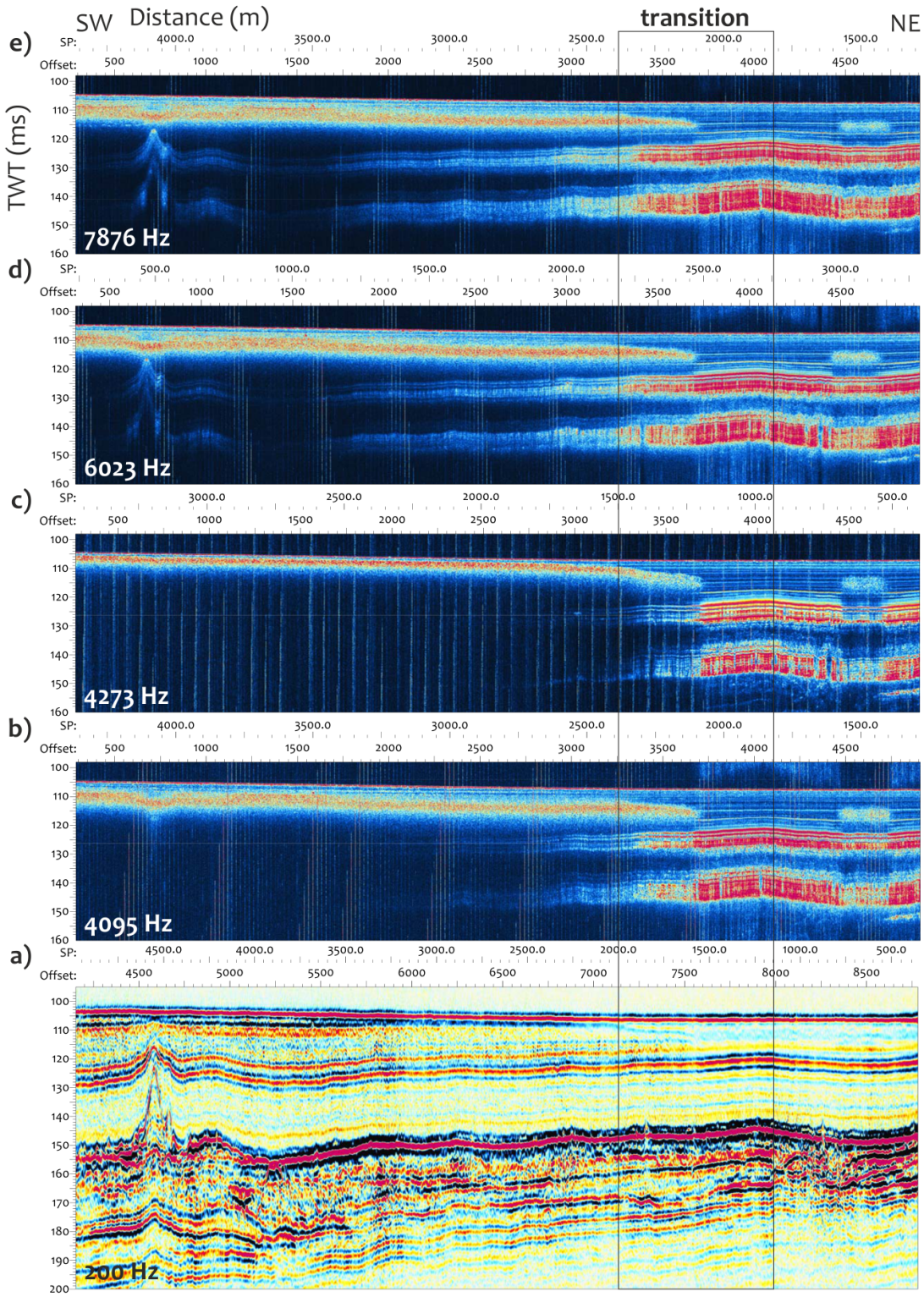


Figure 4.3: a) Multichannel seismic and b)-j) Parasound and SES echosounder data (envelope display) along the same transect in the Bornholm Basin, Baltic Sea. The frequency values indicate the central frequency of the seismic source and the frequency settings of the sediment echosounders. Shallow gas bubbles in the sediment cause different attenuation in different seismo-acoustic frequencies.

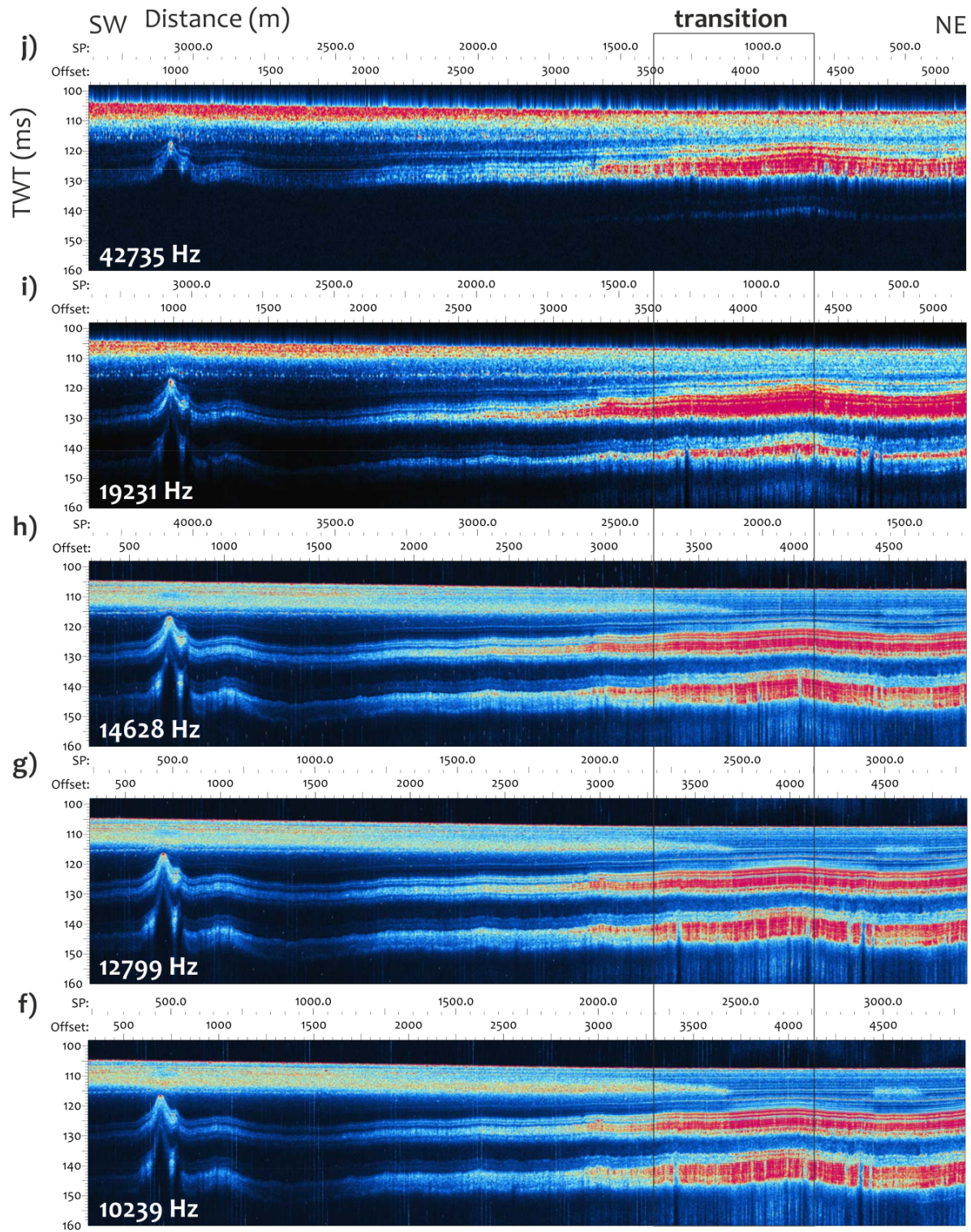


Figure 4.3: (cont.)

4.5 Amplitude analysis

To study the effect of free gas bubbles on seismo-acoustic signal attenuation, we performed an analysis of recorded amplitudes at the transition from non-gassy to gassy sediment (Fig. 4.3). The amplitude of the emitted acoustic signal is unknown, because in case of parametric echosounders, the main signals are generated in the water column near the transducer. Therefore, we estimate the attenuation by comparing the amplitudes of reflectors within the gassy sediment to amplitudes of the same horizons in the non-gassy sediment. The lateral changes in lithology are negligible over this distance (840 m) and we assume that the minor depth variation of the reflectors does not influence the attenuation.

For the analysis, first, the echosounder data were binned with a 1.5 m (inline) bin size in order to cope with the slightly irregular trace distances that result from the ship's slightly variable speed. Then, average envelope traces were calculated along the transect by stacking 40 bins for the echosounder data and 60 bins in case of the already binned MCS data, respectively. This created mean amplitude curves for every 60 m section (Fig. 4.4), but still preserved the gradual lateral changes in the attenuation across the transition from non-gassy to gassy sediment (Fig. 4.3). Then, for the lowest PS and following six SES frequencies, the maximum of the envelope amplitudes was picked and extracted at the seafloor reflection and at 10 sub-bottom reflections, which could be traced above or below the gas front (Fig. 4.4). For the two high frequencies of the PS, the amplitudes of the deeper five horizons (horizons 6-10) could be determined, while the upper five reflections are not visible in these data. In the MCS data, the amplitude of the seafloor and one horizon (horizon 7) was picked, which corresponds to the boundary from the transitional clays to *Ancylus/Yoldia* clays, the first prominent reflector at the base of the Holocene mud (Figs 4.3.a and 4.4).

The amplitude loss (that we take as α , attenuation coefficient) was found using the equation

$$\alpha [dB/m] = \frac{10}{2d} \log_{10} \left(\frac{A_h}{A_{sf}} \right)^2, \quad (4.3)$$

where A_h and A_{sf} are the amplitudes of the horizons in the subsurface and the seafloor, and d is the depth of the horizon below the seafloor. Horizontal change in the seafloor reflection amplitude is very small ($\pm 10\%$, 1s), thus the amplitude of the seafloor can be considered as a good reference level along the transect. We chose to analyse Horizon 7 in detail, which was traceable with all 10 frequencies, but the same basic trend of amplitude change was found for the other horizons beneath the gassy sediment layer (horizons 6-10).

The amplitude of Horizon 7 is always higher in the non-gassy sediment than the seafloor amplitude (Fig. 4.4). This can be attributed to the difference between the reflection coefficients at these interfaces. To correct for this, we estimated the reflection coefficient (R) at the seafloor and Horizon 7 from the sediment

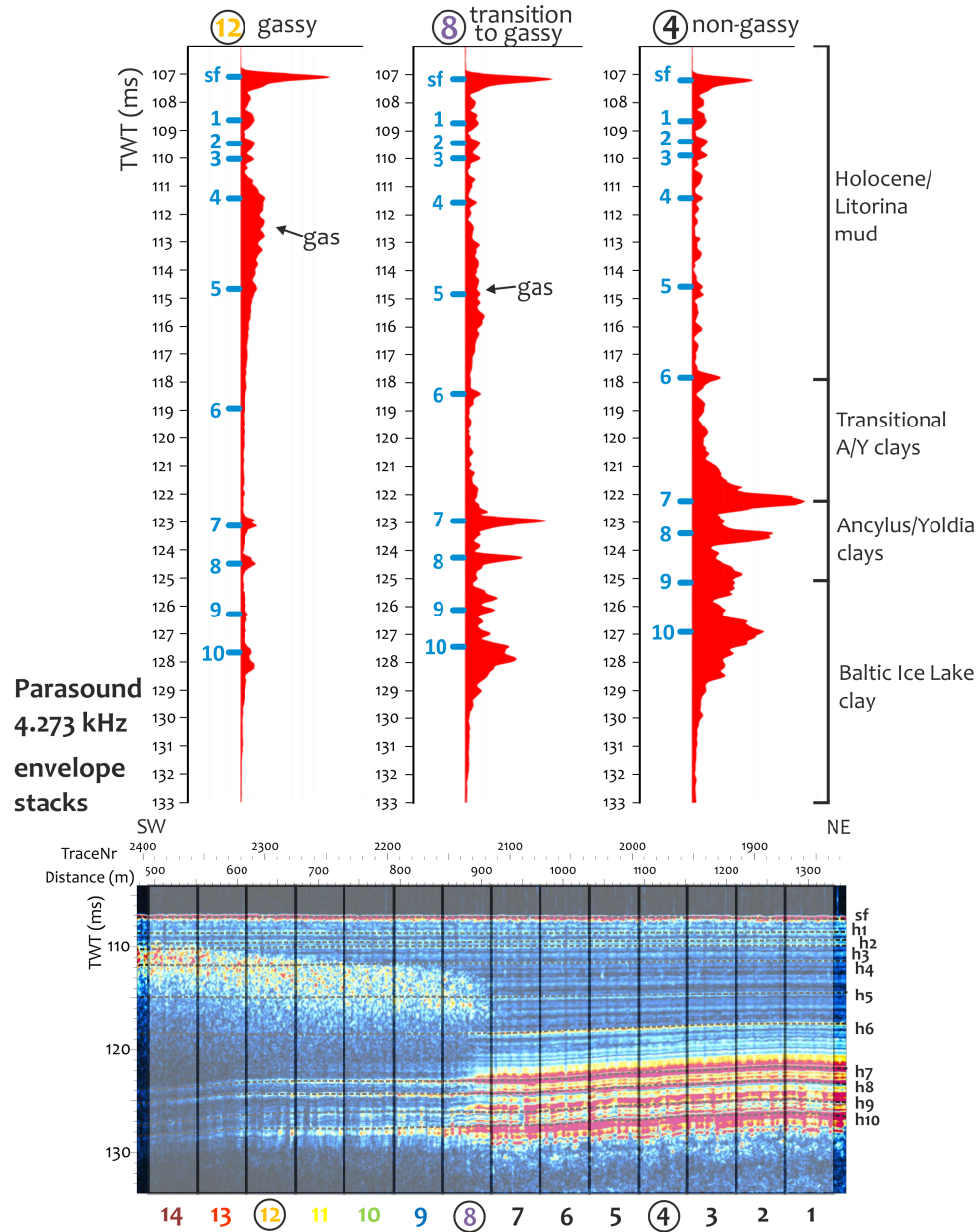


Figure 4.4: At the transition from non-gassy to gassy sediment 14 times, by binning traces every 60 m envelope stacks were created from the seismograms along the transect. The maximum amplitude of the seafloor and denoted horizons were extracted.

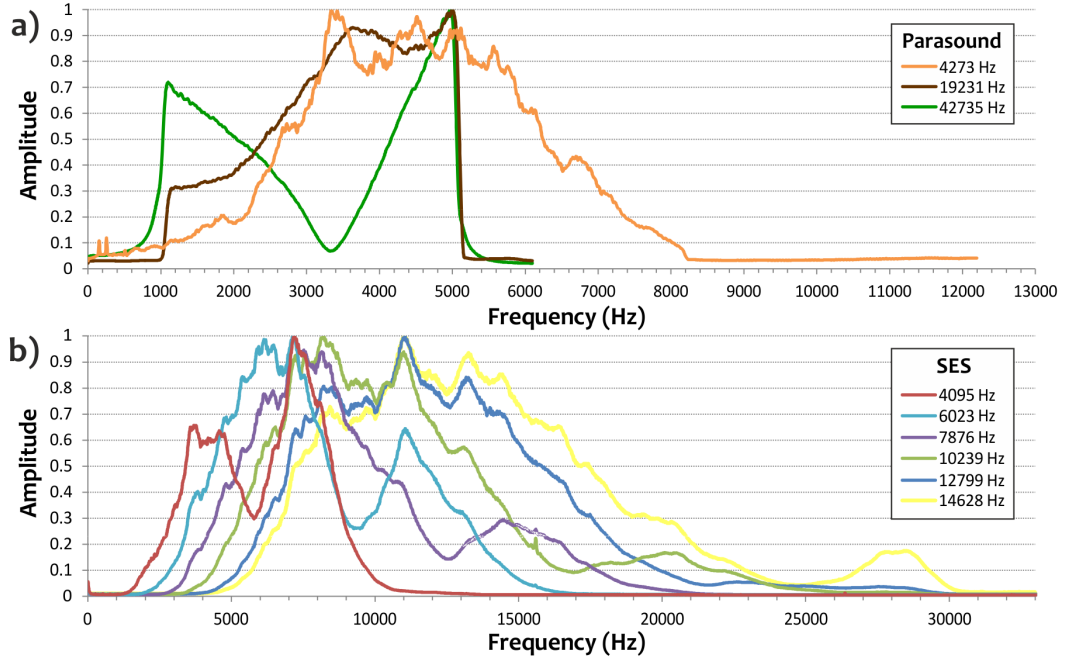


Figure 4.5: Frequency spectra of the a) Parasound and b) SES echosounder data.

wet bulk density (ρ_s) change which was measured on sediment cores. For a seismic wave reflecting off an interface between two media at normal incidence, the expression for the reflection coefficient is:

$$R = \frac{Z_1 - Z_0}{Z_1 + Z_0} = \frac{\rho_{s1}v_1 - \rho_{s0}v_0}{\rho_{s1}v_1 + \rho_{s0}v_0} \approx \frac{\rho_{s1} - \rho_{s0}}{\rho_{s1} + \rho_{s0}}, \quad (4.4)$$

where Z_0 and Z_1 are the acoustic impedances of the first and second medium, respectively. The cores were gravity core 374200-6GC (Jørgensen et al., 2011a), for which physical property logs reach down to Horizon 7 (Lat: 55.249550 Long: 15.435780; the core is located in the Bornholm Basin, but not exactly in the study area), and other short cores taken along the transect by Schneider von Deimling et al. (2013). The reflection coefficient was calculated assuming an almost constant velocity change across these interfaces, which is typical for shallow marine (muddy) sediments (Hamilton, 1970; Breitzke, 2000). R was found to be 2.5 times higher at Horizon 7 than at the seafloor ($R_{sf} \sim 0.013$, $R_{h7} \sim 0.033$), thus the amplitude loss values from Eq.(4.3) were corrected according to this ratio.

The echosounder data reveal a wide bandwidth between 6 and 10 kHz. The frequency spectrum of each echosounder frequency is shown on Fig. 4.5. To overcome the differences in the spectral energy distribution in the echosounder data and to better resolve resonance peak(s), we obtained the amplitude of the reflections in narrower frequency bands. The PS 4.237 kHz and the SES 4.095 kHz data, where the

amplitude loss visibly is the highest (Fig. 4.3.b and c), were filtered using a series of bandpass filters. The bandwidth of these filters was set to 1 kHz and their center frequency ranged from 1 to 10 kHz. Part of the transect with the 1 kHz wide filters applied to the PS data is displayed in Fig. 4.6. We also analysed the MCS data using a series of bandpass filters with a 200 Hz bandwidth in the range of 50 to 1050 Hz to check whether there is a change in amplitude loss towards these lower frequencies.

In the end, the average amplitude loss measured in the gas-free sediment (at locations 1-7) was subtracted from the amplitude losses measured at Horizon 7 in the gassy sediment (locations 8-14), which gave the amplitude loss caused by gas bubbles.

The frequency spectra of the 19.231 and 42.735 kHz PS data show an uneven spectral energy distribution (Fig. 4.5.a) between 1 and 5 kHz. It seems that the 'downmixing' of these high frequency signals, which during recording preserved the spectral bandwidth but shifted the spectrum to lower frequencies, was not properly reconstructing the original energy spectrum in the replay software (the manufacturer Atlas Hydrographic was notified, but could not resolve the problem). However, since original seismogram envelopes could be restored, we can assume that the relative amplitude losses measured across the transition are not affected.

4.6 Results

4.6.1 Multichannel seismic and echosounder data

Seismo-acoustic profiles for all 10 available frequencies is shown in Fig. 4.3. On the low frequency MCS data, shallow gas causes acoustic turbidity in the Holocene mud layer and the gas front towards the center of the gassy area is observed through its interference with the seafloor reflection. Above the peak in the bedrock, the gas front appears as a separate reflection close to the seafloor. On the higher frequency echosounder data, shallow gas causes acoustic blanking, where the gas front is visible on top of the blank zone as a cloud of point scatterers. The gas front appears shallower in the PS echosounder data than the SES data, but the transition from gassy to non-gassy sediment is exactly at the same position two years later. The attenuation caused by the gas bubbles reveals a gradual increase across the transition, as the reflection amplitudes of the underlying sediments (high acoustic impedance contrasts from the *Ancylus/Yoldia*, Baltic Ice Lake clay and the bedrock boundaries) gradually decrease.

The highest amplitude loss is observed on the PS 4.273 kHz data, where the reflections below the gas front disappear most sharply at the edge of the gassy area. On the SES 4.095 kHz the attenuation is slightly lower, and decreases towards the higher frequencies. The two highest PS frequencies do not show the gas front anymore, although the seafloor amplitude is increased. The presence of gas can be inferred from the gradually decreasing reflection amplitudes beneath the gassy sediment layer.

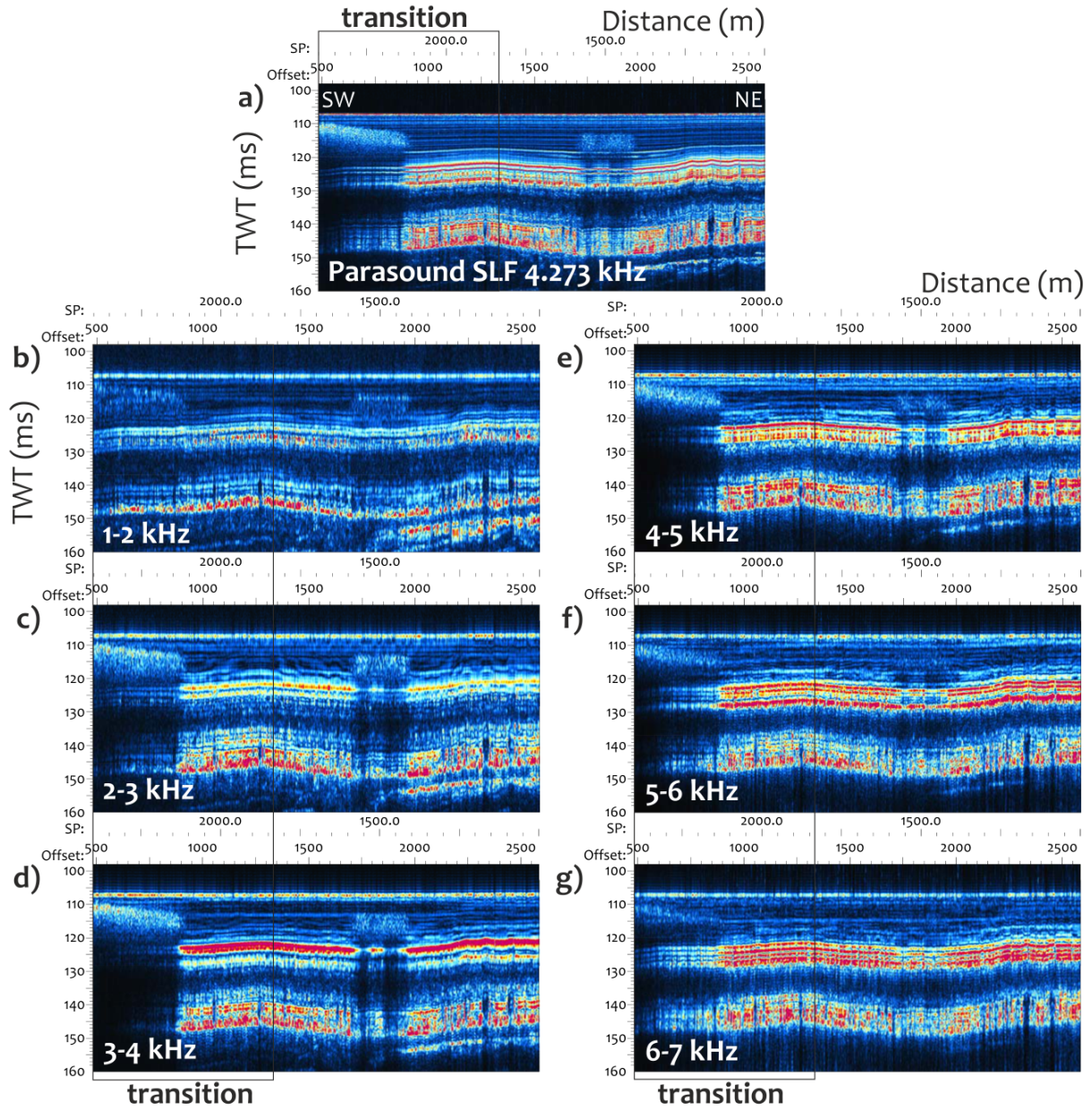


Figure 4.6: a) Part of the transect in the PS SLF echosounder data (envelope display). b)-g) After frequency filtering in the different 1 kHz wide frequency bands.

The amplitude loss caused by gas bubbles measured on Horizon 7 is shown on Fig. 4.7. As it was visible already on the profiles, the amplitude loss due to free gas increases towards the Southwest, the center of the gassy area, or from location 8 (the transition) to 14 (gassy sediment) (Fig. 4.4). The maximum amplitude loss was measured in the 4.273 kHz data at Horizon 7 and it is increasing from the edge of the gassy area towards the center of the gas patch (from location 8 to 14).

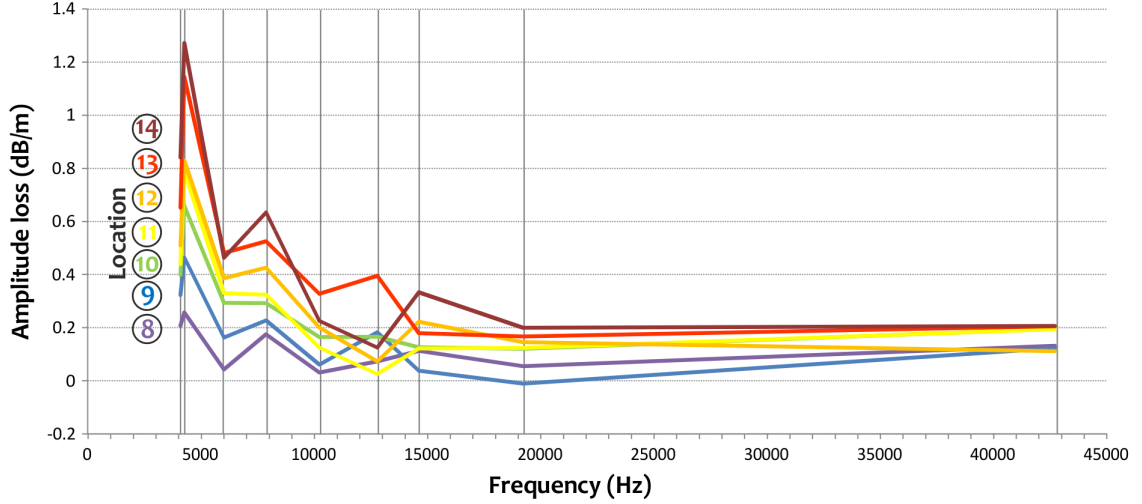


Figure 4.7: Results of the amplitude analysis on the echosounder data. The amplitude loss measured at Horizon 7 in the gassy sediment along the transect (from location 8 to 14 - see Fig. 4.4) as a function of the echosounder measurement frequency.

4.6.2 Multiple filter analysis

The PS 4.273 kHz data after frequency filtering in Fig. 4.6 shows quite a variable picture of the gassy sediment in the different 1 kHz wide frequency bands. Below 2 kHz and above 5 kHz, the gas front is hardly visible in the vicinity of the transition zone, but the underlying reflections appear quite strong. The gas front is imaged with higher amplitudes between 2 and 5 kHz, and in connection with this, the sub-bottom reflectors beneath are strongly attenuated. The highest amplitude loss is observed between 3 and 4 kHz. The multiple frequency band of the SES 4.095 kHz signal essentially shows the same trend (profiles not shown).

The measured amplitude loss (Fig. 4.8.b) is highest on both echosounder data between 3 and 4 kHz at locations 8 through 12 and at locations 13 and 14 between 3 and 5 kHz. The resonance peak of the gas bubbles therefore can be estimated to be within this frequency range, with a small shift towards higher frequencies at the gassy end of the transect. At Horizon 7, the amplitude loss caused by gas bubbles

increases towards the center of the gassy area, from 0.5 to 1.65 dB/m (Table 4.1). Interestingly, there is a separation between the measured PS and SES attenuation curves towards the gassy end of the transect (Fig. 4.8.b). At location 8 no difference in attenuation is observed between the two echosounder data, but towards location 14 the PS signal undergoes higher attenuation than the SES signal, and this difference is most pronounced around the resonance peak.

The amplitude loss measured on the filtered MCS data does not show a clear trend as a function of frequency (Fig. 4.8.a). At these low frequencies, the amplitude loss is generally very small, which indicates that the frequencies below 1 kHz must be far below the resonance frequency range.

4.6.3 Attenuation in the gassy sediment

In the frequency filtered echosounder data, the amplitude loss values were measured at Horizon 7 in dB/m, over the distance of 12 m. However, the acoustic waves go through the gas-charged sediment layer twice, downward and upward, and along this travel path, the attenuation occurs primarily in the gassy sediment layer, while the contribution from the gas-free sediment to the total attenuation is negligible. These dB/m values therefore need to be corrected for the thickness of the gassy layer, which needs to be estimated from the seismic and acoustic profiles. The upper boundary, the gas front, is easily identified in the lowest frequency echosounder data. The lower boundary, however, is more difficult to determine, but we will try to provide an estimate of the thickness based on the available acoustic data. In Fig. 4.4 as an example, the vertical function of scatter energy at location 12 indicates that highest concentration of point scatterers reveal a peak directly beneath the gas front (at 111.5 ms TWT). Further down, scatter strength attributed to gas bubbles gradually decreases down to 119 ms TWT, where background values of the non-gassy sediment are reached. This represents a depth range of 5.6 m of gas-related scattering. However, due to the size of the Parasound emission beam of 4° opening angle, even an infinitely thin gas layer will provide scattering over a vertical range of 3.2 meters. Subtracting this effect, the net thickness of the gas layer at location 12 may be estimated to be in the range of 2-3 meters, with a maximum concentration and highest attenuation near the top. We can further assume that gas bubbles are not likely to exist beneath the Holocene mud, as methane content is minimal in glacial clays. We therefore use an effective gas layer thickness of ~ 2 meters for attenuation values within the gassy layer, and corrected values are given in Table 4.1. It should be noted that location 12 is not in the vicinity of maximum signal attenuation, and values may be even higher throughout the area.

4.6.4 Model-predicted bubble sizes and gas content

A few of the model parameters were measured, but most of them were taken from the literature. All of the physical property values used in the calculation are listed in Table 4.2. The main unknowns in the

Table 4.1: Observed resonance peaks and the attenuation measured at Horizon 7 in the filtered Parasound and SES echosounder data. Based on these, predictions of the Anderson & Hampton model for bubble radius and gas contents along the transition at the edge of the gassy area. For the locations along the profile see Fig. 4.4.

Observations				Model predictions		
Echosounder/ Location	Resonance frequency (kHz)	Attenuation coefficient in 2*12 m (dB/m)	in 2 m (dB/m)	Bubble sizes (mm)	Gas volume fraction (%)	
PS	8	between 3-4	0.4	5.35	2.28-3.04	$5.4 \cdot 10^{-5}$
	9	between 3-4	1.03	12.4	2.28-3.04	$1.3 \cdot 10^{-4}$
	10	between 3-4	1.2	14.6	2.28-3.04	$1.5 \cdot 10^{-4}$
	11	between 3-4	1.3	15.6	2.28-3.04	$1.6 \cdot 10^{-4}$
	12	between 3-4	1.4	16.7	2.28-3.04	$1.7 \cdot 10^{-4}$
	13	between 4-5	1.5	18	1.82-2.28	$1.8 \cdot 10^{-4}$
	14	between 3-4	1.6	19.7	2.28-3.04	$2 \cdot 10^{-4}$
SES	8	between 3-4	0.5	6	2.28-3.04	$6.1 \cdot 10^{-5}$
	9	between 3-4	0.9	10.8	2.28-3.04	$1.1 \cdot 10^{-4}$
	10	between 3-4	0.95	11.4	2.28-3.04	$1.2 \cdot 10^{-4}$
	11	between 3-4	0.94	11.3	2.28-3.04	$1.2 \cdot 10^{-4}$
	12	between 3-4	1.03	12.4	2.28-3.04	$1.3 \cdot 10^{-4}$
	13	between 3-4	1.06	12.7	2.28-3.04	$1.3 \cdot 10^{-4}$
	14	between 3-4	1.1	13.7	2.28-3.04	$1.4 \cdot 10^{-4}$

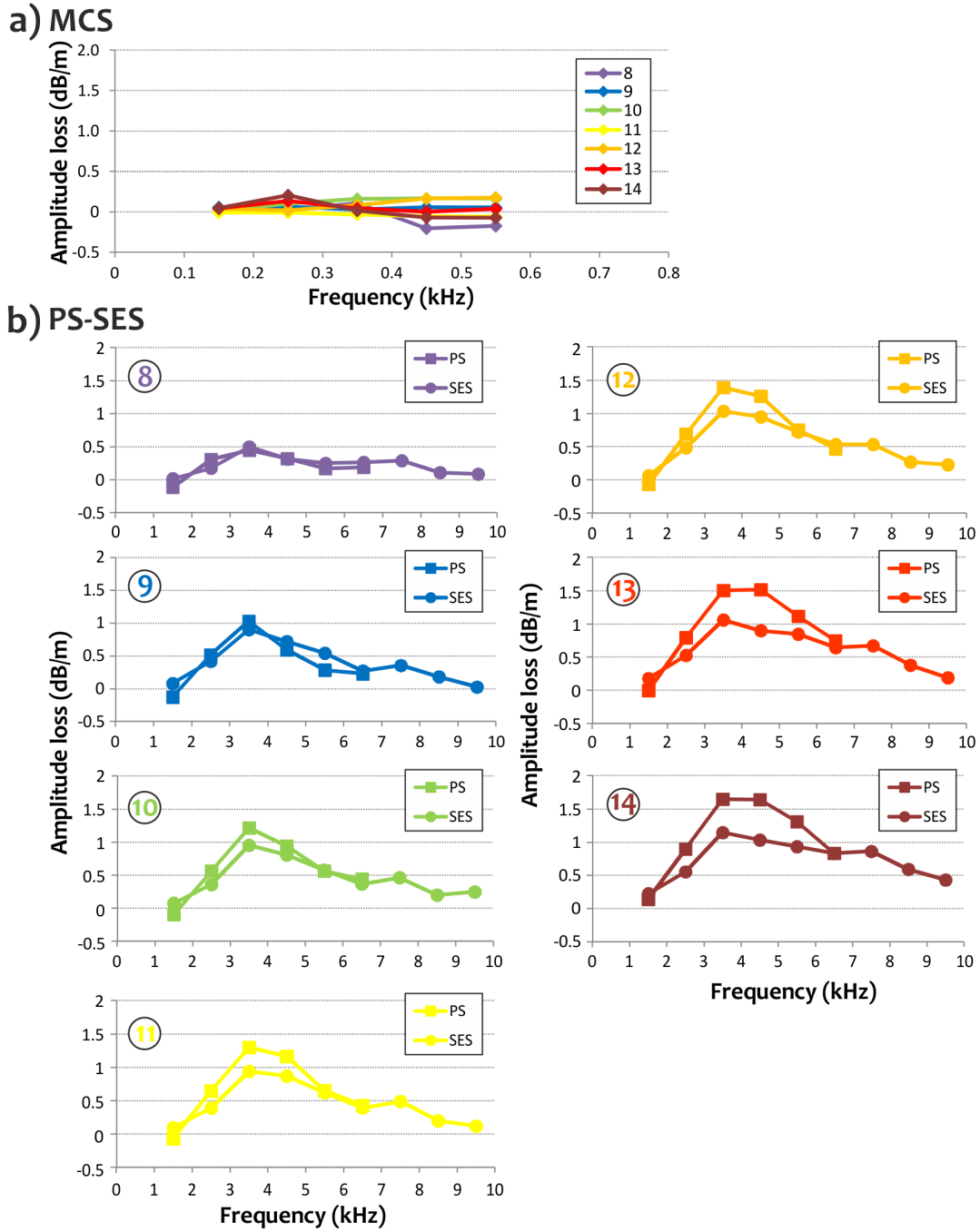


Figure 4.8: Attenuation curves from the filtered a) multichannel seismic (MCS) data and b) filtered Parasound (PS) 4.273 kHz and SES 4.095 kHz data, based on the amplitude losses measured at Horizon 7.

model are the bubble size (radius, r) or more precisely its distribution, which determines the resonance frequency range, and the gas volume fraction (n_g) in the sediment, which essentially determines the magnitude of the attenuation (Fig. 4.1).

The resonance frequency was determined with 1 kHz resolution and the attenuation curves show one distinct peak. The sediment most likely contains bubbles with different sizes, so this one peak can be interpreted as a composite resonance peak or the peak of the bubble size distribution. The Anderson & Hampton model suggests for the resonant peak between 3-4 kHz an equivalent bubble radius range of 2.28-3.04 mm (Eq. (4.2)). This is the radius of a sphere of equivalent volume, as the model assumes a spherical bubble shape. There is one location where the highest attenuation in the PS data is found between 4-5 kHz, for this resonance peak, the model would predict an equivalent bubble radius range of 1.82-2.28 mm (Table 4.1).

Within a 2 m thick gassy sediment layer, gas contents suggested by the model lie between $6.1 \cdot 10^{-5}\%$ and $2 \cdot 10^{-4}\%$ (Table 4.1).

4.7 Discussion

Based on the amplitude loss measurements, resonance effects are indicated in the frequency range between 3 and ~ 15 kHz. The resonance peak between 3 and 5 kHz suggests 2-3 mm gas bubble radius, which represent the larger bubbles, as smaller bubbles contribute to a lesser degree to the scattering strength (Anderson et al., 1998). The resonance peak is wider at the gassy end of the transect (location 13-14), which suggests that the peak of the bubble size distribution is also wider (Fig. 4.8, Table 4.1). In the model, bubble shape is assumed to be spherical, but CT scans of pressurized cores and laboratory experiments revealed that gas bubbles in muddy sediments are 'disk shaped' oblate spheroids (Abegg & Anderson, 1997; Anderson et al., 1998; Boudreau et al., 2005). Deviation of the bubble shape from spherical decreases the bubble resonance frequency because a non-spherical bubble responds dynamically as if it were larger (Anderson et al., 1998). Consequently, if bubbles are indeed non-spherical, the largest gas bubbles sizes in Bornholm Basin sediments may be smaller in equivalent diameter than the determined 4-6 mm.

In the 19.231 and 42.735 kHz PS profiles, the gas bubbles are not observed as a cloud of point scatterers as clearly as in lower frequencies, and acoustic waves are transmitted through the gassy layer. This could indicate that at these high frequencies resonance effects are not significant anymore, so the transition to 'above resonance' begins at ~ 19 kHz. This suggests that the smallest effective bubble radius in Bornholm Basin gassy sediments is 0.48 mm, which is comparable with the findings of Wilkens & Richardson (1998), whose acoustic measurements in the gassy sediments of the Eckernförde Bay indicated the transition to

Table 4.2: Values of parameters used to calculate bubble size and gas content in the gassy sediments of the Bornholm Basin.

Water depth in TWT	107 <i>ms</i>
Water depth (using 1500 m/s)	80.25 <i>m</i>
Depth of horizon 7 in the sediment in TWT	123 <i>ms</i>
Depth of horizon 7 below seafloor (using 1500 m/s) (<i>d</i>)	12 <i>m</i>
Hydrostatic pressure at 1 atm (<i>P</i>)	$1.01325 \cdot 10^5$ <i>Pa</i>
Seawater density (ρ_w)	$1.013 \cdot 10^3$ <i>kg/m³</i> ^c
Pore water bulk modulus (K_w)	$2.14 \cdot 10^9$ <i>Pa</i>
Mineral particle bulk modulus (K_m)	$3.6 \cdot 10^{10}$ <i>Pa</i> ^c
Sediment frame bulk modulus (K_f)	$1.4 \cdot 10^7$ <i>Pa</i>
Shear modulus of the sediment (<i>G</i>)	$2.81 \cdot 10^5$ <i>Pa</i> ^c
Imaginary part of the shear modulus of the sediment (<i>G'</i>)	$1.23 \cdot 10^5$ <i>Pa</i>
Sediment bulk density (ρ_s)	$1.3 \cdot 10^3$ <i>kg/m³</i> ^{a,b}
Fractional porosity (<i>n</i>)	0.8 ^{a,b}
Ratio of specific heats of gas (methane) (γ)	1.31
Specific heat of gas (methane) at constant pressure (<i>s_p</i>)	2.19 <i>kJ/kg°C</i>
Thermal conductivity of gas (methane) (<i>C_g</i>)	0.0311 <i>J/sm°C</i>
Density of gas (methane) (ρ_g)	$0.717 \cdot 10^3$ <i>kg/m³</i>
Sound velocity in saturated sediment (<i>c₀</i>)	1460 <i>m/s</i> ^e

^a core 374280-2RL / PO392; Jørgensen et al. (2011b)

^b cores 31, 32, 101-103 / MSM16/1; Schneider von Deimling et al. (2013)

^c measured in Eckernförde Bay by Wilkens & Richardson (1998)

^d from Part II, Table III of Anderson & Hampton (1980)

^e average from Chapter 3 and Schneider von Deimling et al. (2013)

'above resonance' between 21 and 25 kHz with corresponding bubble radii of 0.3-0.4 mm.

The frequency range indicating 'below resonance' is below 1 kHz, as here the attenuation based on the filtered MCS data is very small and not dependent on frequency (Fig. 4.8).

The increasing attenuation at resonance towards the gassy end of the transect indicates increasing gas volume fractions in the sediment (Fig. 4.8, Table 4.1). Partial acoustic blanking with traceable reflections beneath the gassy sediment layer therefore suggests lower gas concentration at the edge of the gassy area, as not all of the downward propagating acoustic waves are scattered by the gas bubbles, whereas high scattering and complete acoustic blanking occurs for higher gas concentrations. In association with this, the depth of the gas front decreases towards the gassy end of the transect (Fig. 4.3). Decreasing free gas depth along this distance could indicate increasing methane flux (Dale et al., 2009). Increased methane production may be directly linked to an increased thickness of the organic-rich Holocene mud (Flury et al., in prep).

Differences between the amplitude losses measured in the filtered PS and SES data (Fig. 4.8) are not clear, although it may indicate a temporary difference in free gas concentrations (Table 4.1). The two echosounder data were recorded two years apart, the PS data in August, the SES data in October, and there is a visible difference in the depth of the gas front between the two data sets, revealing an increase between 0.7 and 1.3 m (Fig. 4.3.a) towards the gassy area. A possible explanation could be that variation of environmental conditions such as sediment temperature and pressure can influence the amount of free methane gas in the sediment through methane solubility. A shallower gas front indicates more methane in gas phase, which in turn may e.g. derive from a decreased methane solubility as a response to higher sediment temperatures or lower ambient pressure. A depth variation of the gas front reacting to the annual temperature cycle of the atmosphere was shown in the ~ 25 m deep Eckernförde Bay sediments (Wever & Fiedler, 1995; Wever et al., 1998). The depth change occurred with a 3-4 months lag due to slow temperature changes by mixing of the water column and conductive temperature migration in the sediment, and in the Eckernförde Bay the lowest solubility is reached in the warm fall/winter months resulting in a shallow gas front, while high solubility in the cold spring/early summer months leads to a deeper gas front. Although temperature variations can in principle explain the different gas front depths, the situation is the opposite in the Bornholm Basin derived from the echosounder profiles. Maybe the annual variation in sediment temperature is smaller because of the deeper water or the longer lag. Also, stratification of the complete water-column could reduce and phase-shift the effect of the surface temperature cycle at depth. Tidal cycle or sudden fluctuations of the pressure can also cause variations in the gas front depth, even ebullition of gas (Best et al., 2004; Gülsow et al., 2013). However, the water depth was almost the same during the two surveys, and the resulting small difference in pressure would not account for the observed change in the gas front depth alone.

Our measured attenuation values are low compared to the attenuation measured in shallow gas-bearing sediments by other studies. However, considering that a 2 m thick gassy layer at the resonance frequency of gas bubbles allows acoustic transmission and reflectors are visible beneath, the attenuation at the edge of the gassy area is probably not very high. The maximum attenuation measured in situ by Wilkens & Richardson (1998) at 38 kHz was 40-50 dB/m in gassy Eckernförde Bay sediments, while Best et al. (2004) measured 180-220 dB/m at 700-2800 Hz in Dibdan Bay, Southampton. Lower attenuation values could certainly result from inaccuracies in the amplitude analysis and from the corrections applied to the amplitude loss values. Although not highly variable, the seafloor reflection amplitude, as a reference level for measuring the amplitude losses beneath, could cause deviation from real dB/m values. Moreover, the correction for the reflection coefficient difference reduces considerably the dB/m values, therefore an overestimation of this difference could result in lower amplitude losses.

It has been noted before that the model of Anderson & Hampton considerably over estimates attenuation measured at resonance (Wilkens & Richardson, 1998; Robb et al., 2006). As a consequence, the model might suggest a lower gas contents causing the measured attenuation. In addition, if the gassy sediment layer, where we assumed that most of the gas bubbles are concentrated, is thinner than 2 m in reality, then the dB/m values and the predicted gas content would both increase. The gas content determined along the transect can therefore be considered as lower estimates.

4.8 Conclusions

We analysed seismic and acoustic data recorded in 10 frequency bands between 0.2 and 43 kHz over shallow free gas in the muddy sediments of the Bornholm Basin, Baltic Sea. From reflection amplitudes beneath the gas-charged sediment layer we measured the attenuation that gas bubbles cause in the otherwise low-reflective sediment. The multi-frequency seismo-acoustic data demonstrate that the imaging of shallow free gas is dependent on the measurement frequency, as in the resonance frequency range of gas bubbles, compressional wave attenuation considerably increases.

At the resonance frequency of the largest bubbles, high scattering causes complete acoustic blanking beneath the top of the gassy sediment layer. In the wider resonance frequency range, where the effect of smaller bubbles becomes dominant, the attenuation slightly decreases, which allows acoustic waves to be transmitted, and reflections can be observed beneath the gassy sediment layer for higher frequencies. When the acoustic wavelength exceeds the size of gas bubbles and 'above resonance' begins, attenuation is low, but higher than in the gas-free sediments and the presence of gas bubbles can be inferred from the decreased reflection amplitudes beneath the gassy layer. Below resonance, the attenuation is generally very low and not dependent on frequency.

At the edge of gassy areas, gradual amplitude loss is often observed together with the shoaling of the gas front. This increasing attenuation results from increasing gas concentrations and leads to complete acoustic blanking in the center of the gas patch where gas concentrations are probably highest.

Based on the resonance effects identified from seismo-acoustic data, the Anderson & Hampton model suggests gas bubble sizes between 1 and 4-6 mm and gas content up to 0.0002% at the edge of the gassy area. This small amount of gas already considerably attenuates the downward propagating acoustic waves. Estimated based on the seismo-acoustic data, most of the gas bubbles are concentrated in a 2 m thick sediment layer, whose upper boundary is the gas front.

With the multi-frequency acoustic approach and the model of Anderson & Hampton, quantification of free gas in shallow marine environments is possible if the resonance frequency peak can be identified. However, the method presented here, is limited to places with moderate attenuation, where the amplitudes of a reflection can be analysed beneath the gassy sediment layer.

Appendix - Geoacoustic model

Calculation of bubble resonance frequency, compressional wave speed and compressional wave attenuation in gas-bearing sediments after Anderson & Hampton (1980). (The modification of Eq.(4.16) by Best et al. (2004) was included.)

The resonance frequency (f_0) of a gas bubble in the sediment is given by

$$f_0 = \frac{1}{2\pi r} \sqrt{\frac{3\gamma P_0}{A\rho_s} + \frac{4G}{\rho_s}}, \quad (4.5)$$

where r is the bubble radius, γ is the ratio of specific heats of gas (here, methane), P_0 is the ambient hydrostatic pressure, ρ_s is the sediment bulk density, G is the sediment shear modulus (the real part of the complex sediment shear modulus). A is the gas polytropic coefficient, which is given by the following expression

$$A = (1 + B^2) \left[1 + \frac{3(\gamma - 1)}{X} \left(\frac{\sinh X - \sin X}{\cosh X - \cos X} \right) \right], \quad (4.6)$$

where

$$B = 3(\gamma - 1) \left(\frac{X(\sinh X - \sin X) - 2(\cosh X - \cos X)}{X^2(\cosh X - \cos X) + 3(\gamma - 1)(\sinh X - \sin X)} \right), \quad (4.7)$$

$$X = \frac{r\omega\rho_g s_p}{C_g}. \quad (4.8)$$

Here, ρ_g is the density of methane, s_p is the specific heat of methane at constant pressure, C_g is the thermal conductivity of methane, and ω is the angular frequency in radians ($\omega = 2\pi f$).

For compressional wave velocity at or above bubble resonance frequency, the following expression is used to calculate the sound speed ratio, where c and c_0 are the saturated and gassy sediment sound speed:

$$\left(\frac{c}{c_0}\right)^2 = \frac{1}{2}(1 + WX_1) \left\{ 1 \pm \left[1 + \left(\frac{WY_1}{1 + WX_1} \right)^2 \right]^{1/2} \right\}, \quad (4.9)$$

$$W = \frac{K}{\gamma P_0 + \frac{4}{3}G}, \quad (4.10)$$

where K is the saturated sediment composite bulk modulus, which is calculated based on Gassmann's expressions (Gassmann, 1951):

$$K = K_m \left(\frac{K_f + Q'}{K_m + Q'} \right) \quad (4.11)$$

$$Q' = K_w \left(\frac{K_m - K_f}{n(K_m - K_w)} \right) \quad (4.12)$$

Here K_m and K_f are the mineral and frame bulk moduli, n is the fractional porosity, and K_w is the bulk modulus of the pore water. X_1 and Y_1 are coefficients of a gassy medium, for which bubble-size distribution may be expressed as a histogram (Gardner, 2003),

$$X_1 = \frac{n_g(1 - f_*^2)}{(1 - f_*^2)^2 + d_*^2} \quad (4.13)$$

$$Y_1 = \frac{n_g d_*^2}{(1 - f_*^2)^2 + d_*^2} \quad (4.14)$$

where $f_* = f/f_0$, $d_* = df_*$. Here n_g is the gas fraction, f is the measurement frequency, f_0 is the resonance frequency from Eq.(4.9), and d is the damping constant ($d = 1/Q$, Q is the quality factor). Damping is a function of thermal (d_{th}), radiational (d_r) and frame/viscous damping (d_f):

$$d = d_{th} + d_r + d_f \quad (4.15)$$

where

$$d_{th} = B, d_r = kr, d_f = \frac{4G'}{\rho_s \omega^2 r^2} \quad (4.16)$$

Here, k is the acoustic wave number in the saturated sediment ($k = 2\pi/\lambda$, $\lambda = c_0/f$), G' is the imaginary

part of the complex shear modulus ($G^* = G + iG'$).

Attenuation in gas-bearing sediments is caused by frame frictional absorption, absorption due to bubble motion, and scattering from bubbles. Attenuation (α) due to bubble motion is

$$\alpha [Np/cm] = \frac{\pi f}{c_0} \frac{c}{c_0} \frac{KY_1}{\gamma P_0 + \frac{4}{3}G}. \quad (4.17)$$

Acknowledgments

This research received the funding from the European Community's Seventh Framework Programme (FP/2007 - 2013) under grant agreement nr. 217246 made with the joint Baltic Sea research and development program BONUS. We thank Seismic Micro-Technology (The Kingdom Suite) and GEDCO (VISTA 2D/3D Seismic Data Processing) for providing academic software licenses.

Chapter 5

Conclusions and outlook

The aim of this study was to investigate the frequency dependence in seismo-acoustic imaging of shallow free gas, and by utilizing a variety of multi-frequency seismo-acoustic instruments, to develop methods to characterize and estimate free gas content in Baltic Sea sediments. The work concentrated on a seismo-acoustic data set collected over the gassy area of the Bornholm Basin, in the south-western part of the Baltic Sea.

In the first paper, seismo-acoustic signatures of shallow gas were identified and mapped in high frequency Parasound echosounder data and lower frequency multichannel seismic data. The expressions of shallow gas are dependent on the measurement frequency as the relationship between wavelength and gas bubble size varies. Gas bubbles strongly scatter the acoustic energy of a high frequency signal, and the significantly higher attenuation due to gas bubble resonance further prevents transmission through gassy sediment layers. The resulting appearance of shallow gas in the high frequency Parasound data is a cloud of point scatterers and acoustic blanking. Instead, the wavelength of a low frequency airgun-type seismic source is considerably larger than the size of gas bubbles in the sediment. For such low frequencies, free gas content simply changes the medium's overall properties, reducing the compressional wave velocity and slightly increasing attenuation. The seismic waves undergo reflection from the gassy sediment layer, but with sufficient transmission, and the top of the gassy sediment layer typically appears as a reflector with reversed polarity.

Based on high resolution echosounder data, free gas depth varies between 0.5 and 7.5 m beneath the sediment surface in the Bornholm Basin. In multichannel seismic data, free gas modifies the character of the seafloor reflection in different ways depending on the proximity of the gas front to the seafloor. When the gas front is close enough to the seafloor (0.5-1.5 m), interference between the seafloor and the gas reflection results in a more complicated wavelet shape and considerably increases the amplitude

of the composite reflector; when the gas bubbles are very close to the seafloor (> 0.5 m), the seafloor reflection shows a reversed polarity. High reflectivity at this interface can cause stronger multiples and reverberation of the water bottom reflector, as most of the seismic energy becomes trapped in the water column and attenuates slowly with time. When the gas-charged layer is deeper in the sediment, it appears in the seismic data as a single reflection with reversed polarity.

The geophysical descriptions of seismo-acoustic gas signatures may help interpretators in recognizing and mapping free gas in shallow marine sediments. The formation of seismo-acoustic gas signatures are more easily deciphered, when the relationship between wavelength and gas bubble size (size of the scattering objects), and the physical processes of scattering or reflection are considered. Moreover, seismo-acoustic gas signatures also reveal information about the differences in the amount of gas, the concentration of gas bubbles, the distribution of bubble sizes, the depth distribution of free gas in the sediment.

In the second study, a 2D high resolution velocity field was obtained from seismic data to assess free gas in the sediment. The seismic velocities were acquired applying a Migration Velocity Analysis on pre-stack time migrated data. Compressional wave velocities in the sediment are highly sensitive to free gas, and very small amounts of gas cause a significant decrease in the medium velocity. The analysed profile (GeoB10-044) crosses two depressions filled with organic-rich Holocene mud in the western part of the Bornholm Basin and the velocity field reveals two low-velocity patches, which extend from the shallow reversed polarity reflections down to the base of the Holocene mud layer. Average interval velocity values within the gassy mud are lower than the seafloor migration velocity by up to 500 m/s. This decrease in interval velocity, using the geoacoustic model of Anderson & Hampton that relates compressional wave velocity to sediment physical properties and gas content, is caused by an average $\sim 0.045\%$ gas volume fraction in the sediment. The interval velocities in individual cells of the velocity field are reduced to ~ 200 m/s, which predicts up to 3.4% gas content in the volumes of the sediment bounded by the rms velocity picks.

Through the high resolution velocity field, free gas distribution with depth can be investigated. Since reflectors are required for the velocity picks, the velocity field is limited in resolution, but together with the stratigraphic interpretation of the seismic data, geological units containing free gas could be identified. Based on the seismo-acoustic data and the derived interval velocities, shallow gas occurs throughout most of the Holocene mud. Although the distribution of free gas is patchy in the sediment, the gas concentration is likely to have a peak below the sulfate-methane transition zone and gradually decrease below.

This study demonstrated that interval velocities obtained from high resolution shallow water multichannel seismic data can be used for the assessment of free gas concentration at in situ pressure and temperature in shallow marine sediments. The measurement of the velocity reduction caused by free gas

is possible even when only a small amount ($> 0.01\%$) of free gas is present in the sediment. Due to the frequency dependence of the seismic response from gas-bearing sediments, a source frequency well below the resonance frequency of gas bubbles is required to penetrate through the gassy sediment layer, but on the other hand sufficiently high as well to maintain high vertical resolution of the subsurface structures.

In the third study, shallow free gas was investigated in seismo-acoustic data recorded in 10 frequency bands, covering a frequency range between 0.2 and 43 kHz. At the edge of a gassy patch in the Bornholm Basin, compressional wave attenuation caused by the presence of gas bubbles was estimated from reflection amplitudes beneath the gassy sediment layer. The multi-frequency seismo-acoustic data demonstrate that the imaging of shallow free gas is considerably influenced by gas bubble resonance, because in the resonance frequency range, attenuation is significantly increased. At the resonance frequency of the largest bubbles, between 3 and 5 kHz, high scattering causes complete acoustic blanking beneath the top of the gassy sediment layer. In the wider resonance frequency range, roughly between 3 and 15 kHz where the effect of smaller bubbles becomes dominant, the attenuation slightly decreases. This allows acoustic waves to be transmitted and reflections can be observed beneath the gassy sediment layer for higher frequencies. When the acoustic wavelength exceeds the size of gas bubbles 'above resonance', beginning at ~ 19 kHz, attenuation is low, but higher than in the gas-free sediment, and the presence of free gas bubbles can be inferred from the decreased reflection amplitudes beneath the gassy layer. Below the resonance frequency range < 1 kHz, attenuation is generally very low and not dependent on frequency.

A detailed analysis of the seismo-acoustic data revealed that most of the gas bubbles are concentrated in a ~ 2 m thick sediment layer, whose upper boundary is the gas front. Using the geoacoustic model of Anderson & Hampton, the observed frequency boundaries of the resonance effects suggest gas bubble sizes between 1 and 4-6 mm, and a gas volume fraction in the sediment up to 0.0002%. This small amount of gas already considerably attenuates the downward propagating acoustic waves, causing partial acoustic blanking.

With the multi-frequency acoustic approach and the Anderson & Hampton model, quantification of free gas in shallow marine environments is possible if the measurement frequency range allows the identification of the resonance frequency peak. Certainly, the method presented in this case study, is limited to places with only moderate attenuation, where the amplitudes of a reflection can be analysed beneath the gassy sediment layer.

Outlook

Based on the thesis presented, the understanding of seismo-acoustic gas signatures could be further advanced by applying e.g. full waveform modeling, which implies the creation of synthetic seismograms

for a pre-stack data set and includes angular variations of seismic reflections and least squares fit of medium properties. This in turn could also help in the characterization of free gas in the sediment. Synthetic seismograms may be created by varying a number of model input parameters, such as velocity reduction, reflection coefficient, gas front depth, gassy layer thickness, impedance gradients, and thus could reveal more about the amount and vertical distribution of free gas in Baltic Sea sediments.

An important task for the future would be to verify the predicted in situ gas volume fractions by ground truthing and to evaluate the quantification methods presented in this thesis. While measurement of sediment physical properties are needed to improve the estimation, the real validation of the method will be when in situ free gas volume in the sediment can be measured in pressurized cores, e.g. with the application of X-Ray CT scanning. The accuracy and applicability of these quantification methods will certainly depend on the geoacoustic model and its input parameter values, which may have to be further developed if more precise data become available. Nevertheless the characterization of shallow gassy sediments through velocity reduction and attenuation increase as was demonstrated here appears as a feasible method, which should be developed to be a standard seismic method.

Using multichannel seismics to image shallow gas in the Baltic Sea also offers the opportunity to assess free methane gas content in the Holocene mud. Mapping mud thickness in gassy areas and estimating the free gas content and distribution using seismic interval velocities could be used to create regional estimates of the amount of methane stored in the Baltic Sea, contributing to an overall risk analysis related to global warming, but also regional effects.

Appendix A

One year of continuous measurements constraining methane emissions from the Baltic Sea to the atmosphere using a ship of opportunity

Wanda Gülzow, Gregor Rehder, Jens Schneider von Deimling, Torsten Seifert,
Zsuzsanna Tóth

Biogeosciences 10 (2013) 81-99

www.biogeosciences.net/10/81/2013/; doi:10.5194/bg-10-81-2013

Creative Commons Attribution 3.0 License



One year of continuous measurements constraining methane emissions from the Baltic Sea to the atmosphere using a ship of opportunity

W. Gülzow¹, G. Rehder¹, J. Schneider v. Deimling³, T. Seifert¹, and Z. Tóth²

¹Leibniz Institute for Baltic Sea Research Warnemünde, Seestraße 15,
18119 Rostock, Germany

²University of Bremen, Klagenfurter Straße, 28359 Bremen, Germany

³Helmholtz Centre for Ocean Research (GEOMAR), Wischhofstr. 1–3, 24148 Kiel, Germany

Correspondence to: W. Gülzow (wanda.guelzow@io-warnemuende.de)

Received: 24 May 2012 – Published in Biogeosciences Discuss.: 1 August 2012

Revised: 8 November 2012 – Accepted: 23 November 2012 – Published: 8 January 2013

Abstract. Methane and carbon dioxide were measured with an autonomous and continuous running system on a ferry line crossing the Baltic Sea on a 2–3 day interval from the Mecklenburg Bight to the Gulf of Finland in 2010. Surface methane saturations show great seasonal differences in shallow regions like the Mecklenburg Bight (103–507 %) compared to deeper regions like the Gotland Basin (96–161 %). The influence of controlling parameters like temperature, wind, mixing depth and processes like upwelling, mixing of the water column and sedimentary methane emissions on methane oversaturation and emission to the atmosphere are investigated. Upwelling was found to influence methane surface concentrations in the area of Gotland significantly during the summer period. In February 2010, an event of elevated methane concentrations in the surface water and water column of the Arkona Basin was observed, which could be linked to a wind-derived water level change as a potential triggering mechanism. The Baltic Sea is a source of methane to the atmosphere throughout the year, with highest fluxes occurring during the winter season. Stratification was found to promote the formation of a methane reservoir in deeper regions like Gulf of Finland or Bornholm Basin, which leads to long lasting elevated methane concentrations and enhanced methane fluxes, when mixed to the surface during mixed layer deepening in autumn and winter. Methane concentrations and fluxes from shallow regions like the Mecklenburg Bight are predominantly controlled by sedimentary production and consumption of methane, wind events and the

change in temperature-dependent solubility of methane in the surface water. Methane fluxes vary significantly in shallow regions (e.g. Mecklenburg Bight) and regions with a temporal stratification (e.g. Bornholm Basin, Gulf of Finland). On the contrary, areas with a permanent stratification like the Gotland Basin show only small seasonal fluctuation in methane fluxes.

1 Introduction

To constrain the biogeochemical cycle of the greenhouse gas methane (CH₄) and to estimate its future role in climate on earth, processes which influence the strength of its various sources and sinks need to be determined accurately. Numerous studies over the last decades have investigated various methane sources with the aim to quantify their contributions to the global methane budget. Emission estimates of the world's ocean range from 2 % (Bange et al., 1994) to 10 % (Grunwald et al., 2009) of the total global methane source strength to the atmosphere. Significantly smaller emission estimates were calculated for open ocean areas like the Pacific Ocean by Bates et al. (1996) with less than 0.1 % of the atmospheric source strength, and the authors point out the underestimation of coastal zones. Bange et al. (1994, 2006) also comment the underestimation of shallow marine areas due to the lack of data and the uncertainty of the role of estuaries, shelf and coastal areas, which may contribute 75 % of the

total marine methane emissions to the atmosphere. In fact, many studies face the limitations of discrete data measurements to adequately observe methane production parameters or investigate processes. Therefore, the marine methane budget and estimations of the resulting fluxes to the atmosphere still contain large uncertainties.

1.1 Baltic Sea as shallow marginal sea

The Baltic Sea is located in the northern part of Europe and forms one of the largest brackish water reservoirs on earth with an average water depth of 52 m. Today, the Skagerrak and the Kattegat remain the only connection with the North Sea and the open ocean. A series of submarine sills divide the Baltic Sea into several sub-basins, which can be distinguished and characterized by different geochemical and hydrographical gradients. The positive freshwater balance and episodic saline inflow events from the North Sea lead to the formation of a less saline surface layer and a more saline deep and bottom water layer separated by a halocline. The surface salinity gradient decreases from 17 in the west (Belt Sea) to 3 in the northeast (Bothnian Bay). The vertical salinity gradient is leading to a strong density stratification hampering vertical mixing. Especially in the central deep regions of the Baltic Sea this stratification persists throughout the year. The limited ventilation together with high productivity leads to the development of a permanent redoxcline, marking the transition from oxic to sub- or anoxic conditions in the deeper stratified basins.

A comprehensive description of climate and weather in the Baltic Sea region has been provided by Feistel et al. (2008).

1.2 Methane in the Baltic Sea

Glacial and postglacial sedimentary deposits of the Baltic Sea are characterized by fine-grained organic rich clay and mud layers (Holocene sediments; Thießen et al., 2006; Laier et al., 2007; Feistel et al., 2008). Methanogenesis of the organic matter in the organic-rich surface sediments is the major methane source in the Baltic Sea (Whiticar and Faber, 1986; Butler et al., 1989; Thießen et al., 2006). This process leads to the occurrence of shallow gas in the sediment, especially in the Arkona and Bornholm Basin (BB; Thießen et al., 2006; Laier and Jensen, 2007). Methane concentrations in anoxic surface sediments are not only controlled by the production but also by the degradation of methane via bacterial oxidation (Boetius et al., 2000; Thießen et al., 2006), whereby 87–99 % of the produced methane is estimated to be oxidized within the sediment (Berger and Heyer, 1990). Pockmark structures and seep areas are potential sources for methane emissions towards the water column, but only few locations are known in the Baltic Sea (Dando et al., 1994; Bussmann and Suess, 1998; Thießen et al., 2006; Pimenov et al., 2010). Additional methane sources which might affect sea surface methane concen-

trations are riverine input, groundwater discharge, and formation in the upper water column, including production in anaerobic microniches like digestive tracts of zooplankton (DeAngelis and Lee, 1994), fecal pellets and sinking organic particles (Karl and Tilbrook, 1994) or the use of methylated compounds under oxic conditions (Karl et al., 2008).

Methane generated in the sediment transfers into the water column via diffusion, fluid flow or bubble transport. As a consequence, a methane gradient towards the water surface is usually observed in the Baltic, with high concentrations in the deeper layers and low concentrations at the sea surface (Schmale et al., 2010). During the transport through the water column towards the sea surface, methane is substantially reduced by methane oxidation especially in the oxic/anoxic transition layer, as has been shown for the Black Sea (Schmale et al., 2011). Besides oxidation, methane emission to the atmosphere constitutes another major sink of methane in the Baltic Sea.

There are only few assessments of methane concentrations and fluxes to the atmosphere from the Baltic Sea. Bange et al. (1994) determined atmospheric and dissolved methane using an automated gas chromatographic system and described the Southern Belt Sea and the central Baltic Sea as source for atmospheric methane. Bange and coworkers showed strong seasonal variations in surface methane saturations with high values during the summer (e.g. 168 % Arkona Sea, 157 % Bornholm Sea) and lower values during the winter (e.g. 117 % Arkona Sea, 107 % Bornholm Sea). They highlighted the importance of shallow shelf regions for global methane flux estimations. Bange et al. (1998) described the seasonal distribution of methane and nitrous oxide in the Bodden Sea, using an equilibrator combined with a gas chromatograph, postulating that methane emissions from this area account for 17 % of the total Baltic Sea methane emissions. Monthly observations of the water column at Boknis Eck between 2006 and 2008 showed a bimodal seasonality of sedimentary release of methane and elevated methane concentrations in deep water layers after sedimentation of fresh organic material from phytoplankton blooms (Bange et al., 2010). Similar periodic changes of methane fluxes from the sediment into deeper water layers were observed in the coastal zone of Puck Bay along the Hel Peninsula (Reindl and Bolalek, 2012). Abril and Iversen (2002) described methane emissions to the atmosphere along the salinity gradient in the estuarine zone of Randers Fjord (Denmark) from February to December 2000. They observed that the shallow estuarine morphology increases the influence of the sediment on methane dynamics (production and consumption of methane) compared to deeper regions and amplifies rapid changes in methane concentrations and fluxes due to short and episodic weather events (stormy winds).

In this paper we present the results of the first year of almost intervention-free operation of a system allowing continuous measurements of sea surface methane using a

continuous equilibration technique in combination with integrated off axis cavity output spectroscopy in the southern and central parts of the Baltic Sea (Gülzow et al., 2011). The system successfully recorded methane and carbon dioxide in surface waters of the Baltic Sea since its installation in November 2009 on the cargo ship *Finnmaid*. The ferry line connects Travemünde (Germany), Helsinki (Finland) and Gdynia (Poland) and crosses the central Baltic Sea every 2 to 3 days (Fig. 1). The high spatiotemporal data coverage provided by the instrument allows new insights into the seasonal and spatial distribution of methane in the surface water of the Baltic Sea and the governing controls. Selected key areas have been taken for detailed studies of the controlling processes and parameters, including upwelling, stratification and mixing, wind events and water level changes, the seasonal temperature cycle, and the distribution of sedimentary sources.

2 Methods

2.1 Analytical setup on the cargo ship *Finnmaid*

In cooperation with the Finnish Institute of Marine Research (SYKE, ALGALINE Project), the Leibniz Institute for Baltic Sea Research Warnemünde (IOW) installed a fully automated measuring and sampling system on the cargo ship *Finnmaid*, which commutes regularly between Travemünde (Germany), Helsinki (Finland) and Gdynia (Poland) since 1993. The ALGALINE equipment on *Finnmaid* consists of a fluorometer for continuous recording of the chlorophyll *a* fluorescence and a sampling system for the laboratory analysis of inorganic nutrients, dissolved and particulate organic matter, and plankton species composition. Sea surface salinity (accuracy 0.001) and temperature (accuracy 0.001 °C) are recorded using a SeaBird 38 thermosalinograph. The IOW installed a fully automated system for the measurement of surface CO₂ partial pressure in 2003 (Schneider et al., 2006), later extended by optode-based recording of surface oxygen (Schneider et al., 2006). An independent continuous measuring system for methane and carbon dioxide was added in 2009 (Gülzow et al., 2011). The current trace gas measuring system consists of two independent established equilibrators joint with a methane/carbon dioxide analyzer (MCA; Los Gatos Research) and a LICOR gas analyzer, respectively. Details about the analytical set up, equilibration theory, essential calculations as well as temperature correction are given in Körtzinger et al. (1996) and Gülzow et al. (2011). Methane and carbon dioxide were determined with a total uncertainty of < 0.8 % (Thomas, 2011). The response times of the system for methane and carbon dioxide were determined with $\tau = 676$ s and $\tau = 226$ s, respectively (Gülzow et al., 2011). The time constant for methane implies that equilibrium between the gaseous and the water phase is reached after 35 min (3 σ). Hence, with

Table 1. For detailed contemplations of regional differences special key areas were selected to merge methane data (saturation values) with mixing depth or meteorological forcing data derived from the regional forecast model COSMO/EU. The subdivision of the area WoG and GoF reflect a better description of the field of interest than one large box, respectively, and improves the technical approach during modeling.

Selected area	Latitude ° N	Longitude ° E
Mecklenburg Bight (MB)	11.62–12.42	54.25–54.65
Arkona Basin (AB)	13.25–14.05	54.63–55.03
Bornholm Basin (BB)	14.55–15.35	55.29–55.69
West of Gotland (WoG) with		
West of Gotland 1	17.94–18.16	57.58–57.69
West of Gotland 2	18.11–18.34	57.70–57.82
West of Gotland 3	18.29–18.51	57.82–57.94
East of Gotland (EoG)	18.50–18.59	51.11–56.87
Gotland Central Basin (GB)	19.55–20.35	55.74–56.74
Gulf of Finland (GoF) with		
Gulf of Finland 1	22.65–24.05	59.35–59.67
Gulf of Finland 2	21.95–23.35	59.19–59.51
Gulf of Finland 3	23.35–24.75	59.51–59.83

the average ship speed of 22 knots, the resulting methane signal is smoothed and slightly retarded in time (Gülzow et al., 2011).

2.2 Sea surface equilibrium calculations

The atmospheric methane fraction $x_{\text{CH}_4\text{atm}}$ [ppm] of the NOAA station BAL (Baltic Sea, Poland, 55.35° N 17.22° E) were used to calculate sea surface equilibrium concentrations. The station is situated 65 nautical miles offshore. Atmospheric samples are taken using a surface flask sampler positioned at 3 m above sea level. The air samples are collected weekly and analyzed according to the standard evaluation protocol of NOAA (<http://www.esrl.noaa.gov/gmd/ccgg/>; Dlugokencky et al., 2011).

The equilibrium concentration $C_{\text{CH}_4\text{eq}}$ [nM] describes the methane concentration in water at a certain salinity and temperature, which is in equilibrium with the overlaying gaseous phase (atmosphere) and can be calculated using the Bunsen coefficient β after Wiesenburg and Guinasso (1979).

$$C_{\text{CH}_4\text{eq}} = \beta \cdot x_{\text{CH}_4\text{atm}} \quad (1)$$

The ratio of equilibrium concentration $C_{\text{CH}_4\text{eq}}$ and measured seawater concentration $C_{\text{CH}_4\text{aq}}$ [nM] describes the saturation state indicating undersaturation for values below 100 % and oversaturation for values above 100 %. The difference of $C_{\text{CH}_4\text{eq}}$ and $C_{\text{CH}_4\text{aq}}$ is a key parameter for the calculation of sea–air methane fluxes (see Sect. 3.5).

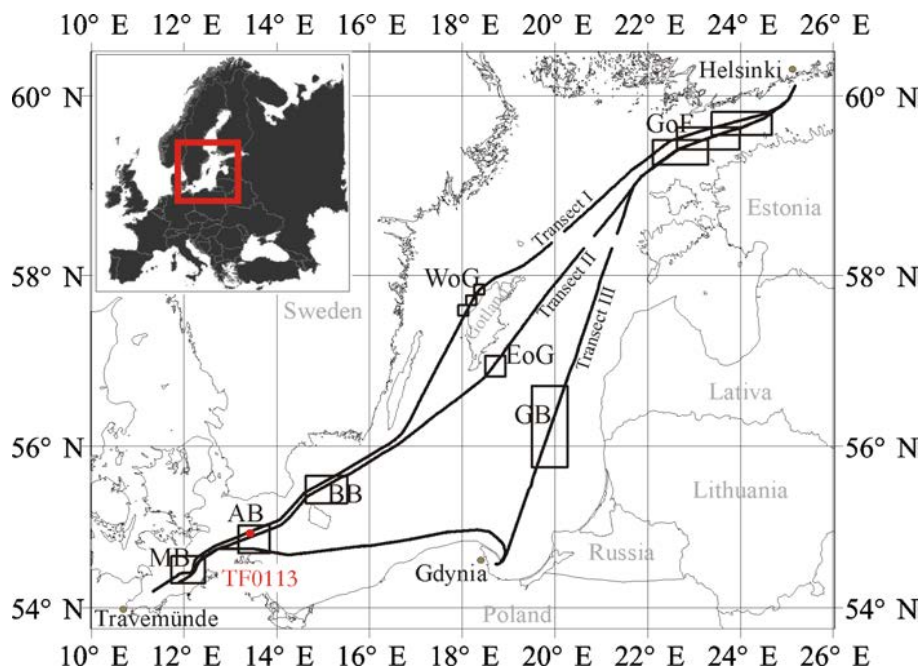


Fig. 1. Cruise tracks of the ship of opportunity *Finnmaid*. The ferry line crosses the Baltic Sea via three transects and connects Travemünde (Germany) with Helsinki (Finland) and Gdynia (Poland) in an interval of 2 to 3 days. Transect I passes the Mecklenburg Bight (MB), Arkona Basin (AB), Bornholm Basin (BB), West of Gotland (WoG) and the Gulf of Finland (GoF). Transect II records the same route but East of Gotland (EoG) to Travemünde. Transect III passes Gdynia and the Gotland Basin (GB). Boxes indicate selected areas for detailed investigations (see also Table 1). Station TF0113 is part of a regular monitoring program of the Leibniz Institute for Baltic Sea Research Warnemünde.

Transect III passes Gdynia and the Gotland Basin (GB). Boxes indicate selected areas for detailed investigations

2.3 Meteorological data (Station 2010). Station TF 0113 is part of a regular monitoring program of the Leibniz Institute for Baltic Sea Research Warnemünde. The model defined wind field were used to derive gas exchange velocities based on the quadratic relation by Wanninkhof (2009).

To estimate the role of wind forcing on sea–air gas exchange in the selected key regions (Table 1) of the Baltic Sea, meteorological forcing data derived from the regional weather forecast model COSMO/EU (former DWD/LME) run by the German Weather Service (DWD) were used (Schulz and Schöttler, 2005; COSMO, 2012). The core documentation of the COSMO model is available on the web site of the international Consortium of Small-scale Modeling (COSMO). The non-hydrostatic, high-resolution model COSMO/EU covers the whole of Europe with a bottom grid spacing of 7 km, resolving even small scale spatial changes. The daily variation of meteorological conditions is adequately represented by prescribing a weather forecast every 3 h and linear interpolation onto the ocean model time steps of 600 s. The coupling atmosphere–ocean fluxes are evaluated in the circulation model MOM-4 according to Beljaars et al. (1994). Point comparisons with observations from two open sea measurement sites at Darß Sill (12.70° E, 54.40° N) and in Arkona Basin (AB, 13.85° E, 54.88° N) reveal that the reliability of COSMO/EU forecasts of air pressure, air temperature, wind speed, wind direction, and relative humidity is of the same degree of accordance as shown by Leuenberger et al. (2010) for ensemble forecasts in view of assimilation, e.g. bias in wind speed is well below -1 ms^{-1} , root mean square deviation is around 1.5 ms^{-1} , and linear correlation exceeds 90 %

2.4 Mixing depth

The COSMO/EU forecasts were used as input parameters to drive the numerical Baltic Sea model which is based on the Modular Ocean Model (MOM4, Griffie et al., 2004). The model domain comprises the entire Baltic Sea with the western boundary at Skagerrak (at 8.25° E). The sea level at the open boundary and the river runoff to the Baltic Sea are prescribed from data provided by the Swedish Meteorological and Hydrological Institute (SMHI). Temperature and salinity at the open boundary are nudged to monthly mean profile derived from climatology (Janssen et al., 1999). The model was started from rest with initial conditions taken from a coarser model simulation, which was corrected with measurements. The model was run for the period September 2002 to December 2010. The model bathymetry is based on a one nautical mile grid (Seifert et al., 2001). The upper water column down to 30 m depth is divided into layers of 1.5 m thickness to resolve the shallow channels and sills in the southwestern Baltic. The layer thickness gradually increases to 5 m at a maximum depth of 268 m, corresponding to the deep basins in the central and northern Baltic. This vertical resolution allows the modeling of the local stratification

and its evolution throughout the year in each of the respective working areas. Sub-grid scale mixing processes are modeled by the MOM-4 adaptation of the scheme (Smagorinski et al., 1963). The development of vertical stratification is simulated by the kpp scheme (Large et al., 1994). Based on the analysis of the stability within the upper water column, fluxes from the sea surface are non-locally distributed to the depth which is mixed by the entrained energy. The mixing depth describes the range of active turbulence in the upper water column. The mixed layer depth is characterized by homogeneous salinity and temperature profiles. Only stronger mixing events are able to diminish the stratification at the bottom of the mixed layer.

2.5 Sea–air methane flux calculations

The flux of methane across the sea–air interface F [$\text{nmol m}^{-2} \text{s}^{-1}$] can be expressed by the concentration difference of methane between the sea surface water $C_{\text{CH}_4\text{aq}}$ and the equilibrium concentration with the atmosphere $C_{\text{CH}_4\text{eq}}$ (Eq. 1) and the gas transfer velocity k [cm h^{-1}].

$$F_{\text{CH}_4} = k \cdot (C_{\text{CH}_4\text{aq}} - C_{\text{CH}_4\text{eq}}) \quad (2)$$

The transfer velocity k was calculated using the quadratic relation of Wanninkhof et al. (2009):

$$k = 0.24 \cdot u^2 \cdot ((S_{\text{Csal}}/660)^{-0.5}) \quad (3)$$

with wind speed u [m s^{-1}] in 10 m height as main driving kinetic parameter and the Schmidt number S_{Csal} interpolated according to the measured salinity

$$S_{\text{Csal}} = [(S_{\text{C35}} - S_{\text{C0}}) \cdot \text{Sal}/35] + S_{\text{C0}}, \quad (4)$$

with Schmidt number S_{C35} for saline water (35 psu), Schmidt number S_{C0} for fresh water (0 psu) after Jähne et al. (1987), and measured salinity Sal [psu].

The parameterization of the transfer velocity k as function of the wind speed u is based on a conceptual model for sea–air gas transfer by relating one gas (e.g. ^{222}Rn) to another gas (e.g. CH_4) on the basis of the physicochemical properties of the gases (Wanninkhof et al., 2009). Although a variety of conceptual models have been introduced over the last decades, the parameterization of k is still under debate (Liss and Merlivat, 1986; Jähne et al., 1987; Wanninkhof, 1992; Nightingale et al., 2000; Sweeney et al., 2007; Weiss et al., 2007; Wanninkhof et al., 2009). For this study, the most recent approximation of Wanninkhof et al. (2009) was used. Equation (3) shows the influence of u on the transfer velocity and methane fluxes in general. To avoid the overestimation of short time changes in wind speed in combination with the infrequently traversing (irregular intervals of transects passing or measuring gaps) by the ferry, methane fluxes were calculated based on monthly averaged parameters to achieve a general pattern. The monthly flux values reported here (see Sect. 3.5) are derived from sea

surface methane concentrations $C_{\text{CH}_4\text{aq}}$ [nM] averaged for each leg crossing a selected area (Fig. 1, Table 1) and averaged for each month. Mean monthly atmospheric methane fractions $x_{\text{CH}_4\text{atm}}$ [ppm] are derived from the NOAA Station BAL (Baltic Sea, Poland; Dlugokencky et al., 2011). S_{Csal} was calculated based on temperature and salinity determined like $C_{\text{CH}_4\text{aq}}$ (averaged for each leg crossing over the selected areas (Fig. 1, Table 1) and then averaged for each month). Monthly mean wind speed was calculated from the COSMO/EU wind field averaged over the selected areas.

2.6 Bottom water temperature

The water temperature observed near the sea floor is used as a proxy for the temperature of the sediment surface. These data were derived from the HELCOM data set available from the ICES (2011) Oceanographic Database. CTD (Conductivity, Temperature, Density) casts, taken at standard depth levels, supply a sufficiently dense database with more than one thousand samples at a series of stations which characterize the typical conditions in the sub-basins of the Baltic Sea since 1960. Only data registered within the lowermost 5 % of the water column have been taken into account to calculate the mean water temperature at the seafloor and its range of variation, which in this work is described by the standard deviation and the observed minimum and maximum temperatures.

2.7 Water column profile

Vertical water profiles were taken at station TF0113 in the Arkona Basin. The data set includes 4 profiles collected with a 24 (121) Niskin-bottle rosette water sampler. For continuous CTD profiling a SeaBird SBE911+ system was attached to the underwater unit. After retrieving the sampler on board, oxygen concentrations were determined using Winkler titration (Grasshoff et al., 1999). Methane was extracted from the water sample using the vacuum degassing method and its mole fraction was determined with a gas chromatograph equipped with a flame ionization detector (Keir et al., 2009).

2.8 Multichannel seismic profile

To observe free gas accumulations in subsurface sediments, seismo-acoustic data were collected in the Arkona Basin (student cruises of the University of Bremen) using a GI gun with a central frequency of 200 Hz and a 50 m long high resolution streamer with 48 channels. The vertical resolution in the seismic profile is approximately 1 to 5 m. Horizontal resolution is determined by the common mid-point (CMP) bin size, which was set to 1 m. Data processing followed a conventional processing flow with special emphasis on the velocity analysis.

3 Results and discussion

The focus in the following sections will be set on the most visited transects I and II, passing west (WoG) and east (EoG) of Gotland (Fig. 1) in 2010. Special emphasis is given to selected key areas (Table 1) in addition to surface methane concentration measurements covering one year. Key controlling parameters such as temperature, wind, and the mixing depth are presented. Data gaps (Fig. 2) due to malfunction/maintenance exist from 9 to 21 April 2010 and from 26 April to 18 May 2010. Smaller data gaps in Fig. 2 are caused by the passing of the ferry along transect III (total of 264 operational days).

First sea surface temperature anomalies were identified indicating local upwelling accompanied by elevated methane concentrations. Highest methane surface values measured throughout the year in the Arkona basin are investigated in regard to the specific environmental setting of shallow gas. A potential linkage between wind and weather-driven hydrostatic pressure changes and methane gas ebullition is suggested. The effects of seasonal sea surface temperature (SST) and mixing depth changes are studied in detail in regard to their control on the surface methane concentration and sea–air flux potential. Finally, a seasonal cycle of monthly averaged methane flux calculations will be presented for all key areas including the ice-influenced Gulf of Finland (GoF) area.

3.1 Overview

3.1.1 Regional aspects

Surface water methane concentrations along transects I and II, passing west and east of Gotland, are shown for all lines gathered in 2010 in Fig. 2, and reveal remarkable regional differences. Strong fluctuations and increased methane concentrations in the westernmost and easternmost parts of each transect have been observed. These regions are covered by both transects in a very similar way. Methane values in the Arkona Basin (Fig. 2, Long: 13° E–14° E, see Fig. 1 for orientation) range from 3.2 nM to 8 nM (97–270 % methane saturation) with exceptionally high concentrations in February, which will be discussed below (Sect. 3.3). The Gulf of Finland (Long: 22° E–26° E) is characterized by elevated methane concentrations throughout the year compared to the other regions. In fact, the western part of the Gulf of Finland shows a strong variability in methane concentrations during the year, ranging from 3.4 nM (106 % methane saturation) to over 22 nM (470 % methane saturation). In the middle of each transect methane concentrations are rather uniform and in general considerably lower. In the area of the island of Gotland (Fig. 2, Long: 18° E–19° E) methane concentrations in the surface water are comparably low, ranging from 3.3 nM (95 % methane saturation) to 4.6 nM (165 % methane saturation). West (WoG) and East of Gotland (EoG; Fig. 2,

Long: 18° E–19° E), episodes of elevated methane concentrations lasting a couple of days were observed during the summer months June till September, when methane values increased more than 3 nM above normal.

3.1.2 Seasonal aspects

The seasonal trend of surface water methane concentrations in the Baltic Sea is characterized by high methane concentrations during winter and lower methane values during summer, except for the very shallow areas like the Mecklenburg Bight (MB) or Arkona Basin (see Sect. 3.4). The diverse pattern illustrated in Fig. 2 shows high fluctuation of the methane concentrations during the winter months compared to the rather uniform values in summer. The strongest annual fluctuation was observed in the area of the Gulf of Finland (Fig. 2, Long: 22° E–26° E), where highest methane concentrations (up to 22 nM; 470 % methane saturation) were measured in February, decreasing in the time following. Lowest methane values of 3.4 nM (106 % methane saturation) were detected during the summer months June till August before concentrations rose again until the end of December.

3.2 Upwelling

Upwelling is a typical, well-documented phenomenon in the Baltic Sea (Alenius et al., 1998; Vahtera et al., 2005; Lehmann and Myrberg, 2008; Lips et al., 2009). The process is characterized by winds blowing predominantly parallel to the coast from a favorable direction. Together with the Coriolis effect, this results in a displacement of the upper water body leading to mixing in the water column and upwelling at the coast (Lehmann and Myrberg, 2008). It involves the mixing of dense, cooler and usually nutrient-rich water towards the sea surface by replacing the warmer mostly nutrient-depleted surface water (Lehmann and Myrberg, 2008). Depending on the strength and period of the favourable winds, upwelling can range from a small scale coastal event to a large scale phenomenon influencing the open sea. Although this process occurs throughout the year, upwelling plays an essential role in the mixing of the water column during the summer season when additional thermal stratification occurs and nutrients in the surface layers are depleted by algal blooms. Sea surface temperature is a good parameter to indicate upwelling especially during the summer months, when the surface water is warmer than the deeper layers. Then, upwelling can be detected by a local sharp temperature drop in the surface water, which can last a couple of days. A well-developed method to observe this phenomenon, recurring in time and location, is satellite imaging of the sea surface temperature (Siegel et al., 1994, 2005; Lass et al., 2010).

During the measuring campaign with the ferry line *Finnmaid*, the effect of upwelling on the local surface methane concentrations was recorded several times at different

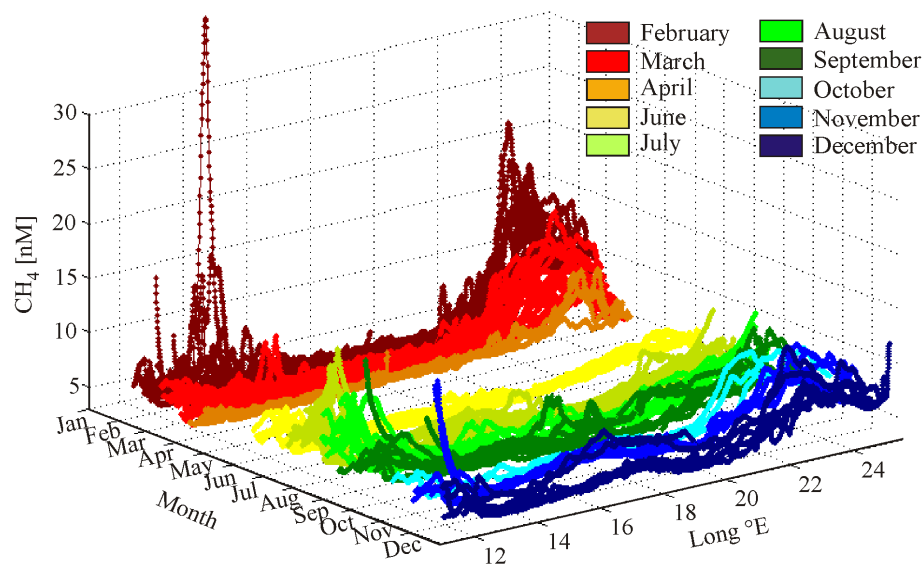


Fig. 2. Methane concentrations of all lines along transect I and II in 2010 color coded for each month. During most of April and May no data could be gathered due to maintenance. Later gaps in the continuous data set are in part due to the passage of the ferry along the transect III.

Fig. 2. Methane concentrations of all lines along transect I and II in 2010 color-coded for each month. During most of April and May no data could be gathered due to maintenance. Later gaps in the continuous data set are in part due to the passage of the ferry along the transect III.

locations of the Baltic Sea. Especially in the area around the island of Gotland, various events could be observed. In Fig. 3; methane (a), methane saturation (b), partial pressure of carbon dioxide (c) and sea surface temperature (d) are shown for the area north-west of Gotland for the year 2010. Sharp drops of the sea surface temperature (Fig. 3d) on 24 July (light green line) and 3 September (dark green line) can be pointed out with values reaching down well below 5 °C. We highlight these two lines in the following, though various weaker events were observed over the course of the year. For both dates, a property–property plot of methane versus sea surface temperature (Fig. 3e) shows a significant inverse correlation demonstrating the strong coherence of rising cold water masses and increased methane values at the surface (Rehder et al., 2002).

Whereas methane concentrations in July (Fig. 3a, transparent light green lines) vary in general between 3.5 nM and 4.5 nM, methane values reach up to 6.8 nM in the surface water on 24 July (Fig. 3a light green line). On 3 September methane concentrations increase even up to 8 nM (Fig. 3a, dark green line). Strong increases during the upwelling events could also be observed in the recorded carbon dioxide concentrations (Fig. 3c) and salinity (data not shown). Usually, all parameters show elevated values for the same time and at the same locations for all recorded upwelling events. The finding reflects the transport of deeper water towards the surface, which are characterized by colder temperatures (Umlauf et al., 2010), enhanced $p\text{CO}_2$ from organic matter remineralization (Thomas and Schneider, 1999) and often enhanced methane concentrations (Schmale et al., 2010). Methane saturation values (Fig. 3b) increase during the major upwelling events in July and September, but the recorded sig-

nals vary significantly from the methane signal (Fig. 3a). Although upwelled waters are enriched in methane, the increase in saturation values is less pronounced than the methane signal (Fig. 3a) because lower temperatures imply higher solubility. During the upwelling event on 3 September methane values reach 8 nM and oversaturation of 194 % at water temperatures of 3.6 °C (Fig. 3a and b dark green line) was observed. With a water temperature of 22 °C, this surface methane concentration would reach over saturation values of more than 300 %. Still, the transport of deeper water towards the surface and the increase of the sea surface methane concentration change temporally the saturation of methane in the surface water, influencing the emission of methane towards the atmosphere, which will be discussed below. Unfortunately, due to the changing frequency of transects passing the western coast of Gotland no continuous data recording could be achieved in this area. Therefore, the persistence of the upwelling-induced methane (and carbon dioxide) oversaturation and the timeframe for dilution/evasion to the atmosphere could not be tracked.

The different signal widths of the corresponding curves for carbon dioxide and methane, shown in Fig. 3, need to be highlighted. The crossing of the investigated area north-west of Gotland had a duration of approximately 4 h 15 min on 24 July (Fig. 3, outstanding light green), and 5 h 15 min on 3 September (Fig. 3, outstanding dark green line). Although both records show a similar line characteristic, the methane signal is wider than the corresponding records of carbon dioxide. To a large extent, the different shapes of the methane and carbon dioxide curves might reflect the different response times of the system for the two gases, with the time constant for CH_4 approximately four times

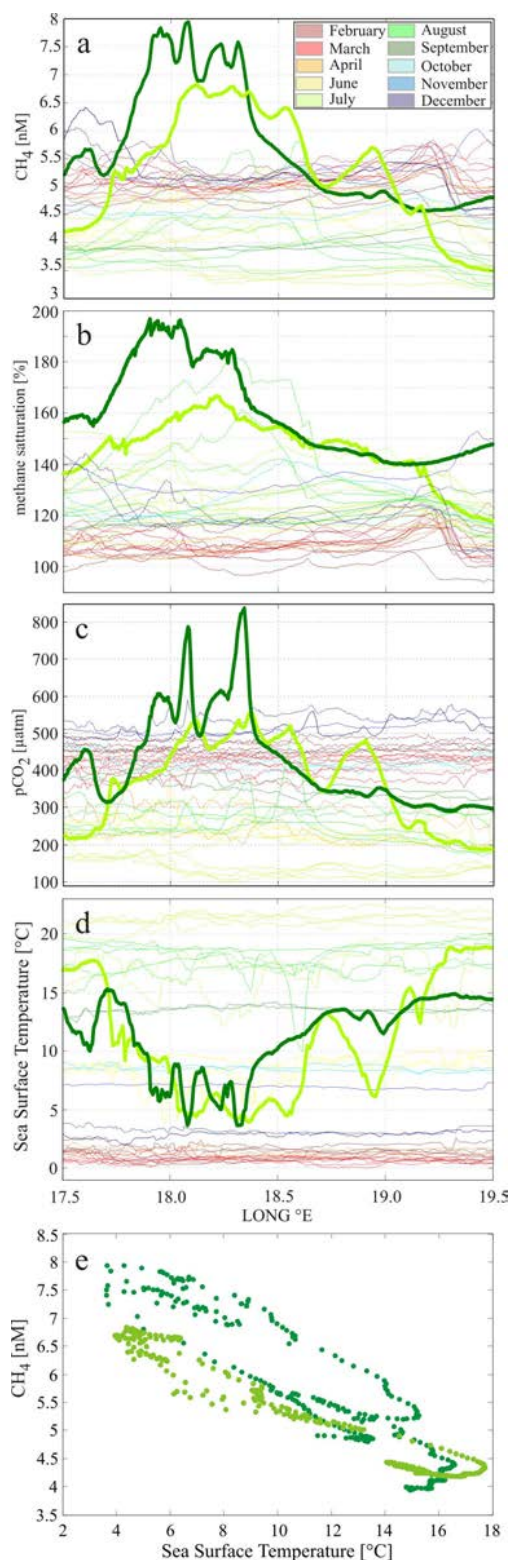


Fig. 3. (a) Methane, (b) methane saturation, (c) carbon dioxide and (d) sea surface temperature of the area West of Gotland for the year 2010. All data in transparent thin lines color coded for each month. Two significant upwelling events in July and September are highlighted with outstanding light green (24 July) and dark green (3 September) lines. For these dates, methane versus sea surface temperature is shown using the same color coding (e).

longer than for CO_2 (for detailed discussion, see Gülzow et al., 2011). On the other hand, methane concentrations and carbon dioxide partial pressures do not have to be directly related. Though both properties generally increase underneath the mixed layer (Thomas and Schneider, 1999; Schmale et al., 2010), the $p\text{CO}_2$ increase, mostly resulting from organic matter degradation, will start immediately underneath the mixed layer, while stronger enhancement of methane is generally observed at greater depth. The oval shaped characteristic of the plot of methane concentration versus sea surface temperature and methane (Fig. 3e), can be explained by the faster response time of the temperature signal compared to the slower MCA-signal in respect to changing water masses. The signal reflects the “in and out”-passage through the inhomogeneous upwelling water mass.

3.3 Pressure-induced liberation of methane from the seafloor

On 2, 4 and 5 February, extraordinarily high methane concentrations were measured in the surface waters of the Arkona Basin rising up to 38 nM (832 % methane saturation), 15 nM (321 % methane saturation) and 16.5 nM (360 % methane saturation), respectively (Fig. 4). Elevated methane concentrations could be measured until 6 days after the event, with decreasing values until concentrations prior to the event were reached. These exceptionally high methane concentrations in the surface water were accompanied by a longer period of strong winds, starting in the middle of January, which resulted in an oscillation of the sea level of almost 1.5 m within a day in the Arkona Basin (Fig. 4, gray line, station Sassnitz, Bundesanstalt für Wasserbau BAW). Further, the wind-induced mixing depth of the water column was calculated to reach down to the sediment surface at 45 m depth during this period (Fig. 4, blue line). The data can be interpreted with additional data of dissolved methane measurements in the water column sampled during 4 research cruises between December 2009 and August 2010 (Fig. 5) in the Arkona Basin at station TF0113 (Lat: 54.92° N; Long: 13.50° E, for location see Fig. 1). Methane concentrations in the upper water layer were approximately 10 times higher than usual on 28 January, with concentrations around 50 nM down to 30 m depth (Fig. 5) and increasing towards the seafloor to a maximum concentration of 420 nM at 40 m depth. The parameters salinity, oxygen and temperature indicate mixing of the entire upper water column by uniform values down to nearly 40 m depth in accordance to the model-derived mixing depth (Fig. 4). Further towards the seafloor a gradual increase in temperature and salinity marks the existence of a narrow bottom layer. In contrast, the average methane concentration in the water column in December 2009 at Station TF0113 (Fig. 5) was 7.7 nM. Methane profile taken during cruises in July and August 2010 show similar low methane concentrations of 5.1 nM and 10.8 nM on average for the mixed layer, respectively. Turbidity signals of station TF0113 (data not

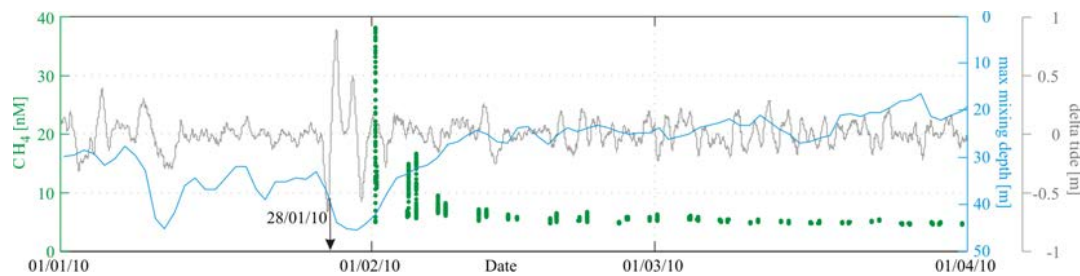


Fig. 4. Data from a three month survey of the Arkona Basin. Sea surface methane concentrations (green dots, representing measured methane concentrations along each leg crossing the selected area “Arkona Basin”, Table 1), daily maximum mixing depths (blue line) and sea level data (gray line, measured at station Sassnitz, Bundesanstalt für Wasserbau). Delta tide indicates the gradient of oscillation of the sea level around 0.

shown) on 28 January increase significantly from 0.4 NTU (Nephelometric Turbidity Unit, average of upper 40 m water column; data not shown) to 1.02 NTU in the bottom water layer, indicating enhanced shear stress at the sediment–water interface. For comparison, turbidity measurements at this station on 1 August show values below 0.5 NTU for the entire water column.

Based on acoustic data collected throughout the Arkona Basin, free gas accumulations in the Holocene mud are known to be widespread (Mathys et al., 2005; Thießen et al., 2006). While these gas layers originate from organic matter degradation within the mud where gas bubbles are efficiently trapped, only one seabed feature has been found in the region so far, which may indicate focused gas escape from the subsurface. This is shown in the seismic section in Fig. 6 (Lat: 54.90° N Long: 13.61° E), where a subtle 1 m deep depression in the seafloor of slightly elongated shape with a maximum diameter of ~ 120 m is associated with a strong, but reversed polarity seafloor return and structural disturbance beneath. This indicates the actual presence of free gas at the seabed, as the phase reversal is a result of the decrease of bulk density and/or seismic velocity in the gas-charged sediment. The pockmark is surrounded with high amplitude seafloor reflection on both sides forming a few hundred meter wide ring (data not shown). The deeper one of the double reflector near the seafloor represents the top of the gas-charged sediment layer. A further distinct reflector with reversed polarity appears at 23 ms TWT b.s.f. (two way travel time below seafloor) and at 44 ms TWT b.s.f., a strong reflection marks a density/velocity increase from glacial clay to compacted till or Cretaceous basement. Evident is the structural disturbance in the vicinity of the pockmark, as well as a positive relief of a sedimentary unit between 78 and 88 ms TWT. Together with a potential fault system at 1100 m offset, we see typical indications for deeper gas migration (absence of reflections circular anomaly, anomalous sedimentary unit), which distinctly differs from the typical appearance of shallow gas elsewhere in the Baltic Sea.

TF0113 is located only 6.5 nautical miles apart from this feature and, in combination with the recorded sea

level, we suggest a pressure-induced seepage event (Wever et al., 2006; Schneider v. Deimling et al., 2010) to have caused extraordinarily high methane values in the entire water column. It can be assumed that the oscillation of the sea level and the resulting sudden pressure drop lead to the abrupt transition of dissolved (pore water) methane into free gas followed by ebullition of free gas to the water column, or by a pressure-induced (amplified by wind and waves) pumping impulse on the pore water of the sediment and thus, seepage of methane-enriched water to the water column. For the situation at station TF0113, both mechanisms would produce the same signal with the observed enhanced but uniform distribution of methane due to the almost complete mixing of the water column (Fig. 5). In contrast, gas transport and advection/diffusion of dissolved methane can be clearly distinguished in waters with a density stratification which greatly reduces diapycnal mixing of the water and thus, the vertical transport of dissolved constituents, while not hindering gas bubble mediated transport (Schneider v. Deimling et al., 2011).

3.4 Seasonal patterns of CH₄ concentration and oversaturation in the main basins of the Baltic Sea

The annual cycles of surface methane concentration and oversaturation show some distinct seasonal trends in the individual basins, which in the following sections are discussed in the framework of the key controlling parameters, e.g. sea surface temperature, mixing depth, sea–air exchange, and potential direct connection of the upper water body to the sediment (Fig. 7, Table 1).

3.4.1 Water temperature

The average sea surface temperature of the Baltic Sea ranged from 0 °C in February to almost 23 °C in July in 2010 with strong regional differences (Fig. 7, red lines). Strongest fluctuations of sea surface temperature were observed in the area of the Gulf of Finland with widespread ice-coverage during February and March. Highest surface temperatures in the Gulf of Finland were measured in July reaching up to 24 °C.

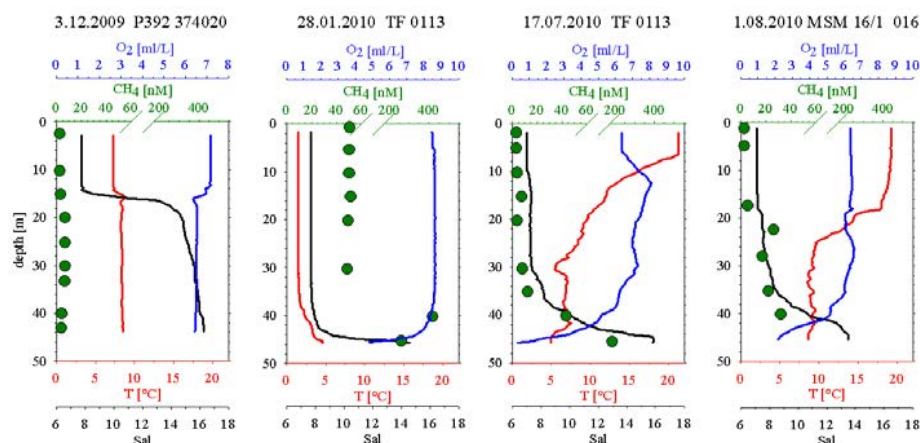


Fig. 5. Data of water column properties and methane concentration of profile at station TF0113 taken during four cruises in December 2009 (*Poseidon* P392), January 2010 (*Heincke* 06HK 1001), July 2010 (*Alkor* 06 AK1003) and (*Maria S. Merian* MSM 16/1). Methane concentration (green dots), temperature (red line), salinity (black line) and oxygen values (blue line). The sampling dates of the profile are marked as well in time scale of the subplot AB in Fig. 7.

Sea surface temperature of the Gotland Basin (GB) ranges from 4 °C to 21 °C in comparison. The rise in temperature mainly takes place between early April and July. During this period, a continuous increase in methane saturation was observed (Fig. 7, black broken line) in all basins.

The temperature strongly influence the methane solubility in water and seawater, in which on average 2.4 % less methane can be dissolved for each degree of temperature rise (Wiesenburg and Guinasso, 1979). Thus, a water mass which is warmed will be increasingly oversaturated with respect to the atmosphere without an increase in the absolute concentration, in accordance to our observations. However, the induced oversaturation will stimulate the transfer of methane to the atmosphere (see Sect. 3.5 and Fig. 8).

The warming of the sea surface beginning in April leads to the warming of parts of the water column below, and can also cause warming of the sediments, especially in shallow regions with a temporarily well-mixed water column. The water temperature observed near the sea bottom is used as a proxy for the temperature of the sediment surface. Bottom water temperatures in the Arkona Basin, for example, show annual fluctuation between -0.32 °C (minimum) and 15.6 °C (maximum; ICES, 2011). In deeper basins the annual fluctuation of the surface sediment temperature can be expected to be much smaller than the fluctuations at the sea surface (Mogollón et al., 2011). The sediment temperature influence the solubility of methane in pore water and the depth of the shallow gas boundary layer (Wever et al., 2006). With the warming of the sediment it can be expected, that less methane is solved in the pore water and saturated pore waters might get oversaturated, resulting in a lower depth of the free gas boundary layer or in an increased emission rate of sedimentary methane towards the water column. Further,

temperature is a key control for the production of methane by methanogenic microbes (Heyer and Berger, 2000).

3.4.2 Stratification

The Baltic Sea can be distinguished in areas with permanent (e.g. GB) and temporal stratification (e.g. AB, GoF; Feistel et al., 2008). The warming of the surface water layers lead to a stratification of the water column and the formation of the temporal thermocline during the summer months. The stratification beginning in April, separates the water column above the permanent halocline (where existent) into two sublayers with different physical properties, the lower one mostly defined by the winter surface water generated during maximum mixing depth in winter. Like the halocline, the thermocline reduces vertical mixing and the methane transport in particular between the deep water masses and sediment to the surface water. The deeper bottom layers, disconnected from the surface, start to get enriched in methane due to the steady supply of methane from the seabed or the methane-enriched water below the halocline. In contrast, the surface water gets depleted in methane due to loss to the atmosphere by sea–air exchange, in part driven by the temperature-induced decreasing solubility.

3.4.3 Wind, mixing depth, and sea–air exchange

The sustainability of the stratification of the water column depends on the annual changing wind energy and the resulting mixing intensity and the temperature-gradient-driven heat exchange. In general, wind velocities in the Baltic Sea are higher during the winter season and lower during the summer months. As a consequence, the depth of the mixed layer is shoaling until midsummer, leading to the formation of water layers with different properties (including methane

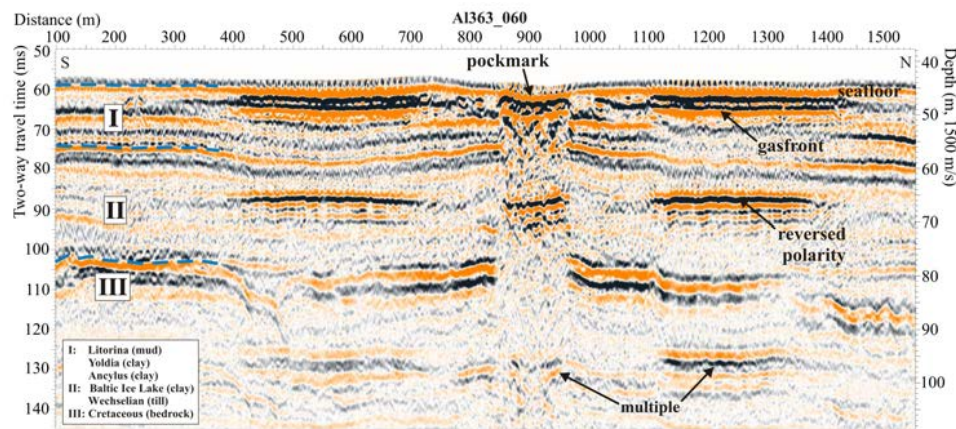


Fig. 6. Multichannel seismic profile showing a pockmark and its vicinity in the Arkona Basin. The seismic section is running from south (Lat: 54.90° N, Long: 13.61° E) to north (Lat: 54.91° N, Long: 13.61° E). The presence of free gas beneath the seabed is indicated by the reversed polarity compared to the normal polarity of the seafloor outside the pockmark. The blue lines indicate layer boundaries.

After reaching a minimum in the summer, the mixing depth deepens again by wind stirring and thermal convection until it reaches its maximum in winter (Fig. 7, blue lines). In the shallower and not permanently stratified basins, this can lead to occasional complete homogenization of the water column.

The wind speed also controls the gas transfer velocity k (which in this work scales with u^2 ; Eq. (3), Wanninkhof et al., 2009), and the air–sea exchange of methane (see Sect. 2.5). Figure 9 shows k , which is low from April till July (main warming of the sea surface) and increases in mid-summer. A higher transfer velocity fosters the relaxation of the disequilibrium between surface water concentrations and atmospheric equilibrium. The mixing depth determines the thickness of the water body from which a net sea–air flux can be sustained. Thus, at a given k , relaxation towards methane equilibrium increases with increasing mixing depth.

3.4.4 Methane concentrations according to seasonal changes

The patterns of sea surface methane during 2010 in the different sub-basins result from the combination of the influencing parameters temperature and wind with the conveyed controls of mixing depth, stratification and change of the gas transfer velocity as described above. In spite of data gaps due to maintenance problems of the measuring system in April/May, the general trend of the surface methane distribution can be perceived and is confirmed by measurements of the year 2011 (data not shown). The combination of the controlling factors result in distinct patterns of oversaturation and methane flux into the atmosphere in different sub-regions of the Baltic, in particular contrasting areas with at least occasional interaction between the sediment, deeper water and surface water (e.g. MB, AB), and areas with a permanent decoupling of

presence of free gas beneath the seabed is indicated by the reversed polarity compared to the normal polarity of

concentrations. After reaching a minimum in the summer, the mixing depth deepens again by wind stirring and thermal convection until it reaches its maximum in winter (Fig. 7, blue lines). In the shallower and not permanently stratified basins, this can lead to occasional complete homogenization of the water column.

The winter period January–March is characterized by low sea surface temperatures and high wind velocities. Highest measured methane concentrations were recorded during this winter period especially in the regions of Arkona Basin, Bornholm Basin and Gulf of Finland (Fig. 7, green dots, and three day average: black solid line) with maximum values in January and declining concentrations towards March (with the exception of the GoF, see below). A high wind-induced energy input to the water column in combination with cooling from the atmosphere results in a maximum mixing depth and the mixing of the entire water column down to the sediment in some of the regions of the Baltic Sea, except for regions with a permanent halocline (e.g. GB). The intense mixing accelerates the transport of methane from the sediment to the sea surface. Enhanced transport from the bottom layer and sediment surface into the water column can occur in completely unstratified conditions because of enhanced shear stress at the sediment–water interface. On the contrary, strong wind forces enhance the gas transfer velocity at the air–sea boundary, leading to an overall decrease of methane in the surface water later in winter (Fig. 7, green dots and black solid line).

During the period from early April till July/August, sea surface temperatures increase in all regions of the Baltic Sea (Fig. 7, red lines) and the mixing depth decreases with the development of the thermocline and summer stratification (Fig. 7, blue lines). In general, the stratification of the water column hampers the methane transport between deeper layers and the sea surface in the Baltic Sea (Schmale et al., 2010). The temperature-driven solubility decrease leads to an increase in methane saturation values in all regions of the Baltic Sea (Fig. 7, black broken lines), which could account for up to approximately 50 % of additional methane saturation, assuming a temperature

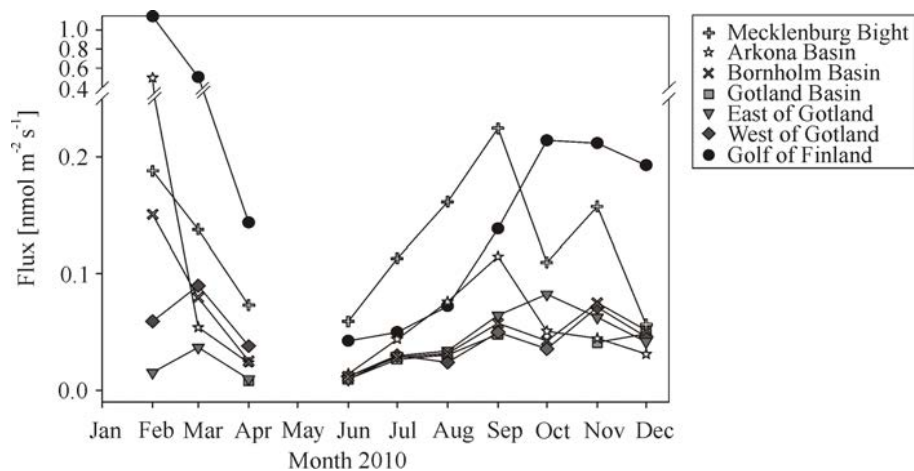


Fig. 8. Methane fluxes F ($\text{nmol m}^{-2} \text{s}^{-1}$) calculated as monthly average for selected areas of the Baltic Sea using the equation described in Wanninkhof et al. (2009). Atmospheric methane data from the NOAA station in Poland were used for the calculation of the equilibrium concentration.

in Poland were used for the calculation of the equilibrium concentration.

After its maximum in August, sea surface temperature starts to decrease around September (Fig. 7, red lines), causing an increase in the solubility of methane in the water. Winds intensify, resulting in deeper mixing of the water column. With increasing mixing depth, water layers with elevated methane content are mixed to the surface, increasing the surface methane concentrations. For this period, strong regional differences of the methane saturation can be pointed out between the shallow regions (MB and AB) and the deeper regions of the Baltic Sea, e.g. Gotland Basin or Gulf of Finland. In the deeper basins (e.g. GB, BB, WoG, GoF), the deepening of the mixed layer leads to entrainment of methane-enriched deeper waters into the surface layer, increasing methane concentrations. Despite the deepening of the mixing depth in the Gotland Basin, the stratification of the water column sustains, and the deep water volume with high methane values as described in Schmale et al. (2010) is not mixed to the surface. Cooling of the mixed layer partly dampens the effect of increasing concentrations on the oversaturation. The latter, in connection to enhanced wind speeds (and thus transfer velocities) lead to enhanced flux towards the atmosphere (see Sect. 3.5). Interestingly, the net result of these co-acting processes for Bornholm Basin, West of Gotland and Gotland Basin is an increase in concentrations in connection to an increase in oversaturation until the end of the year.

The Gulf of Finland generally follows a similar trend, but methane concentrations increase more strongly and oversaturation increases steadily towards the end of the year with increasing mixing depth. This is consistent with the finding that the sub-thermocline waters in the Gulf of Finland are more enriched in methane than in the other central basins addressed above (Schmale et al., 2010). Another interesting finding is that the highest concentrations and levels of over-

saturation are found in February/March, though the maximum mixing depth has been reached before, an effect of partial ice coverage. We assume that methane concentrations and saturation values of more than 200 % in this region in late winter indicate methane accumulations in the water column under the ice cover (Berger and Heyer, 1990) which result in elevated emission rates (discussed below) in ice free areas of the Gulf of Finland due to the main water currents along the coast (Alenius et al., 2009). However, the influence of ice coverage on sea surface methane concentrations in the Gulf of Finland needs to be investigated in more detail in the future.

An exception from these annual patterns of methane surface concentration and oversaturation occurs in the very shallow area of the Mecklenburg Bight and, to a lesser extent, the Arkona Basin. In both basins, methane oversaturation strongly follows the trend of sea surface temperature. In the Mecklenburg Bight, methane concentrations increase during the summer, reaching a maximum in August and leading to the high saturation value of 290 % (Fig. 7). We suggest that wind-induced mixing remains relevant for the transport of methane from the sediment and that summer stratification is neither capable nor sufficient to suppress the methane transport from the sediment to the sea surface in these shallow basins for longer time scales. The observed high fluctuation in methane concentrations throughout the year (MB, Fig. 7, green dots) can be related to short-time wind events with enhanced mixing of the water column. Additionally, the importance of boundary mixing is enhanced and the volume of water below the thermocline will always be small in relation to the volume of the mixed surface layer in MB. As a consequence, no build up of a large methane inventory can counteract the annual variation of solubility by temperature changes, which is mirrored in the parallel trends of sea

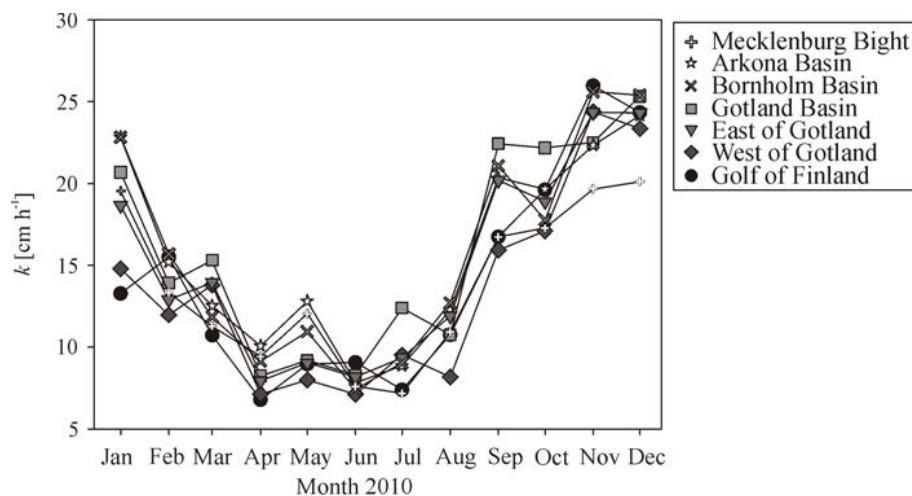


Fig. 9. Transfer velocity k during 2010 for selected areas of the Baltic Sea with $k = 0.24 u^2$ after Wanninkhof et al. (2009); whereas u is defined as daily average wind speed in m s^{-1} .

surface temperature and methane saturation. However, the amplitude of the seasonal trend is far too large to be caused by the temperature effect alone, even considering the reduced sea–air exchange from spring to summer. Apparently, the source strength for methane into the waters of the Mecklenburg Bight is modulated by sediment temperature. The variation of water temperature at sea bottom from 0 °C to above 15 °C (ICES, 2011) is comparable to sea surface temperature changes (Fig. 7). Potential consequences are increased microbial methanogenesis due to increasing sediment temperatures as well as higher methane emissions from the sediment to the water column (Heyer and Berger, 1990, 2000), because of the solubility effect on pore waters and shallow gas accumulations.

The Arkona Basin can be characterized as an intermediate between shallow regions like the Mecklenburg Bight and deeper regions like the Bornholm Basin or Gulf of Finland. The Arkona Basin is deeper than the Mecklenburg Bight and therefore the direct influence of the sediment and bottom water towards the surface layer as described above is assumed to be less dominant than in the Mecklenburg Bight, resulting in lower methane saturation values not exceeding 160 % in August (Fig. 7, black broken line). It is notable, that the maximum methane saturation value in the Arkona Basin is reached later than in the Mecklenburg Bight, and that the duration of this peak is longer (several weeks) than in the Mecklenburg Bight (couple of days). Accordingly, the mixing depth increases during this period by more than 10 m (August–September) until it reaches the bottom layer and the sediment in November. Similar to the Mecklenburg Bight but little delayed in time, saturation values start to decrease in September according to the temperature-induced solubility effect until lowest saturation values are reached by December. This leads to the assumption that no methane reservoir could be established in the water column of the Arkona Basin

like in the Bornholm Basin or Gulf of Finland, where saturation values remain elevated until the following spring season. Comparing the volume of water below the thermocline of shallow regions like the Mecklenburg Bight to deeper regions like the Bornholm Basin or Gulf of Finland, deeper basins contain a much larger volume of water, implying a larger methane-enriched reservoir which can be mixed to the surface. It is remarkable that the three day average of methane concentration (Fig. 7, black solid line) in the Arkona Basin shows almost constant methane values in the surface water from April until December. That shows the intermediate character of the Arkona Basin, being between the deeper basins with methane concentration minima in summer and the shallow region of the Mecklenburg Bight with maximum concentrations during this period.

A basic proof of concept for our interpretation of the processes after the peak of the summer stratification based on a mass balance approach is given in Sect. 3.6 for the Arkona Basin.

3.5 Flux – methane emissions to the atmosphere

Our data show that the Baltic Sea remains a source for atmospheric methane with a positive sea–air methane flux throughout the year in all regions (Fig. 8). Average wind speeds and thus, transfer velocities, show a similar pattern for all areas in the Baltic Sea, with decreasing values during the spring period, very low values during the summer period, a sharp increase in August and persistent high values in fall and early winter. Figure 9 shows calculated transfer velocities k (after Wanninkhof et al., 2009) for methane in the Baltic Sea for selected areas in 2010.

Methane fluxes during the period from April to August remain in generally low, ranging from 0.008 to 0.162 $\text{nmol m}^{-2} \text{s}^{-1}$ in comparison to the period

September–November with fluxes ranging from 0.036 to $0.225 \text{ nmol m}^{-2} \text{ s}^{-1}$ (Fig. 8). The general increase of methane fluxes from June–August can be explained with the temperature induced solubility effect and the resulting increasing methane oversaturation in combination with a relatively low and uniform average gas transfer coefficient. All basins show a considerable increase in the calculated methane flux in August (Fig. 8) as a consequence of the transition to the regime of high wind velocities (see k , Fig. 9).

Beginning in October, strong differences in the general flux distribution occur, with decreasing values in the Mecklenburg Bight and Arkona Basin compared to relatively stable or increasing values in deeper regions like Bornholm Basin, West of Gotland, East of Gotland, or Gulf of Finland, a consequence of the regional differences in the seasonal development of methane oversaturation as discussed in Sect. 3.4. Whereas fluxes in the areas of the Bornholm Basin, Gotland Basin and around the island of Gotland show a very similar pattern, fluxes in the area of the Mecklenburg Bight and the Gulf of Finland deviate significantly. The Mecklenburg Bight shows generally elevated methane fluxes compared to the Arkona Basin, Bornholm Basin, Gotland Basin, West of Gotland, and East of Gotland, and significantly outstanding methane fluxes during the period of June–September. This can be explained by the mechanisms causing increasing surface water concentrations until late summer discussed in Sect. 3.4, leading to increasing emission rates to the atmosphere. Methane fluxes in the Mecklenburg Bight drop from $0.225 \text{ nmol m}^{-2} \text{ s}^{-1}$ in September to $0.108 \text{ nmol m}^{-2} \text{ s}^{-1}$ (Fig. 8) in October and further on until December despite of an increase of k , again mirroring the (here decreasing) trend in sea surface methane concentration during this period. For the deeper basins, the constantly high average transfer velocities in combination with the relatively stable oversaturation sustained by mixed layer deepening lead to the stable enhanced methane sea–air fluxes from September until the end of the year (Fig. 8, BB, GB, WoG, EoG). The Arkona Basin is considered as an intermediate between the very shallow Mecklenburg Bight and the deeper basins. Here, a methane flux of $0.497 \text{ nmol m}^{-2} \text{ s}^{-1}$ in February might have been caused by the described seepage event in the Arkona Basin (see also Sect. 3.3). The Gulf of Finland shows comparable high flux values throughout the year (Fig. 8). Gassy sediments and temporal anoxic conditions in bottom layers of the Gulf of Finland during the summer period (Alenius et al., 1998) result in high amounts of methane (dissolved in the deeper layers), which are mixed to the surface in autumn and winter. The origin of extraordinary methane fluxes of $1.145 \text{ nmol m}^{-2} \text{ s}^{-1}$ and $0.506 \text{ nmol m}^{-2} \text{ s}^{-1}$ in February and March, respectively, have to be regarded with caution because of the potential role of sea ice. The ice coverage starts at the Finnish coast line of the Gulf of Finland in January and reaches its largest expansion during March (data not shown, Swedish Meteorological and Hydrological Institute, SMHI). During the pe-

riod of ice coverage no or very limited sea–air exchange of methane can be expected. Nevertheless, the southwestern part of the Gulf of Finland remained principally ice free during the winter period in 2010 just as the main ship traffic route of Helsinki (SMHI). Here, changing conditions of drifting ice shields with suppressed sea–air exchange and open water with high dissolved methane concentrations in the surface water (Fig. 2) as well as high wind speeds and transfer velocities (Fig. 9) can be assumed to influence methane fluxes to the atmosphere significantly but will need further investigation.

For the area of the Gotland Basin very low monthly averaged sea–air fluxes with $0.0008 \text{ nmol m}^{-2} \text{ s}^{-1}$ in December 2009 (data not shown) and $0.008 \text{ nmol m}^{-2} \text{ s}^{-1}$ in April 2010 were calculated (Fig. 8). Looking at averaged methane saturation values of single lines crossing the Gotland Basin in April, values of 96 % saturation with respect to the atmosphere were calculated. Observations in 2011 show saturation values of 94 % in February and April (data not shown), indicating that during the period December–April the direction of the net flux for methane might change frequently in the Gotland Basin. However, this occasional undersaturation of methane can be explained by the enhanced solubility of methane at lower temperatures and has only little effect on the general flux trend in this region.

Bange et al. (1994) calculated methane sea–air fluxes during July/August to be $1.17\text{--}13.9 \text{ nmol m}^{-2} \text{ s}^{-1}$ and $0.11\text{--}0.17 \text{ nmol m}^{-2} \text{ s}^{-1}$ during February, indicating a larger flux during summer than during winter. Their flux estimates are based on results of atmospheric and dissolved methane concentrations determined using an automated gas chromatographic system during two Baltic cruises (Southern Belt Sea, AB, BB, GB) in February 1992 (63 stations) and July/August 1992 (23 stations) following Liss and Merlivat (1986). The large data set underlying the flux estimations presented here provides monthly mean methane fluxes for the whole year 2010. Methane fluxes in February and July/August amounted to $0.151\text{--}0.080 \text{ nmol m}^{-2} \text{ s}^{-1}$ and $0.010\text{--}0.076 \text{ nmol m}^{-2} \text{ s}^{-1}$ for the Arkona Sea, Bornholm Sea and Gotland Sea. The summer fluxes calculated here are significantly lower than those presented by Bange et al. (1994). General seasonal changes of methane saturations with low values during winter (e.g. 107 % BB) and higher values during summer (e.g. 157 % BB) could be confirmed in this study (e.g. 116 % February – 134 % July/August, BB). Still, averaged methane supersaturation values of 3757 % based on measurements at two stations during the summer sampling campaigns by Bange and coworkers disagree with results presented in this study, showing averaged methane saturation values of 290 % for the Mecklenburg Bight for July and August. We therefore assume that estimated summer fluxes were overestimated by Bange et al. (1994). Further, Fig. 8 shows that the seasonality of methane fluxes is characterized by maximum values during winter and lowest values during summer for the Baltic Sea.

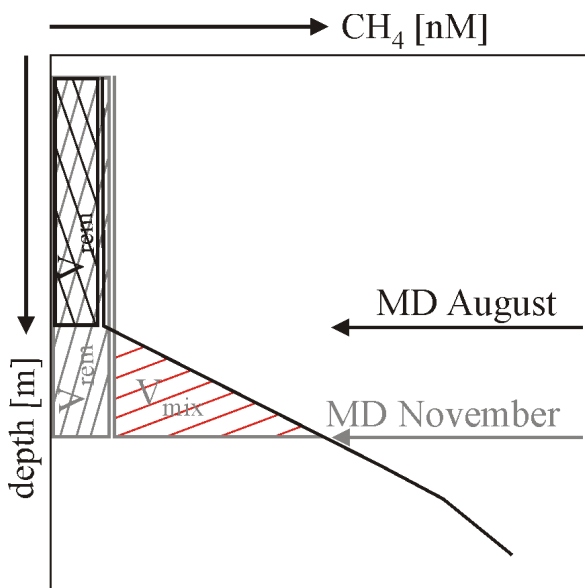


Fig. 10. Scheme illustrating a methane concentration profile (black solid line) in August and the deepening of the mixing depth (MD) from August (black arrow) to November (grey arrow). The amount of dissolved methane remaining in the homogeneous mixed upper water column V_{rem} is estimated according to the surface methane concentration measured in August and November, respectively. The amount of dissolved methane V_{mix} is mixed into the upper water column during the period August–November.

3.6 Methane mass balance during the period of mixed layer deepening

As proof of concept, a rough methane mass balance for the development of the methane concentration in the mixed layer, the water below and the sea–air flux for the period of mixed layer deepening has been calculated using the water column methane profile of station TF0113 (1.8.2010, AB, Fig. 5) as starting condition. A scheme illustrating the approach is given in Fig. 10, showing a simplified methane concentration profile of the water column and the mixing depth for August and November. The amount of methane remaining in the upper water column V_{rem} is estimated based on sea surface methane concentrations in August and November assuming a homogeneous upper water column. V_{mix} illustrates the amount of methane, which is mixed into the upper water column during the period August–November. Based on methane profile TF0113 and the model-derived mixing depth (see Sect. 2), V_{mix} is approximated to be 203 μmol and can be compared to the flux of 303 μmol during the period August–November. The rough mass balance shows that the deepening of the mixing depth causes significant entrainment of methane into the upper water column and accounts for elevated methane saturation values during the period August–September as described in Sect. 3.4. A model-based

estimation of sea–air exchange of methane as described in Bange (2004) was not attempted at this point due to the lack of available time series of water column methane concentration profile of the Baltic Sea in the period of August to November 2010.

4 Conclusions

The first year of successful, continuous, and autonomous measurements of methane in the surface water of the Baltic Sea shows large regional and seasonal variations, influenced by a series of parameters. Processes controlling methane distributions in the surface water were identified on various temporal and spatial scales. In the area around the island of Gotland several upwelling events could be observed, elevating the local methane concentration in the surface water. Elevated methane concentrations in the surface water and water column of the Arkona Basin in February 2010 with up to 832 % oversaturation could be related to a longer period of strong winds, resulting in a potential pressure-induced gas release from the underlying methane-bearing upper sediments. Upwelling, seepage or wind events develop on a rather short temporal and spatial scale; yet such events influence local methane distributions significantly. Temporal stratification and low mixing depths of the water column of the Baltic Sea occur on a longer time scale and inhibit methane transport from methane-enriched deeper water layers to the sea surface during summer. Thus, especially in deeper regions like Bornholm Basin and Gulf of Finland a methane reservoir is formed during the summer period, which is partly mixed to the surface from the beginning of autumn, leading to elevated methane concentrations for several months. Stratification in shallower regions like the Mecklenburg Bight is less dominant and no methane reservoir in deeper water persisting of longer periods of time can establish. We suggest that these regions are rather influenced by microbial methanogenesis in the sediment and emission of methane into the water column, short-time wind events and reduced solubility of methane by higher water temperatures during summer.

The Baltic Sea is a source of atmospheric methane with high emission values during the winter season ($0.015\text{--}1.145\text{ nmol m}^{-2}\text{ s}^{-1}$) and low emissions during the spring and summer seasons ($0.008\text{--}0.162\text{ nmol m}^{-2}\text{ s}^{-1}$). Parameters controlling the methane fluxes alternate during the seasons depending on the region. Methane fluxes in shallow regions like the Mecklenburg Bight ($0.057\text{--}0.225\text{ nmol m}^{-2}\text{ s}^{-1}$) are higher compared to deeper regions like the Gotland Basin ($0.008\text{--}0.049\text{ nmol m}^{-2}\text{ s}^{-1}$) and show significant changes during the seasons in connection with temperature-driven methane solubility changes and methanogenesis in the sediment. Methane fluxes in areas with a permanent stratification like the Gotland Basin were found to be less variable during the year and mostly

influence by temperature-induced solubility and annual development of the mixed layer. Highest methane fluxes were derived for the Gulf of Finland in February 2010 with $1.145 \text{ nmol m}^{-2} \text{ s}^{-1}$. Here the influence of changing ice coverage needs to be investigated in more detail in the future.

The general seasonal trend of the surface water methane distribution in the Baltic Sea presented in this study could be confirmed by interannual patterns recorded in 2011. Interannual changes will be presented elsewhere once more data become available.

Acknowledgement. The research leading to these results has received funding from the European Community's Seventh Framework Programme (FP7/2007–2013) under grant agreement Nr. 217246 made with the joint Baltic Sea research and development program BONUS. The Swedish Meteorological and Hydrological Institute (SMHI) is acknowledged for providing data on river runoff to the Baltic Sea and sea level records at Kungsvik. Provision of COSMO/EU data for the Baltic Sea region by German Weather Service is appreciated. The National Oceanic and Atmospheric Administration (NOAA) is acknowledged for providing atmospheric methane data. We appreciate the cooperation with Seppo Kaitala (Algaline project leader) of the Finnish Environment Institute (SYKE) Helsinki and the ferry line company Finnlines. We gratefully acknowledge the technical support of Bernd Sadkowiak and Heiko Witt (IOW).

Edited by: S. W. A. Naqvi

References

- Abril, G. and Iversen, N.: Methane dynamics in a shallow non-tidal estuary (Randers Fjord, Denmark), *Mar. Ecol.-Prog. Ser.*, 230, 171–181, 2002.
- Alenius, P., Myrberg, K., and Nekrasov, A.: The physical oceanography of the Gulf of Finland: a review, *Boreal Environ. Res.*, 3, 97–125, 1998.
- Bange, H. W., Bergmann, K., Hansen, H. P., Kock, A., Koppe, R., Malien, F., and Ostrau, C.: Dissolved methane during hypoxic events at the Boknis Eck time series station (Eckernförde Bay, SW Baltic Sea), *Biogeosciences*, 7, 1279–1284, doi:10.5194/bg-7-1279-2010, 2010.
- Bange, H. W.: Nitrous oxide and methane in European coastal waters, *Estuar. Coast. Shelf S.*, 70, 361–374, 2006.
- Bange, H. W.: Air-sea exchange of nitrous oxide and methane in the Arabian Sea: A simple model of the seasonal variability, *Indian J. Mar. Sci.*, 33, 77–83, 2004.
- Bange, H. W., Bartell, U. H., Rapsomanikis, S., and Andreae, M. O.: Methane in the Baltic and North Seas and a reassessment of the marine emissions of methane, *Global Biogeochem. Cy.*, 8, 465–480, 1994.
- Bange, H. W., Dahlke, S., Ramesh, R., Meyer-Reil, L. A., Rapsomanikis, S., and Andreae, M. O.: Seasonal study of methane and nitrous oxide in the coastal waters of the Southern Baltic Sea, *Estuar. Coast. Shelf S.*, 47, 807–817, 1998.
- Bates, T. S., Kelly, K. C., Johnson, J. E., and Gammon R. H.: A reevaluation of the open ocean source of methane to the atmosphere, *J. Geophys. Res.*, 101, 6953–6961, 1996.
- Berger, U. and Heyer, J.: Distribution and activity of methanotrophic bacteria in a brackish water ecosystem, *Limnologia*, 8, 141–144, 1990.
- Beljaars, A. C. M.: The parameterization of surface fluxes in large-scale models under free convection, *Q. J. Roy. Meteor. Soc.*, 121, 255–270, 1994.
- Boetius, A., Ravensschlag, K., Schubert, C. J., Rickert, D., Widdel, F., Gieseke, A., Amann, R., Jorgensen, B. B., Witte, U., and Pfannkuche, O.: A marine microbial consortium apparently mediating anaerobic oxidation of methane, *Nature*, 407, 623–626, 2000.
- Bussmann, I. and Suess, E.: Groundwater seepage in Eckernförde Bay (Western Baltic Sea): effect on methane and salinity distribution of the water column, *Cont. Shelf Res.*, 18, 1795–1806, 1998.
- Butler, J., Elkins, L. W., Brunson, C. M., Thompson, T. M., and Hall, B. D.: Trace Gases in and over the west pacific and east indian oceans during the El Niño southern oscillation event of 1987, *J. Geophys. Res.*, 94, 865–877, 1989.
- COSMO: Core documentation of the COSMO-model, available at: <http://www.cosmo-model.org/content/model/documentation/core/default.htm>, last access: 17 December 2012.
- Dando, P. R., Bussmann, I., Niven, S. J., O'Hara, S. C. M., Schmaljohann, R., and Taylor, L. J.: A methane seep area in the Skagerrak, the habitat of the pogonophore *Siboglinium poseidoni* and the bivalve mollusc *Thyasira sarsi*, *Mar. Ecol. Prog.-Ser.* 107, 157–167, 1994.
- DeAngelis, M. A. and Lee, C.: Methane production during zooplankton grazing on marine phytoplankton, *Limnol. Oceanogr.*, 39, 1298–1308, 1994.
- Drugokencky, E. J., Lang, P. M., and Masarie, K. A.: Atmospheric Methane Dry Air Mole Fractions from the NOAA ESRL Carbon Cycle Cooperative Global Air Sampling Network, 1983–2010, Version: 2011-08-11, 2011.
- Feistel, R., Nausch, G., and Wasmund, N.: State and Evolution of the Baltic Sea, 1952–2005: A Detailed 50-Year Survey of Meteorology and Climate, Physics, Chemistry Biology and Marine Environment, John Wiley and Sons, Inc., Hoboken, New Jersey, 2008.
- Grasshoff, K., Kremling, K., and Ehrhardt, M.: Methods of seawater analysis, 3rd Edn., Verlag Chemie, Gulf Publishing Houston, 1999.
- Griffies, S. M., Harrison, M. J., Pacanowski, R. C., and Rosati, A.: A technical guide to MOM4. GFDL Ocean Group Technical Report No. 5, Geophysical Fluid Dynamics Laboratory, Princeton, 342 pp., 2004.
- Grunwald, M., Dellwig, O., Beck, M., Dippner, J. W., Freund, J. A., Kohlmeier, C., Schnetger, B., and Brumsack, H.-J.: Methane in the southern North Sea: sources, spatial distribution and budgets, *Estuar. Coast. Shelf S.*, 81, 445–456, 2009.
- Gülzow, W., Rehder, G., Schneider, B., Schneider v. Deimling, J., and Sadkowiak, B.: A new method for continuous measurement of methane and carbon dioxide in surface waters using off-axis integrated cavity output spectroscopy (ICOS): an example from the Baltic Sea, *Limnol. Oceanogr.-Meth.*, 9, 176–184, 2011.

- Heyer, J. and Berger, U.: Methane emission from the coastal area in the southern Baltic Sea, *Estuar. Coast. Shelf S.*, 51, 13–30, 2000.
- Heyer, J., Berger, U., and Suckow, R.: Methanogenesis in different parts of a brackish water ecosystem, *Limnologia*, 20, 135–139, 1990.
- Heyer, J., Berger, U., Kuzin, I. L., and Yakovlev, O. N.: Methane emissions from different ecosystem structures of the subarctic tundra in Western Siberia during midsummer and during the thawing period, *Tellus B*, 54, 231–249, 2002.
- ICES (Oceanographic Database and Services): International Council for the Exploration of the Sea, <http://ocean.ices.dk/helcom>, last access: November 2011.
- Jähne, B., Heinz, G., and Dietrich, W.: Measurement of the diffusion coefficient of sparingly soluble gases in water, *J. Geophys. Res.*, 92, 10767–10776, 1987.
- Janssen, F., Schrumm, C., and Backhaus, J. O.: A climatological dataset of temperature and salinity for the North Sea and the Baltic Sea, *Dt. Hydrogr. Zs., Supplement* 9, 245 pp., 1999.
- Karl, D. M. and Tilbrook, B. D.: Production and transport of methane in oceanic particulate organic matter, *Nature*, 368, 732–734, 1994.
- Karl, D. M., Beversdorf, L., Björkman, K. M., Church, M. J., Martinez, A., and DeLong, E. F.: Aerobic production of methane in the sea, *Nature Geosci.*, 1, 473–478, 2008.
- Keir, R., Schmale, O., Seifert, R., and Sültenfuß, J.: Isotope fractionation and mixing in methane plumes from the logatchev hydrothermal field *Geochem. Geophys. Geosyst.*, 10, 1–19, doi:10.1029/2009GC002403, 2009.
- Körtzinger, A., Thomas, H., Schneider, B., Gronau, N., Mintrop, L., and Duiker, J. C.: At-Sea intercomparison of two newly designed underway $p\text{CO}_2$ system-encouraging results, *Mar. Chem.*, 52, 133–145, 1996.
- Laier, T. and Jensen, J.: Shallow gas depth-contour map of the Skagerrak-Western Baltic Sea region, *Geo.-Mar. Lett.*, 27, 127–141, 2007.
- Large, W., McWilliams, J., and Doney, S.: Oceanic vertical mixing: a review and a model with a nonlocal boundary layer parameterization, *Rev. Geophys.*, 32, 363–403, 1994.
- Lass, H. U., Mohrholz, V., Nausch, G., and Siegel, H.: On phosphate pumping into the surface layer of the eastern Gotland Basin by upwelling, *J. Marine Syst.*, 80, 71–89, 2010.
- Leuenberger, D.: Statistical analysis of high-resolution COSMO Ensemble forecasts in view of Data Assimilation, 48 pp., Tech. Rep., edited by: Milelli, M., ARPA Piemonte Printed at Deutscher Wetterdienst, Offenbach, May, 2010.
- Lehmann, A. and Myrberg, K.: Upwelling in the Baltic Sea – a review, *J. Marine Syst.*, 74, S3–S12, 2008.
- Lips, I., Lips, U., and Liblik, T.: Consequences of coastal upwelling events on physical and chemical patterns in the central Gulf of Finland (Baltic Sea), *Cont. Shelf Res.*, 29, 1836–1847, 2009.
- Liss, P. S. and Merlivat, L.: Air-Sea Exchange Rates: Indruduction and Synthesis, Springer, New York, 113–127, 1986.
- Mathys, M., Thießen, O., Theilen, F., and Schmidt, M.: Seismic characterization of gas-rich near surface sediments in the Arkona Basin, Baltic Sea, *Mar. Geophys. Res.*, 26, 207–224, 2005.
- Mogollón, J. M., Dale, A. W., L'Heureux, I., and Regnier, P.: Impact of seasonal temperature and pressure changes on methane gas production, dissolution, and transport in unfractured sediments, *J. Geophys. Res.*, 116, G03031, doi:10.5194/bg-9-1915-2012, 2011.
- Nightingale, P. D., Malin, G., Law, C. S., Watson, A. J., Liss, P. S., Liddicoat, M. I., Boutin, J., and Upstill-Goddard, R. C.: In situ evaluation of air-sea gas exchange parameterizations using novel conservative and volatile tracers, *Global Biogeochem. Cy.*, 14, 373–387, 2000.
- Pimenov, N., Ulyanova, M. O., Kanapatsky, T. A., Veslopolova, E. F., Sigalevich, P. A., and Sivkov, V. V.: Microbially mediated methane and sulfur cycling in pockmark sediments of the Gdansk Basin, Baltic Sea, *Geo.-Mar. Lett.*, 30, 439–448, 2010.
- Rehder, G., Collier, R. W., Heeschen, K., Kosro, P. M., Barth, J. and Suess E.: Enhanced marine CH_4 emissions to the atmosphere off Oregon caused by coastal upwelling, *Global Biogeochem. Cy.*, 16, 11 pp., 2002.
- Reindl, A. and Bolalek, J.: Methane flux from sediment into near-bottom water in the coastal area of the Puck Bay (Southern Baltic), *Oceanol. Hydrobiol. St.*, 41, 40–47, 2012.
- Schmale, O., Schneider v. Deimling, J., Gülzow, W., Nausch, G., Wanek, J. J., and Rehder, G.: The distribution of methane in the water column of the Baltic Sea, *Geophys. Res. Lett.*, 37, L12604, doi:10.1029/2010GL043115, 2010.
- Schmale, O., Haeckel, M., and McGinnis, D. F.: Response of the Black Sea methane budget to massive short-term submarine inputs of methane, *Biogeosciences*, 8, 911–918, doi:10.5194/bg-8-911-2011, 2011.
- Schneider, B., Kaitala, S., and Maunula, P.: Identification and quantification of plankton bloom events in the Baltic Sea by continuous $p\text{CO}_2$ and chlorophyll-*a* measurements on a cargo ship, *J. Mar. Syst.*, 59, 238–248, 2006.
- Schneider v. Deimling, J., Greinert, J., Chapman, N. R., Rabbel, W., and Linke, P.: Acoustic imaging of natural gas seepage in the North Sea: sensing bubbles under control of variable currents, *Limnol. Oceanogr.-Meth.*, 8, 155–171, 2010.
- Schneider v. Deimling, J., Rehder, G., Greinert, J., McGinnis, D., Boetius, A., and Linke, P.: Quantification of seep-related methane gas emissions at Tommeliten, North Sea., *Cont. Shelf Res.*, 31, 867–878, doi:10.1016/j.csr.2011.02.012, 2011.
- Schulz, J.-P. and Schättler, U.: Kurze Beschreibung des Lokal-Modells LME und seiner Datenbanken auf dem Datenserver des DWD, Technical Report FE13, Deutscher Wetterdienst, Offenbach, 65 pp., 2005.
- Seifert, T.: Comparison of weather model data with station measurements, Internal Report, Institute for Baltic Sea Research, Warnemünde, 33 pp., 2010.
- Seifert, T., Tauber, F., and Kayser, B.: A high resolution spherical grid topography of the Baltic Sea-revised edition, Baltic Sea Science Congress, 25–29 November 2001, Stockholm, Sweden, Poster 147, available at: www.io-warnemuende.de/iowtopo (last access: December 2012), 2001.
- Siegel, H., Gerth, M., Rudloff, R., and Tschersich, G.: Dynamical features in the western Baltic Sea investigated by NOAA-AVHRR-Data, *Deutsche Hydrographische Zeitschrift*, 3, 191–209, 1994.
- Siegel, H., Seifert, T., Schernewski, G., Gerth, M., Reißmann, J., Ohde, T., and Podsetchine, V.: Discharge and transport processes along the German Baltic Sea, *Coast. Ocean. Dynam.*, 55, 47–66, 2005.

- Smagorinski, J.: General circulation experiments with the primitive equations: I. The basic experiment, *Mon. Weather Rev.*, 91, 99–164, 1963.
- Sweeney C., Gloor, E., Jacobson, A. R., Key, R. M., McKinley, G., Sarmiento, J. L., and Wanninkhof, R.: Constraining global air-sea gas exchange for CO₂ with recent bomb 14C measurements, *Global Biogeochem. Cy.*, 21, GB2015, doi:10.1029/2006GB002784, 2007.
- Thießen, O., Schmidt, M., Theilen, F., Schmitt, M., and Klein, G.: Methane formation and distribution of acoustic turbidity in organic-rich surface sediments in the Arkona Basin, Baltic Sea, *Cont. Shelf Res.*, 26, 2469–2483, 2006.
- Thomas, H. and Schneider, B.: The seasonal cycle of carbon dioxide in Baltic Sea surface waters, *J. Marine Syst.*, 22, 53–67, 1999.
- Thomas, S.: Vergleich und Optimierung analytischer Methoden zur Bestimmung des Methangehaltes in Seewasser, Diploma Thesis, University of Rostock, Institute for Chemistry Germany, 2011.
- Umlauf, L., Arneborg, L., Hofmeister, R., and Burchard, H.: Entrainment in shallow rotating gravity currents: a modeling study, *J. Phys. Oceanogr.*, 40, 1819–1834, 2010.
- Vahtera, E., Laanemets, J., Pavelson, J., Huttunen, M., and Kononen, K.: Effect of upwelling on the pelagic environment and bloom-forming cyanobacteria in the western Gulf of Finland, Baltic Sea, *J. Marine Syst.*, 58, 67–82, 2005.
- Wanninkhof, R.: Relationship Between wind speed and gas exchange over the ocean, *J. Geophys. Res.*, 97, 7373–7382, 1992.
- Wanninkhof, R., Asher, W. E., Ho, D. T., Sweeney, C., and McGillis, W. R.: Advances in quantifying air-sea gas exchange and environmental forcing, *Ann. Rev. Mar. Sci.*, 1, 213–244, 2009.
- Weiss, A., Kuss, J., Peters, G., and Schneider, B.: Evaluating transfer velocity-wind speed relationship using a long-term series of direct eddy correlation CO₂ flux measurements, *J. Marine Syst.*, 66, 130–139, 2007.
- Wever, T. F., Lühder, R., Vo, H., and Knispel, U.: Potential environmental control of free shallow gas in the seafloor of Eckernförde Bay, Germany, *Mar. Geol.*, 225, 1–4, 2006.
- Whiticar, M. J. and Faber, E.: Methane oxidation in sediment and water column environments – isotope evidence, *Org. Geochem.*, 10, 759–768, 1986.
- Wiesenburg, D. A. and Guinasso, N. L.: Equilibrium solubilities of methane, carbon monoxide, and hydrogen in water and sea water, *J. Chem. Eng. Data*, 24, 356–360, 1979.

Appendix B

A low frequency multibeam assessment: Spatial mapping of shallow gas by enhanced penetration and angular response anomaly

Jens Schneider von Deimling, Wilhelm Weinrebe, Zsuzsanna Tóth,
Henrik Fossing, Rudolf Endler, Gregor Rehder, Volkhard Spieß

Marine and Petroleum Geology 44 (2013) 217-222

<http://dx.doi.org/10.1016/j.marpetgeo.2013.02.013>

Reprinted with permission from Elsevier



A low frequency multibeam assessment: Spatial mapping of shallow gas by enhanced penetration and angular response anomaly



J. Schneider von Deimling^{a,b,*}, W. Weinrebe^a, Zs. Tóth^c, H. Fossing^d, R. Endler^b, G. Rehder^b, V. Spieß^c

^a Helmholtz Centre for Ocean Research (GEOMAR), Wischhofstr. 1–3, 24148 Kiel, Germany

^b Leibniz Institute for Baltic Sea Research Warnemünde (IOW), Seestr. 15, 18119 Rostock, Germany

^c University of Bremen, Department of Geosciences, Klagenfurter Str., 28359 Bremen, Germany

^d Aarhus University, Department of Bioscience, Vejlsvæj 25, DK-8600 Silkeborg, Denmark

ARTICLE INFO

Article history:

Received 11 August 2012

Received in revised form

15 November 2012

Accepted 23 February 2013

Available online 16 March 2013

Keywords:

Multibeam

Hydroacoustics

Methane

Shallow gas

Bubbles

Backscatter

Acoustic penetration

Baltic Sea

Angular response

ABSTRACT

This study highlights the potential of using a low frequency multibeam echosounder for detection and visualization of shallow gas occurring several meters beneath the seafloor. The presence of shallow gas was verified in the Bornholm Basin, Baltic Sea, at 80 m water depth with standard geochemical core analysis and hydroacoustic subbottom profiling. Successively, this area was surveyed with a 95 kHz and a 12 kHz multibeam echosounder (MBES). The bathymetric measurements with 12 kHz provided depth values systematically deeper by several meters compared to 95 kHz data. This observation was attributed to enhanced penetration of the low frequency signal energy into soft sediments. Consequently, the subbottom geoacoustic properties contributed highly to the measured backscattered signals. Those appeared up to 17 dB higher inside the shallow gas area compared to reference measurements outside and could be clearly linked to the shallow gas front depth down to 5 m below seafloor. No elevated backscatter was visible in 95 kHz MBES data, which in turn highlights the superior potential of low frequency MBES to image shallow sub-seafloor features. Small gas pockets could be resolved even on the outer swath (up to 65°). Strongly elevated backscattering from gassy areas occurred at large incidence angles and a high gas sensitivity of the MBES is further supported by an angular response analysis presented in this study. We conclude that the MBES together with subbottom profiling can be used as an efficient tool for spatial subbottom mapping in soft sediment environments.

© 2013 Elsevier Ltd. All rights reserved.

1. Introduction

Methane is considered the most important greenhouse gas on Earth after water vapor and CO₂. Recent studies suggest an even higher impact of CH₄ on global warming (Shindell et al., 2009) compared to earlier assumptions (Lelieveld et al., 1993). Marine methane has been reported to occur worldwide especially on the continental margins, in estuaries and river deltas, where the gas is often hosted in sediments a few decimeters to meters below the seafloor (Judd and Hovland, 2007). Global warming and eutrophication can accelerate natural seabed gas generation by enhancing organic matter accumulation which upon burial is converted to

methane. Gas generation and respective bubble formation have a strong impact on the structural integrity and load-bearing capabilities of the sediment (Briggs and Richardson, 1996). Therefore an understanding of presence and distribution of shallow gas in the sediment is of great importance e.g. with regard to offshore construction safety issues. Best et al. (2006) argued that abnormally high levels of methane gas in seafloor sediments could pose a major hazard to coastal populations within the next 100 years through the impact on climate change and sea level rise.

Indications of shallow gas occurrence in the seafloor can be derived from geochemical analyses in the water column and on sediment cores. Even small amounts of free gas may significantly alter the geoacoustic properties of the seafloor, giving rise to highly enhanced acoustic scattering compared to the surrounding sediment/pore water mixture (Anderson and Hampton, 1980; Lyons et al., 1996). Thus, vessel-operated hydroacoustic subbottom profilers were established as a standard tool for remote sensing of shallow gas (Fleischer et al., 2001).

* Corresponding author. Helmholtz Centre for Ocean Research (GEOMAR), Marine Geodynamics, Wischhofstr. 1–3, 24148 Kiel, Germany. Tel.: +49 431 600 2660; fax: +49 431 600 2922.

E-mail address: jschneider@geomar.de (J. Schneider von Deimling).

Today a wide range of multibeam echosounder (MBES) mapping systems is available covering frequencies between 12 kHz and 700 kHz. High frequencies offer high resolution at the cost of higher attenuation and low seafloor penetration. In contrast, low frequency multibeam sounders have lower resolution but allow greater operating ranges and potentially deeper seafloor penetration. Recent developments in hardware and processing have significantly improved MBES data and today additional seafloor information can be derived from backscatter analyses and statistical approaches (Brown et al., 2011; Simons and Snellen, 2009; Preston, 2009). Those studies mainly examine high frequency data (~100 kHz) for seafloor classification based on the relation between seafloor roughness and backscattering strength. Fonseca et al. (2002) demonstrated the potential of MBES for shallow gas sensing, however, their 95 kHz signals only allowed for a decimeter penetration into the seafloor.

Early studies performed with the sidescan sonar GLORIA (Mitchell, 1993) demonstrated the potential of low frequency approaches at low grazing angles for sediment investigations. Data in the focus of this study were gathered with a low frequency multibeam echosounder (see description below). Our approach was to make use of an enhanced seafloor penetration of a few meters with this low frequency MBES to promote increased subbottom volume scattering and thus mapping of shallow gas over large areas.

2. Methods

Data were acquired on the German R/V Maria S. Merian (Cruise 16/1) in August 2010. A Kongsberg EM120 (12 kHz, hull-mounted), an EM1002 (95 kHz, moonpool), and an ATLAS PARASOUND DS3 (PS, 4 kHz, hull-mounted) system were connected to a Seapath DGPS positioning and motion reference unit. Keel sound velocity and vertical sound velocity profile data were derived from online thermosalinographic and CTD cast measurements. Both MBES used a $2^\circ \times 2^\circ$ TX/RX aperture forming 191 and 111 beams, and covered a 140° and 150° swath, respectively. The pulse length was set shortest (2 ms, 0.2 ms) to achieve a maximum range resolution. Depth below seafloor estimates were performed by multiplication of the subbottom travel time (s) with the value of the deepest sound velocity measurement sampled close to the seabed ($v = 1459 \text{ m s}^{-1}$). Corrections accounting for seawater attenuation and geometrical spreading were applied by the recording software SIS. Then average backscattering strength (BS) values were computed by the system for data around the detected depth-time sample in each beam. The recorded soundings were cleaned and gridded using the MB System software package. Backscatter data were extracted by MB System (raw) and QPS-IVS Geocoder 7.3 (corrected). The MBES systems were calibrated for roll, pitch, yaw, and latency, but not for absolute echo level voltage measurements. Accordingly all BS data must be regarded as relative values with an accuracy specified by the manufacturer to $\pm 1 \text{ dB}$. The data in this paper were acquired at shallow water depth; thus near-field effects add as an extra uncertainty.

3. Field site & survey

The study area is located in the Bornholm Basin – a 90 m deep sedimentary basin in the western part of the Baltic Sea (Fig. 1). The basin reflects deeper structures and has been influenced by tectonics during the Cenozoic and Mesozoic. Recently, sediments have been deposited in the late Pleistocene during and after deglaciation. The uppermost layer of several meters thickness consists of organic rich silt (Holocene mud) deposited after the Littorina transgression (Fig. 2a, upper layer). Morphology and thickness variation of the muddy unit are strongly controlled by postglacial basin development

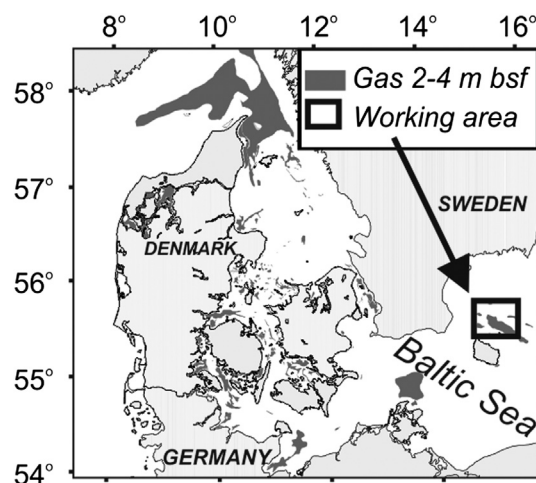


Figure 1. Shallow gas distribution map modified after Laier and Jensen (2007). The working area plots within an area hosting shallow gas between 2 and 4 m bsf.

and bottom current pathways. Within this layer widespread occurrences of shallow gas were observed (Hinz et al., 1971; Laier and Jensen, 2007, Fig. 2a left part). Recent measurements of water column methane concentrations close to the seabed (Schmale et al., 2010) further indicated the presence of significant shallow methane sources in the seabed of this area.

Six survey lines of approximately 2 nautical miles length were run in the northern part of the Bornholm Basin at 4 knots recording EM120 and PS data in parallel; two survey lines were repeated with the EM1002 MBES. Finally, Rumohr Lot (RL) cores were taken at each of five stations along the transect line and respective CH_4 concentrations were measured onboard.

4. Results and discussion

4.1. Evidence of shallow gas from seismic and geochemical profiling

PS records and Rumohr Lot core data disclosed two regimes, A and B, where Holocene mud appeared with and without free methane gas. To the left in Figure 2a a scattering reflector is interpreted as the upper gas front within the Holocene mud between 1 m and 5 m below seafloor (bsf). Below this depth methane gas bubbles efficiently absorbed the acoustic energy and thus 'blanked' any information from the underlying sedimentary strata. In the middle of the profile (Fig. 2a) a transition zone T between A and B is characterized by the down-dipping shallow gas front from 2 m to 5 m bsf. To the right the blanking effect is absent revealing the 12 m thick layer of acoustically transparent Holocene mud followed by well-layered deposits of earlier Baltic Sea stages (Ancyclus to late Pleistocene). Five core samples along the recorded PS profile (positions see Fig. 2a) support the findings from the seismic records, i.e. the measured methane concentration gradients in 1 m long RL cores are high in A and low in B. Sampling procedures for dissolved methane in pore waters were optimized to minimize gas loss even when concentrations exceed solubility at 1 atm (Fig. 2b) by drilling into the core liner and immediate sampling. Loss of gas from the base of the core is evident at the gas-rich core c31 (Fig. 2b). From core c31 the free gas depth is estimated to be around 0.9 m bsf from Figure 2b by assuming a linear gradient between the sulfate–methane transition zone and the level where gas saturation and consequently free gas occurrence is reached. The horizon of shallow gas occurrence is gradually appearing at greater sediment depth for cores c103, c102, and c101. No free gas is expected at core site c32.

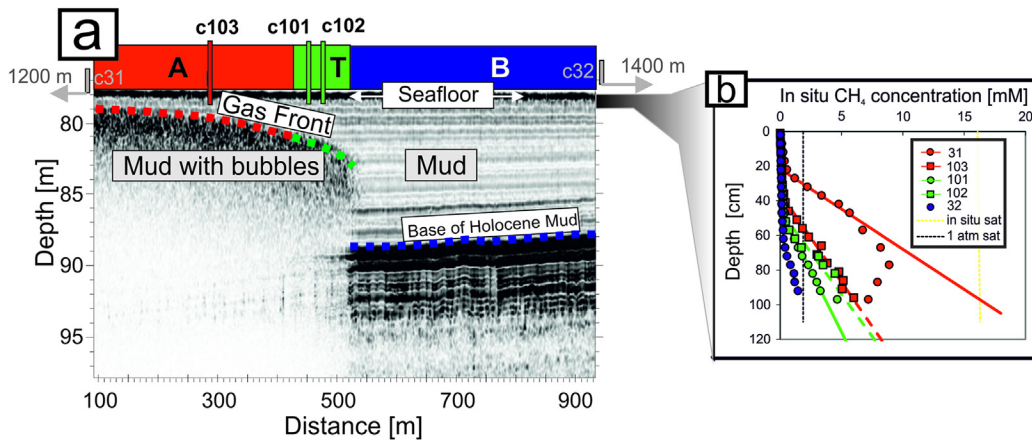


Figure 2. Presentation of a transition zone in Holocene mud between areas with and without shallow methane gas (a) PS subbottom profile P1 starting with the seafloor at 78 m water depth. A zone with shallow gas occurs to the left (A, red) and is followed by the transition zone (T, green). To the right no shallow gas is present and the Holocene base appears beneath the mud (B, blue). Colored vertical bars mark the position of sediment sampling (Station c31 and c32 are outside of the seismo-acoustic picture, see Fig. 3 for location). (b) CH_4 concentration depth profile measured for five cores. Methane concentrations were linearly extrapolated to estimate the depth of methane saturation in the seabed at the intersection with the in situ saturation concentration (16.6 mM, yellow line). Also indicated is the solubility relative to a methane gas pressure of 1 atm (black line).

Physical property measurements of short core samples (0–0.7 m bsf) reveal very low wet bulk density values of $1040\text{--}1280\text{ kg m}^{-3}$, high fractional porosities of $0.96\text{--}0.82$ and sound velocity ratios between sediment and seawater of $0.995\text{--}0.980$ (first number indicate the value at the top, second number the value at the bottom of the core). The steepest gradient of the parameters occurs within the uppermost 10 cm of the muddy deposits. All parameters are highly correlated and controlled by the high content of organic carbon, which is indicated by an ignition loss of $22\%\text{--}15\%$. Both sound velocity and wet bulk density of the uppermost mud are very close to the corresponding parameters of the overlying seawater resulting in an acoustic transmission

coefficient close to 1 with high acoustic energy transfer into the bottom. The sound velocity of the uppermost mud is slightly lower than the water sound velocity. Therefore sound waves are refracted toward the vertical at the water seabed interface and there is no critical angle. This phenomenon is not only restricted to the Baltic Sea but also applies to some silty clay deep-sea sediments (Hamilton, 1974).

4.2. Assessing the shallow gas front in 2D

Two multibeam surveys at 12 kHz and 95 kHz were performed around the echosounder profile P1 shown in Figure 2a. Figure 3a

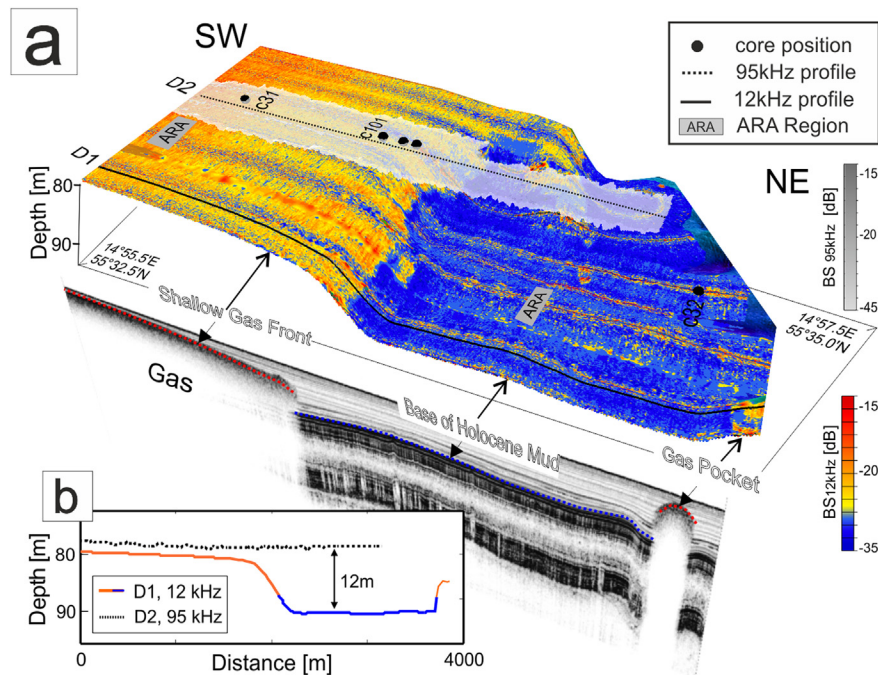


Figure 3. (a) Backscatter chart of EM120 (12 kHz, colored) and 95 kHz (gray, transparent) both draped onto their respective bathymetric grids. Strong variations in backscatter and bathymetry occur in the 12 kHz data with high backscattering strength values (BS) to the left (red, gas) and low ones (blue, no gas) to the right part of the figure. This corresponds to the underlying subbottom findings visible in the vertical curtain image (with depth offset for better visibility). The 95 kHz data (gray surface) plots on top of the 12 kHz surface and shows neither amplitude nor bathymetric changes across- or alongtrack (b) depth profiles D1 and D2 gathered from 12 kHz to 95 kHz bathymetric grids. Depth differences of up to 12 m occur between both data (for location see (a)).

presents the backscatter amplitude draped onto the respective bathymetric grid of the 12 kHz and 95 kHz surveys. The 95 kHz data reveal no alongtrack changes in backscatter and a featureless and flat topography in the range between 78.0 m in the NE and 77.6 m in the SW. The depth of the 95 kHz data exactly matches the visually determined seafloor reflector in the subbottom data (e.g. Fig. 2a). Compared to the high frequency data the depth values of the 12 kHz system systematically appear 1–5 m deeper in the Southwest, and up to 12 m deeper in the Northeast. A closer inspection of Figures 3a and b reveals that the bottom detector “misinterprets” the 12 kHz signals backscattered from the top of the shallow gas front and the ones backscattered from the base of the Holocene mud as seafloor echoes. With the low-frequency MBES system the significant bottom misdetection was even observed with sonar settings optimized for shallow water seafloor detection and on the outermost parts of the swath, making it possible to resolve small gas pockets (Fig. 3a, right side). A correlation between 3170 depth values of the shallow gas front depth and the Holocene base (identified with the PS data, Fig. 2a) and the depth difference between the 95 kHz and 12 kHz grids reveals a very clear linear correlation ($R^2 = 0.93$). Thus, the bathymetric grid in Figure 3a presents the spatial distribution of the shallow gas front in the Southwest and the base of the Holocene mud in the Northeast, and in neither case the seafloor. Those artifacts are fostered by the sedimentological properties with low seafloor backscatter, low attenuation of the underlying mud, and high scattering from gas bubbles and the base of the Holocene mud.

The backscatter data generally mimic the bathymetric artifacts. In contrast to the uniform 95 kHz backscatter record, the 12 kHz backscatter image shows a severe alongtrack change of backscattering strength across the transition zone. The shallower the gas front depth is located the higher the subbottom amplitude values get, reaching up to -15 dB (Fig. 3a, left side). This spatial correlation is attributed to an increasing acoustic attenuation with increasing sediment thickness above the shallow gas front. Jackson and Richardson (2007) estimated an attenuation coefficient of 0.1 – 0.2 dB m^{-1} kHz $^{-1}$ for Holocene mud in the Baltic Sea. The MBES' time varying gain only corrects for a two-way travel attenuation in seawater, being orders of magnitude lower than for mud. Accordingly, for a 2 m bsf deep buried scatterer and attenuation coefficients between 0.1 and 0.2, the recorded backscatter levels from the 12 kHz MBES are considered to be ~ 4 – 9 dB too low due to the uncompensated attenuation from the overlying sediments.

Very high backscattering strength values have also been observed by Lyons et al. (1996) for gas bearing Holocene mud in the Western Baltic Sea with BS values between -10 and -20 dB for a 15 kHz normal incidence signal. Given the clear relation between the high MBES backscatter together with the existence of shallow gas occurring in subbottom records we attribute the alongtrack backscatter anomalies to enhanced scattering from gas bubbles in the seabed. It should be noted that only relative dB values can be determined, and uncertainties may derive particularly from near-field effects and uncertain amount of attenuation.

Recent investigations in the Baltic Sea had shown a close relationship between the depth of the shallow gas front and the vertical methane flux within the sediment (Dale et al., 2009). Thus, with this approach and under certain circumstances we foresee low frequency multibeam echo-sounding as a promising, dependable and above all fast spatial mapping tool for shallow gas occurrences in soft sediment.

4.3. Angular response of areas with and without gas

More detailed information about the seafloor can be derived by analyzing the intrinsic behavior of backscatter amplitude over

angle via the angular range analysis (Fonseca and Mayer, 2007). While the 95 kHz data reveal normal decay of backscatter strength with angle, significant anomalies appear in the 12 kHz data. Figure 4 shows an averaged angular response plot for 12 kHz raw data (BSr) and those corrected using QPS-IVS Geocoder 7.3 (Fonseca and Calder, 2005). These corrections account for bathymetric slope and sonar specific parameters such as source level, beam patterns, receiver sensitivity, and time varying gains. It appears that raw and corrected values are very similar, which we attribute to the flat bathymetry.

The angular response outside the gassy regime gives -10 dB at 0° incidence angle and a Lambert like decay toward the outer beams to -35 dB, thus resembling the angular response of soft sediments without gas. Backscatter values gathered within the gassy area reveal virtually no angular changes with a high average backscattering strength around -19 dB – much higher than would be expected from mud. Taking into account that BS data were not corrected for unknown sub-seabed attenuation, the real BS values are expected to be even higher. At incident angles greater than 45° the BSc in the gas-prone area even increases. Those findings are confirmed by several angular response analyses (compare Fig. 4) in gassy areas at various locations, all showing similar results and have never been reported so far.

Previous experimental and modelling efforts addressing the angular response of 12 kHz MBES data revealed a noticeable decrease of the backscattering strength amplitude toward outer angles (deMoustier and Alexandrou, 1991). Fonseca et al. (2002) showed for a 95 kHz system angular response from gassy sediments revealing -25 to -27 dB backscattering strength between 30° and 60° with an averaged 5 dB difference for areas with and without shallow gas. In contrast, our 12 kHz data reveal -19 dB between 30° and 60° in the gassy area and 13 dB averaged difference compared to the area without shallow gas. Possible reasons for the much higher response to 12 kHz signals in shallow gas environments might be increased volume backscattering due to bubble resonance phenomena (Anderson and Hampton, 1980) and the fact, that a 12 kHz pulse is 8 times less attenuated in mud without gas bubbles than a 95 kHz pulse. Richardson and Briggs (1996) reported lower surficial compressional wave velocities than seawater (slow reflector) for Holocene mud in the Baltic Sea with total transmission of sound into the seafloor at the angle of “intramission” at low grazing angles (Jackson and Richardson, 2007) – a potential

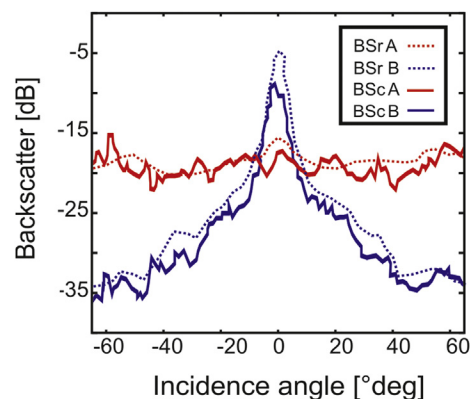


Figure 4. Angular response/range analysis (ARA) for 30 pings showing very distinct differences between backscattering strength (BS) over incidence angle behavior for data gathered within (A, red) and outside of the shallow gas regime (B, blue). BSr (raw) denote uncorrected backscatter values, whereas BSc values were generated with corrections for bathymetric slope and beam patterns realized through GEOCODER. BSr and BSc data were not corrected for unknown sub-seabed attenuation effects. See Figure 3 for exact location.

explanation for the higher backscattering toward the outer angle. Additionally, the backscatter might also be significantly biased with an angular behavior linked to ray path length variations inside the sediment layer.

An adaption of the prevailing model for a quantitative inversion of backscatter into gas volume was left as a challenging future task. Fonseca et al. (2002) treated gas bubbles as individual discrete scatterers, where the backscattering strengths of individual bubbles simply sum up. At frequencies around 12 kHz several gas bubbles are expected to occur within one wavelength and thus, multiple scattering effects have to be addressed. Moreover, Fonseca et al. (2002) assumed a fixed size distribution of spherical gas bubbles in his model, which will need further justification from field data.

Overall, in 12 kHz data the amplitude difference in areas with and without gas reached -10 dB at nadir and up to $+17$ dB toward the outer swath at 65° . As the highest differences in backscattering strength between areas with and without gas were measured at the outermost beams, we attribute highest gas-sensitivity of the MBES to the outer angle stressing the benefits of a swath mapping approach.

5. Recommendations

While the method seems to be particularly applicable in shallow water, 12 kHz multibeam systems are mostly available on deep sea vessels carrying the larger and more expensive transducer arrays. Given the linear behavior of attenuation and frequency, less penetration is expected at higher frequencies for the benefit of smaller transducers. By using a 50 kHz system as a compromise, we expect 3 m penetration into muddy sediments (according to 12 m for 12 kHz), and such systems can therefore be used as mobile versions on smaller vessels for spatial gas mapping.

Data presented in this study were acquired at 80 m water depth in a very soft sediment environment. Mapping of sub-seabed features with low frequency MBES could also be applied in deeper water, where sediments with low values for acoustic velocity, attenuation and reflection coefficients commonly occur (Hamilton, 1974) fostering acoustic penetration. Due to lower attenuation loss from the bubbles at higher ambient pressure even higher sensitivity for shallow gas is expected in deeper water (Fonseca et al., 2002). However, bathymetric artifacts caused from sub-seabed features presented in this study are expected to be less prominent in deeper water due to acoustic pulse stretching and beam widening with greater ranges both reducing the spatial resolution.

In the meantime, modern MBES allow for recording time series data for all beams and full ranges (water column imaging data). Thus, the recorded backscatter data and the bottom detection can be reviewed during postprocessing, and erroneous seafloor detection may be identified as well as subsurface scattering layers. Together with geologic interpretation of center beam subbottom records we consider the inspection of MBES time series data as promising in regards to future sub-seabed investigations.

6. Conclusion

This study demonstrates that shallow gas down to 5 m bsf can be unambiguously spatially assessed in muddy sediments by use of low frequency multibeam echo-sounding. The 12 kHz data indicate at least 12 m deep penetration into the soft seabed with wrong bottom detection, which we used for subbottom interpretations and spatial mapping of shallow gas. The gas front can be reliably identified across the entire multibeam swath from abrupt depth offsets and distinct backscatter anomalies, which is confirmed by

seismo-acoustic subbottom records and geochemical core sampling results. Spatial measurements by high resolution MBES even allow resolving smaller individual gas pockets and potentially other high scattering objects buried in soft sediment. It remains to be investigated how this approach would apply in geological settings with sediments having higher acoustic attenuation.

Backscatter investigations demonstrate a high sensitivity of the 12 kHz MBES with shallow gas mapping. Thus an angular response analysis was performed revealing a unique gas-mediated angular response pattern and increasing gas sensitivity toward the outer swath, a finding which is unprecedented in literature and augmenting the potential of MBES for gas detection and classification in shallow water.

Acknowledgments

The research leading to these results has received funding from the European Community's Seventh Framework Programme (FP/2007–2013) under grant agreement n° 217246 and n° 03F0488C made with the joint Baltic Sea research and development programme BONUS. Further research contributing to this paper was funded by the German Ministry of Education and Research through grant n° 03G0819A (SUGAR II).

References

- Anderson, A.L., Hampton, L.D., 1980. Acoustics of gas-bearing sediments I. Background. *Journal of Acoustical Society of America* 67, 1865–1889. <http://dx.doi.org/10.1121/1.384453>.
- Best, A.L., Richardson, M.D., Boudreau, B.P., Judd, A.G., Leifer, I., Lyons, A.P., Martens, C.S., Orange, D.L., Wheeler, S.J., 2006. Shallow seabed methane gas could pose coastal hazard. *Eos* 87 (22), 213–220. <http://dx.doi.org/10.1029/2006EO220001>, 2010.
- Briggs, K.B., Richardson, M.D., 1996. Variability in in situ shear strength of gassy muds. *Geo-Marine Letters* 16 (3), 189–195. <http://dx.doi.org/10.1007/BF01204508>.
- Brown, C.J., Smith, S.J., Lawton, P., Anderson, J.T., 2011. Benthic habitat mapping: a review of progress towards improved understanding of the spatial ecology of the seafloor using acoustic techniques. *Estuarine, Coastal and Shelf Science* 92 (3), 502–520.
- Dale, A.W., Regnier, P., Van Cappellen, P., Fossing, H., Jensen, J.B., Jørgensen, B.B., 2009. Remote quantification of methane fluxes in gassy marine sediments through seismic survey. *Geology* 37 (3), 235–238. <http://dx.doi.org/10.1130/G25323A.1>.
- deMoustier, C., Alexandrou, D., 1991. Angular dependence of 12-kHz seafloor acoustic backscatter. *Journal of Acoustical Society of America* 90 (1), 522–531.
- Fleischer, P., Orsi, T.H., Richardson, M.D., Anderson, A.L., 2001. Distribution of free gas in marine sediments: a global overview. *Geo-Marine Letters* 21 (2), 103–122.
- Fonseca, L., Mayer, L., Orange, D., Driscoll, N., 2002. The high-frequency backscattering angular response of gassy sediments: model/data comparison from the Eel River Margin, California. *Journal of Acoustical Society of America* 111 (6), 2621–2631. <http://dx.doi.org/10.1121/1.1471911>.
- Fonseca, L., Calder, B., 2005. Geocoder: an efficient backscatter map constructor. In: *Proceedings of the U.S. Hydrographic Conference*, San Diego, CA.
- Fonseca, L., Mayer, L., 2007. Remote estimation of surficial seafloor properties through the application angular range analysis to multibeam sonar data. *Marine Geophysical Research* 28 (2), 119–126.
- Hamilton, 1974. Prediction of deep-sea sediment properties: state of the art. In: *Inderbitzen, A.L. (Ed.), Deep-sea Sediments, Physical and Mechanical Properties*. Plenum Press.
- Hinz, K., Kögler, F., Richter, I., Seibold, E., 1971. Reflexionsseismische Untersuchungen mit einer pneumatischen Schallquelle und einem Sedimentecholot in der westlichen Ostsee. Teil II Untersuchungsergebnisse und geologische Deutung. *Meyniana* 21, 17–24.
- Jackson, R.D., Richardson, M.D., 2007. High-frequency Seafloor Acoustics. Springer. <http://dx.doi.org/10.1121/1.2782933>.
- Judd, A.G., Hovland, M., 2007. Seabed Fluid Flow Environment. Cambridge University Press, New York. <http://dx.doi.org/10.2277/0521819504>.
- Laier, T., Jensen, J.B., 2007. Shallow gas depth-contour map of the Skagerrak-western Baltic Sea region. *Geo-Marine Letters* 27 (2), 127–141. <http://dx.doi.org/10.1007/s00367-007-0066-2>.
- Lelieveld, J., Crutzen, P., Bruhl, C., 1993. Climate effects of atmospheric methane. *Chemosphere* 26 (1–4), 739–768. [http://dx.doi.org/10.1016/0045-6535\(93\)90458-H](http://dx.doi.org/10.1016/0045-6535(93)90458-H).
- Lyons, A.P., Duncan, M.E., Anderson, A.L., Hawkins, J.A., 1996. Predictions of the acoustic scattering response of free-methane bubbles in muddy sediments. *Journal of Acoustical Society of America* 99 (1), 163–172. <http://dx.doi.org/10.1121/1.414500>.

- Mitchell, N.C., 1993. A model for attenuation of backscatter due to sediment accumulations and its application to determine sediment thicknesses with GLORIA sidescan sonar. *Journal of Geophysical Research* 98 (B12), 22,477–22,493. <http://dx.doi.org/10.1029/93JB02217>.
- Preston, J., 2009. Automated acoustic seabed classification of multibeam images of Stanton Banks. *Applied Acoustics* 70 (10), 1277–1287.
- Richardson, M.D., Briggs, K.B., 1996. In situ and laboratory geoacoustic measurements in soft mud and hard-packed sand sediments: implications for high-frequency acoustic propagation and scattering. *Geo-Marine Letters* 16, 196–203.
- Schmale, O., Schneider von Deimling, J., Gülzow, W., Nausch, G., Waniek, J.-J., Rehder, G., 2010. Distribution of methane in the water column of the Baltic Sea. *Geophysical Research Letters* 37 (L12604), 1–5. <http://dx.doi.org/10.1029/2010GL043115>.
- Shindell, D.T., Faluvegi, G., Koch, D.M., Schmidt, G.A., Unger, N., Bauer, S.E., 2009. Improved attribution of climate forcing to emissions. *Science* 326, 716–718. <http://dx.doi.org/10.1126/science.1174760>.
- Simons, D.G., Snellen, M., 2009. A Bayesian approach to seafloor classification using multi-beam echo-sounder backscatter data. *Applied Acoustics* 70 (10), 1258–1268. <http://dx.doi.org/10.1016/j.apacoust.2008.07.013>.

Appendix C

Sulphate and methane fluxes and organic matter mineralization across a Holocene mud layer of increasing thickness in Aarhus Bay (Baltic Sea)

Sabine Flury, Andrew W. Dale, Hans Røy, Henrik Fossing, Zsuzsanna Tóth, Volkhard Spieß, Jørn Bo Jensen, Bo Barker Jørgensen

Manuscript

Sulphate and methane fluxes and organic matter mineralization across a Holocene mud layer of increasing thickness in Aarhus Bay (Baltic Sea)

Sabine Flury^{1,6*}, Andrew W. Dale^{2*}, Hans Røy¹, Henrik Fossing³, Zsuzsanna Tóth⁴,
Volkhard Spieß⁴, Jørn Bo Jensen⁵, Bo B. Jørgensen¹

¹ Center for Geomicrobiology, Department of Bioscience, Aarhus University, Ny Munkegade 114, DK-8000 Aarhus, Denmark

² GEOMAR | Helmholtz Centre for Ocean Research Kiel, Wischhofstrasse 1-3, D-24148 Kiel, Germany

³ Department of Bioscience, Aarhus University, Vejlsovej 25, DK-8600 Silkeborg, Denmark

⁴ Department of Geosciences, University of Bremen, Klagenfurter Straße, 28359, Bremen, Germany

⁵ GEUS, Ø. Voldgade 10, DK-1350 Copenhagen, Denmark

⁶ present address: Leibniz-Institute of Freshwater Ecology and Inland Fisheries, Müggelseedamm 301, 12587 Berlin, Germany

*Corresponding authors: sabine.flury@biology.sdu.dk, adale@geomar.de

ABSTRACT

Shallow gas accumulates in coastal marine sediments when the burial of reactive organic matter beneath the sulfate zone is high and the methanogenic sediment is sufficiently deep. We studied the transition from gas free into gas bearing sediment with the objective to understand how the methane flux is affected when the in situ solubility threshold for methane is exceeded. Twelve 5-7.5 m long gravity cores were taken 20-50 m apart along a 400 m long seismo-acoustic transect in Aarhus Bay (Denmark). The porewater was analyzed for dissolved methane (CH_4), sulfate (SO_4^{2-}), total dissolved carbon dioxide (TCO_2), and ammonium (NH_4^+), while sulfate reduction rates (SRR) were measured experimentally by radiotracer method. The depth of organic-rich Holocene mud increased along the transect and shallow gas appeared when the mud thickness exceeded 8-9 m. Diffusive fluxes of CH_4 , SO_4^{2-} , TCO_2 and NH_4^+ also increased along the transect while the depth of the sulfate methane transition zone (SMTZ) shallowed from >4 m to 2.5 m. Based on the measured SRR, the depth distribution of mineralization rates did not show a systematic change along the transect. Extrapolation of the log-log linear trend of mineralization rates down into the methanogenic zone allowed us to analyze the controls on methane fluxes in sediment without and with gas. Interestingly, the deepening of the methanogenic mud layer had apparently little effect but the shallowing of the SMTZ had a large effect because the highest rates of mineralization, and thus of methanogenesis, take place in the youngest sediment. As the deep and the shallow enhanced methanogenesis were coupled, we conclude that there is a positive feedback which explains the abrupt appearance of gas when a threshold thickness of Holocene mud is exceeded.

1. INTRODUCTION

Methane (CH_4) is a powerful greenhouse gas, being 25 times more potent than carbon dioxide by mass (IPCC, 2007). Around 40% of the total CH_4 emission to the atmosphere originates from natural sources such as ruminants, termites, wetlands, and oceans (IPCC, 2007). Despite large accumulations of CH_4 in coastal marine sediments, this reservoir plays a minor role as a CH_4 source for the atmosphere. Microorganisms in the sediment efficiently assimilate dissolved methane that diffuses up from below and oxidize it with oxygen or sulfate (e.g. Sansone and Martens 1978, Reeburgh, 1980; Martens et al., 1998; Claypool et al., 2006; Jensen and Bennike, 2009). Not all CH_4 is present in the dissolved form, however. Free gas occurs widespread as bubbles in unconsolidated coastal sediments where it can be detected by shallow seismo-acoustic methods (Judd and Hovland, 1992; Best et al., 2006). In many areas of the Baltic Sea, the free gas appears when the organic-rich Holocene mud layer (HML), deposited since the end of the last ice age, exceeds a thickness of 5-10 m (Whiticar, 2002; Thiessen et al., 2006; Jensen and Bennike, 2009). Environmental change such as warming or eutrophication may shift the balance between CH_4 production, consumption and accumulation in marine sediments (Best et al., 2006) and thereby enhance the emission of CH_4 to the overlying water column and to the atmosphere.

The potential for CH_4 production in sediments is determined by the amount of particulate organic matter (POM) that is deposited on the sea floor and the rate at which it is mineralized or buried (e.g. Borowski et al., 1999 and references in there). The sequence of electron acceptors that control this process includes aerobic respiration, denitrification, iron reduction and sulfate (SO_4^{2-}) reduction (e.g. Canfield and Thamdrup, 2009). When SO_4^{2-} is exhausted, generally at several meter beneath the sediment surface, the degradable organic matter is converted into CH_4 by methanogenic archaea. Most of the CH_4 produced in the deep sediment layers moves upwards to the sulfate-methane transition zone (SMTZ) by diffusion. In some sediments the diffusive flux can be enhanced by migration of gas bubbles as Treude et al (2005) suggested for a study in Eckernförde Bay. In the SMTZ, anaerobic oxidation of methane (AOM) is coupled to the reduction of SO_4^{2-} (Sansone and Martens 1978) and can be mediated by a consortium of methanotrophic archaea and sulfate reducing bacteria (Boetius et al., 2000) or by methanotrophic archaea alone (Milucka et al., 2012). The depth of the SMTZ depends on a balance between the total production and upward flux of methane and the downward diffusion of SO_4^{2-} from the sediment surface to the SMTZ (Borowski et al., 1996). If the partial pressure of CH_4 exceeds the hydrostatic pressure in the methanogenic sediment below the SMTZ, CH_4 bubbles will form. The potential for bubble formation depends on the water depth, on the depth of the SMTZ, on the depth integrated rate of methanogenesis, on the presence of other dissolved gases (e.g. CO_2) and on the transport coefficients for CH_4 and SO_4^{2-} in the sediment.

The overall production of methane is difficult to determine because reliable CH_4 concentration data are usually only available for the uppermost part of the CH_4 gradient and there is no constraint on the lower boundary of the methanogenic zone. To overcome these difficulties we studied a sediment area in Aarhus Bay (Denmark) where organic-rich post-glacial mud overlies late-glacial organic-poor clay. The goal was to understand a) whether the deepening of the Holocene mud deposit is initiating shallow gas formation, b) whether there is a positive feedback which pushes the SMTZ upward once free gas has formed, and c) how the migration of gas bubbles may enhance the upwards flux of CH_4 . We took 12 gravity cores along a 400-m long transect that extended from gas free to gas bearing sediment with a gradual increasing thickness of the Holocene mud layer (HML). Based on porewater and solid phase chemical analyses and on experimental mineralization rate measurements we could indeed identify such a positive feedback mechanism. The critical question is how the feedback works.

2. MATERIALS AND METHODS

2.1. Study site

Aarhus Bay is located in western Kattegat on the North Sea - Baltic Sea transition. The seabed in Aarhus Bay consists of late Quaternary sediments with a clear glacial imprint, caused by glacial deformation and till related to the Weichselian ice advance and the ice marginal deposits from the final Baltic advance (Houmark-Nielsen, 1987). Glaciodynamic morphologic elements show up as shallow ridges in areas of the seabed with no mud deposition (Fig. 1) (Jensen and Bennike, 2009). The Holocene Littorina Sea transgression flooded the northern entrance to the Great Belt about 9.5 kyr BP (Jensen et al., 2004) during an initial brackish estuarine phase. The oldest marine shells from Aarhus Bay have been dated to 8.7 kyr BP (Jensen and Bennike, 2009), which marks the beginning of fully marine conditions. Since then, marine mud has accumulated until today and formed up to >10 m deep organic-rich deposits.

The central and eastern basin of the bay is 15–20 m deep and characterized by mud and sandy mud. Seismic studies show that gas bearing sediment extends over a large part of the bay in areas where more than 5 m thick mud has accumulated (Fig. 1). The lithology suggests that most CH₄ is formed in the HML with little contribution from deeper layers of organic-poor late-glacial clay (Jensen and Bennike, 2009).

2.2. Sediment coring

The 12 coring stations were 20 to 50 m apart and located on a straight line corresponding to the shallow-seismic Chirp profile METROL-502110 recorded during the EU project METROL in 2003 (Fig. 1 and 2a). The total distance between the two terminal stations, M22A (N56° 6.745', E10° 24.880') and M30 (N56° 6.636', E10° 25.208'), was 408 m, with a slight increase in water depth from 18.8 to 19.3 m. Stations M22A to M26 were positioned in the gas-free area whereas M27 to M30 were located within the gas bearing sediments (Fig. 2a). Station M26 was located only 12 m west of the transition where acoustic blanking was first observed on the seismic image (Fig. 2a, Table 1). The HML thickness was observed to increase steadily towards the gassy sediments, from 4.7 m at M22A to 8.7 m at M26, but was then obscured due to acoustic blanking by gas bubbles (Fig. 2a). Stations M22 to M30 were cored in October 2009, while additional cores (with the suffix A) were retrieved in May 2010.

We retrieved one gravity core of 3 to 7.5 m length from each site. Each gravity core was supplemented by a shorter Rumohr Lot core (<1 m) to obtain undisturbed surface sediments. The sediment loss (8 to 22 cm) from the top of the gravity cores was determined by matching the SO₄²⁻ profiles of the two cores (Jørgensen et al., 2004). Immediately after the gravity core was on deck, a sample for CH₄ analysis was taken at every 25 cm or 33 cm (starting from the core catcher) by drilling holes through the core liner and extracting 3 mL of sediment with a cut off syringe (see details in 2.4.1.). The gravity cores were then sectioned on deck into 1 m or 2 m lengths, capped, and stored at 4°C until further processing (within 72 h). The initial CH₄ samples were analyzed immediately upon return to the laboratory by gas chromatography (see below) to determine the position of the SMTZ. The gravity cores were then sub-sampled in the laboratory at 12.5 cm depth resolution. The Rumohr Lot cores and the SMTZ of the gravity cores were sampled at 5 cm depth resolution.

2.3. Seismic survey

To determine the base of the Holocene mud beneath the gas bearing sediment, multichannel seismic data were collected along the coring transect in April 2012. While high frequency Chirp signals are strongly attenuated in the gas bearing sediment layer (Fig. 2a), lower frequency airgun seismics penetrate the gas layer and image geological structures below the free gas. We used a micro GI gun (0.1 l) with a main frequency of 200 Hz (~7.5 m wavelength) and a 60 m long high resolution digital streamer with 60 channels. Seismic data processing followed a conventional marine processing flow with special emphasis on precise velocity modeling. In order to correct properly for the velocity decrease in and beneath the gas bearing sediment layer, the initial velocity field was improved through additional Migration Image Velocity Analysis (in the seismic processing software VISTA). For the analysis, the seismic data were pre-stack time migrated by varying the initial velocity field by 1% between 80 and 120%, and the best image velocity was picked for every reflector. These velocity values were used to convert two-way travel time (TWT) to depth. Accuracy of the depth calculation depends on several factors: sample rate and noise level of the seismic data, accuracy in picking the TWT of the reflectors, accuracy of the velocity determination and the variability in the geological structure as well. The error of the depth calculation considering these factors was estimated to ~25 cm.

2.4. Analytical methods

2.4.1. Methane concentration

For CH₄, 3 mL of sediment was sampled with cut off syringes and immediately transferred to 20 mL glass vials containing 6 mL 2.5% NaOH and crimp capped. Samples were shaken thoroughly and stored upside down at 4 °C until analysis. Prior to analysis, the samples were again shaken to equilibrate the CH₄ and 20 µL of head space was injected with a Hamilton glass syringe into a gas chromatograph equipped with a 0.91 m packed silica gel column (3.1 mm diameter) and a flame ionization detector (SRI 310C, SRI Instruments). Despite efforts to subsample the core for CH₄ as quickly as possible, CH₄ concentrations were scattered at concentrations above approx. 2.5 mM due to degassing of dissolved CH₄ from the sediment upon core retrieval. These scattered and underestimated data are presented but were not considered in the calculation of diffusive fluxes.

2.4.2. Sulfate concentration

Porewater samples for SO₄²⁻ were collected with Rhizons pushed into the whole core through holes drilled in the core liner. The extracted porewater was acidified with HCl and stripped for hydrogen sulfide (H₂S) by shaking the samples on a Vortex mixer. SO₄²⁻ was analyzed on an ion chromatograph (Dionex IC 2000) equipped with a GP50 Gradient Pump (flow 1 mL min⁻¹), EG50 Eluent Generator, ED50 Electrochemical Detector, AS50 Thermal compartment, ASRS–UltraII 4 mm suppressor, an AS50 Auto sampler, and an AS18 Column (column temperature 30 °C). Depending on the expected concentration the porewater samples were diluted up to 100-fold before measurements.

2.4.3. Dissolved calcium and magnesium concentrations

Porewater samples for analysis of dissolved calcium (Ca²⁺) and magnesium (Mg²⁺) were collected with Rhizons and stored at 4 °C until analyzed. Porewater samples were then analyzed by inductively coupled plasma emission spectrometry (Perkin Elmer Plasma II). Concentrations were determined by comparing peak areas to standard solutions

with a similar salinity matrix. Standards were run for every 10 samples. Samples were diluted 1:100 in triplicate and run in triplicate. The wavelength for Ca^{2+} was 317.933 nm and for Mg^{2+} 285.213 nm. The average standard error for Mg^{2+} and Ca^{2+} was around 1.2 %.

2.4.4. Total carbon and nitrogen

Five to 10 mL of sediment was collected at 50 cm depth intervals with cut-off syringes from the gravity core. After drying and grinding the sediment the content of total carbon (TC) and total nitrogen (TN) were determined on a CN-analyzer (Europa Scientific) by complete combustion of ca. 50 mg dried sediment sample. Concentrations are reported in dry weight percent (wt %) with a precision of about 2% for both TC and TN.

2.4.5. Sediment density and porosity

Density (ρ , in g cm^{-3} of wet sediment) was determined from wet weight and volume. Water content (w , in $\text{cm}^3 \text{ g}^{-1}$ of wet sediment) was determined from weight loss following drying at 80 °C until constant weight. Porosity, ϕ , was then calculated as $\rho \times w$.

2.4.6. Sulfate reduction rates

Sulfate reduction rates (SRR) were determined in sediment sampled in October 2009. For the analysis, 3 mL of sediment was collected with cut off syringes at 5, 10, 20 and 55 or 60 cm (length-depending) in the Rumohr Lot core and at 120 and 240 cm (measured from the top) from the gravity core. Samples for SRR were kept anoxic at 4 °C for up to 24 h until incubation. Rates were measured by injecting 100 kBq carrier free $^{35}\text{SO}_4^{2-}$ tracer into 3 mL of sediment directly in the sampling syringes followed by 3.5 days of incubation at 4 °C in oxygen free and gas tight plastic bags. The O_2 was stripped from the plastic bags, by adding an Oxoid AnaeroGen™ pad (Oxoid A/S, c/o Thermo Fisher Scientific, Roskilde, Denmark). The incubation was terminated by freezing the sediment samples at -20 °C without opening the bags. The samples were stored at -20 °C up to 4 weeks before analysis. The frozen samples were extruded frozen into 3 mL 20% (w/v) Zn-Acetate and thawed. After thawing the total reduced inorganic sulfur (TRIS = H_2S , S^0 , FeS , and FeS_2) was separated from SO_4^{2-} by a single step cold chromium distillation (Kallmeyer et al., 2004). The radioactivity of $^{35}\text{SO}_4^{2-}$ and TRIS was counted in 20 mL scintillation cocktail (Ecoscint A, National Diagnostics) on a TriCarb 2900TR liquid scintillation analyzer (Packard Instrument Company). SRR was then calculated as:

$$\text{SRR} = \frac{F \cdot [\text{SO}_4^{2-}] \cdot 1.06}{t} \cdot \phi \quad \text{Eq. (1)}$$

where F is the fraction of $^{35}\text{SO}_4^{2-}$ reduced (i.e. $F = \frac{A_{\text{TRIS}}}{A_{\text{SO}_4^{2-}} + A_{\text{TRIS}}}$; with A denoting the activity (cpm) in TRIS and $^{35}\text{SO}_4^{2-}$, respectively), $[\text{SO}_4^{2-}]$ is the porewater concentration, t is incubation time and ϕ is porosity. The constant of 1.06 corrects for the assumed discrimination factor during sulfate reduction between the isotopes ^{35}S and ^{32}S (Jørgensen 1978a).

The seasonal temperature in the bottom water of Aarhus Bay varies between 5 and 11 °C and propagates into the upper meters of sediment towards an annual mean temperature of 9 °C. However, the SRR were determined at 4 °C and therefore the measured rates were recalculated to a mean annual SRR at each depth in the sediment. To achieve this, the

daily temperature profile in the upper 10 meters of the sediment column was first simulated (using Comsol Multiphysics software) by considering the annual time series of bottom water temperature, the thermal conductivity and the heat capacity of the sediment (Dale et al., 2008). The mean annual SRR corresponding to the *ex situ* measured rate was then calculated using a Q_{10} value of 2 (Dale et al., 2008):

$$SRR = \frac{1}{365} \times \sum_{day=1}^{365} \frac{SRR_{ex}}{Q_{10}^{\frac{T_{ex}-T_{in}}{10}}} \quad \text{Eq. (2)}$$

where SRR_{ex} is the measured SRR at 4 °C, T_{ex} the *ex situ* temperature of the incubation (4 °C) and T_{in} is the simulated in situ daily depth-dependent temperature. Using this approach the rates were revised upwards by a factor of 1.3 to 1.4 depending on depth.

2.5. Modeled fluxes

2.5.1. Methane and sulfate fluxes

Diffusive fluxes of SO_4^{2-} , and CH_4 , were estimated from the concentration gradient in the porewater profiles using Fick's First Law:

$$J_i = -\phi \cdot D_i \cdot \frac{\partial C_i}{\partial z} \quad \text{Eq. (3)}$$

where J_i is the diffusive flux of species i ($nmol\ cm^{-2}\ d^{-1}$), C_i is the concentration ($mmol\ cm^{-3}$), z is depth (cm), ϕ is the mean porosity over the depth interval where the flux was calculated. D_i is the diffusion coefficient ($cm^2\ d^{-1}$) in the sediment calculated using diffusion coefficients in free solution (Boudreau, 1997) for a salinity of 30 and the mean annual temperature of 9 °C (Dale et al., 2008):

$$D_{CH_4} = 0.918\ cm^2\ d^{-1}$$

$$D_{SO_4^{2-}} = 0.570\ cm^2\ d^{-1}$$

where the diffusion coefficient for TCO_2 was taken to be that for the bicarbonate ion (HCO_3^-) since this is the major carbonate species (~95 % of TCO_2) at pH of 7 to 8 typically encountered in subsurface marine sediments. Diffusion coefficients were corrected for tortuosity by dividing by $1-\ln(\phi^2)$ using the mean porosity value at the SMTZ (Boudreau, 1997).

In this paper, fluxes of SO_4^{2-} were estimated from the linear portion of the concentration gradients in the 100 cm above the SMTZ whereas CH_4 fluxes were estimated from linear concentration gradients (mathematically fitted for the data points lying on a straight line) below the SMTZ. The depth of the SMTZ was defined as the depth of equimolar SO_4^{2-} and CH_4 concentrations. SO_4^{2-} fluxes were always directed downwards (into the sediment), whereas CH_4 fluxes were always directed upwards (out of the sediment). All fluxes are reported in positive units.

2.5.2. Depth integrated SRR as gross rate of methanogenesis

The depth integrated gross rate of methanogenesis, was estimated by extrapolating the log-log linear trend in mineralization rates in the sulfate zone down into the methane zone (i.e. below the SMTZ). The idea behind this extrapolation is that the SRR (and thus organic carbon mineralization rates) should not be specific to the sulfate reduction zone but continue down into the methanogenic zone and that the SRR observed in the sulfate zone decrease

according to a power law: $SRR = A \times z^{-b}$, where A and b are constants determined from the experimental SRR measurements. It is assumed that this power law trend of mineralization continues into the methanogenic zone where the organic carbon oxidation rate equals the net rate of methane formation. Thus, we fitted a straight line to log-log transformed data of SRR vs. depth from 10 cm below the sediment water interface to the deepest measured point, and extrapolated the line to the bottom of the HML (cf. Jørgensen and Parkes, 2010). Extrapolation after log-log transformation, however, skews the data because high rates lose significance relative to low rates. Mean rates at specific depths predicted from the power law function will therefore be underestimated. This underestimation is a fixed factor down through the core when the variance in the transformed data is constant down through the core. We therefore corrected the power function with a constant factor so that the average of all modeled rates agreed with the average of all measured rates.

3. RESULTS

3.1. Seismic profile and depth of the Holocene mud layer

The seismic profile GeoB12-035 (Fig. 2b) shows the sedimentary strata and structures along the transect down to 90 m below the seafloor. The deep Quaternary till deposits have a hummocky appearance with an uneven upper boundary and are overlaid by late Glacial clay (see also Jensen and Bennike, 2009). Marine deposits lie on top of the late Glacial clay. The oldest, sandy unit Marine 1 forms a wedge shaped structure with a sharp upper boundary. The clay-mud unit Marine 2 (corresponding to the HML) lays over the wedge. The gas bearing mud appears as a high amplitude reflector with reversed polarity, which causes acoustic blanking in the Chirp profile (Fig. 2a). Below the shallow free gas, the base of the marine units is marked by a sharp erosional boundary (Jensen and Bennike, 2009), traceable along the transect. Deeper sedimentary structures below late Glacial deposits are dominated by acoustic multiples. The interference from several reflectors at the transition from non-gassy to gassy sediment (top and base of the gas bearing sediment layer, the base of units Marine 1 and 2) obscure reflector imaging. However, with the use of, e.g. the instantaneous phase seismic attribute, the base of the HML (Table 1) could be clearly mapped below the free gas, thereby revealing the termination of unit Marine 1 near the transition and an almost constant thickness of unit Marine 2 (8.5 m with a variability of ± 25 cm along the profile, Table 1) in the gassy part.

3.2. Particulate constituents

The gradients of TC and TN were very similar at all stations along the transect (Appendix A, Fig. A1). The TC content showed little change with depth with concentrations ranging between 2 and 3 %. At M22 where the HML thickness was only 4.7 m and the gravity core penetrated into the underlying organic poor glacial till, the C:N ratio jumped up from ca. 9 to 18 at 5.5 m depth.

3.3. Dissolved constituents

SO_4^{2-} concentrations decreased with depth with a slightly concave down curvature (Fig. 3). Below the SMTZ, SO_4^{2-} concentrations were 0.1 - 0.2 mM. The SMTZ shifted upwards along the transect from 4.05 m at M23 to 2.57 m at M30 m (Table 1).

Dissolved Ca^{2+} and Mg^{2+} showed only a very slight downward decreasing trend in Ca^{2+} , indicating that net carbonate precipitation or dissolution are of minor importance (Appendix A, Fig. A2) (Table 1).

The shallowing SMTZ was accompanied by steeper SO_4^{2-} and CH_4 gradients and thus higher SO_4^{2-} and CH_4 fluxes. Diffusive SO_4^{2-} fluxes at the depth of the SMTZ showed a marked increase between the gas-free and the gas-bearing sediments (Fig. 4a). The mean ($\pm \sigma$) SO_4^{2-} flux at the gas-free stations (M22A to M26) was $5.7 \pm 1.0 \text{ nmol cm}^{-2} \text{ d}^{-1}$, compared to $11.2 \pm 2.3 \text{ nmol cm}^{-2} \text{ d}^{-1}$ at the gas bearing stations (M27 to M30) (Table 1). CH_4 fluxes just below the SMTZ increased roughly in proportion to the SO_4^{2-} fluxes (Fig. 4b). The ratio of SO_4^{2-} flux to CH_4 flux in the SMTZ ranged from 1 to 2.2 averaging 1.5 ± 0.4 for the entire transect (Fig. 4c). Mean fluxes of Ca^{2+} and Mg^{2+} into the sediment, estimated by pooling available data, were 0.3 ± 0.2 (mean $\pm \sigma$) $\text{nmol cm}^{-2} \text{ d}^{-1}$ (Table 1).

3.4. Sulfate reduction rates

The depth distributions of sulfate reduction rates (SRR) generally decreased from $> 60 \text{ nmol cm}^{-3} \text{ d}^{-1}$ in the upper 10 cm to $< 0.1 \text{ nmol cm}^{-3} \text{ d}^{-1}$ at 100 cm which is typical of muddy coastal sediments. In a log-log transformed plot of SRR versus depth the data showed a negative linear relation which implied that the depth distribution of the rates can be approximated by a power law function (Jørgensen 1978b; Jørgensen and Parkes, 2010; Holmkvist et al., 2011). The best-fit line for each station was calculated, excluding measurements from the top 0-10 cm to avoid the surface zone where sulfate is not the primary terminal electron acceptor (Appendix A, Fig. A3). There was no systematic difference between the sulfate reduction rate profiles across the transect (Appendix A, Fig. A3). Thus all the SRR data are compiled in one log-log graph (Fig. 5) and the best fit linear correlation, corrected for skewing by XXX (see section 2.5, last paragraph for more explanation), takes the following form:

$$\log \text{SRR} = \log a - b \times \log z \quad \text{or} \quad \text{SRR} = a \times z^{-b} \quad \text{Eq. (4)}$$

$$\text{SRR} = 5700 \times z^{-2.33} \text{ nmol cm}^{-3} \text{ d}^{-1} \quad \text{Eq. (5)}$$

The depth integrated SRR in $\text{nmol cm}^{-2} \text{ d}^{-1}$ was calculated by integration of Eq. (5). The rate predicted at the bottom of the bioturbated layer at 10 cm depth ($z=10 \text{ cm}$) ($22 \text{ nmol cm}^{-3} \text{ d}^{-1}$) was used as a mean rate within the upper mixed layer. The cumulative rate is shown in Fig. 5b. The cumulative rate distribution or organic matter mineralization coupled to sulfate reduction (Eq. (5)) was extrapolated down into the methane zone and all the way to the bottom of the HML. Thus the integration between the depth of the SMTZ and the bottom of the HML represents the depth integrated gross rate of methanogenesis. The underlying assumption is that the rate function of C_{org} mineralization vs. depth is dependent on the degradability of buried organic matter and not on whether the terminal process is sulfate reduction or methanogenesis. If we now assume a C_{org} oxidation state of zero, then the moles of SO_4^{2-} reduced are stoichiometrically equivalent to the moles of CH_4 produced when carbon mineralization is via methanogenesis rather than via sulfate reduction. The depth integrated methanogenesis estimated in this way is, as a first estimate, assumed to result in a corresponding upwards methane flux. The methane production ($J_{\text{CH}_4, \text{ex}}$) predicted from this SRR extrapolated calculation follow the same trend as the diffusive fluxes calculated from porewater gradients but are only $24 \pm 4 \%$ of the diffusive fluxes across the transect (Fig. 4b and 4d). This difference is discussed below in section 4.2.

4. DISCUSSION

4.1. The role of Holocene mud thickness and upward shift of SMTZ

The depth of the SMTZ depends on several factors such as a) the depth and intensity of bioirrigation, b) the balance of CH_4 production and SO_4^{2-} consumption, c) the mineralization rate of C_{org} , and thus the quality and quantity of the buried organic material, and d) the sedimentation rate, and thus the age of the organic matter at different depths in the

sediment (Toth and Lerman, 1977; Westrich and Berner, 1984; Canfield, 1991; Borowski et al., 1996; Borowski et al., 1999). Since the water depth is the same across the short Aarhus Bay transect and all stations are located in close proximity, it can be assumed that the organic matter deposited on the seafloor and concurrently being buried is of the same source and initially of the same quality. This assumption is supported by the fact that we see no trend along the transect of (i) total carbon or total nitrogen concentration (Appendix A1.1., Fig. A1), (ii) measured sulfate reduction rates (Appendix A.1.3., Fig. A3), and (iii) C_{org} mineralization stoichiometry including $r_{C:S}$ and $r_{C:N}$ mineralization ratios (see Appendix B.1.). An estimated 95% of all the organic matter mineralization takes place within the upper 50 cm at all stations (Fig. 5b) with a similar predominance of sulfate reduction as seen in other anoxic coastal sediments (Holmkvist et al., 2011; Jørgensen et al., 1990). Below 50 cm, SO_4^{2-} concentrations decrease down to the SMTZ with a quasi-linear gradient driven by AOM (e.g. Borowski et al., 1996; Borowski et al., 1999). Although the measured SRR are very similar at all stations, the SMTZ depth becomes increasingly shallow towards the gas bearing area. This shift in the depth of the SMTZ is likely due to processes occurring deeper in the sediment. If solute transport depended only on molecular diffusion then the depth of the SMTZ would depend linearly on the CH_4 flux from below the SMTZ (Dale et al., 2009) and, therefore, on the depth integrated rate of methanogenesis. Indeed, the shallowing of the SMTZ in the gas free area is accompanied by an increase in the thickness of the methanogenic HML (Table 2) and by an increase in the upward CH_4 flux (J_{CH_4} , Fig. 4b). However, the HML appears to have a rather constant thickness in the gas bearing area (Fig. 2b) and yet, the SMTZ (Table 1) and upward CH_4 fluxes (J_{CH_4} , Fig. 4b) continue to increase. This indicates that rather the upward shift of the SMTZ than the thickening of the HML is responsible for the additional formation of CH_4 . To illustrate this we use M24 as a starting point. The depth-integrated methanogenesis rate from the SMTZ (at 428 cm sediment depth) down to the base of the Holocene mud layer (at 724 cm sediment depth) calculated by integration of Eq. (5) is $0.68 \text{ nmol cm}^{-2} \text{ d}^{-1}$ at this station (Fig. 4d). The contribution of the deepening mud layer to methanogenesis at stations M25 to M30 can then be determined by integration of Eq. (5) at M25 to M30 from 428 cm down to the bottom of the HML at each station (Fig. 6). The calculated increase in depth integrated CH_4 production with increasing HML depth is relatively small (Fig. 6). At station M29A, for example, the HML is ca 1.8 m (or 24%) thicker than at M24 (Table 1 and Fig. 2). Yet the corresponding increase in methanogenesis at depth is only $0.17 \text{ nmol cm}^{-2} \text{ d}^{-1}$. This is an order of magnitude smaller than the total depth integrated CH_4 production ($2.02 \text{ nmol cm}^{-2} \text{ d}^{-1}$) at this station. The shortfall is accounted for by the upward shift of the SMTZ by 1.6 m between M24 and M29A. In other words, only 8% of the total increase in CH_4 production is due to the downwards thickening of the HML while the remaining 92 % is due to the 1.6 m upwards shift of the SMTZ towards the sediment surface. This shift pushes the methanogenic zone up into layers with much more labile organic carbon (as is evident from Fig. 5a) which thereby becomes available for CH_4 production. Thus, a positive feedback is created, whereby an upward shift of the SMTZ exposes more labile organic carbon to methanogenesis, thereby leading to more overall CH_4 production, further upward migration of the SMTZ, and eventually to formation of free gas. This shows that the HML thickening enhances the total volume of methanogenic sediment but that the main increase in overall methanogenesis is due to the expansion of the methanogenic zone upwards as the SMTZ rises towards the sediment surface. A steady state is reached for each coring site when the total depth integrated methanogenesis leading to upward methane flux is balanced by the downward flux of SO_4^{2-} .

The formation of free gas bubbles occurs when the partial pressure of the total dissolved gases in the porewater exceeds the hydrostatic pressure. The critical partial pressure of CH_4 for bubble formation, decreases in the presence of other gases (e.g. N_2 , CO_2 , H_2S), thus making it possible to form bubbles at lower CH_4 concentrations than saturation

concentrations for pure CH₄ gas (Schmid et al., 2003). The presence of gas bubbles can increase the molecular diffusion coefficient of CH₄ through the sediment as the diffusion coefficient of gases is four orders of magnitude higher in gaseous media than in aqueous solution (Luo and Zhou, 2006). Furthermore, Treude et al. (2005), suggested that ebullition processes in sediments can stimulate anaerobic methane oxidation and enhance SO₄²⁻ and CH₄ fluxes, thus pushing the SMTZ further up to the sediment surface. Hence, ebullitive processes could be a 3rd mechanism contributing to the feedback loop and exasperate CH₄ formation. As can be noted from Fig. 4 the total CH₄ production based on the extrapolated and integrated SRR ($J_{CH_4,ex}$) is only ca 24 % of the CH₄ fluxes calculated by Fick's First Law from porewater gradients. Nevertheless, both flux estimates show almost an identical shape along the transect indicating that not the absolute values, but the relative changes are important to understand the processes. A detailed discussion on reconciling depth-extrapolated methanogenesis rates and upwards methane fluxes can be found in Appendix C.

5. SUMMARY

As revealed from the discussion above, the HML has to have a certain thickness in order to enable sulfate depletion at depth and thus to initiate methane production. The minimal thickness of the HML to initiate CH₄ production depends on several factors such as the amount of POM that is deposited on the sea floor, the rate at which it is buried or mineralized by sulfate reducers and the amount and quality of POM that is buried below the SMTZ (e.g. Borowski et al., 1999 and references in there). Unfortunately we were not able to put a number on the minimal thickness necessary to initiate the production of CH₄, since it is dependent on too many factors and it needs to be modeled. However, we learned a great deal on the controlling mechanisms of CH₄ accumulation and the feedback loops leading to increasing CH₄ concentrations and fluxes along a transect in the sediment and cannot be derived from the presented results. However, we were able to clearly show (Fig. 6) that the upward shift of the SMTZ creates a positive feedback loop and therefore exasperates the in situ CH₄ production and fluxes towards the sediment surface while the HML thickening loses importance in the CH₄ formation process once the SMTZ begins to shift upwards. Additionally we suggest that the fluxes of CH₄ are potentially enhanced due to the faster diffusion of CH₄ (and other gases) in gas bearing sediments.

Acknowledgements. The research was partly funded by the European Community's Seventh Framework Programme (FP/2007-2013) under grant agreement n° 217246 made with the joint Baltic Sea research and development program BONUS, by the Swiss National Science Foundation (Grant no: PBEZP2-129527), the Danish National Science Foundation, ECO-CLIM (The Danish Council for Strategic Research) and the German Max Planck Society. We are grateful to Torben Vang and the ship crew of 'Susanne A' for their help during field work. Furthermore, we thank Mark Lever, Britta Gribsholt and Laura Lapham for their help with porewater sampling and Jeanette Johansen and Debbie Lemming for sampling and analysis. We also thank Laura Lapham and Dan McGinnis for insightful discussions.

6. REFERENCES

- Arnosti, C., 2004. Speed bumps and barricades in the carbon cycle: substrate structural effects on carbon cycling. *Mar. Chem.* **92**, 263-273.
- Bennike, O. and Jensen, J. B., 1998. Late- and postglacial shore level changes in the Southwestern Baltic Sea. *Bulletin of the Geological Society of Denmark* **45**, 27-38.
- Berner, R. A., 1977. Stoichiometric models for nutrient regeneration in anoxic sediments. *Limnol. Oceanogr.* **22**, 781-786.
- Best, A. I., Richardson, M. D., Boudreau, B. P., Judd, A. G., Leifer, I., Lyons, A. P., Martens, C. S., Orange, D. L., and Wheeler, S. J., 2006. Shallow seabed methane gas could pose coastal hazard. *EOS* **87**, 213-220.

- Boetius, A., Ravensschlag, K., Schubert, C. J., Rickert, D., Widdel, F., Gieseke, A., Amann, R., Jørgensen, B. B., Witte, U., and Pfannkuche, O., 2000. A marine microbial consortium apparently mediating anaerobic oxidation of methane. *Nature* **407**, 623-626.
- Borowski, W. S., Paull, C. K., and Ussler, W., 1999. Global and local variations of interstitial sulfate gradients in deep-water, continental margin sediments: Sensitivity to underlying methane and gas hydrates. *Mar. Geol.* **159**, 131-154.
- Boudreau, B. P., 1997. *Diagenetic models and their implementation. Modeling transport and reactions in aquatic sediments*. Springer-Verlag, Berlin, Heidelberg, New York, London, Paris, Tokyo, Hong Kong.
- Bower, C. E. and Holmhansen, T., 1980. A salicylate-hypochlorite method for determining ammonia in seawater. *Can. J. Fish. Aquat. Sci.* **37**, 794-798.
- Burdige, D. J. and Komada, T., 2011. Anaerobic oxidation of methane and the stoichiometry of remineralization processes in continental margin sediments. *Limnol. Oceanogr.* **56**, 1781-1796.
- Canfield, D. E., 1991. Sulfate reduction in deep-sea sediments. *Am. J. Sci.* **291**, 177-188.
- Canfield, D. E. and Thamdrup, B., 2009. Towards a consistent classification scheme for geochemical environments, or, why we wish the term 'suboxic' would go away. *Geobiology* **7**, 385-392.
- Claypool, G. E., Milkov, A. V., Lee, Y. J., Torres, M. E., Borowski, W. S., and Tomaru, H., 2006. Microbial methane generation and gas transport in shallow sediments of an accretionary complex, southern Hydrate Ridge (ODP Leg 204), offshore Oregon, USA. In *Proc. ODP, Sci. Results*, **204** (eds. A. M. Trehu, G. Bohrmann, M. E. Torres, and F. S. Colwell). pp 1-52.
- Dale, A. W., Aguilera, D. R., Regnier, P., Fossing, H., Knab, N. J., and Jørgensen, B. B., 2008. Seasonal dynamics of the depth and rate of anaerobic oxidation of methane in Aarhus Bay (Denmark) sediments. *J. Mar. Res.* **66**, 127-155.
- Dale, A. W., Regnier, P., Van Cappellen, P., Fossing, H., Jensen, J. B., and Jørgensen, B. B. 2009. Remote quantification of methane fluxes in gassy marine sediments through seismic survey. *Geology* **37**, 235-238.
- Gustafsson, B. G. and Westman, P., 2002. On the causes for salinity variations in the Baltic Sea during the last 8500 years. *Paleoceanography* **17**.
- Holmkvist, L., Ferdelman, T. G., and Jørgensen, B. B., 2011. A cryptic sulfur cycle driven by iron in the methane zone of marine sediment (Aarhus Bay, Denmark). *Geochim. Cosmochim. Acta* **75**, 3581-3599.
- Houmark-Nielsen, M., 1987. Pleistocene stratigraphy and glacial history of the central part of Denmark. *Bulletin of the Geological Society of Denmark* **36**, 189.
- IPCC, 2007. *Climate Change 2007: The physical science basis. Contribution of working group I to the fourth assessment report of the Intergovernmental Panel on Climate Change*. Cambridge University Press, Cambridge, United Kingdom and New York, NY, USA.
- Jensen, J. B. and Bennike, O., 2009. Geological setting as background for methane distribution in Holocene mud deposits, Aarhus Bay, Denmark. *Cont. Shelf Res.* **29**, 775-784.
- Jensen, J. B., Bennike, O., Lemke, W., and Kuijpers, A., 2004. The Sorebaelt gateway to the Baltic. *GEUS Bulletin* **7**, 45-48.
- Jørgensen, B. B., 1978a. Comparison of methods for the quantification of bacterial sulfate reduction in coastal marine sediments. 1. Measurement with radiotracer techniques. *Geomicrobiol. J.* **1**, 11-27.
- Jørgensen, B. B., 1978b. Comparison of methods for the quantification of bacterial sulfate reduction in coastal marine sediments. 2. Calculation from mathematical models. *Geomicrobiol. J.* **1**, 29-47.
- Jørgensen, B. B., Bang, M., and Blackburn, T. H. 1990. Anaerobic mineralization in marine sediments from the Baltic Sea-North Sea transition. *Mar Ecol. Prog. Ser.* **59**, 39-54.
- Jørgensen, B. B., Böttcher, M. E., Luschen, H., Neretin, L. N., and Volkov, II, 2004. Anaerobic methane oxidation and a deep H₂S sink generate isotopically heavy sulfides in Black Sea sediments. *Geochim. Cosmochim. Acta* **68**, 2095-2118.
- Jørgensen, B. B. and Kasten, S., 2006. Sulfur cycling and methane oxidation. In: Schulz, H. D. and Zabel, M. Eds.), *Marine Geochemistry*. Springer, Berlin.
- Jørgensen, B. B. and Parkes, R. J., 2010. Role of sulfate reduction and methane production by organic carbon degradation in eutrophic fjord sediments (Limfjorden, Denmark). *Limnol. Oceanogr.* **55**, 1338-1352.
- Judd, A. G. and Hovland, M., 1992. The evidence of shallow gas in marine sediments. *Cont. Shelf Res.* **12**, 1081-1095.
- Kallmeyer, J., Ferdelman, T. G., Weber, A., Fossing, H., and Jørgensen, B. B., 2004. A cold chromium distillation procedure for radiolabeled sulfide applied to sulfate reduction measurements. *Limnol. Oceanogr-Methods* **2**, 171-180.

- Martens, C. S., Albert, D. B., and Alperin, M. J., 1998. Biogeochemical processes controlling methane in gassy coastal sediments - Part 1. A model coupling organic matter flux to gas production, oxidation and transport. *Cont. Shelf Res.* **18**, 1741-1770.
- McGinnis, D. F., Greinert, J., Artemov, Y., Beaubien, S. E., and Wüest, A., 2006. Fate of rising methane bubbles in stratified waters: How much methane reaches the atmosphere? *J. Geophys. Res.-Oceans* **111**.
- Meyers, P. A., 1994. Preservation of elemental and isotopic source identification of sedimentary organic matter. *Chem. Geol.* **114**, 289-302.
- Milucka, J., Ferdelman, T. G., Polerecky, L., Franzke, D., Wegener, G., Schmid, M., Lieberwirth, I., Wagner, M., Widdel, F., Kuypers, M. M. (2012) Zero-valent sulphur is a key intermediate in marine methane oxidation. *Nature* xxxx
- Mogollon, J. M., Dale, A. W., Fossing, H., and Regnier, P., 2011. Timescales for the development of methanogenesis and free gas layers in recently-deposited sediments of Arkona Basin (Baltic Sea). *Biogeosciences Discussions* **8**, 7623-7669.
- Reeburgh, W. S., 1980. Anaerobic methane oxidation - rate depth distributions in Skan Bay sediments. *Earth Planet. Sc. Lett.* **47**, 345-352.
- Sansone, F. J. and Martens, C. S., 1978. Methane oxidation in Cape Lookout Bight, North-Carolina. *Limnol. Oceanogr* **23**, 349-355.
- Thiessen, O., Schmidt, M., Theilen, F., Schmitt, M., and Klein, G., 2006. Methane formation and distribution of acoustic turbidity in organic-rich surface sediments in the Arkona Basin, Baltic Sea. *Cont. Shelf Res.* **26**, 2469-2483.
- Toth, D. J. and Lerman, A., 1977. Organic matter reactivity and sedimentation rates in ocean. *Am. J. Sci.* **277**, 465-485.
- Westrich, J. T. and Berner, R. A., 1984. The role of sedimentary organic matter in bacterial sulfate reduction - The G Model tested. *Limnol. Oceanogr* **29**, 236-249.
- Whiticar, M. J., 2002. Diagenetic relationships of methanogenesis, nutrients, acoustic turbidity, pockmarks and freshwater seepages in Eckernförde Bay. *Mar. Geol.* **182**, 29-53.

TABLES

Table 1. Solute fluxes and stoichiometry of mineralization across the transect. Station position is given as the distance from the gas free to gas bearing sediment. All fluxes (J) are in $\text{nmol cm}^{-2} \text{ d}^{-1}$ and are calculated at the depth of the sulfate methane transition zone (SMTZ). The depth of the Holocene mud layer (HML) and the SMTZ are indicated. The mean oxidation state of organic matter (Appendix B.1.), ox , is calculated as $4-8/r_{C:S}$ (cf. Burdige and Komada, 2011), where $r_{C:S}$ is the ratio between moles of total CO_2 produced per mole of SO_4^{2-} reduced during sulfate reduction. $r_{C:N}$ is the C:N ratio of the organic material being mineralized (Appendix B.1.).

Station	Distance from transition (m) ^a	Depth of HML (cm) ^b	SMTZ (cm)	J_{SO_4}	J_{CH_4}	J_{TCO_2}	J_{NH_4}	J_{Ca}	J_{Mg}	$r_{C:S}$	ox	$r_{C:N}$
M22A	-207	466	—	5.2		8.7	0.4	0.2	0.1	1.3	-2.0	8.1
M22	-166	488	—	6.0		10.6	0.4			1.8	-0.5	14.0
M23	-116	613	405	7.2	3.2	18.3	0.9			1.8	-0.4	11.8
M24	-75	724	428	4.3	3.2	5.2	1.4			1.9	-0.2	7.5
M25	-46	883	391	5.8	3.2	18.6	1.9			2.2	0.4	9.0
M26	-12	868	373	6.0	5.0	11.9	1.9			2.2	0.3	7.9
M27	34	843	328	6.9	6.2	29.0	2.2			2.3	0.5	10.0
M27A	54	972	284	13.0	7.9	25.5	2.5	0.3	0.3	3.3	1.6	8.9
M28	77	820	265	11.1	8.2	34.6	2.6			2.6	1.0	11.1
M29	113	864	238	12.5	7.5	33.1	2.9			2.2	0.4	10.3
M29A	162	900	268	13.0	9.5	30.5	2.5	0.5	0.5	3.7	1.8	10.0
M30	201	807	257	10.6	9.3	33.2	2.8			1.9	-0.3	9.7
Mean, no gas				5.7	3.6	12.2	1.1			1.9	-0.4	9.7
$\pm 1\sigma$				1.0	0.9	5.4	0.7			0.3	0.9	2.6
Mean, gas		868		11.2	8.1	31.0	2.6			2.7	0.8	10.0
$\pm 1\sigma$		61		2.3	1.2	3.4	0.2			0.7	0.8	0.7
Mean, transect				8.4	6.3	21.6	1.9	0.3	0.3	2.3	0.2	9.9
$\pm 1\sigma$				3.3	2.5	10.7	0.9	0.2	0.2	0.7	1.0	1.8

^a negative = gas free sediment; positive = gas bearing sediment

^b error = ± 25 cm

^c see Appendix B.1. for explanation

FIGURES

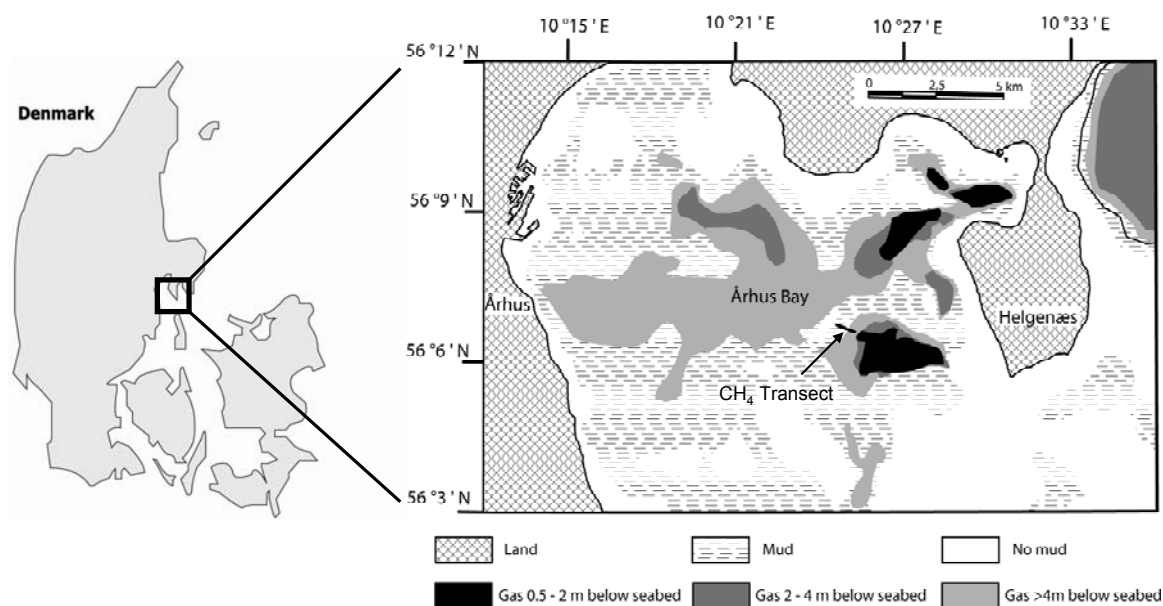


Fig. 1. Location of the sampling transect in Aarhus Bay. The map shows the distribution of Holocene mud and of gas with the upper gas front at different depths below seafloor (modified from Jensen and Bennike, 2009). Areas without mud consist mainly of glacial till and sand.

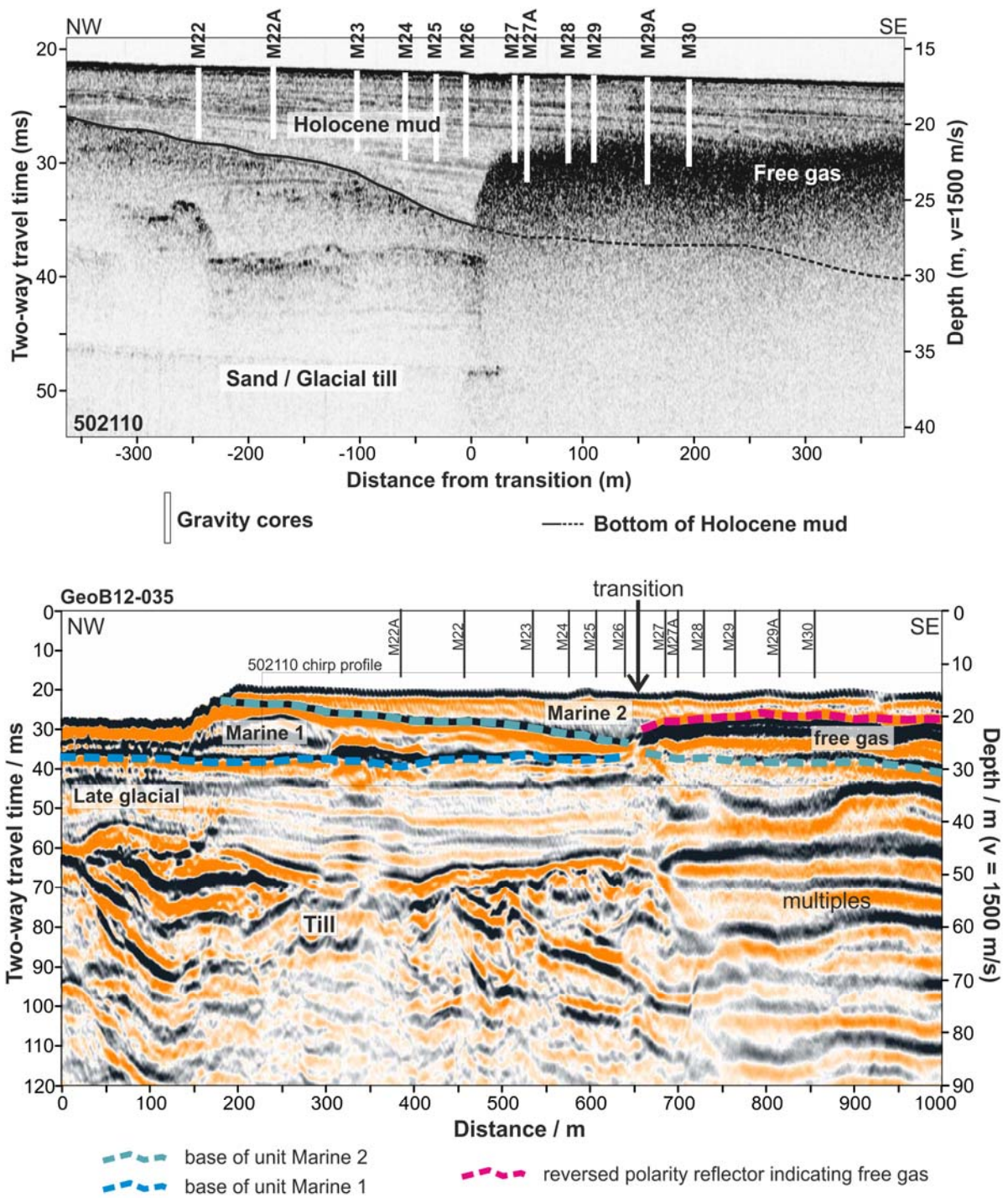
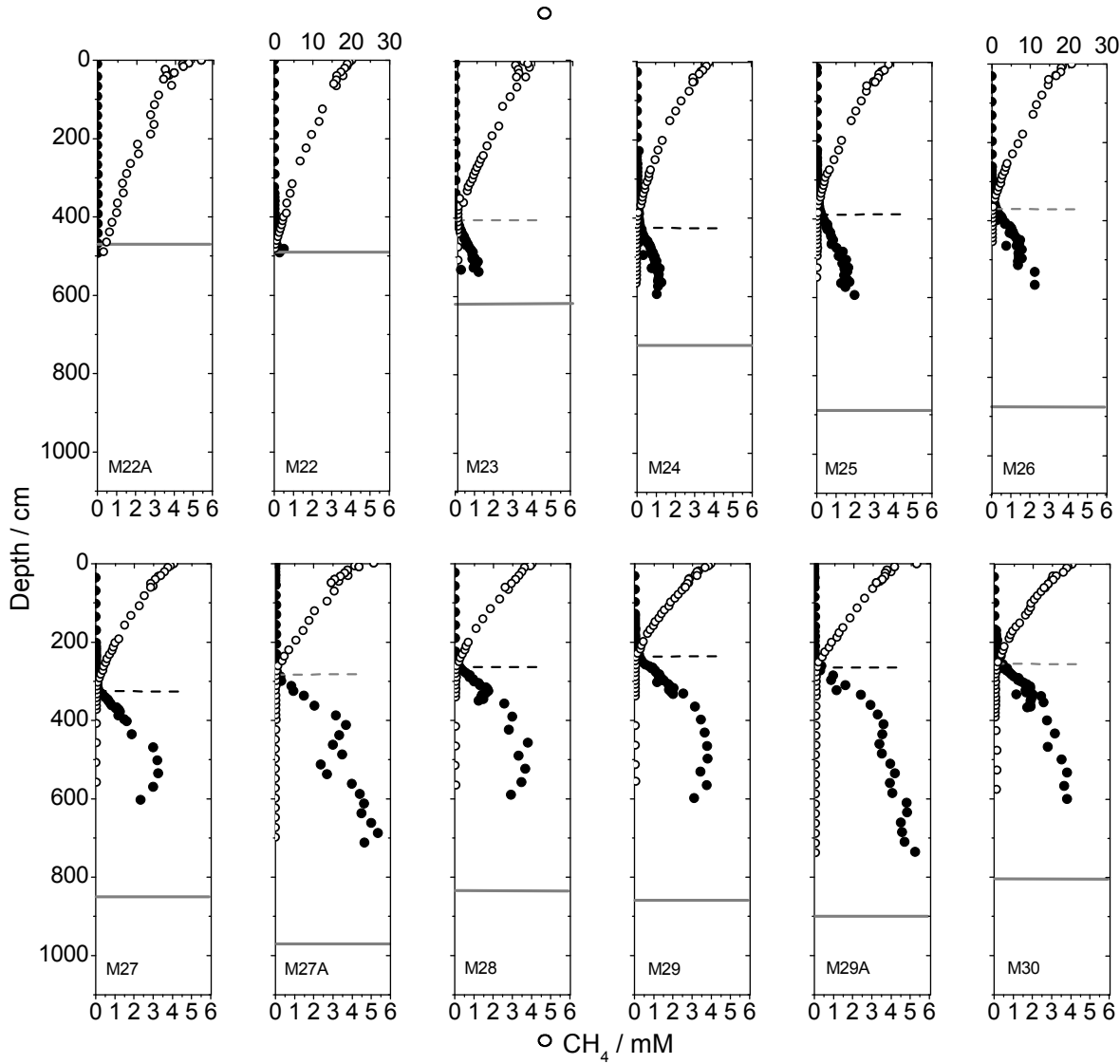


Fig. 2. (a) Single channel seismic (Chirp) transect (METROL-502110) showing coring positions, penetration depths of gravity cores, and free gas distribution, The bottom of the Holocene mud layer (=Marine Unit 2) of the Chirp transect is highlighted with a black line. (b) Multichannel seismic profile along the same transect as (a). The multichannel seismic profile penetrates through the methane gas and reveals an early Holocene sand layer (Marine

Unit 1) and a later Holocene mud layer (Marine Unit 2). The vertical arrow points to the transition between gas-free and gas bearing sediment.



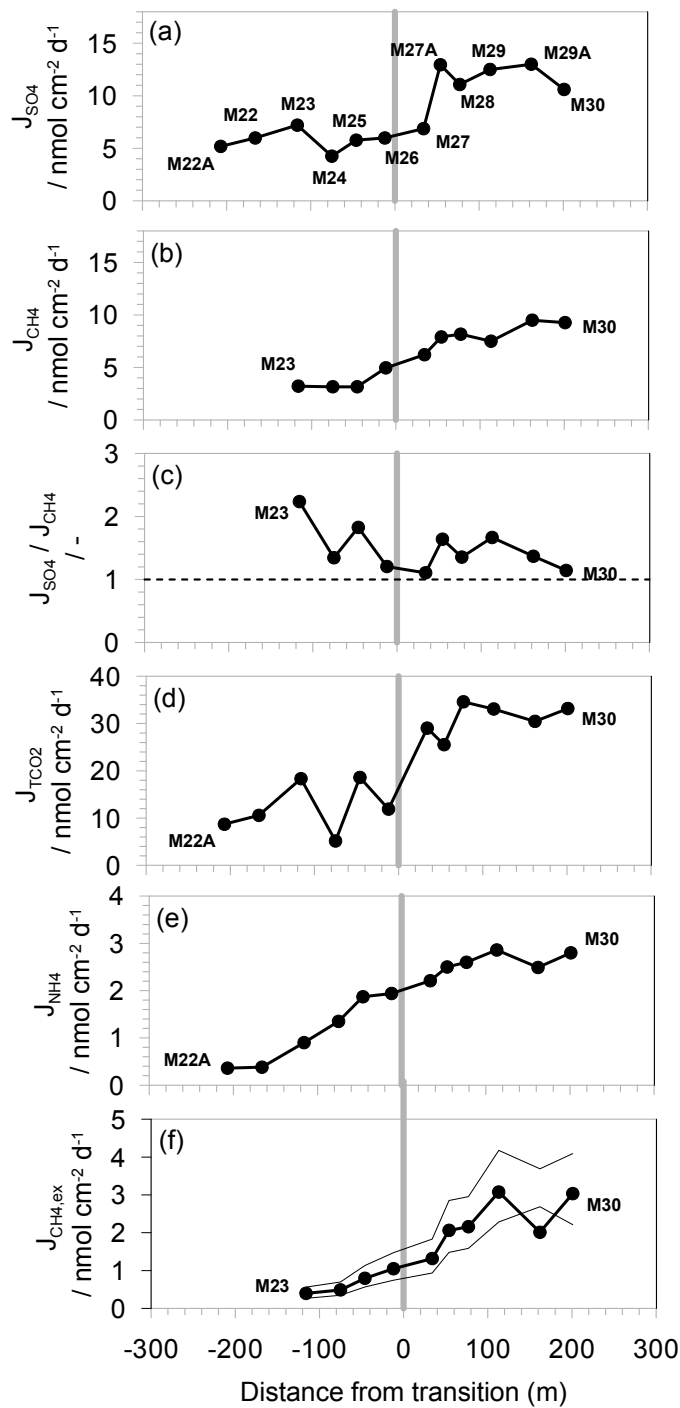


Fig. 4. Diffusive fluxes of (a) sulfate (J_{SO_4}) and (b) methane (J_{CH_4}) to the sulfate methane transition zone (SMTZ) along the transect, and (c) their ratio (J_{SO_4}/J_{CH_4}) where the horizontal dashed line indicates the 1:1 ratio (see also Appendix B.1., Table B1). Panel (d) shows the CH_4 production calculated by extrapolation of measured SRR from the SMTZ down to the bottom of the HML (see section 2.5.2.). The thin lines in (d) represent the uncertainty in the fluxes as $\pm 1\sigma$ of the pooled SRR in Fig 5a while the vertical gray lines denote the transition between gas free and gas bearing sediments. All fluxes are in units of $\text{nmol cm}^{-2} \text{ d}^{-1}$. Methane was not observed at stations M22A and M22 (within the depth of the sediment cored) and therefore CH_4 fluxes were not calculated at these stations.

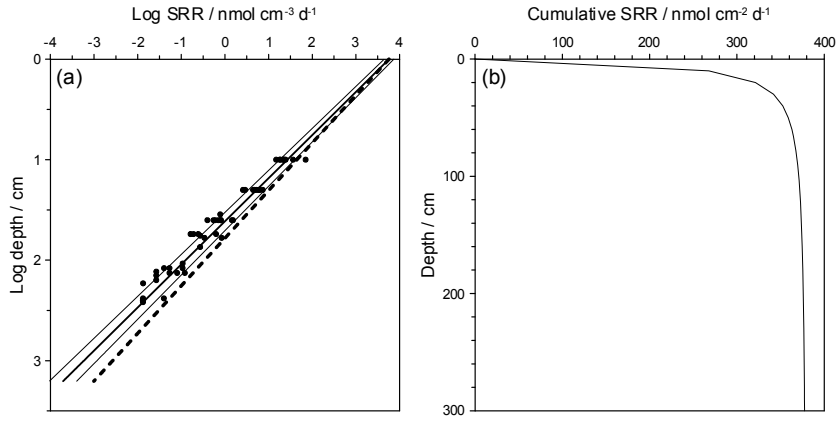


Fig. 5. (a) Log₁₀-transformed sulfate reduction rates for all cores along the transect using data from Fig. A3 without outliers. The solid black line shows the best fitted power law function corrected for skewing ($SRR = 5700 \times z^{-2.33}$ nmol cm⁻³ d⁻¹; $R^2 = 0.xx$). Thin lines show the 95% confidence interval. The thick broken line represents the power law represented by $SRR = 5700 \times z^{-2.10}$ nmol cm⁻³ d⁻¹ (Eq. C.1.) which provides the best agreement with the methane fluxes calculated from porewater gradients when integrated over the methane zone (see Appendix C.1. and Fig. C1). (b) Cumulative SRR calculated as $5700 \int_0^z z^{-2.33} dz$ nmol cm⁻³ d⁻¹ and used as an estimate for organic matter mineralization.

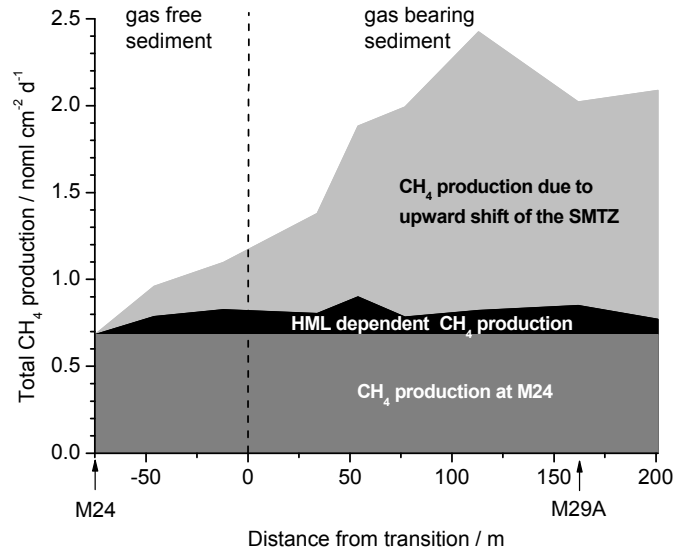


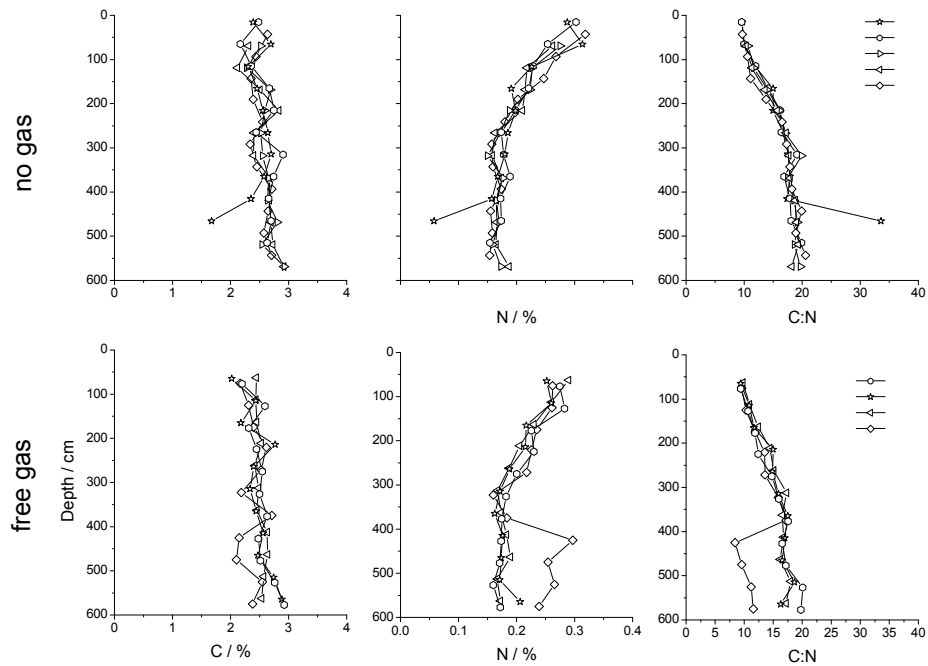
Fig. 6. Separation of the extrapolated depth-integrated rates of methanogenesis in Fig. 4d calculated using Eq. (5) into the contribution from the upward shift of the SMTZ (light gray) and the contribution from the deepening of the HML (black) with reference to the methane production rate at M24 (dark gray). Production of CH₄ is calculated in defined intervals either from the SMTZ to the reference depth of 428 cm at station M24 (contribution of SMTZ shift to the total CH₄ production) or from the reference to the bottom of the the HML (contribution of the HML to the total CH₄ production).

APPENDIX A

A.1. Methods and Results

A.1.1. Total carbon and total nitrogen

Total carbon and nitrogen have been analyzed in order to have an insight on the C and N distribution and to detect any strong differences in sediment quality along the transect. The dried and ground sediment samples were analyzed on a CN-analyzer as described in greater details in section 2.4.4. (main text). The TC and TN content was very similar at all stations across the transect (Fig. A1). TC content was in the range of 2-3% and showed little change with depth and across the transect. At M22 the gravity core penetrated into the the glacial organic poor till and only reached a depth of ca 4.7 m. This is reflected by the large change in C:N ratio from ca 9 to 18 at 5.5 m depth. The small variation of the C and N content along the transect indicates similar sediment quality at all stations.



Mg^{2+} and Ca^{2+} are decreasing only slightly with depth, indicating that net carbonate precipitation or dissolution are of minor importance. The mean fluxes are calculated with Fick's First Law (main text, section 2.5.1., Eq. 3) and result for both constituents in 0.3 ± 0.2 (mean $\pm \sigma$) $\text{nmol cm}^{-2} \text{d}^{-1}$.

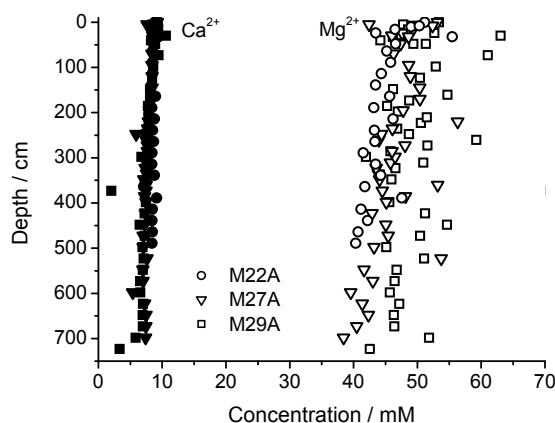


Fig. A2. Dissolved calcium (filled symbols) and magnesium (open symbols) concentrations measured at three stations in May 2010.

A.1.3. SRR at individual stations

The distribution of sulfate reduction rates along the transect and with depth give further indirect insight in the distribution of the C quality in terms of mineralization rates. Sulfate reduction rates (SRR) were measured at each station sampled in October 2009 (Fig. A3). A detailed description of the SRR measurements can be found in the main text section 2.4.6.. The SRR generally decreased with depth according to a power law as has been described in previous studies (e.g. Jørgensen 1978b; Jørgensen and Parkes, 2010; Holmkvist et al., 2011). The best-fit line for each station was calculated, excluding measurements from the top 0-10 cm to avoid the surface zone where sulfate is not the primary terminal electron acceptor (Fig. A3). As can be seen from the slopes represented in Fig. A3, there is no systematic difference between the SRR profiles across the transect.

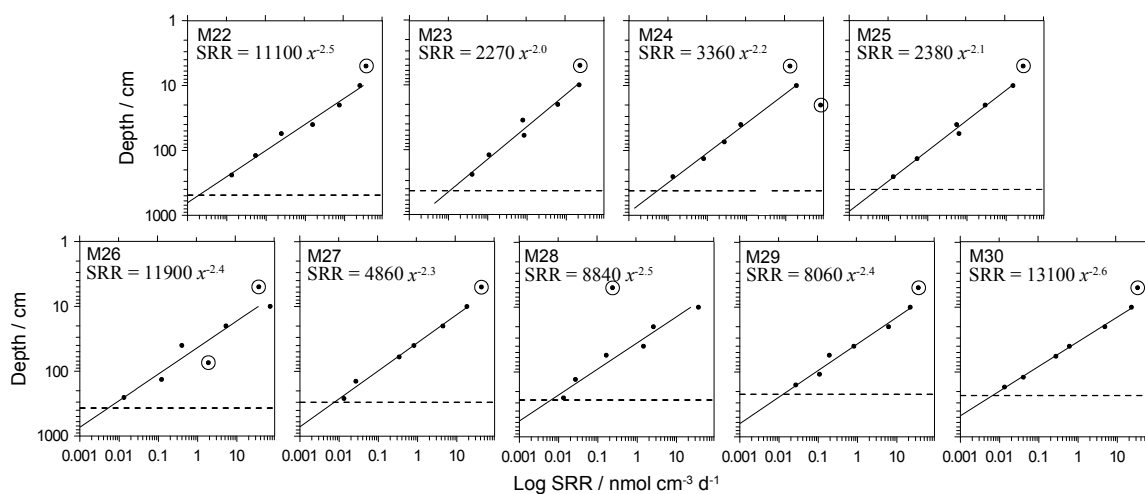


Fig. A3. Sulfate reduction rates at all stations sampled in October 2010 in double logarithmic plots. The dashed lines show the depth of the sulfate methane transition zone (SMTZ) where $[\text{CH}_4] = [\text{SO}_4^{2-}]$. Full lines show the best log-log linear fit and indicate the power law of SRR = $a \times z^{-b}$ (omitting the encircled outliers). R^2 is > 0.95 for all plots.

A.1.4. Dissolved ammonium and dissolved inorganic C

A.1.4.1. Dissolved ammonium concentration

Porewater extracted with Rhizons for ammonium (NH_4^+) analysis was stored in Eppendorf vials at 4 °C until analysis. NH_4^+ was measured photometrically according to the Danish Standard DS 224 protocol adapted for seawater samples (Bower and Holmhansen, 1980). The porewater was diluted 100 fold prior to the addition of 120 μL of the salicylic acid catalyst (22 g sodium salicylate and 0.014 g dihydrous sodium nitroprusside dissolved in 50 mL Mili-Q water) to 1 mL of diluted porewater sample. The sample was shaken vigorously. Thereafter, 200 μL of alkaline hypochlorite solution (consisting of 1 part 5% sodiumhypochlorit and 9 parts alkaline citrate [18.5 g sodium hydroxide plus 120 g dihydrous tri-sodium-citrate dissolved in 1000 mL Mili-Q water]) was added and mixed thoroughly. After incubating the samples for 1 h in the dark at room temperature the absorbance was measured at 640 nm on a BioTek PowerWave XS2 plate reader.

NH_4^+ concentrations increased at all stations with depth due to mineralization of buried organic matter (Fig. A4).

A.1.4.2. Dissolved inorganic carbon concentration

Dissolved inorganic carbon was analyzed on porewater extracted with Rhizons. Samples were stored head space free in 2 mL glass vials (Zinsser) at 4 °C until analysis. Gas tight Exetainer® vials were flushed with He-gas for 5 min and 50 μL of phosphoric acid (85% w/v) was added. Thereafter, between 50 and 300 μL of sample was added to the Exetainer® vial and equilibrated for 24 h before measurement on a Finnigan GasBench II (Thermo Fisher Scientific) connected to a Delta Plus V isotope ratio mass spectrometer (IRMS) via a ConFlo IV interface. Total dissolved inorganic carbon is denoted TCO_2 ($= \text{CO}_2 + \text{H}_2\text{CO}_3 + \text{HCO}_3^- + \text{CO}_3^{2-}$).

TCO_2 concentrations increased at all stations with depth due to mineralization of buried organic matter (Fig. A4).

A.1.4.3. Modeled fluxes of ammonium and dissolved inorganic carbon.

Diffusive fluxes of NH_4^+ and TCO_2 were estimated from the concentration gradient in the porewater profiles using Fick's First Law and applying Eq. 3 (main text) with the following diffusion coefficients:

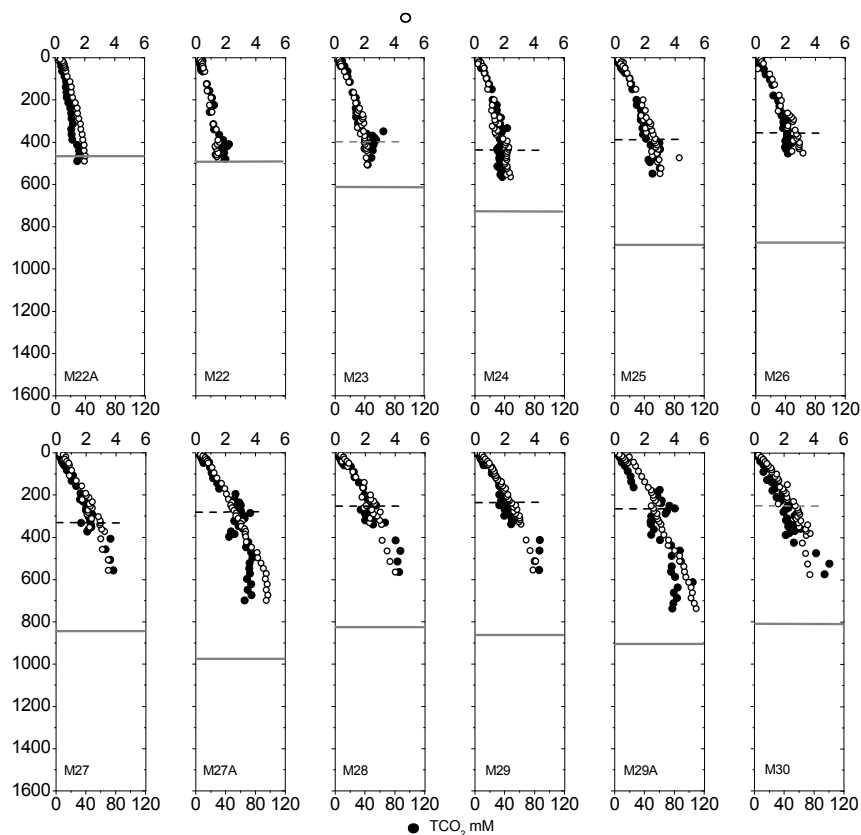
$$D_{\text{NH}_4^+} = 1.081 \text{ cm}^2 \text{ d}^{-1}$$

$$D_{\text{TCO}_2} = 0.616 \text{ cm}^2 \text{ d}^{-1}$$

The diffusion coefficient for TCO_2 was taken to be that for the bicarbonate ion (HCO_3^-) since this is the major carbonate species (~90-95 % of TCO_2) at pH of 7 to 8 typically encountered in subsurface marine sediments. Diffusion coefficients were corrected for tortuosity by dividing by $1 - \ln(\phi^2)$ using the mean porosity value at the SMTZ as well as for salinity of 30 and temperature (Boudreau, 1997; Dale et al., 2008).

Scatter in the NH_4^+ and TCO_2 data prevented their fluxes to be calculated from a linear fit through the data points. Thus, these data were fitted by a polynomial curve of the type $\alpha + \beta \times z + \gamma \times z^2$ followed by determination of the parameters α , β and γ using the `NonlinearModelFit` function in MATHEMATICA v 7.0. The derivative of the polynomial curve at the SMTZ depth was then calculated and substituted into Eq. (3) (main text). NH_4^+ and TCO_2 fluxes were always directed upwards (out of the sediment). All fluxes are reported in positive units.

TCO_2 fluxes out of the SMTZ increased from $12.2 \pm 5.4 \text{ nmol cm}^{-2} \text{ d}^{-1}$ to $31.0 \pm 3.4 \text{ nmol cm}^{-2} \text{ d}^{-1}$ along the transect (Fig. A5, Table 1) while NH_4^+ fluxes increased from $1.1 \pm 0.7 \text{ nmol cm}^{-2} \text{ d}^{-1}$ to $2.6 \pm 0.2 \text{ nmol cm}^{-2} \text{ d}^{-1}$ (Fig. A5, Table 1)



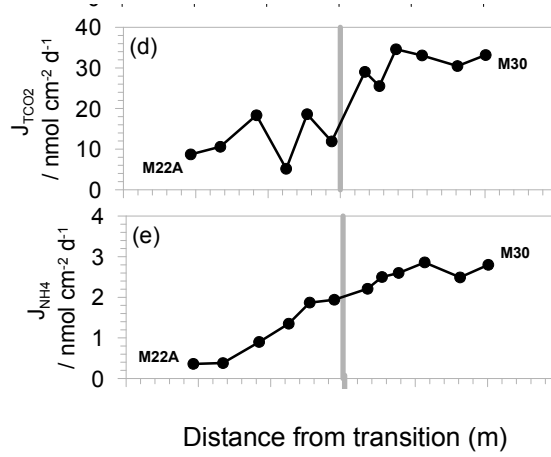


Fig. A5. Diffusive fluxes of (a) total carbon dioxide (TCO₂, i.e. H₂CO₃, HCO₃⁻, CO₃²⁻, and CO₂; J_{TCO2}) and (b) ammonium (NH₄⁺) out of the top of the SMTZ. The vertical gray lines denote the transition between gas-free and gas-bearing sediments.

APPENDIX B

B.1. Stoichiometry of organic matter mineralization

The concentration profiles of porewater TCO₂, NH₄⁺ (Fig. A4) and SO₄²⁻ (main text, Fig. 3) were used to calculate the stoichiometry of sulfate reduction and methanogenesis in the sediment and compare to the theoretical Redfield stoichiometry (Table B1). The oxidation state (*ox*) of organic carbon being mineralized in the sediment can be derived from the following Eq. (B.1) (Berner, 1977; Burdige, 2006; Burdige and Komada, 2011):

$$r_{C:S} = 8/(4-ox) \text{ or rearranged: } ox = 4-(8/r_{C:S}) \quad \text{Eq. (B.1)}$$

where $r_{C:S}$ is the ratio between moles of TCO₂ produced per mole of SO₄²⁻ reduced during sulfate reduction. The $r_{C:S}$ values were thus estimated from linear plots of TCO₂ versus SO₄²⁻ (for SO₄²⁻ > 1 mM) (Fig. B1a) using the equation:

$$r_{C:S} = -\frac{dTCO_2}{dSO_4^{2-}} \cdot \frac{D_{TCO_2}}{D_{SO_4^{2-}}} \quad \text{Eq. (B.2)}$$

where $dTCO_2 / dSO_4^{2-}$ is the slope of the linear regression line (through origin) and D is the diffusion coefficient (cm² d⁻¹) of TCO₂ or SO₄²⁻. Similarly, the C_{org}:N_{org} ratio of the organic material being mineralized ($r_{C:N}$) was calculated from plots of TCO₂ versus NH₄⁺ (Fig. B1b)

$$r_{C:N} = -\frac{dTCO_2}{dNH_4^+} \cdot \frac{D_{TCO_2}}{D_{NH_4^+}} \quad \text{Eq. (B.3)}$$

These calculations assume that POC mineralization dominates the distribution of the porewater solutes in Aarhus Bay and that the contribution of carbonate dissolution and precipitation to the total TCO₂ pool is negligible.

Using the slopes of these correlations in Fig. B1 and Eq. (B.2) and Eq. (B.3), the number of moles of TCO₂ produced per mole of SO₄²⁻ reduced and the moles NH₄⁺ produced during mineralization were calculated. The ratio

($r_{C:S}$) increased from 1.3 at M22A to a maximum of 3.7 at M29A with a mean value of 2.3 ± 0.7 (main text, Table 1). There was a great deal of scatter in the TCO_2 profiles indicative of sampling or analytical artifacts. The $\text{C}_{\text{org}}:\text{N}_{\text{org}}$ ratio of the material being mineralized ($r_{C:N}$) was 9.9 ± 1.8 (main text, Table 1) and was in accordance with the measured TC:TN ratios (Appendix Fig. A1). Since the fluxes of Ca^{2+} and Mg^{2+} were only a small fraction of the TCO_2 fluxes (main text, Table 1), the error in $r_{C:S}$ and $r_{C:N}$ associated with carbonate dissolution or precipitation is likely to be insignificant.

Carbon oxidation states, ox , calculated using Eq. (B.1) were -0.4 ± 0.9 at the stations without gas and $+0.8 \pm 0.8$ in gas-bearing sediments, giving an overall mean of 0.2 ± 1.0 for the transect (main text, Table 1). A slightly positive oxidation state of 0.2 means that slightly less than 0.5 mole of SO_4^{2-} is reduced per mole of C_{org} mineralized during sulfate reduction compared to the simplified formulation in Table B1. Similarly, more TCO_2 will be produced relative to CH_4 during methanogenesis. If the number of moles of SO_4^{2-} reduced to C_{org} oxidized is $1/r_{C:S}$, then 47 moles of SO_4^{2-} will be reduced per 106 moles of C_{org} mineralized. Similarly, the amount of CH_4 and TCO_2 produced during methanogenesis per 106 moles of C_{org} mineralized is equal to $106 \times (4 - ox)/8$ and $106 \times (4 + ox)/8$, respectively (Burdige and Komada, 2011), giving a $\text{CH}_4:\text{TCO}_2$ stoichiometry of 50:56 instead of 53:53 (Table B1).

Collating this information, the porewater profiles of SO_4^{2-} , NH_4^+ and TCO_2 are consistent with the following stoichiometry for SO_4^{2-} reduction and methanogenesis:

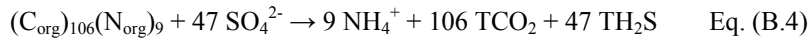
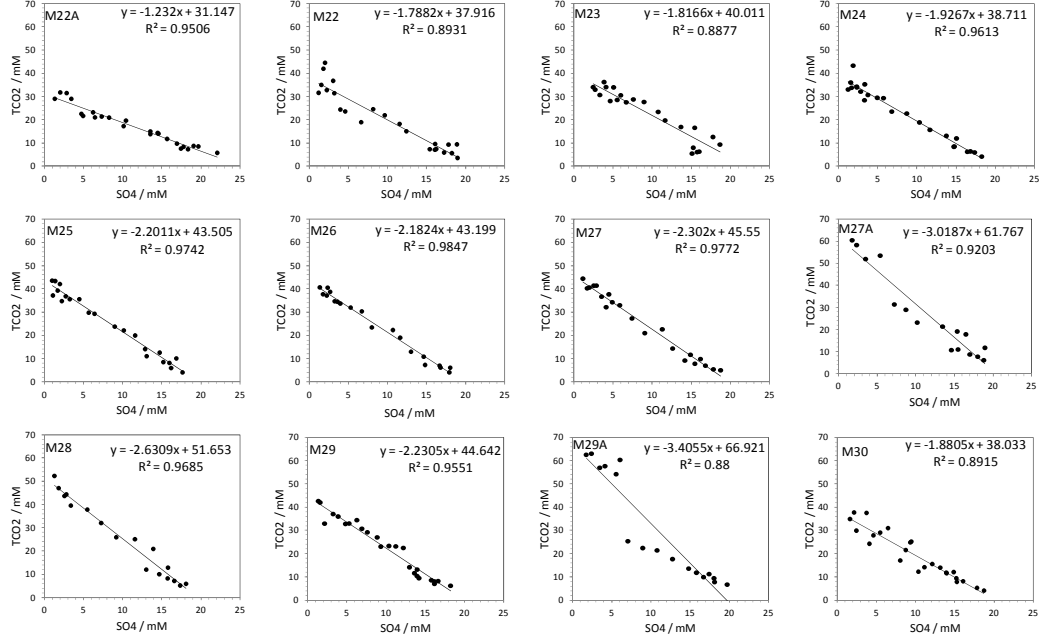
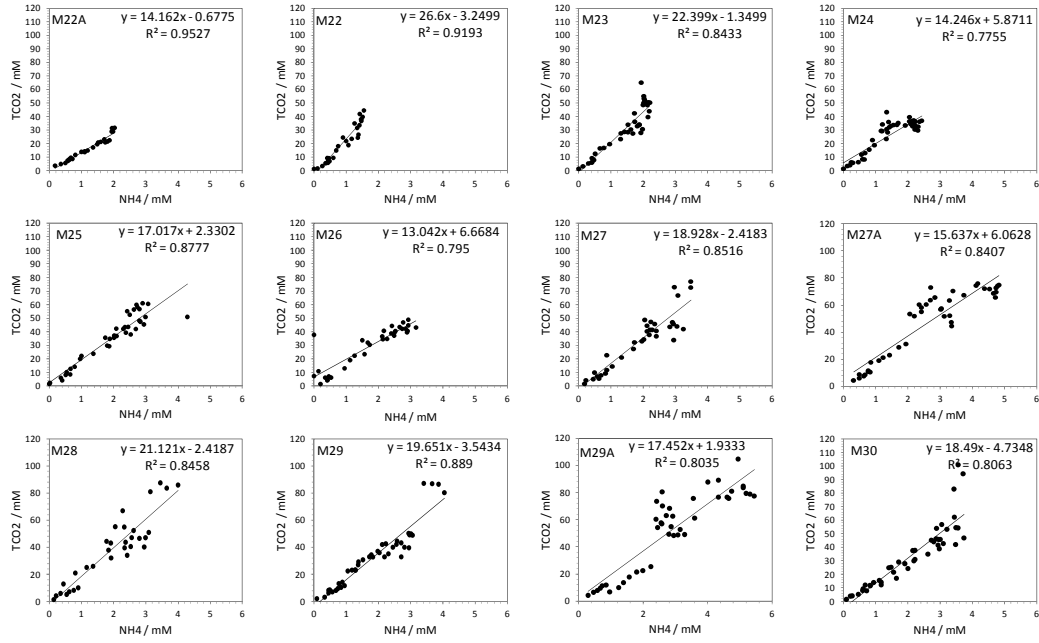


Table B1. Stoichiometric ratios for mineralization of organic matter by sulfate reduction and methanogenesis assuming Redfield stoichiometry ($\text{C}_{\text{org}}/\text{N}_{\text{org}} = r_{C:N} = 6.6$) and a carbon oxidation state of zero ($\text{C}_{\text{org}} \approx [\text{CH}_2\text{O}]$). Also shown is the stoichiometry of anaerobic oxidation of methane (AOM). $r_{C:S}$ is the $\text{C}_{\text{org}}/\text{SO}_4^{2-}$ ratio.

Process	Stoichiometry	$r_{C:S}$	$r_{C:N}$
Sulfate reduction	$(\text{C}_{\text{org}})_{106}(\text{N}_{\text{org}})_{16} + 53\text{SO}_4^{2-} \rightarrow 106\text{CO}_2 + 16\text{NH}_4^+ + 53\text{H}_2\text{S}$	2	6.6
Methanogenesis	$(\text{C}_{\text{org}})_{106}(\text{N}_{\text{org}})_{16} \rightarrow 53\text{CO}_2 + 53\text{CH}_4 + 16\text{NH}_4^+$	—	6.6
AOM	$\text{CH}_4 + \text{SO}_4^{2-} \rightarrow \text{CO}_2 + \text{H}_2\text{S}$	1	—



(a)



(b)

Fig. B1. (a) Parameter plots of concentrations of total carbon dioxide (TCO₂, i.e. H₂CO₃, HCO₃⁻, CO₃²⁻, and CO₂) versus SO₄²⁻ for all data where SO₄²⁻ > 1 mM. (b) Parameter plots of concentrations of total carbon dioxide (TCO₂, i.e. H₂CO₃, HCO₃⁻, CO₃²⁻, and CO₂) versus NH₄⁺.

APPENDIX C

C.1. Reconciling depth-extrapolated methanogenesis rates and upwards methane flux

The fact that the predicted CH_4 production $J_{\text{CH}_4,\text{ex}}$ accounts for a constant fraction of the porewater gradient estimated J_{CH_4} at all stations indicates that the factor(s) responsible for the difference is not related to the presence of free gas. Neither is it related to the HML thickness in the gas-bearing sediments used in the extrapolation procedure, since the extrapolated rates decrease logarithmically with depth, such that the rates quickly become negligible in the deepest mud layers. For example, from Eq. (5) (main text) the rate of methanogenesis immediately below the SMTZ (233 cm) at M29 would be $18 \text{ pmol cm}^{-3} \text{ d}^{-1}$, but at twice this depth the rate falls to only $4 \text{ pmol cm}^{-3} \text{ d}^{-1}$. At the base of the HML at M29 (864 cm), the rates are an order of magnitude lower still. The mismatch between the porewater CH_4 fluxes and the fluxes estimated from the integration of SRR (Eq. 5) may have one or more of the following explanations:

- (1) An overestimation of the upward CH_4 flux ‘approximated’ from the measured CH_4 concentration in the SMTZ.
- (2) There have been significant changes in the bulk sedimentation rate during the Holocene.
- (3) There have been significant changes in the accumulation rate of organic carbon during the Holocene.
- (4) The depth trend of organic carbon mineralization observed from the measured SRR underestimates mineralization rates in the methanogenic zone.

The first explanation is based on the fact that the fitted linear function to determine the gradient for the CH_4 fluxes includes the data points that visually seem to lie on a straight line. Depending on the person’s observation that is fitting the line, the fluxes may therefore either be over- or underestimated.

The second and third explanations question whether the accumulation of bulk sediment and its organic carbon content have been in a quasi steady state over the last 8 kyr. A sedimentation rate of 1 mm yr^{-1} in the period 2.5 – 1.3 kyr BP and 1.5 mm yr^{-1} in the period 1.3 – 0.6 kyr BP was estimated based on AMS radiocarbon dating of a 3 m long core located close to the present transect (Jensen and Bennike, 2009). These ages correspond to sediment located within the sulfate reduction zone whereas a detailed age model for the methane zone is not available. The TC data show at all stations a very subtle increase with depth that could indicate that organic matter deposition was higher in the past (Bennike and Jensen, 1998). At the end of the ice age, the water depth at the present site would only have been a few meters compared to 20 m today. Unfortunately, data on the inorganic carbon content are lacking, so we cannot definitively attribute the trend in TC to higher organic fluxes when sea level was low during the ice age. Nonetheless, contemporary porewater Ca^{2+} and Mg^{2+} concentration gradients indicate very little or no carbonate precipitation (Appendix A, Fig. A4). In fact, the apparent decrease in these solutes with depth may simply be due to increases in salinity over the last 8 kyr (Gustafsson and Westman, 2002). A slight freshening down core is also indicated by a downward decrease in Cl^- concentrations (data not shown). The above discussion could imply that organic carbon fluxes were higher in the past. However, higher fluxes *per se* reveal nothing about the reactivity of the material being deposited, especially if the relative proportions of marine and terrestrial components changed over time. If the overall rate of carbon mineralization in the deeper layer is in fact higher due to the presence of more reactive organic carbon than assumed, then it is not reflected in the rates derived from the power law slope based on

SRR measured above the SMTZ. Without further data from the deep sediments, the presence of a deep layer of relatively labile organic carbon remains a possible answer to the discrepancy.

The fourth explanation questions the approach used to calculate methanogenesis rates using the power law. The power law extrapolation of mineralization rates from measured SRR down through the methanogenic zone relies on the idea that the rate limiting step in anaerobic carbon mineralization is the initial enzymatic attack on organic material (Jørgensen and Parkes, 2010). The depth and age trend of anaerobic mineralization should therefore theoretically be independent of whether the terminal step is sulfate reduction or methanogenesis. It could be, however, that the measured rates using $^{35}\text{SO}_4^{2-}$ are underestimated, with the relative underestimation becoming increasingly greater closer to the SMTZ than near the surface. In this case, the true exponential coefficient ($-b$, Eq. 4, main text) may be less negative than the one indicated by the SRR data, leading to a less steep curve on the log-log plot (Fig. 9a, main text) and, hence, more sulfate reduction at depth. The thick dotted line in Fig. 9a (main text) would reconcile the diffusive CH_4 fluxes (J_{CH_4}) with the extrapolated methanogenesis rates ($J_{\text{CH}_4,\text{ex}}$). This curve has the following form:

$$\text{SRR} = 5700 \times z^{-2.10} \text{ nmol cm}^{-3} \text{ d}^{-1} \quad \text{Eq. (C.1)}$$

The extrapolated methanogenesis predicted by this function show a close correspondence with the fluxes calculated from the porewater gradients (Fig. C1). The exponent, -2.10, is less negative than the value of -2.33 derived from the original power law function (Eq. (5), main text), meaning that the rates decrease less rapidly with sediment depth. Despite the estimate of the underestimation at the surface and at depth, we cannot pinpoint the reason, why the underestimation of the rates at depth is greater than at the sediment surface.

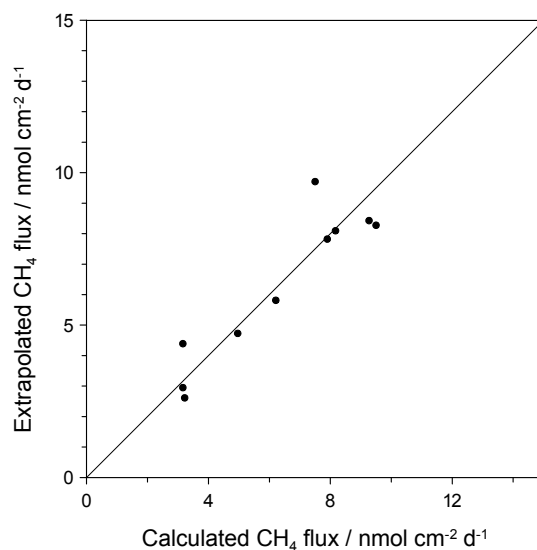


Fig. C1. Methane flux towards the sulfate methane transition zone (SMTZ) calculated from the porewater CH_4 concentrations gradient (x axis) compared to the depth-integrated methanogenesis calculated from extrapolation of mineralization rates based on SRR data (y axis) (see main text section 2.5.2, and Fig. 5a; thick dotted line). The line shows the 1:1 relationship.

Bibliography

- Abegg, F., Anderson, A. L., 1997: The acoustic turbid layer in muddy sediments of Eckernförde Bay, Western Baltic: methane concentration, saturation and bubble characteristics. *Mar. Geo.* 137, 137-147
- Albert, D. B., Martens, C. S., Alperin, M. J., 1998: Biogeochemical processes controlling methane in gassy coastal sediments – Part 2: groundwater flow control of acoustic turbidity in Eckernförde Bay sediments. *Cont. Shelf Res.* 18, 1771-1793
- Algar, C. K., Boudreau, P. B., 2010: Stability of bubbles in a linear elastic medium: Implications for bubble growth in marine sediments. *J. Geophys. Res.* 115, F03012
- Algar, C. K., Boudreau, B. P., Barry, M. A., 2011: Initial rise of bubble in cohesive sediments by a process of viscoelastic fracture. *J. Geophys. Res.* 116, B04207
- Anderson, A. L., Hampton, L. D., 1980: Acoustics of gas-bearing sediments I-II. *J. Acoust. Soc. Am.* 67, 1865-1903
- Anderson, A. L., Bryant, W. R., 1990: Gassy sediment occurrence and properties: Northern Gulf of Mexico. *Geo-Mar. Lett.* 10, 209-220
- Anderson, A. L., Abegg, F., Hawkins, J. A., Duncan, M. E., Lyons, E. P., 1998: Bubble populations and acoustic interaction with the gassy floor of Eckernförde Bay. *Cont. Shelf Res.* 18, 1807-1839
- Baltic Gas, 2012: Final scientific report, compiled by Bo Barker Jørgensen and Henrik Fossing. <http://balticgas.au.dk/>
- Andrén, E., Andrén, T., Sohlenius, G., 2000: The Holocene history of the southwestern Baltic Sea as reflected in a sediment core from the Bornholm Basin. *Boreas* 19, 233-250
- Andrén, T., Björk, S., Andrén, E., Conley, D., Zillén, L., Anjar, J., 2011: Development of the Baltic Sea Basin during the last 130 ka. In: J. Harff et al. (Eds.) *The Baltic Sea Basin. Central and Eastern European Development Studies (CEEDES)*, Springer

- Baltzer, A., Tessier, B., Nouzé, H., Bates, R., Moore, C., Menier, D., 2005: Seistec seismic profiles: A tool to differentiate gas signatures. *Mar. Geophys. Res.* 26, 235-245
- Bertin, X., Chaumillon, E., 2005: New insights in shallow gas generation from very high resolution seismic and bathymetric surveys in the Marennes-Oléron Bay, France. *Mar. Geophys. Res.* 26, 225-233
- Best, A. I., Huggett, Q. J., Harris, A. J. K., 2001: Comparison of in situ and laboratory acoustic measurements on Lough Hyne marine sediments. *J. Acoust. Soc. Am.* 110, 695-709
- Best, A. I., Tuffin, M. D. J., Dix, J. K., Bull, J. M., 2004: Tidal height and frequency dependence of acoustic velocity and attenuation in shallow gassy marine sediments. *J. Geophys. Res.* 109, B08101
- Best, A. I., Richardson, M. D., Boudreau, B. P., Judd, A. G., Leifer, I., Lyons, A. P., Martens, C. S., Orange, D. L., Wheeler, S. J., 2006: Shallow seabed methane gas could pose coastal hazard. *EOS* 87, 213-217
- Björk, S., 1995: A review of the history of the Baltic Sea, 13.0-8.0 ka BP. *Quatern. Int.* 27, 19-40.
- Boetius, A., Ravensschlag, K., Schubert, C. J., Rickert, D., Widdel, F., Gieseke, A., Amann, R., Jørgensen, B. B., Witte, U., Pfannkuche, U., 2000: A marine microbial consortium apparently mediating anaerobic oxidation of methane. *Nature* 407, 623-626
- Borowski, C. et al., 2005: Methane flux control in ocean margin sediments (METROL) Final scientific report, compiled by Christian Borowski
- Boudreau, B. P., Algar, C., Johnson, B. D., Croudace, I., Reed, A., Furukawa, Y., Dorgan, K. M., Jumars, P. A., Grader, A. S., Gardiner, B., S., 2005: Bubble growth and rise in soft sediments. *Geology* 33, 517-520
- Boudreau, B. P., 2012: The physics of bubbles in surficial, soft, cohesive sediments. *Mar. Petrol. Geol.* 38, 1-18
- Breitzke, M., 2000: Acoustic and elastic characterization of marine sediments by analysis, modelling, and inversion of ultrasonic P wave transmission seismograms. *J. Geophys. Res.* 105, 21411-21430
- Breitzke, M., 2006: Physical Properties of Marine Sediments. In: *Marine Geochemistry*, Springer
- Christoffersen, P. L., Christiansen, C., Jensen, J. B., Leipe, T., Hille, S., 2007: Depositional conditions and organic matter distribution in the Bornholm Basin, Baltic Sea. *Geo-Mar. Lett.* 27, 325-338
- Dale, A. W., Regnier, P., Van Cappellen, P., Fossing, H., Jensen, J. B., Jørgensen, B. B., 2009: Remote quantification of methane fluxes in gassy marine sediments through seismic survey. *Geology* 37, 235-238

- Davy, B., 1992: Seismic reflection profiling on southern Lake Rotorua - evidence for gas-charged lakefloor sediments. *Geothermics* 21, 97-108
- Dix, C. H., 1955: Seismic velocities from surface measurements. *Geophysics* 20, 68-86
- Duarte, H., Menezes Pinheiro, L., Curado Teixeira, F., Monteiro, J. H., 2007: High-resolution seismic imaging of gas accumulations and seepage in the sediments of the Ria de Aveiro barrier lagoon (Portugal). *Geo-Mar. Lett.* 27, 115-126
- Ecker, C., Dvorkin, J., Nur, A. M., 2000: Estimating the amount of gas-hydrate and free gas from marine data. *Geophysics* 65, 565-573
- Evans, R. J., Stewart, S. A., Davies, R. J., 2007: Phase-reversed seabed reflections in seismic data: examples related to mud volcanoes from the South Caspian Sea. *Geo-Mar. Lett.* 27, 203-212
- Fleischer, P., Orsi, T. H., Richardson, M. D., Anderson, A. L., 2001: Distribution of free gas in marine sediments: a global overview. *Geo-Mar. Lett.* 21, 103-122
- Flodén, T., Winterhalter, B., 1981: Pre-Quaternary geology of the Baltic Sea. In: Voipio, A. (Ed.): *The Baltic Sea*. Elsevier
- Floodgate, G. D., Judd, A. G., 1992: The origins of shallow gas. *Cont. Shelf Res.* 12, 1145-1156
- Flury, S., Dale, A. W., Røy, H., Fossing, F., Tóth, Zs., Spieß, V., Jensen, J. B., Jørgensen, B. B., in prep: sulphate and methane fluxes and organic matter mineralization across a Holocene mud layer of increasing thickness in Aarhus Bay (W Baltic Sea)
- Fossing, H., 2005: Biogeochemistry and physical properties in core GT04-314GC. doi:10.1594/PANGAEA.327657
- Fu, S. S., Wilkens, R. H., Frazer, L. N., 1996: In situ velocity profiles in gassy sediments: Kiel Bay. *Geo-Mar. Lett.* 16, 249-253
- Garcia-Gil, S., Vilas, F., Garcia-Garcia, A., 2002: Shallow gas features in incised-valley fills (Ría de Vigo, NW Spain): a case study. *Cont. Shelf. Res.* 22, 2303-2315
- Gardner, T. N., 2000: An acoustic study of soils that model seabed sediments containing gas bubbles. *J. Acoust. Soc. Am.* 107, 163-176
- Gardner, T. N., Sills, G. C., 2001: An examination of the parameters that govern the acoustic behavior of sea bed sediments containing gas bubbles. *J. Acoust. Soc. Am.* 110, 1878-1889

- Gardner, T., 2003: Modeling signal loss in surficial marine sediments containing occluded gas. *J. Acoust. Soc. Am.* 113, 1368-1378
- Gassmann, F., 1951: Über die Elastizität poröser Medien. *Vierteljahrsschrift der Naturforschenden Gesellschaft in Zürich* 96, 1-23
- Graversen, O., 2009: Structural analysis of superposed fault systems of the Bornholm horst block, Tornquist Zone, Denmark. *Bulletin of the Geological Society of Denmark*, 57, 2549
- Gülzow, W., Rehder, G., Schneider von Deimling, J., Seifert, T., Tóth, Zs., 2013: One year of continuous measurements constraining methane emissions from the Baltic Sea to the atmosphere using a ship of opportunity. *Biogeosciences* 10, 81-99
- Hagen, R. A., Vogt, P. R., 1999: Seasonal variability of shallow biogenic gas in Chesapeake Bay. *Mar. Geo.* 158, 75-88
- Hajnal, Z., Sereda, I. T., 1981: Maximum uncertainty of interval velocity estimates. *Geophysics* 46, 1543-1547
- Hamilton, E. L., 1970: Sound velocity and related properties of marine sediments, North Pacific. *J. Geophys. Res.* 75, 4423-4446
- Hamilton, E. L., 1972: Compressional-wave attenuation in marine sediments. *Geophysics* 4, 620-646
- Hart, B.S., Hamilton, T.S., 1993: High resolution acoustic mapping of shallow gas in unconsolidated sediments beneath the strait of Georgia, British Columbia. *Geo-Mar. Lett.* 13, 49-55
- HELCOM, 2009: Eutrophication in the Baltic Sea An integrated thematic assessment of the effects of nutrient enrichment and eutrophication in the Baltic Sea region: Executive Summary. *Balt. Sea Environ. Proc.* No. 115A and No. 115B
- Hempel, P., Spieß, V., Schreiber, R., 1994: Expulsion of shallow gas in the Skagerrak - Evidence from sub-bottom profiling, seismic, hydroacoustical and geochemical data. *Eustar. Coast. Shelf S.* 38, 583-601.
- Hovland, M., 1992: Pockmarks and gas-charged sediments in the eastern Skagerrak. *Cont. Shelf Res.* 12, 1111-1119
- IPCC, 2007: The Physical Science Basis. Contribution of Working Group I to the Fourth Assessment Report of the Intergovernmental Panel on Climate Change 2007
- Jackson, D. R., Richardson, M. D., 2007: High-frequency seafloor acoustics. Springer

- Jensen, J. B., Bennike, O., 2009: Geological setting as background for methane distribution in Holocene mud deposits, Arhus Bay, Denmark. *Cont. Shelf Res.* 29, 755-784
- Johnson, B. D., Boudreau, B. P., Gardiner, B. S., Maass, R., 2002: Mechanical response of sediments to bubble growth. *Mar. Geol.* 187, 347-363
- Jørgensen, B. B. et al., 2011: Pore water methane content, density, porosity, C/N content and pore water chemistry of sediment core 374200-6GC, Bornholm Basin, Baltic Sea. doi:10.1594/PANGAEA.763057
In: Jørgensen, B. B., Fossing, H., Endler, R., 2011: Chemistry of sediment cores of RV Poseidon cruise PO392. doi:10.1594/PANGAEA.762358
- Jørgensen, B. B. et al., 2011: Pore water methane content, density, porosity and C/N content of sediment core 374280-2RL, Bornholm Basin, Baltic Sea. doi:10.1594/PANGAEA.763012 In: Jørgensen, B. B., Fossing, H., Endler, R., 2011: Chemistry of sediment cores of RV Poseidon cruise PO392.
- Judd, A. G., 2003: The global importance and context of methane escape from the seabed. *Geo-Mar. Lett.* 23, 147-154
- Judd, A. G., 2004: Natural seabed gas seeps as sources of atmospheric methane. *Environ. Geol.* 46, 988-996
- Judd, A. G., Hovland, M., 1992: The evidence of shallow gas in marine sediments. *Cont. Shelf Res.* 12, 717-725
- Judd, A. G. & Hovland, M., 2007: *Seabed Fluid Flow*. Cambridge University Press
- Kallweit, R. S., Wood, L. C., 1982: The limits of resolution of zero-phase wavelets. *Geophysics* 47, 1035-1046
- Kim, D. C., Lee, G. S., Lee, G. H., Park, S. C., 2008: Sediment echo types and acoustic characteristics of gas-related acoustic anomalies in Jinhae Bay, southern Korea. *Geosciences Journal* 12, 47-61
- Kögler, F-C., Larsen, B., 1979: The West Bornholm basin in the Baltic Sea: geological structure and Quaternary sediments. *Boreas* 8, 1-22
- Laier, T., Jørgensen, N. O., Buchardt, B., Cederberg, T., Kuijpers, A., 1992: Accumulation and seepages of biogenic gas in northern Denmark. *Cont. Shelf Res.* 12, 1173-1186
- Laier, T., Jensen, J.B., 2007: Shallow gas depth-contour map of the Skagerrak-western Baltic Sea region. *Geo-Mar. Lett.* 27, 127-141

- Lee, M. W., Hutchinson, D. R., Dillon, W. P., Miller, J. J., Agena, W. F., Swift, B. A., 1993: Method of estimating the amount of in situ gas hydrates in deep marine sediments. *Mar. Petrol. Geol.* 10, 493-506
- Lee, M. W., Hutchinson, D. R., Collett, T. S., Dillon, W. P., 1996: Seismic velocities for hydrate-bearing sediments using weighted equation. *J. Geophys. Res.* 101, 20347-20358
- Liu, X., Flemings, P. B., 2006: Passing gas through the hydrate stability zone at southern Hydrate Ridge, offshore Oregon. *Earth Planet. Sc. Lett.* 241, 211-226
- Martens, C. S., Albert, D. B., Alperin, M. J., 1998: Biogeochemical processes controlling methane in gassy coastal sediments – Part 1. A model coupling organic matter flux to gas production, oxidation and transport. *Cont. Shelf Res.* 18, 1741-1770
- Mathys, M., Thiessen, O., Theilen, F., Schmidt, M., 2005: Seismic characterization of gas-rich near surface sediments in the Arkona Basin, Baltic Sea. *Mar. Geophys. Res.* 26, 207-224
- Mayne, W. H., 1962: Common reflection point horizontal data stacking techniques. *Geophysics*, 27, 927-938
- Milucka, J., Ferdelman, T. G., Polerecky, L., Franzke, D., Wegener, G., Schmid, M., Lieberwirth, I., Wagner, M., Widdel, F., Kuypers, M. M. M., 2012: Zero-valent sulphur is a key intermediate in marine methane oxidation. *Nature* 491, 541-546
- Missiaen, T., Murphy, S., Loncke, L., Henriot, J-P., 2002: Very high-resolution seismic mapping of shallow gas in the Belgian coastal zone. *Cont. Shelf. Res.* 22, 2291-2301
- Mogollón, J. M., Dale, A. W., L'Heureux, I., Regnier, P., 2011: Impact of seasonal temperature and pressure changes on methane gas production, dissolution, and transport in unfractured sediments. *J. Geophys. Res.* 116, G03031
- Mogollón, J. M., Dale, A. W., Fossing, H., Regnier, P., 2012: Timescales for the development of methanogenesis and free gas layers in recently-deposited sediments of Arkona Basin (Baltic Sea). *Biogeosciences* 9, 1915-1933
- Papatheodorou, G., Hasiotis, T., Ferentinos, G., Gas-charged sediments in the Aegean and Ionian Seas, Greece. *Mar. Geo.* 112, 171-184
- Popescu, I., Lericolais, G., Panin, N., De Batist, M., Hervé, G., 2007: Seismic expression of gas and gas hydrates across the western Black Sea. *Geo-Mar. Lett.* 27, 173-183
- Reeburgh, W. S., 2007: Oceanic Methane Biogeochemistry. *Chemical Reviews* 107, 486-513

- Reeburgh, W. S., 1969: Observations of gases in Chesapeake Bay sediments. *Limnol. Oceanogr.* 14, 368-375
- Richardson, M. D., Briggs, K. B., 1996: In situ and laboratory geoacoustic measurements in soft mud and hard-packed sand sediments: Implications for high-frequency acoustic propagation and scattering. *Geo-Mar Lett.* 16, 196-203
- Robb, G. B. N., Leighton, T. G., Dix, J. K., Best, A. I., Humphrey, V. F., White, P. R., 2006: Measuring bubble populations in gassy marine sediments: a review. *Proceedings of the Institute of Acoustics* 28, Pt.1, 60-68
- Sansone, F. J. and Martens, C. S., 1978. Methane oxidation in Cape Lookout Bight, North-Carolina. *Limnol. Oceanogr.* 23, 349-355
- Schneider von Deimling, J., Weinrebe, V., Tóth, Fossing, H., Endler, R., Rehder, G., Spieß, V., 2013: A low frequency multibeam assessment: Spatial mapping of shallow gas by enhanced penetration and angular response anomaly. *Mar. Petrol. Geol.* 44, 217-222
- Schroot, M. B., Klaver, G. T., Schüttenhelm, R. T. E., 2005: Surface and subsurface expressions of gas seepage to the seabed - examples from the Southern North Sea. *Mar. Petrol. Geol.* 22, 499-515
- Schüler, F., 1952: Untersuchungen über die Mächtigkeit von Schlackschichten mit Hilfe des Echographen. *Deutsche Hydrographische Zeitschrift* 5:220-231
- Sills, G. C., Wheeler, S. J., Thomas, S. D., Gardner, T. N., 1991 Behaviour of offshore soils containing gas bubbles. *Géotechnique*, 41, 227-241
- Simm, R., White, R., 2002: Phase, polarity and the interpreter's wavelet. *First Break* 20, 277-281
- Sivkov, V., Gorbatskiy, V., Kuleshov, A., Zhurov, Y., 2002: Muddy contourites in the Baltic Sea: an example of a shallow-water contourite system. *Deep-Water Contourite Systems: Modern Drifts and Ancient Series, Seismic and Sedimentary Characteristics*. Geological Society, London, Memoirs, 22, 121-136
- Stoll, R. D., Batista, E. O., 1998: Using the Biot theory to establish a baseline geoacoustic model for seafloor sediments. *Cont. Shelf Res.* 18, 1839-1857
- Sviridov, N. I., Frandsen, J. V., Larsen, T. H., Friis-Christensen, V., Madsen, K. E., Lykke-Andersen, H., 1995: The Geology of Bornholm Basin. *Aarhus Geoscience* 5, 15-35
- Taylor, D. I., 1992: Nearshore shallow gas around the U.K. coast. *Cont. Shelf Res.* 12, 1135-1144

- Thießen, O., Schmidt, M., Theilen, F., Schmitt, M., Klein, G., 2006: Methane formation and distribution of acoustic turbidity in organic-rich surface sediments in the Arkona Basin, Baltic Sea. *Cont. Shelf Res.* 26, 2469-2483
- Treéhu, A. M., Flemings, P. B., Bangs, N. L., Chevallier, J., Grá cia, E., Johnson, J. E., Liu, C.-S., Liu, X., Riedel, M., Torres, M. E., Feeding methane vents and gas hydrate deposits at south Hydrate Ridge. *Geophys. Res. Lett.* 31, L23310
- van Kesteren, W., van Kessel, T., 2002: Gas bubble nucleation and growth in cohesive sediments. In: Winterwerp, J. C., Kranenburg, C. (Eds.), *Proceedings in Marine Science, Fine Sediment Dynamics in the Marine Environment*, 5, 329-341
- Vejbæk, O. V., 1985: Seismic stratigraphy and tectonics of sedimentary basins around Bornholm, southern Baltic. *Danmarks Geologiske Undersøgelse Serie A* 8, 30
- Wever, T. F., Fiedler, H. M., 1995: Variability of acoustic turbidity in Eckernförde Bay (southwest Baltic Sea) related to the annual temperature cycle. *Mar. Geo.* 125, 21-27
- Wever, T. F., Abegg, F., Fiedler, H. M., Fechner, G., Stender, I. H., 1998: Shallow gas in the muddy sediments of Eckernförde Bay, Germany. *Cont. Shelf Res.* 18, 1715-1739
- Wheeler, S. J., 1988: A conceptual model for soils containing large gas bubbles. *Géotechnique* 38, 389-397
- Wheeler, S. J., Gardner, T. N., 1989: The elastic moduli of soils containing large gas bubbles. *Géotechnique* 39, 333-342
- Wheeler, S. J., 1990: Movement of large gas bubbles in unsaturated fine-grained sediments. *Mar. Geotechnol.* 9, 113-129
- Whiticar, M. J., 2002: Diagenetic relationships of methanogenesis, nutrients, acoustic turbidity, pockmarks and freshwater seepages in Eckernförde Bay. *Mar. Geol.* 182, 29-53
- Widess, M. B., 1973: How thin is a thin bed? *Geophysics* 38, 1176-1180
- Wilkens, R. H., Richardson, M. D., 1998: The influence of gas bubbles on sediment acoustic properties: in situ, laboratory, and theoretical results from Eckernförde Bay, Baltic Sea. *Cont. Shelf Res.* 18, 1859-1892
- Wood, W. T., Stoffa, P. L., Shipley, T. H., 1994: Quantitative detection of methane hydrate through high-resolution seismic velocity analysis. *J. Geophys. Res.* 99, 9681-9695
- Yilmaz, Ö., 2001: *Seismic Data Analysis: Processing, Inversion, and Interpretation of Seismic Data*, DVD edition, SEG.

- Yuan, F., Bennell, J. D., Davis, A. M., 1992: Acoustic and physical characteristics of gassy sediments in the western Irish Sea. *Cont. Shelf Res.* 12, 1121-1134

Acknowledgement

First and foremost, I would like to thank my parents for all their support and advice and belief that I was capable of taking on the PhD. It would not have been possible for me to write this thesis without their encouragement and support.

I would like to thank my supervisor, Volkhard Spieß for his patience at all times, and our very long discussions from which I have learnt a great deal. His guidance pushed me in the right directions and helped me understand my research topic (part of the world!) better. I would also like to thank the members of my thesis committee and my project, Baltic Gas. Special thanks to Bo Barker Jørgensen and Henrik Fossing for the coordination of the research project, and Gregor Rehder for the research cruise, where I got most of my data from. I enjoyed the time spent together during our workshops, the Baltic Sea cruise and the conferences. It was motivating to be a part of something with important goals and joined efforts. For the successful cooperations, thank you to Jørn Bo Jensen, Tim Ferdelman, Jens Schneider von Deimling, Wanda Gülzow, Sabine Flury. I am particularly grateful for the help given by José Mogollón, who, I felt, was always looking out for me and my work.

I thank my fellow PhD students, postdocs and master students in the working group, Benedict Preu, Luisa Palamenghi, Stefan Wenau, Wenfang Fan, Junhui Xing, Noémi Fekete, Tillmann Schwenk, Hanno Keil, Florian Meier, Niklas Allroggen, Antje Lenhart, Carlos Ramos, who have taken some parts of this journey with me. Research and writing can be a very lonely experience, so thanks for your help in data processing, for the discussions, for listening, for reading, and for all the fun we have had in the last four years.

A huge thank you to my sister and my brother, my best friend, my friends in Budapest and in Bremen, for your friendship, all the moral support, motivation, hugs, chats, laughs, and kindness.

This PhD study was funded through the project Baltic Gas, in the European Community's Seventh Framework Programme (FP/2007 - 2013) under grant agreement nr. 217246 made with the joint Baltic Sea research and development program BONUS.

Name: Zsuzsanna Tóth

Anschrift: Frankfurter Straße 8, 28203 Bremen

ERKLÄRUNG

Hiermit versichere ich, dass ich

1. die Arbeit ohne erlaubte fremde Hilfe angefertigt habe,
2. keine anderen als die von mir angegebenen Quellen und Hilfsmittel benutzt habe und
3. die den benutzten Werken wörtlich oder inhaltlich entnommenen Stellen als solche kenntlich gemacht habe.

Bremen, den 31.08.2013

.....